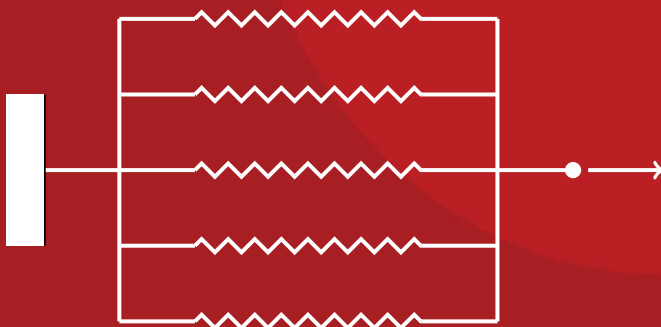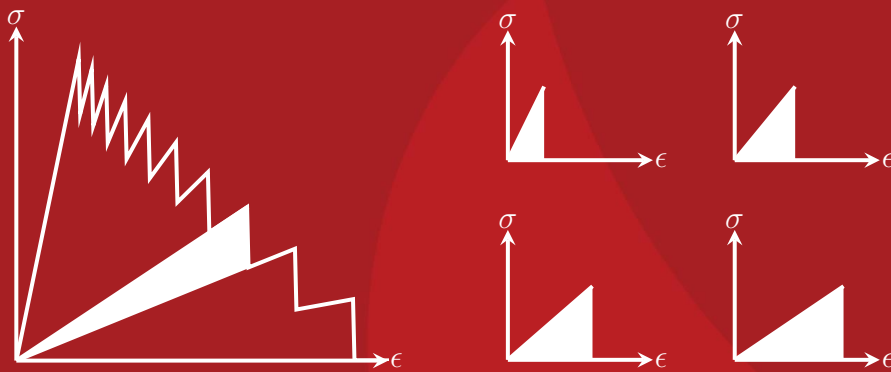# Mimicking a rotating crack model within sequentially linear analysis using an elastic-perfectly brittle sublayer model

Djonno Bresser

TUDelft

DELFT UNIVERSITY OF TECHNOLOGY

MASTER'S THESIS

Mimicking a rotating crack model within sequentially linear analysis using an elastic-perfectly brittle sublayer model

Author:
Djonno BRESSER

Supervisors:
Prof. Dr. Ir. J.G. ROTS
Dr. Ir. M.A.N. HENDRIKS
Ir. M. PARI
Dr. Ir. G.M.A. SCHREPPERS
Ir. L.J.M. HOUBEN

*A thesis submitted in partial fulfillment of the requirements
for the degree of Master of Science*

in

Structural Engineering
Faculty of Civil Engineering and Geosciences

July 5, 2019

"To engineers who, rather than blindly following the codes of practice, seek to apply the laws of nature."

T.Y. Lin, 1955

Preface

In this Master thesis, I present the results of my research on mimicking a rotating crack within the framework of sequentially linear analysis using a sublayer model, as performed in the period between December 2018 and July 2019, conducted in order to obtain my Master's degree in Civil Engineering at the Delft University of Technology at the faculty of Civil Engineering and Geosciences.

Sequentially linear analysis has become an alternative for incremental iterative approaches to simulate the nonlinear fracture behaviour of quasi-brittle materials, without issues related to the lost of convergence. To this end, it is a current topic of research, directed by Jan Rots and Max Hendriks. I am proud to say that I have had the opportunity to contribute to their research program and I would like to thank Max Hendriks for his guidance and for introducing me to this intriguing and challenging subject. The starting point of this thesis, an innovative concept by Hendriks and Rots, was a source of motivation, continuously making me think about new improvements and test cases.

The contributions of all members of the graduation committee are gratefully acknowledged. The comments and dedication of all members are highly appreciated. I would like to thank Jan Rots for his broad knowledge and his passion and enthusiasm during the entire project. In particular, I thank Manimaran Pari for our valuable bi-weekly meetings and for the time spent on preparing the correct implementation of Diana and solving bugs accordingly. Furthermore, I would like to thank Gert-Jan Schreppers from DIANA FEA for sharing his expertise and allowing me to work with the Dev. version of the software. Also, I thank Lambert Houben for his coordinating role and for completing the graduation committee.

Finally, I would like to thank my girlfriend and my family for their understanding and support during this intensive time of research.

Djonno Bresser

Spijkenisse, July 2019

Graduation committee:

Prof. Dr. Ir. J.G. Rots (chairman)	Delft University of Technology
Dr. Ir. M.A.N. Hendriks	Delft University of Technology
Ir. M. Pari	Delft University of Technology
Dr. Ir. G.M.A. Schreppers	DIANA FEA BV.
Ir. L.J.M. Houben	Delft University of Technology

Summary

Master of Science

Mimicking a rotating crack model within sequentially linear analysis using an elastic-perfectly brittle sublayer model

by Djonno BRESSER

Throughout the years, incremental iterative approaches have been shown to be excellent tools in describing the complex behaviour of structures under a wide range of circumstances. However, robustness issues arise for quasi-brittle structures due to the potential lost of convergence during the development of abrupt fracture mechanisms. Although advanced approaches have been developed to tackle these issues, analysts in engineering practice are generally not educated to make use of this wide variety of complicated methods that require a substantial level of expertise. In order to overcome these robustness issues, the framework of sequentially linear analysis (SLA) has been proposed: an event-by-event strategy in which a sequence of scaled linear analyses with decreasing secant stiffness is performed, representing local damage increments. The continuous stress-strain softening curve is replaced by a discontinuous saw-tooth curve. The current SLA-framework is based on a fixed crack approach, potentially causing the development of severe spurious stresses and inaccuracies due to the misalignment of the crack with the principal stress directions. To this end, Hendriks and Rots proposed a model consisting of several parallel fractions or layers, from now on called the sublayer model. Each of the layers is elastic-perfectly brittle, but has different properties, chosen such to represent the overall constitutive softening behaviour as accurate as possible. The layers fail independent of each other and have their own specific crack direction. The main idea is to mimic a rotating crack by a superposition of sublayers with a fixed crack direction. The main goal of this thesis is to further elaborate, generalize and verify the sublayer model for quasi-brittle materials and capture the influence of rotating cracks on the structural response within the framework of existing regular sequentially linear analysis.

In this thesis, the frameworks of regular SLA and the sublayer model were connected by a general transition from any saw-tooth law to sublayer material properties. An externalized procedure was created to automatically generate an input file for DIANA FEA and thereby facilitate verification of the sublayer model. Furthermore, the 2-dimensional framework of the sublayer model has been extended towards 3-dimensional structures to broaden the range of application. On top of that, concepts were proposed to improve the sublayer model: the tapered ripple band, reducing the required number of sublayers to reach a specific state by adding more saw-teeth near the end of the softening curve, and an improved algorithm, making use of the fact that the order of brittle fracture of the sublayers is known in advance, such that only those integration points that can actually become critical are monitored, thereby reducing computational efforts significantly.

From single element problems, it was concluded that the superposition of sequentially cracking elastic-perfectly brittle sublayers approximates a rotating crack model quite well, such that pronounced differences with fixed crack regular SLA are observed. For multi-element problems, the reduction of spurious stresses at single element level inherently reduced the generation of spurious stresses in surrounding elements, thereby leading to differences at structural level as well.

In the first place, the sublayer model consistently exhibited sharper crack localization and thereby less wide bands of spurious stresses around the main crack path, less stress-locking and therefore less energy dissipation compared to regular SLA. As a result, a more flexible post-peak response was observed in the load-displacement graphs of the sublayer model compared to regular SLA, which became especially clear for the case studies on the notched beam and the shear notched beam. For regular SLA, the crack direction is fixed upon initiation and during subsequent steps, misalignment with the principal stress direction causes spurious shear stresses to develop within the crack plane, while the sublayer model accommodates a stepwise multi-directional crack rotation, thereby better approximating the principal directions and reducing the generation of spurious shear stresses.

In the second place, it was concluded that the advantage of SLA to follow asymmetric failure modes and circumvent bifurcations, comes with the disadvantage of potentially enforcing locally asymmetric failure modes for symmetric problems, as have been encountered for the notched beam and double-edge-notched beam case studies. On the other hand, the sublayer model is still able to overcome bifurcations by following asymmetric failure modes, but is meanwhile able to correct itself when the asymmetric failure mode is undesired. For both the notched beam and double-edge-notched beam, regular SLA inherently resulted in a gradually increasing locally asymmetric crack path since damage increments could only be performed at one location at a time. With the aid of the sublayer model, the development of this local asymmetry was found to be restricted.

Lastly, the sublayer model has been proven to be better able to adapt to changing stress states, which for example take place for non-proportional loading, stress redistributions and crack-closure. Especially for the performed case studies on full scale problems (a full scale masonry facade under monotonic lateral load and a full scale concrete dam subjected to static overflow load), more physically justified collapse mechanisms have been observed for the sublayer model. Based on these three observations, it was concluded that also at structural level, a rotating crack model is mimicked by the sublayer model. The sublayer model well mimics the rotating crack model, while at the same time it preserves the charm of SLA in being more robust than alternative incremental-iterative approaches.

Throughout the thesis, several element types were applied. It is recommended to make use of quadratic elements, which consistently showed to reduce effects of mesh-directional bias for both regular SLA and the sublayer model. However, for SLA-type of procedures in general (thus both methods), mesh-directional bias issues were observed despite the reducing effects of quadratic elements. On top of that, it was concluded that the rotating crack model in conventional incremental-iterative analysis might increase mesh-directional bias even more. As the sublayer model tries to mimick a rotating crack, the user must be aware of this phenomenon.

For the 3D-implementation, a case study was performed on an inclined notched beam and consistent results with the 2D-framework were found, such that all conclusions for 2D hold for 3D as well. On top of that, both regular SLA and the sublayer model proved to be equivalent to their incremental iterative counterparts, being the

fixed crack model and rotating crack model respectively, although both regular SLA and the sublayer model exhibited a more narrow band of spurious stresses.

Furthermore, the tapered ripple band, which was introduced to more effectively discretize the softening curve and reduce the relative influence of sublayers with out-dated fixed crack directions, reduced the required number of sublayers by 26% for a case study on the notched beam, thereby considerably limiting computational costs. To allow for application in engineering practice, reduction of computational efforts of the sublayer model is a must: compared to regular SLA, 4 to 5 times more computational efforts are required by the current externalized implementation of the sublayer model, where regular SLA in itself is already computationally demanding compared to incremental iterative approaches. However, the man-hour costs to steer the complicated analyses with brittle failures are reduced considerably with both regular SLA and the sublayer model compared to incremental-iterative analyses.

For future research to the sublayer model, it is recommended to focus on the proposed improvements and extensions, especially on the tapered ripple band and the improved computational algorithm that considerably reduces the required number of integration points that should be monitored during the analysis. The former improvement has already been shown to effectively reduce computational efforts and the latter improvement is only discussed conceptually (although a considerable improvement of computational efforts is expected). Furthermore, further research is required to reduce mesh-directional bias, for example by implementing a crack tracking algorithm, although it is noted that mesh-directional bias is a general issue for any crack-band model in a finite element context. Thirdly, it is recommended to perform further research on crack-closure. Although the sublayer model proved to be able to overcome crack-closure by redistribution of stresses, the stiffness was not able to recover during stress-reversal, thereby leaving room for improvement. Lastly, it is noted that for application in engineering practice, the framework should be extended towards reinforced concrete, rather than focusing on merely plane concrete structures.

Contents

Chapter 1

Introduction

This chapter gives an introduction on the thesis by describing both the background of the subject as well as the motivation for performing this research in Section 1.1. Then, the research goals are defined, together with the scope of this research in Section 1.2. Lastly, the thesis approach and outline are briefly touched upon in Section 1.3.

1.1 Background and motivation

For centuries, quasi-brittle materials like concrete and masonry have been prevalently used as building material in the construction industry; a trend that will continue in the next centuries. Concrete is used for its high compressive strength and favourable durability [30, 81]. However, concrete has some significant drawbacks: concrete has a small tensile load-bearing capacity and shows quasi-brittle failure behaviour, meaning that after the initiation of damage only a (relatively) small residual deformation capacity is available and hence, the structure cracks quite abruptly and very locally. These abrupt cracks induce peaky behaviour in the load-displacement curve. Around these peaks, standard incremental iterative analysis, also called non-linear finite element analysis (NLFEA), shows convergence problems as a result of alternative equilibrium paths and hence, the robustness of the solution procedure is strongly affected by quasi-brittle fracture, as has been found by many authors (a.o. [9, 29, 32, 51, 58, 66]). Pari [58] mentions three causes for the occurrence of alternative equilibrium paths:

- Material softening leads to negative tangent stiffness and therefore ill conditioning of the stiffness matrix.

- Within a load step, multiple integration points can reach the damaged state at the same time, generating multiple alternative equilibrium paths, thus creating a bifurcation point.

- Snap-trough, snap-back and divergence situations, which are characteristic for brittle fracture, are potentially troubling, although not necessarily with the aid of path-following techniques, for incremental iterative approaches.

The analysis of a shear critical reinforced concrete beam without shear reinforcement by Slobbe et al. [73] is a good example of problematic quasi-brittle fracture behaviour. In their study, they considered a simply supported single-span beam loaded by a mid-span point load and compared numerical solutions with sample *'beam six'* from experiments performed by Sarkhosh et al. [69]. The considered beam was designed to withstand bending and anchorage failure, such that shear failure
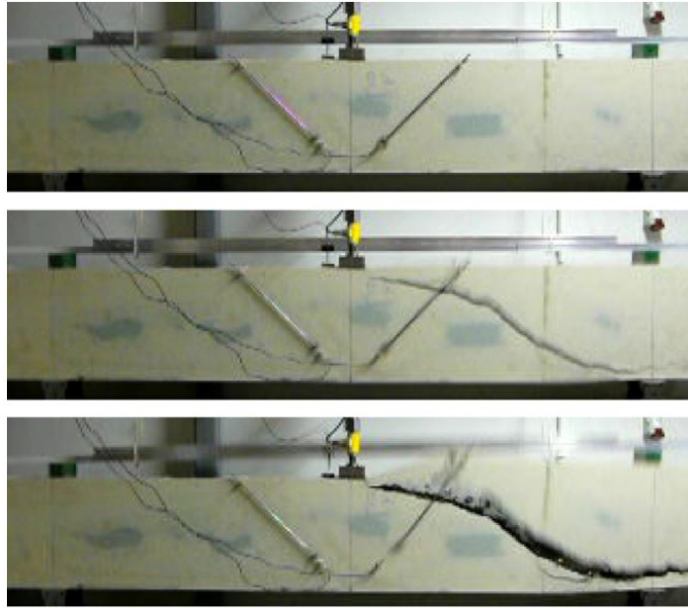
FIGURE 1.1: Three consecutive snap-shots from the failure of beam
six with time steps of 0.03s, taken from [73]

became governing. The moment of failure is shown in Figure 1.1 by three consecutive pictures from the experiment, with time steps of 0.03 seconds in between. From this pictures can be seen that the beam fails in a brittle way; the load-bearing capacity is lost after the formation of the diagonal crack, which is very localized and abrupt. Slobbe et al. performed a nonlinear finite element analysis and were able to simulate the behaviour up until the moment prior to diagonal cracking. As cracking occurred abruptly, the nonlinear finite element analysis was not able to obtain converged load steps. This case exemplifies the robustness issues regarding computational modelling of concrete failure.

Robustness problems are even more pronounced for large-scale structures, of which the size is several orders of magnitude larger then regular fundamental experiments like the notched beam, as discussed by Van de Graaf [29]. The ratio between the stored elastic energy and the dissipated energy upon fracture is a measure for the brittleness of the structure. For very brittle structures, this ratio is large [66]. Large-scale structures made of quasi-brittle material show localized cracking (e.g. in a specific corner of the facade), meaning that the amount of dissipated energy during fracture is small compared to the stored elastic energy over the complete structure and hence, large-scale structures show even more brittle response, inducing more emphasized robustness issues.

In order to overcome these robustness issues, Rots [63] proposed the framework of *sequentially linear analysis* (SLA). SLA is an event-by-event strategy, in which a sequence of scaled linear analyses with a decreasing secant stiffness is performed, representing local damage increments. The idea is partially inspired by concrete engineering practice, where the stiffness of concrete is reduced in areas where cracking is expected, and a linear elastic analysis is performed. In this way, the influence of cracking on the stress distribution is accounted for. In the SLA-procedure, the constitutive relation is discretized to a stepwise secant material law (a so-called saw-tooth curve). During SLA, representative unit loads are put on the structure and a linear elastic analysis is performed. The critical element or integration point, which is the element for which the ratio between the maximum principal stress and

the strength is the highest, is searched for and the loading is scaled to the strength of the critical element via the so-called critical load multiplier. Next, a damage increment is performed for the critical element (a step in the saw-tooth curve) and a new linear elastic analysis is executed for the damaged structure. From the results of the damaged structure, a new critical element is found etc. This procedure is repeated until damage is fully developed or when the damage reached a certain user-specified state. In Chapter 3, the principles of SLA are further elaborated. With the aid of this event-by-event strategy, based on linear elastic analysis, no convergence problems are obtained, leading to a robust numerical analysis of quasi-brittle structures. On the other side, current SLA is not able to handle crack-closure as a result of stress reversal and stress redistribution due to the assumed secant unloading [58]. Furthermore, some difficulties are found for non-proportional loading, as finding the critical element and its corresponding critical load multiplier is not as straightforward anymore. DeJong et al. [21] described an algorithm to encounter non-proportional loading, as will be further discussed in Chapter 3.

In regular SLA, upon initiation of damage in a specific element, the direction of the crack for that element is fixed perpendicular to the maximum principal stress at the considered moment, thus following a fixed crack approach, which will be discussed in more detail together with other cracking models in Chapter 2. As explained by Rots [62], the principal stresses might rotate due to rotating loads and/or stress distributions. However, the crack does not rotate, causing a misalignment of the principal directions and crack directions and consequently, spurious shear stresses are generated in the plane of the crack. These spurious shear stresses cause additional energy dissipation and as a result, the structure behaves stiffer. If the crack co-rotates with the principal stresses, which is the case for a rotating cracking model (see Section 2.3), no spurious shear stresses in the cracking plane are found.

In an attempt to mimick rotating cracks within sequentially linear analysis, Hendriks and Rots [31] proposed a model consisting of several parallel fractions or layers, from now on called the *sublayer model*. Each of the layers is elastic-perfectly brittle, but has different properties, chosen such to represent the constitutive behaviour as accurate as possible. The layers fail independent of each other and have their own specific crack direction. The main idea is to mimick a rotating crack by a superposition of sublayers with a fixed crack direction. The sublayer model will be in more detail described in Chapter 4. As mentioned by Hendriks and Rots, softening is in fact a gradual reduction of the cross-sectional area due to the formation of micro-cracks, hereinafter the sublayer model actually considers softening in a more physical way compared to regular SLA. The first test results as presented in [31] are promising: no over-stiff behaviour of the model is observed, thus indicating a rotating crack model to be simulated.

The sublayer model fits well within sequentially linear analysis and, since the sublayer model has not been fully developed yet and is only tested for a limited number of cases, this thesis will proceed the work of Hendriks and Rots.

1.2   Research goals and scope

As mentioned in Section 1.1, the sublayer model as proposed by Hendriks and Rots [31] has not been fully developed and tested yet. Furthermore, the paper presents case-specific saw-tooth curves instead of a (for programming purposes) desired general approach. Therefore, the main goal of this Master's thesis is defined as follows:

*The goal of this Master's thesis is to further **elaborate**, **generalize** and **verify** the sublayer model for quasi-brittle materials and capture the influence of rotating cracks on the structural response **within** the framework of existing regular sequentially linear analysis.*

Once the layer-properties of the sublayer model have been determined, the sublayer model follows the same procedure as regular sequentially linear analysis and therefore, it is aimed to develop a method that works within the framework of regular SLA. By doing so, the sublayer model can be combined with existing extensions of regular SLA like non-proportional loading [21] and Coulomb shear failure [29]. In this way, there is no need to reinvent these extensions for the sublayer model, which makes it possible to implement the model **within** the framework of existing regular SLA in a straightforward manner.

In order to achieve the main goal of this Master's thesis, multiple sub-goals have been defined, each corresponding to different parts of the threefold main goal (namely elaborate, generalize and verify the sublayer model):

1. **generalize** - *Describing a general transition from the saw-tooth law to the sublayer model* for tension softening and compressive crushing to obtain equivalent sublayer properties. The inputted saw-tooth law is the same as the one used by regular SLA, which will be discussed in Section 3.4.

2. **elaborate** - *Implementing the sublayer model in DIANA FEA* by developing a practical algorithm such that it can be applied to practical cases. The algorithm can also be externalized (outside the environment of DIANA) as a type of pre-processing approach.

3. **verify** - *Verification of the created model in DIANA FEA* regarding both the correctness of the sublayer model and the correctness of the written algorithm. Some basic numerical tests like fundamental element tests and notched beam tests are performed to analyze the performance of the created sublayer model.

4. **elaborate** - *Defining a "sublayer" model in 3D*. During the development of the sublayer model by Hendriks and Rots, no possible extension to 3D has been considered. In 3D, the name "sublayer" model becomes a bit vague, since the three dimensions probably require the use of sub-volumes.

5. **elaborate** - *Implementing concrete cracking and crushing in one material point* in the sublayer model. In 2D, a material point can be loaded in two principal directions in both tension and compression (for example, the tensile capacity is depending on the perpendicular compressive stress). The goal is to find a way to take account of this interaction.

6. **elaborate** - *Describing crack closure/stress reversal effects*. Since the damage increments in SLA are permanent and secant unloading is assumed, it is not possible to consider unloading and crack closure. Once the stress state changes from tension to compression, the damaged stiffness is maintained in the compressive regime for regular SLA where the undamaged stiffness should be used.

Each of the goals is given a different priority and desired level of sophistication. Subgoals 1 to 4 are top priority and should be performed and discussed in a detailed manner. Subgoals 5 and 6 are elaborated on a lower level of detail and the goal is rather the conceptual idea rather than a detailed verification study. Possibly, tests

on single element level are performed to support the findings of subgoals 5 and 6. To this end, subgoals 5 and 6 are interpreted as extensions of the main developed procedure in subgoals 1 to 4.

This study aims to contribute to the ongoing research into sequentially linear analysis and proceeds on the works of many others. When not stated otherwise, 2D behaviour and plane stress conditions are considered. Furthermore, only homogeneous quasi-brittle materials that behave linear elastic isotropic prior to cracking are considered. The focus is on plane concrete behaviour: reinforced concrete structures are not considered. On top of that, only (quasi-) static loads are considered, meaning that equilibrium between internal and external loads is not influenced by dynamic inertial effects. In literature, many detailed studies on specific parameters (crack band, softening/hardening laws, mesh properties etc.) are performed in order to represent experimental results as good as possible. Although it is tempting to focus on matching the experimental results as accurate as possible by the sublayer model, the main goal of this thesis is to mimic the results of a rotating crack nonlinear finite element analysis by a robust sequentially linear analysis. In this study, the comparative analyses with regular SLA and NLFEA are both performed using standard simplified parameters, not making use of sophisticated crack band definitions, crack tracing algorithms, complex elasto-plastic material laws and irregular meshes. Therefore, it makes more sense to compare the results of the sublayer model with the results of regular SLA and NLFEA instead of experimental results (which often require sophisticated approaches), as all analyses are performed based on the same material laws and meshes etc. Off course, the damage propagation obtained by the sublayer model is qualitatively compared with experimental outcomes as well to review the physical correctness of the approach.

1.3 Thesis approach and outline

The contents of this thesis are built up following the flowchart of Figure 1.2. First, a literature study is performed in Chapters 2 and 3 on non-linear computational modelling of concrete and sequentially linear analysis respectively. Next, the theoretical framework of the sublayer model is described by Chapter 4, together with some alternative approaches from literature. Hereinafter, Chapter 5 couples the sublayer model to the current SLA framework. In order to physically understand the behaviour of the proposed sublayer model, single element tests are performed in Chapter 6. Subsequently, the sublayer model is validated with the aid of a wide range of structural case studies in Chapter 7. The framework is extended towards 3-dimensional problems in Chapter 8 and rather conceptual improvements to the sublayer model are proposed in Chapter 9. Lastly, Chapter 10 summarizes the new developments of this thesis, lists the conclusions and gives recommendations for further research.

Literature study

Chapter 2: NLFEA

Chapter 3: regular SLA

Chapter 5: general transition SLA to sublayer model

Chapter 4: sublayer model

Verification

Chapter 6: single element tests 2D

Chapter 7: structural tests 2D

Chapter 8: single element and structural tests 3D

Chapter 9: improvements and extensions

Chapter 10: conclusions and recommendations
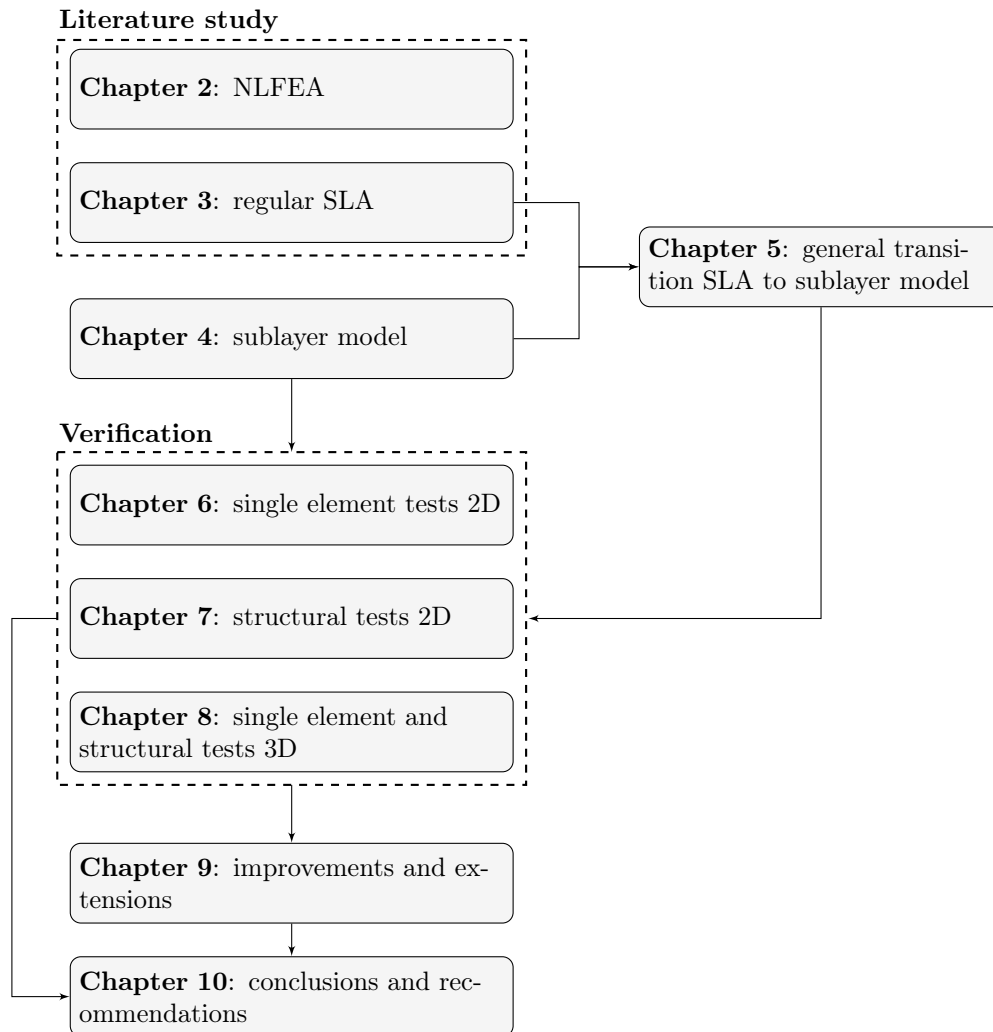
FIGURE 1.2: Flowchart of thesis outline

Chapter 2

Nonlinear modelling of concrete

In this chapter, different approaches to model the cracking behaviour of concrete are discussed. First, general principles of concrete behaviour are elaborated in Section 2.1. Then, the two main concepts of concrete fracture modelling, namely discrete and smeared cracking, are explained in Sections 2.2 and 2.3 respectively. This chapter is focussed on concrete fracture in tension, although concrete fracture in compression is briefly discussed in Section 2.3.5. It should be noted that the aim of this chapter is rather the description and understanding of models in a physical way then considering the theoretical backgrounds.

2.1 General

In Section 1.1, concrete has been described as a quasi-brittle material, meaning that, after the initiation of damage, limited deformation capacity is obtained. Quasi-brittle behaviour is schematized together with brittle and ductile behaviour in the load-displacement curve of Figure 2.1. Ductile materials like steel show large residual deformation capacity, which is favourable for design purposes. On the contrary, brittle materials like glass do not have any deformation capacity and result in immediate failure.
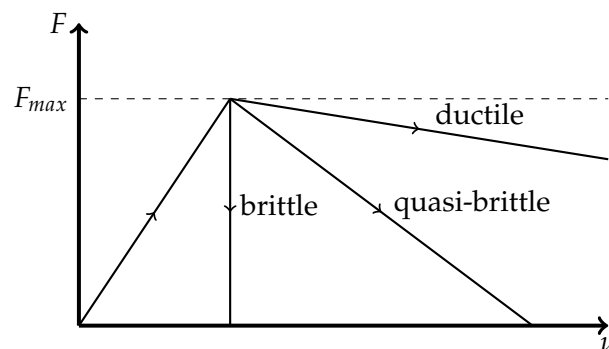
FIGURE 2.1: Schematization of brittle, quasi-brittle and ductile behaviour in the load-displacement curve

Cracking and crack propagation in concrete is mostly governed by the material behaviour in tension, so in literature, most of the studies on concrete fracture are focused on the response in tension. Concrete fracture in compression is briefly touched upon in Section 2.3.5. As described by Rots et al. [68], experiments have shown that the tensile response of concrete shows multiple stages: 1) a limited number of micro-cracks is formed everywhere throughout the specimen; 2) once a certain strength limit is reached somewhere in the specimen, all additional deformation
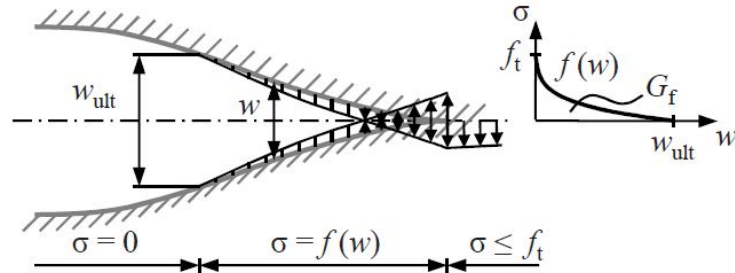
FIGURE 2.2: Representation of fictitious crack model from Hillerborg
et al., taken from Slobbe [71]

due to micro-cracking is localized in the so-called *fracture zone*; 3) within the fracture
zone, tension softening takes place, meaning that the local stresses decrease and
strains increase and 4) at the end of the tension softening, the micro-cracks unite into
one stress-free macro-crack. The aforementioned fracture process has been physi-
cally described by Hillerborg et al. [35] with the *fictitious crack model*, which is repre-
sented by Figure 2.2, showing the different stages of cracking. This model assumes
the existence of a fictitious crack, which can transfer a certain amount of stresses,
prior to the real crack, which does not transfer stresses. The work of Hillerborg et
al. followed and adapted the cohesive zone model of Dugdale [22] and Barenblatt
[3], which is suited for elastic-perfect plastic materials like steel. The function $f(w)$,
valid inside the fracture zone, is the tension softening function, which gradually
decreases to 0 upon increasing displacements w within the fracture zone, hence sim-
ulating the transition from localizing micro-cracks to a stress-free macro-crack. In
Section 2.2, some specific tension softening functions will be discussed. At the crack
tip, the stress is equal to the strength limit f_t. The energy required to generate a full
developed crack over a unit area is called the *fracture energy* G_f and is a measure
for the ductility of a material (e.g. for ductile materials, large fracture energies are
found). As the fracture energy of a specific material is approximately constant, it
can be assumed to be a material property, following the approach of many authors
(e.g. [4, 29, 62, 68]). Material outside the fracture zone unloads as a result of the
localization of deformation within the fracture zone, causing micro-cracks outside
the fracture zone to arrest or close.

The fracture as shown in Figure 2.2 is a mode I fracture, meaning that the concrete
deforms perpendicular to the cracking plane and only crack opening displacements
are found during cracking stages 3 and 4. On top of that, mode II fracture can be
considered, in which deformation parallel to the cracking plane via crack sliding
displacements are observed. Off course, mixed mode fracture problems are possible.

Cracking stage 2 is initiated once a certain strength limit is reached. For uni-axial
loading cases with mode I fracture, the tensile strength f_t of the concrete is used as a
criteria. For bi-axial loading cases, interaction between the two principal stresses is
observed and the strength limit becomes stress-dependent [30, 43]. This dependency
is visualized by Figure 2.3. As a result of this interaction, lower tensile strength limits
are found for laterally compressed concrete.

Generally, there are two ways to implement the fictitious crack model within fi-
nite element analyses: *discrete* and *smeared* cracking. For discrete cracking, the crack
is simulated by geometric discontinuities between the elements using so-called inter-
face elements, which are able to separate element edges, see Figure 2.4a. For struc-
tural behaviour that is mainly governed by the formation of dominant cracks, the
discrete cracking model gives proper results. However, the discrete cracking model
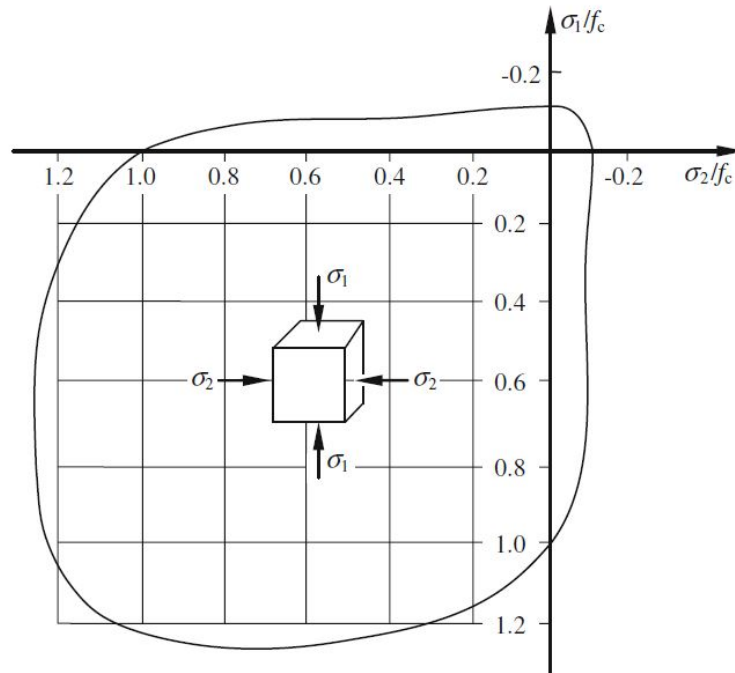
FIGURE 2.3: Example interaction graph concrete strength under biax-
ial stress according to Kupfer et al. [43], taken from [30]

(A) Discrete cracking model

(B) Smeared cracking model
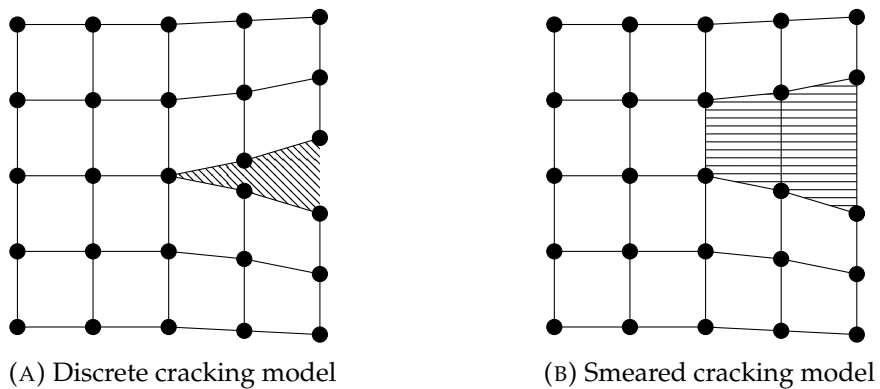
FIGURE 2.4: Representation of discrete and smeared cracking of a
simple mesh with linear elements
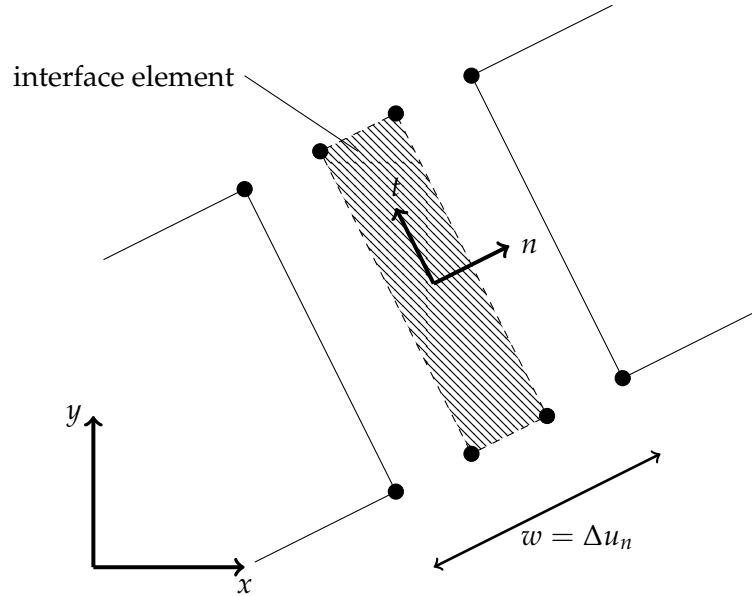
FIGURE 2.5: Discrete cracking model with linear 2-D interface element and coordinate definitions

is not suited to capture diffused cracking patterns, meaning distributed cracking throughout the structure, because one would need to use a very fine mesh with interface elements throughout the complete structure. For that purpose, the smeared cracking model has been developed. In the smeared cracking model, the discontinuities are included in the constitutive laws of the elements, meaning that the crack is 'smeared out' over a so-called crack band instead of localized within an interface element, as can be seen in Figure 2.4b. The size of the crack band depends on the properties of the finite element model (e.g. element type and size) [62]. As cracking is included within the constitutive behaviour of each of the elements, diffused cracking patterns can be captured. Both of the cracking models will be further elaborated in Sections 2.2 and 2.3.

2.2   Discrete cracking model

The discrete model, as shown in Figure 2.4a, represents the crack by geometric discontinuities between the elements using interface elements and is based on fracture mechanics, as the behaviour within the cracking plane is described. The development of discrete crack modelling started with the work of Ngo and Scordelis [54] and later on Hillerborg [34]. They added the possibility to separate continuum elements, which is achieved by including interface elements within the finite element discretization (so prior to the calculation to maintain mesh topology during the calculation). The interface element is located between two element edges, as shown in Figure 2.5, and is activated once a certain threshold stress is reached and thereby mimics the formation of a crack. In the finite element geometry, the interface element has zero thickness. By definition, cracks are only allowed to form at locations where interface elements are placed, inherently causing the cracks to form in predefined crack paths. When the crack path is known in advance, the interface elements can be located to follow the expected crack path and hence, proper and straightforward results can be found. However, the cracking model has trouble with cases

where the cracking path is not known in advance. During later researches (e.g. by Blaauwendraad and Grootenboer [8]), automatic remeshing techniques have been developed to capture random cracking patterns. However, these are not further considered in this thesis.

The fictitious crack model, as discussed in Section 2.1, is implemented in the discrete element model with the use of a traction-separation law as constitutive relation for the interface elements. In order to have no influence of the interface element prior to cracking, high dummy stiffness are required for the initial elastic stage. It should be mentioned that these dummy values can not be taken too high, since this might induce ill-conditioning of the stiffness matrix [71]. The traction-separation law of the interface elements relates the forces acting on the interface to the relative displacements in between the two element edges. For the elastic uncracked stage, the interface normal traction t_n and shear traction (in tangential direction) t_t depend on the relative normal displacement Δu_n, defined in Figure 2.4, and shear displacement Δu_t via

$$\begin{bmatrix} t_n \\ t_t \end{bmatrix} = \begin{bmatrix} k_{n,0} & 0 \\ 0 & k_{t,0} \end{bmatrix} \begin{bmatrix} \Delta u_n \\ \Delta u_t \end{bmatrix} \tag{2.1}$$

in which $k_{n,0}$ and $k_{t,0}$ are the aforementioned high dummy stiffness values to have a rigid connection between the two considered elements prior to cracking. In case of mode I fracture, which is often governing in concrete structures due to it's low tensile strength, the crack is initiated when the normal traction $t_n = f_t$, with f_t being the tensile strength of the concrete. At crack initiation, the constitutive relation of Equation 2.1 is changed to

$$\begin{bmatrix} t_n \\ t_t \end{bmatrix} = \begin{bmatrix} k_n & 0 \\ 0 & k_t \end{bmatrix} \begin{bmatrix} \Delta u_n \\ \Delta u_t \end{bmatrix} \tag{2.2}$$

with k_n and k_t as secant normal and shear stiffnesses. From the fictitious crack model follows that, after the initiation of cracking, the stresses reduce due to tension softening. With the discrete crack model, this is obtained by reducing the normal and shear stiffnesses for increased displacements according to a certain tension softening law $f(w)$. Assuming that the dummy stiffness for the elastic stage are high, the relative displacements prior to cracking are assumed to be 0, hence the crack opening displacement $w = \Delta u_n$ and the crack sliding displacement $s = \Delta u_t$. As the normal and shear components are assumed to be independent, they can be considered separately. In literature, many tension softening curves are found. One of the most simple tension softening curves is linear tension softening, given by

$$t_n(w) = \begin{cases} f_t \left(1 - \frac{w}{w_u}\right) & \text{if } w \leq w_u \\ 0 & \text{if } w > w_u \end{cases} \tag{2.3}$$

with $w_u = 2G_f^I/f_t$ as the maximum crack width and G_f^I being the fracture energy required to form a completely developed mode I crack. Once w_u is reached, a stress-free macro-crack is formed. Figure 2.6 shows linear and exponential tension softening. The latter is given by

$$t_n = f_t \exp\left(-\frac{f_t}{G_f^I} w\right) \tag{2.4}$$

As the exponential function of Equation 2.4 does not have a maximum crack width w_u, it is assumed that full cracking has occurred after 98% of the fracture

(A) Linear tension softening

(B) Exponential tension softening
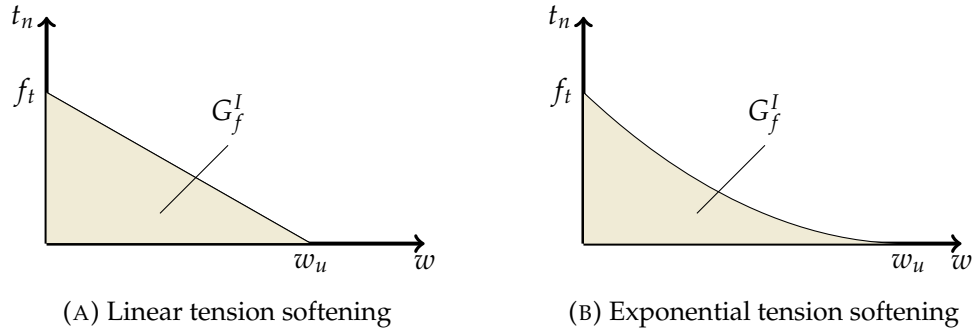
FIGURE 2.6: Selection of mode I tension softening relations for a discrete cracking model

energy G_f^I has been released. Furthermore, nonlinear tension softening curves can be applied, for example the Moelands and Reinhardt [60] and the Hordijk et al. tension softening curves [19] (for more info, the reader is referred to the mentioned reports).

Until now, only mode I fracture has been considered. However, the interface element might also fail in mode II fracture, also known as sliding type of failure. Prior to cracking, the initial Equation 2.1 is still valid. Mode II cracking can be described using the Coulomb-friction model, as is extensively discussed by Van de Graaf [29]. According to the Coulomb-friction model, the sliding resistance depends on the normal traction t_n and the cohesion c and hence, the mode II crack initiation criterion is given by

$$|t_t| = -t_n \tan\phi + c \tag{2.5}$$

with ϕ being the friction angle. After crack initiation, the sliding behaviour might be influenced by multiple types of action, e.g. frictional softening, cohesion softening and hardening [29]. In Equation 2.2, implicitly no coupling between the normal and tangential components of the traction was assumed. This assumption does not hold for materials for which *dilatancy* becomes relevant, meaning that there is some coupling between the normal and tangential components and hence, the diagonal terms in Equation 2.2 are not zero anymore and uplifting of an element upon sliding is obtained. In this way, a physical representation of aggregate-interlock can be formulated. This is however not further discussed in this thesis.

2.3 Smeared cracking model

Describing cracking with discrete discontinuities between two crack surfaces is in line with our physical understanding of cracking. However, in experiments often bands of micro-cracking are formed within the concrete, which can be better captured with the concept of smeared cracking [68]. Within the smeared crack model, local discontinuities are distributed over some area of the considered finite element, creating a *crack band*, as shown by Figure 2.4b. By including the cracked state within the constitutive relations, continuum stress-strain relations can be used to completely describe the process of cracking. Because the cracks are represented by strains, a continuous displacement field is obtained at the element edges, where the discrete crack model provides a discontinue displacement field. As cracking is implemented within the constitutive laws, cracks can form over the complete structure without the

(A) Cracked eight-noded element

(B) Definition of coordinate system
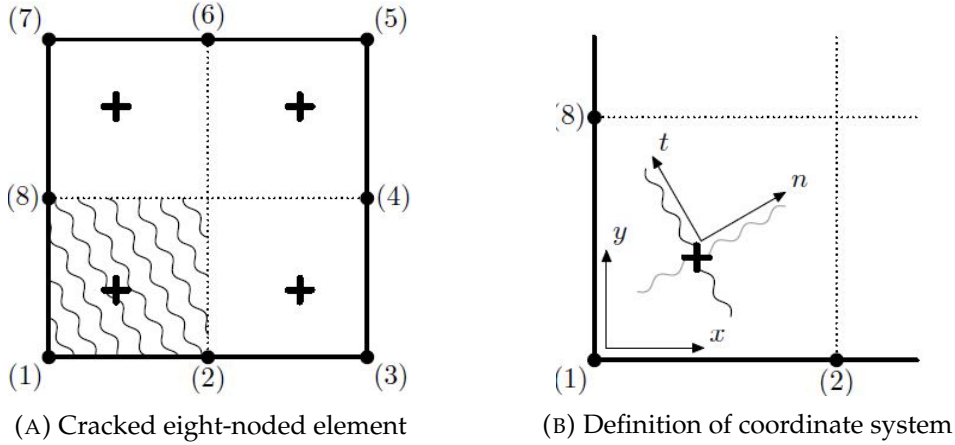
FIGURE 2.7: Representation of the smeared cracking model for an eight-noded plane stress element with the definition of the coordinate system in the plane of the primary crack, taken from [29]

disadvantages of a predefined crack-path. To combine the advantages of both discrete and smeared cracking, some researchers also considered combining both (e.g. Munjiza et al. [53]). However, this option is not further considered in this thesis.

Prior to cracking, the two-dimensional concrete behaviour is described by the linear elastic isotropic formulation given by

$$
\begin{bmatrix} \sigma_{xx} \\ \sigma_{yy} \\ \sigma_{xy} \end{bmatrix} = \frac{E_0}{1 - v_0^2} \begin{bmatrix} 1 & v_0 & 0 \\ v_0 & 1 & 0 \\ 0 & 0 & \frac{1-v_0}{2} \end{bmatrix} \begin{bmatrix} \epsilon_{xx} \\ \epsilon_{yy} \\ \gamma_{xy} \end{bmatrix}
\tag{2.6}
$$

In the earliest version of the smeared crack model by Rashid [59], Poisson effects were not considered and only the stiffness parallel to the crack was maintained after the initiation of the crack (the stiffness normal to the crack and the crack shear stiffness were set to zero upon cracking). This abrupt transition in stiffness is not realistic, as experiments show a gradual cracking by tension softening. Furthermore, changing the stiffness directly to zero resulted in numerical issues [62]. Therefore, a more gradual reduction of stiffness has been applied for both the normal as the shear stiffness components, where the latter is only necessary when shear stresses are active in the cracking plane. Bazant and Oh [5] stated that the original smeared crack formulation included a mesh size dependency as a result of the crack being spread over an element with a certain size and therefore proposed the *crack band approach*. In this approach, the fracture energy is spread over the cracked area, as appears from Figure 2.7a, which is characterized by a certain crack band length h. By doing so, the constitutive curve depends on the size of the crack band such that the fracture energy absorbed by a specific cracks becomes independent of the mesh size. For linear two-dimensional elements, $h = \sqrt{2A}$ and for higher-order two-dimensional elements, $h = \sqrt{A}$, with A the area of the element. For more information on the size of the crack band, the reader is referred to [62]. For this thesis, it is important to understand that the crack band depends merely on the finite element geometry and element type.

The coordinate system of the cracked element is defined in the same way as for discrete cracking, as appears from Figure 2.7b: the normal n-axis is pointed perpendicular to the crack direction and the tangential t-axis is pointed parallel to the

crack. Once the primary crack is formed, a secondary crack might form perpendicular to the primary crack. Within the framework of the smeared crack model, three conceptual ideas can be separated:

1. *Fixed crack model*: the direction of the crack is fixed upon initiation.

2. *Fixed multidirectional crack model*: multiple fixed non-orthogonal cracks, with a certain threshold angle in between, can form.

3. *Rotating crack model*: the direction of the crack is updated continuously.

Each of these three concepts will be discussed in the subsequent sections. For the smeared crack model, two starting points can be used: the total strain and the decomposed strain model. The former model is most used in engineering practice and is implemented in DIANA based on the work of Feenstra et al. [25]. The latter model is proposed by De Borst and Nauta [10] and splits the fracture zone in the contribution of 1) the uncracked concrete between the micro-cracks and 2) the opening of micro-cracks in the cracked concrete, allowing the concrete and the crack interface to be treated separately. Furthermore, the influences of other nonlinear influences like plasticity and shrinkage can be captured in the decomposed strain framework. The total strain model assumes that both of these two contributions can be captured with a total strain constitutive law by

$$\epsilon = \epsilon^{el} + \epsilon^{cr} \tag{2.7}$$

where ϵ^{el} and ϵ^{cr} are the elastic strain and crack strain respectively. Before cracking occurs, the response is fully elastic. Once cracking takes place, the response is determined by superposition of the elastic and crack components and the stress at the crack gradually decreases, reducing the influence of the elastic strain component. When reaching the ultimate strain, for which zero stress transfer is found, the response is fully governed by the crack strain component. According to Rots et al. [68], the total strain formulation of Equation 2.7 holds if 1) only one crack occurs at a sampling point, 2) concrete behaves linear elastic and 3) no coupling between failure modes I and II takes place. For the purpose of these thesis, the fixed and rotating crack model can be elaborated using the total strain formulation. The multidirectional crack model does not fulfill requirement 1) and hence, a strain decomposition is necessary.

2.3.1   Fixed total strain smeared crack model

As mentioned in Section 2.3, the fixed crack model as used in this thesis is based on the total strain formulation (although a decomposed strain formulation is also possible). In this model, the direction of the crack is fixed upon initiation and is found by the principal stress directions n and t (Figure 2.7b) at that specific moment. After the crack-initiation, the principal directions might change while the crack direction is maintained and therefore, shear stresses are developed within the cracking plane. Prior to cracking, the isotropic formulation of Equation 2.6 holds. At the onset of cracking, this expression is replaced by (from [21, 29])

$$\begin{bmatrix} \sigma_{nn} \\ \sigma_{tt} \\ \sigma_{nt} \end{bmatrix} = \frac{1}{1 - \nu_{tn}\nu_{nt}} \begin{bmatrix} E_n & \nu_{nt}E_n & 0 \\ \nu_{tn}E_t & E_t & 0 \\ 0 & 0 & (1 - \nu_{tn}\nu_{nt})\,G_{red} \end{bmatrix} \begin{bmatrix} \epsilon_{nn} \\ \epsilon_{tt} \\ \gamma_{nt} \end{bmatrix} \tag{2.8}$$

(A) Linear tension softening

(B) Exponential tension softening
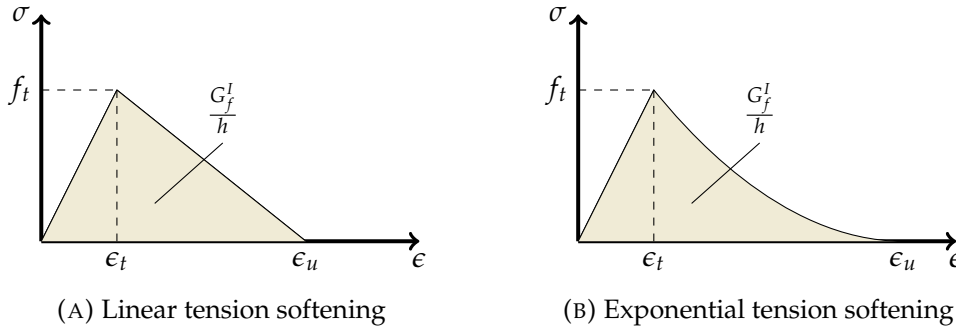
FIGURE 2.8: Selection of mode I tension softening relations for a
smeared cracking model

where E_n, E_t, G_{red}, ν_{nt} and ν_{tn} are the damaged apparent properties. After the formation of a primary crack, the direction of the crack is fixed and a reduced normal stiffness E_n is inserted according to the applied tension softening law and E_t is kept E_0, since this direction is not cracked. With the orthotropic damage formulation of Equation 2.8, compressive struts can form parallel to the crack, which is especially relevant for reinforced concrete structures [21, 29, 71]. Within the considered model, a second crack is allowed to form perpendicular to the primary crack. Then, the tangential stiffness E_t is also reduced according to the softening law. Normal to the crack, large strains may develop causing large Poisson effects to influence the behaviour in the tangential direction. To limit these effects, the Poisson ratio is assumed to reduce at a similar rate as the corresponding stiffness.

$$\nu_{nt} = \nu_0 \frac{E_t}{E_0} \quad \text{and} \quad \nu_{tn} = \nu_0 \frac{E_n}{E_0} \tag{2.9}$$

Hence, when a crack is completely opened and the stiffness perpendicular to the crack has reduced to zero, no Poisson effect parallel to the crack is obtained. In the normal and tangential directions, mode I cracking occurs, so the apparent stiffness E_n and E_t can be found with the aid of a tension softening curve in a similar way as for the discrete crack model. However, the smeared crack elements differ from the interface elements as they have pre-cracking elastic deformations that can not be neglected, as has been visualized for linear and exponential tension softening in Figure 2.8. Also, the dependency of the constitutive law on the crack band, as introduced by Bazant and Oh [5], becomes clear from this figure. The continuum constitutive law describing linear tension softening in a smeared crack formulation is in line with Equation 2.3 and is given by

$$\sigma(\epsilon^{cr}) = \begin{cases} f_t \left(1 - \dfrac{\epsilon^{cr}}{\epsilon_u^{cr}} \right) & \text{if } \epsilon^{cr} \leq \epsilon_u^{cr} \\ 0 & \text{if } \epsilon^{cr} > \epsilon_u^{cr} \end{cases} \quad \text{with} \quad \epsilon_u^{cr} = \frac{2G_f^I}{f_t h} \tag{2.10}$$

with ϵ_u^{cr} as the ultimate crack strain, being equal to the ultimate total strain ϵ_u as the elastic strain ϵ^{el} is reduced to zero. Linear tension softening is depicted by Figure 2.8a. Following Equation 2.4, exponential tension softening in a continuum formulation is described by

$$\sigma(\epsilon^{cr}) = f_t \exp\left(-\frac{f_t}{G_f^I} \epsilon^{cr} \right) \tag{2.11}$$

Figure 2.8b visualizes exponential tension softening. Defining the ultimate strain ϵ_u^{cr} as the strain for which 98% of the fracture energy has been released, the ultimate strain is approximately $3.91 G_f^I / f_t h$. Lastly, the nonlinear continuum softening function proposed by Hordijk [19] is described by

$$
\sigma(\epsilon^{cr}) = \begin{cases} f_t \left[\left(1 + \left(c_1 \dfrac{\epsilon^{cr}}{\epsilon_u^{cr}} \right)^3 \right) \exp\left(-c_2 \dfrac{\epsilon^{cr}}{\epsilon_u^{cr}} \right) \\ \qquad - \dfrac{\epsilon^{cr}}{\epsilon_u^{cr}} (1 + c_1^3) \exp\left(-c_2 \right) \right] & \text{if } \epsilon^{cr} \leq \epsilon_u^{cr} \\ \\ 0 & \text{if } \epsilon^{cr} > \epsilon_u^{cr} \end{cases}
\tag{2.12}
$$

with $c_1 = 3$ and $c_2 = 6.93$ and the ultimate strain equal to $5.136 G_f^I / f_t h$. Besides the given tension softening relations, other relations are possible, for example the Moelands and Reinhardt curve [60] and multilinear tension softening curve. These are however not further elaborated in this thesis. When large elements are used, the crack band h increases and the ratio G_f^I / h reduces, meaning that the area underneath the tension softening curve also reduces. For linear tension softening the ultimate strain $\epsilon_u = 2 G_f^I / f_t h$ might even become smaller than the elastic strain $\epsilon_t = f_t / E_0$, leading to a constitutive snap-back. This type of behaviour is numerically troubling when using a Newton-Raphson type of approach, as the negative slope in the tangent stiffness might lead to unstable behaviour [37].

For fixed crack models, the definition of a tension softening law for E_n and E_t is not sufficient, as the principal directions might start to deviate from the crack direction introducing shear stresses on the cracking plane. Hence, also the development of shear stresses and especially the shear stiffness G_{red} during cracking must be considered. During the years, many experimental and finite element research has been performed on mode II shearing during cracking (e.g. by Walraven [82]). From this research followed interaction between normal and tangential components (between tension softening and aggregate interlock). This observation is the result of dilatancy, as has also been discussed for discrete cracking in Section 2.2. For smeared cracking, dilatancy leads to numerical difficulties and is therefore often neglected [71] and decoupled behaviour is assumed. The shear behaviour during cracking is then described using a *shear retention* factor $G_{red} = \beta G_0$. The shear retention factor can be a constant (mostly ≈ 0.2) or a variable depending on the shear strain. For this thesis, the shear retention relation as proposed by DeJong et al. [21] is used

$$
G_{red} = \frac{E_{min}}{2 \left(1 + \nu_0 \frac{E_{min}}{E_0} \right)}
\tag{2.13}
$$

where $E_{min} = \min(E_n, E_t)$.

After crack initiation, the stresses and strains are considered in the local (n,t)-coordinate frame. When simplifying Equation 2.8 to

$$
\sigma_{nt} = D_{nt}\, \epsilon_{nt}
\tag{2.14}
$$

it can be rotated to the global (x, y)-coordinate frame via the rotation matrix T, which describes the relation $\sigma_{nt} = T\sigma_{xy}$ and hence,

$$
\sigma_{xy} = T^{-1} D_{nt} T\, \epsilon_{xy}
\tag{2.15}
$$

with $\boldsymbol{T}$ given by

$$\boldsymbol{T} = \begin{bmatrix} \cos\theta^2 & \sin\theta^2 & \sin\theta\cos\theta \\ \sin\theta^2 & \cos\theta^2 & -\sin\theta\cos\theta \\ -2\sin\theta\cos\theta & 2\sin\theta\cos\theta & \cos\theta^2 - \sin\theta^2 \end{bmatrix} \tag{2.16}$$

For the fixed crack approach, angle θ is kept fixed after the initiation of cracking.

2.3.2 Fixed multidirectional decomposed strain crack model

The development of shear stresses in the cracking plane for fixed crack models makes that the principal directions do not longer align with the crack directions and therefore, principal tensile stresses larger than the tensile strength might be found (because the stresses are considered in the cracking plane) and incorrect structural behaviour is predicted. In this way, the phenomena *stress locking* takes place, meaning that non-physical stresses are generated. As energy is dissipated by these non-physical stresses, stiffer structural behaviour is found. In order to reduce stress locking effects, De Borst and Nauta [10] developed the multi-directional non-orthogal fixed crack model. The algorithm is very simple and delicate: once an element is cracked, a second crack is allowed to form after the principal directions changed more than a certain threshold angle α. Following the same idea, third and fourth cracks can also form. Each of the formed cracks can have multiple states like opened, unloading, closed and even re-opening. Based on this algorithm, multiple non-orthogonal cracks can be described at one integration point.

As mentioned in Section 2.3, multiple cracks can not be modelled using a total strain formulation and therefore, the decomposed strain formulation, as pioneered by Litton [48] and given by

$$\boldsymbol{\epsilon} = \boldsymbol{\epsilon}^{co} + \boldsymbol{\epsilon}^{cr} \tag{2.17}$$

is required. Equation 2.17 consists of two components: the strain of the uncracked concrete $\boldsymbol{\epsilon}^{co}$ to model the linear elastic behaviour of the material between the cracks and the strain of the crack plane $\boldsymbol{\epsilon}^{cr}$ to model crack-opening stresses (e.g. tension softening effects). With the aid of this decomposition, the distribution of multiple cracks can be taken into account by

$$\boldsymbol{\epsilon}^{cr} = \boldsymbol{\epsilon}^{cr}_1 + \boldsymbol{\epsilon}^{cr}_2 + ... + \boldsymbol{\epsilon}^{cr}_n \tag{2.18}$$

with n the number of cracks. The constitutive law of each of the cracks is employed and the system is solved in an incremental iterative manner. During the increments, the principal directions are monitored and once they have changed more than a threshold angle α (generally in between 30 and 60 degrees), a new crack is formed in that specific direction. Furthermore, the state of the other cracks is monitored during the increments. Due to the decomposed strain approach, other nonlinearities can be included in a straightforward manner. However, these are not considered in the scope of this thesis. Lastly, De Borst and Nauta neglected the influences of crack dilatancy, for the same reasons as mentioned in Section 2.3.1.

2.3.3 Rotating total strain crack model

The third crack model that is discussed is the rotating crack model. In the fixed crack model, the angle θ is fixed upon initiation, leading to stress locking. In the rotating

crack model, proposed by Cope et al. [18], the direction of the crack plane is constantly updated and therefore co-rotates with the principal stress directions. In this way, coaxiality between principal stresses and the cracks is maintained and the development of spurious stresses is resolved, where the aforementioned methods did not. In essence, the rotating crack model uses the same principles as explained in Section 2.3.1 and the total strain approach is aplied. In the fixed crack model, the choice of a shear retention factor is sometimes quite arbitrary and difficult. This inconvenience, together with the development of spurious stresses, is solved by the rotating crack model, as mentioned by Li and Zimmerman [47]. The shear retention factor is chosen based on the *principle of coaxiality*, enforcing the directions of principal strains and principal stresses to coincide according to

$$G_{red} = \frac{\sigma_{nn} - \sigma_{tt}}{2(\epsilon_{nn} - \epsilon_{tt})} \tag{2.19}$$

where the *n*- and *t*-directions are the updated principal stress directions. The principle of coaxiality can be explained using the assumption of material orthotropy [62], meaning that the response of the material is direction-dependent. This assumption generally causes the principal stress direction to deviate from the principal strain direction. Upon rotation of an existing crack, the principal strains are directly co-rotated because the crack is inherently incorporated in the strain field (which is the nature of the smeared crack model). The rotation of the strain field causes a rotation of the stress field as the stress is related to the strain via the orthotropic constitutive law. As the strains follow from the multiplication of the constitutive D-matrix and the local strain field, the rotations of the stress and strain fields do not by definition coincide, potentially troubling the complete method as principal stresses and strains are not considered within the same plane. Obtaining coaxiality between the principal stresses and strains is however possible by requiring the shear stiffness term G_{red} in the orthotropic constitutive law to follow Equation 2.19. For mathematical proof of this explanation, the reader is referred to [62].

According to Rots [62], the rotating crack model can be understood as the limit case of multidirectional fixed cracking, because the rotating crack is actually the continuous creation of new cracks in an updated direction, where only the last formed crack is active and the previous cracks are closed. Under the assumption that, in an integration point, only one crack is active at a time and that coaxility is maintained by Equation 2.19 (in general the multidirectional fixed crack model does not require coaxiality for the principal stresses and strains, but in this case coaxiality is enforced to be in line with the rotating crack model), the multidirectional fixed crack model with a threshold angle α approaching zero actually reduces to the rotating crack model. Under these assumptions, a rotating crack can be physically explained as the formation of new micro-cracks in the updated principal stress direction, while previously formed micro-cracks are closed.

2.3.4   Numerical issues regarding smeared crack model

Besides the many advantages of the smeared crack model, the model also suffers from some disadvantages, especially when considering the numerical implementation. This section mentions the most relevant numerical issues and gives a brief description. For more information, the reader is referred to the given references.

- *Element size dependency*: the smeared crack model suffers to a certain amount of element size and type dependency. Although the dependency significantly

reduces with the aid the crack band model by Bazant and Oh [5], it is still hard do exactly define a crack band that gives a fracture energy that is objective with respect to the element-size. Slobbe [71] gives an elaborate description on ways to obtain an objective solution.

- *Directional mesh bias*: as discussed by Rots [62] and Cook et al. [17], smeared crack model suffer from strain localization along continuous mesh lines. Or in other words: the crack, represented by a band of strain localization, prefers to follow continuous mesh lines. In this way, a directional mesh bias is introduced. This issue can be reduced using a cross-diagonal pattern of triangles [62] or a crack tracking algorithm (e.g. [17]).

- *Stress locking*: as discussed in Section 2.3.2, fixed smeared cracking models suffer from a type of stress locking as a result of the spurious (shear) stresses in the plane of cracking. Due to the crack not co-rotating with the principal stresses, unrealistic stresses are found in the cracking plane (e.g. a high shear retention value might lead to large shear stresses for a completely developed crack, which is stress-free). This kind of stress locking is not found for rotating crack models. However, as described by Jirasek and Zimmermann [39], a certain amount of stress locking also follows from the inability of finite elements to reproduce the discontinuous nature of the actual displacement field around a crack, meaning that the finite elements are not compatible and spurious stresses are found. This phenomena is present for both fixed as rotating smeared crack models and especially becomes relevant for well-developed cracks. In order to overcome these issues, Jirasek and Zimmermann [40] proposed the rotating crack model with a transition to scalar damage. The scalar damage law ensures that no spurious stresses develop for widely opened cracks.

- *Convergence*: within an incremental iterative (NLFEA) approach, the smeared crack model might lead to local snap-back behaviour, as mentioned in Section 2.3.1. As a result of this, general Newton-Raphson type of procedure might encounter stability problems and more advanced procedures might be required.

2.3.5   Concrete in compression

Up until now, the elaboration of concrete fracture has been limited to tensile (mode I) cracking. However, concrete fracture might also take place under compression, possibly combined with tension. In the past decades, many experiments have been performed to investigate the compressive behaviour of concrete, for example by Van Mier et al. [76] and Kotsovos [42]. In both research programs, concrete specimens are subdued to uniaxial compressive loading and the influence of different boundary conditions is studied. When concrete fails in compression, *concrete crushing* is observed, meaning that the cohesion between aggregate particles is lost. The behaviour during concrete crushing is highly depending on material properties, like compressive strength and stiffness, which show significant variations [30]. On top of that, the crushing behaviour is highly nonlinear and hence, concrete crushing has been a topic of debate in literature. During the years, many advanced models have been developed to capture the compressive fracture behaviour (e.g. plasticity models, damage models or combined plasticity-damage models) possibly combined with perpendicular tensile loads. However, for implementation in the SLA framework (see Chapter 3), it is more convenient to apply the same type of approach as

(A) Thorenfeldt compressive crushing
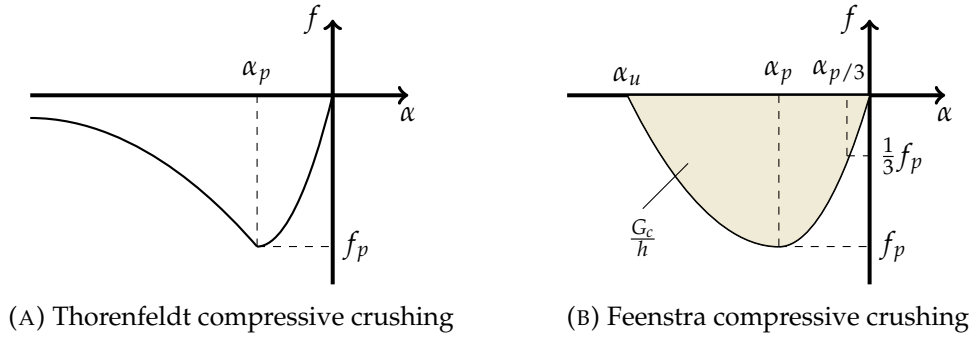

(B) Feenstra compressive crushing

FIGURE 2.9: Selection of compressive softening/hardening relations
for a smeared cracking model

for tension softening. Therefore, compressive crushing is described with the aid of constitutive softening/hardening laws, without making use of plasticity type of formulations. In this section, relevant constitutive laws from literature are discussed.

As a starting point, the *modified compression-field theory* from Vecchio and Collins [77, 78] is used. In this theory, cracked concrete is treated as a different material with its own stress-strain relations. Application of the modified compression-field theory becomes especially relevant for reinforced concrete, as the structural coherency is maintained during cracking and compressive struts parallel to the crack might develop. Laterally cracked (reinforced) concrete has been observed to exhibit lower strength and stiffness in compression compared to uniaxially loaded concrete specimens as deterioration of the concrete during cracking results in a reduced compressive resistance and therefore, a certain amount of *compression softening* occurs [77]. The amount of compression softening of a specific base constitutive curve is described by parameter β. Generally speaking, both the peak stress f_c and the corresponding strain ϵ_c of a base curve (several base curves will be discussed later) could be reduced by a different β, causing the actual peak stress f_p and corresponding strain α_p to be found by

$$
\begin{aligned}
f_p &= \beta_\sigma f_c \\
\alpha_p &= \beta_\epsilon \epsilon_c
\end{aligned}
\tag{2.20}
$$

and the actual stress f and strain α by

$$
\begin{aligned}
f &= \beta_\sigma \sigma \\
\alpha &= \beta_\epsilon \epsilon
\end{aligned}
\tag{2.21}
$$

In literature, many constitutive compressive base curves can be found. The most simple base curve is the bilinear stress-strain relation, which increases linearly until the strength is reached and continues horizontally until the maximum strain is reached. Thorenfeldt et al. [75] proposed the compressive crushing curve as shown in Figure 2.9a. The Thorenfeldt constitutive curve is described by

$$
f = -f_p \frac{\alpha}{\alpha_p} \left(\frac{n}{(n-1) + \left(\frac{\alpha}{\alpha_p}\right)^{nk}} \right)
\tag{2.22}
$$

with

$$n = 0.80 + \frac{f_c}{17} \quad \text{and} \quad k = \begin{cases} f_c & \text{if } \alpha_p < \alpha < 0. \\ 0.67 + \dfrac{f_c}{62} & \text{if } \alpha \leq \alpha_p. \end{cases} \tag{2.23}$$

and f_p and α_p found by Equations 2.20. For high strength concretes, a steeper second branch is obtained in the Thorenfeldt curve, inducing more brittle behaviour. Note that Equation 2.23 is not depending on the crack band size h and the compressive fracture energy G_c. On the contrary, the constitutive curve used by Feenstra [24] depends on both the crushing crack bandwidth h and fracture energy G_c, fitting the same framework as tension softening behaviour. The Feenstra curve is shown in Figure 2.9b and described by

$$f = \begin{cases} -\frac{1}{3} f_c \frac{\alpha}{\alpha_{p/3}} & \text{if } \alpha_{p/3} < \alpha \leq 0 \\ -\frac{1}{3} f_c \left(1 + 4 \left(\frac{\alpha - \alpha_{p/3}}{\alpha_p - \alpha_{p/3}} \right) - 2 \left(\frac{\alpha - \alpha_{p/3}}{\alpha_p - \alpha_{p/3}} \right)^2 \right) & \text{if } \alpha_p < \alpha \leq \alpha_{p/3} \\ -f_c \left(1 - \left(\frac{\alpha - \alpha_p}{\alpha_u - \alpha_p} \right)^2 \right) & \text{if } \alpha_u < \alpha \leq \alpha_p \\ 0 & \text{if } \alpha \leq \alpha_u \end{cases} \tag{2.24}$$

with

$$\alpha_{p/3} = -\frac{1}{3} \frac{f_c}{E} \quad \text{and} \quad \alpha_p = 5\alpha_{p/3} \quad \text{and} \quad \alpha_u = \alpha_p - \frac{3}{2} \frac{G_c}{h f_c} \tag{2.25}$$

As can be seen in Equations 2.24 and 2.25, the Feenstra curve makes use of the crushing crackband approach. Furthermore, the area enclosed by the Feenstra curve is equal to G_c/h, with G_c approximately 50 to 100 times the tensile fracture energy G_f [24]. Besides the curves of Thorenfeldt and Feenstra, many other curves can be found in literature (e.g. the Hognestad parabola [36]). However, for the purpose of this thesis, they are not further elaborated.

The work of Vecchio and Collins [77] becomes relevant when considering the behaviour of laterally cracked concrete (a tensile crack in direction of principal strain ϵ_1). As a result of softening parameters β_σ and β_ϵ, the base curve σ_2-ϵ_2 relation changes to a f-α relation, according to Equation 2.21. Vecchio and Collins developed two models to capture the influences of lateral cracking on the base curve: model A and model B. Both models take the Thorenfeldt curve as a base curve, as this curve was found to have good correlation with experimental data. It is not known whether the approach can be combined with other base curves. The softening parameters of model A are found based on statistical evaluations of the data of 443 experiments:

$$\begin{aligned} \beta_{\sigma,A} &= \frac{1}{1 + K_{c,A} K_{f,A}} \\ \beta_{\epsilon,A} &= \beta_{\sigma,A} \end{aligned} \tag{2.26}$$

where $K_{c,A}$ is a factor taking account of the lateral tensile strain relative to the compressive strain via

$$K_{c,A} = 0.35 \left(\frac{-\epsilon_1}{\epsilon_2} - 0.28 \right)^{0.80} \geq 1.0 \tag{2.27}$$

and $K_{f,A}$ is a multiplier taking account of the influence of the concrete compressive strength, as softening in high strength concrete was found to be more pronounced, given as

$$K_{f,A} = 0.1825\sqrt{f_c} \geq 1.0 \tag{2.28}$$

In model A, both the (peak) stress and corresponding strain are reduced and a ratio experimental to calculated stresses of 0.996 with a coefficient of variation of 18.8% is obtained [77]. Model B is a simplified model, leading to a slightly weaker correlation with the test data. A ratio experimental to calculated stresses of 1.022 with a coefficient of variation of 21.1% is obtained. In this model, only the stresses are reduced to account for softening:

$$\begin{aligned} \beta_{\sigma,B} &= \frac{1}{1 + K_{c,B}} \\ \beta_{\epsilon,B} &= 1 \end{aligned} \tag{2.29}$$

with $K_{c,B}$ a factor taking account of the lateral strain relative to the compressive strain ϵ_c belonging to the peak strain in the Thorenfeldt base curve, given by

$$K_{c,B} = 0.27 \left(\frac{\epsilon_1}{\epsilon_c} - 0.37 \right) \tag{2.30}$$

Lastly, compressive behaviour of concrete under biaxial stress states is discussed. It has already been discussed that the biaxial strength of concrete under combined tension and compression depends on the stresses in both principal directions (Figure 2.3). However, if concrete is laterally confined, meaning that it is under compression in each of the principal directions, the compressive strength and ductility increase significantly [30]. Eventually for the limit case of triaxial equal loading, no compressive failure is obtained. The influence of lateral confinement is not further considered in this thesis, as the complex constitutive behaviour of lateral confined concrete is hard and possibly not achievable to capture within the framework of sequentially linear analysis.

Chapter 3

Sequentially Linear Analysis

In this chapter, the sequentially linear analysis is further elaborated. First, an introductory example is discussed in Section 3.1 in which cracked concrete is modelled using a spring. Then the development and general theory of SLA are described in Sections 3.2 and 3.3 respectively. A characteristic feature of SLA is the set-up of a saw-tooth law, as discussed in Section 3.4. Lastly, Section 3.5 mentions and briefly discusses the application issues regarding SLA.

3.1 Example 1: modelling cracked concrete with a spring

When concrete in tension starts cracking, it effectively loses a certain amount of stiffness as the bond between aggregates and the cement is locally lost. Furthermore, the maximum stress in the cross-section reduces as only the effective uncracked cross-section can be fully loaded up until f_t. The micro-cracks in the cracked part of the cross-section follow the tension softening laws as discussed in Chapter 2. The main concept of sequentially linear analysis is exemplified using the following simple example of a single spring in tension. A spring with initial stiffness $\beta_1 k$, with for simplicity $\beta_1 = 1$, as shown in Figure 3.1, is loaded with a tensile load F. The spring will be used to model uncracked and cracked concrete in uniaxial tension.
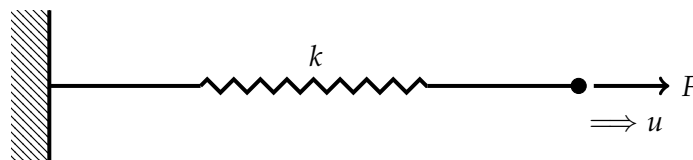
FIGURE 3.1: Model of a single spring with stiffness k loaded by a
tensile load F

The spring has a maximum load capacity of $\alpha_1 F_m$, with for simplicity $\alpha_1 = 1$, and once $\alpha_1 F_m$ is reached, the spring fails, is completely unloaded and is replaced by a more flexible and weaker spring in order to simulate the behaviour of cracked concrete. The replacement of a spring at a critical load is called a *damage increment*. This weaker spring has a stiffness $\beta_2 k$ and strength $\alpha_2 F_m$ with α_2 and β_2 in between 0 and 1. Once load $\alpha_2 F_m$ is reached, the spring is again unloaded and replaced by an even more flexible and weaker spring, with stiffness $\beta_3 k$ and strength $\alpha_3 F_m$, mimicking the increase of damage. This process is repeated until the complete load carrying capacity is lost. In this way, the nonlinear progression of damage is simulated with the aid of linear calculations according to $F = k u$. The choice of factors α_i and β_i results in a specific load path. The inverse of this statement also holds once the number of damage increments is defined: the choice of a specific load path results in factors α_i and β_i.
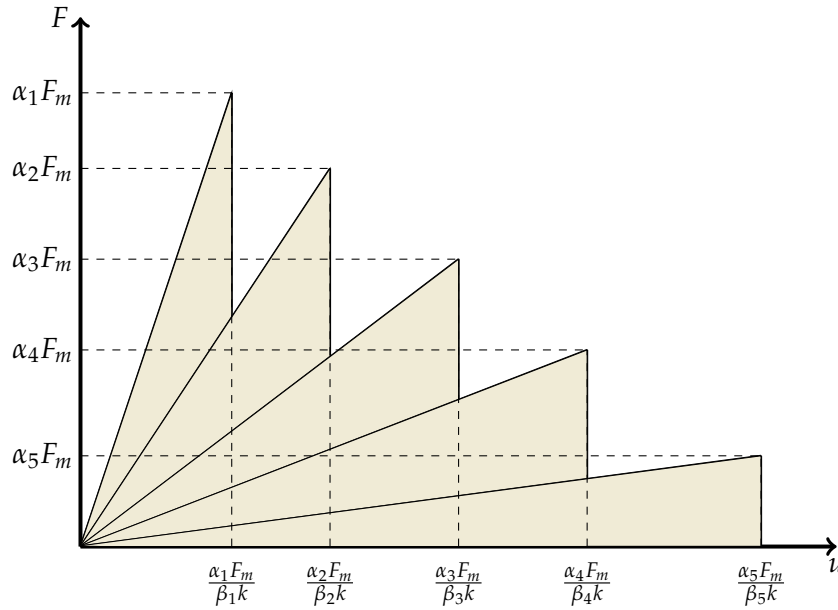
FIGURE 3.2: Piece-wise load-displacement curve belonging to the different springs, describing the progression of damage in a single element with the aid of 5 damage increments

For the case with 5 damage increments, the load-displacement curve of the constantly replaced spring is given by Figure 3.2. This curve is based on the 5 individual contributions of the springs. In this figure, the damage increments are shown by the force drops, with the last drop leading to zero load capacity, hence representing a completely damaged state. The factors α_i and β_i are not specified and can be chosen arbitrarily to obtain an arbitrary load-displacement curve. Up until the first load drop, uncracked concrete behaviour is obtained and past this point, tension softening behaviour of cracked concrete is simulated. Following this line of thinking, the concept of sequentially linear analysis has been developed, as will be discussed later in this section.

3.2   Development of SLA

As discussed in Section 1.1, the quasi-brittle fracture behaviour of concrete often causes trouble regarding stability of the incremental iterative approach (also known as non-linear finite element analyses/NLFEA). The basic idea behind incremental iterative methods is to apply the loads in increments or steps (e.g. load, displacement or arclength steps). For each step, a Newton-Raphson type of solver is used to solve the non-linear set of governing equations and the next increment is performed once the dis-balance between internal and external forces is within user-specified tolerances [9]. Concrete cracks in a rather abrupt and localized way, leading to sharp material softening [32] and hence, peaky behaviour in the load-displacement curve is obtained (as shown for the example in Section 1.1). Within one increment, multiple integration points might enter the cracked state. Because cracking occurs very abruptly, it is likely that the incremental iterative scheme jumps over some stages of the crack-formation and is therefore not able to obtain a converged solution. Also, alternative equilibrium paths might occur [58]. Besides, localized cracking might induce localized unloading in neighbouring elements, resulting in negative tangent

stiffness and therefore stability problems. During the years, more advanced finite element approaches have been developed to improve the numerical stability, for example the arclength control method based on energy release by Verhoosel, Remmers and Gutierrez [79], which is able to propagate in steps through the formation of damage.

As mentioned by Van de Graaf [29], the problem is not that researchers are not able to capture the quasi-brittle behaviour of concrete. In fact, an overwhelming number of options are offered to converge to a solution. The real problem is found in the practice of structural engineering, where analysts are generally not educated to make use of this wide variety of methods. Furthermore, most methods are developed using small scale experiments, where in practice often large scale problems are found. In fact, the complicated nature of computational modelling of concrete fracture and its numerical stability leads to robustness issues, as concluded by many authors (a.o. [9, 29, 32, 51, 58, 66]). For that purpose, it is aimed to develop a method that leads to a more robust solution procedure.

The answer to robustness issues was found in linear elastic analysis. This type of analysis does by definition always converge and does not require an incremental iterative approach. For linear elastic analysis, a linear system of equations $f = k u$ is straightforwardly solved and the method is therefore very appealing to obtain a robust method. Because a single linear analysis over-simplifies the physical problem since it neglects all non-linear effects (e.g. tension softening), the solution is sought in *event-by-event* procedures. The first event-by-event procedure found in literature is developed by Herrmann et al. [33]. In their study, a continuum is modelled by a network of elastic truss or beam elements (a lattice), each representing material behaviour at a local scale. The elements break as soon as their limit stress is reached. In this context, an event is seen as the failure of an element. A linear elastic analysis is performed and the element that breaks first is removed from the model. Then, a new linear elastic analysis is performed on the updated geometry. In this way, damage propagation is followed in an event-by-event strategy. Schlangen and Van Mier [70] were able to simulate experimental results, although small scale, with a lattice model. Beranek and Hobbelman [6] proposed a similar model, in which the lattice is replaced by a collection of spheres representing the structure of the material. The strength of the material is described via the contact surface between two spheres and an event-by-event strategy is used to follow damage propagation.

Inspired by the lattice models, Rots [63] proposed the framework of *Sequentially Linear Analysis*, often abbreviated as SLA. Where lattice models require a discretization in space, SLA makes use of a continuum formulation. SLA is an event-by-event strategy, in which a sequence of scaled linear analysis with a decreasing secant stiffness is performed, representing local damage increments. In this line of thinking, the example of Section 3.1 can be understood as a sequentially linear analysis. The replacement of a spring once the capacity is reached is in fact the increment of local damage in SLA. The idea of SLA is also partially inspired by concrete engineering practice, where the stiffness of concrete is reduced in areas where cracking is expected, and a linear elastic analysis is performed. In this way, the influence of cracking on the stress distribution is accounted for. In the SLA-procedure, the constitutive relation is discretized to a stepwise secant material law (a so-called saw-tooth curve), where the continuum nonlinear approach makes use of continuous damage formulations. Since in SLA only positive secant slopes are obtained, no convergence problems are found. Instead of increasing the load on a structure, the approach increases the damage of the considered structure, such that no damage is missed and
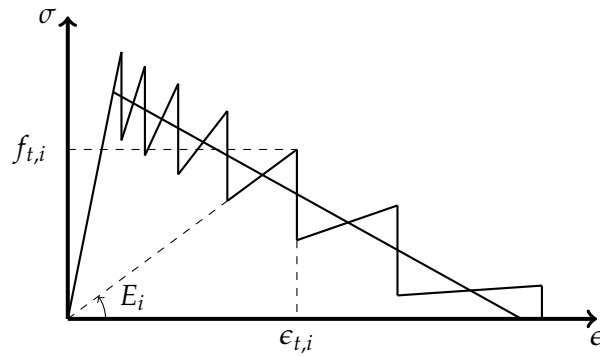
FIGURE 3.3: Example of the transition from a continuum constitutive
relation to a discrete saw-tooth curve

the complete load-displacement path can be followed. Since the damage is only increased at 1 point at a time, bifurcations are circumvented [32, 67]. In Section 3.3, more theoretical information on sequentially linear analysis will be given.

In recent research by Yu et al. [84], SLA has been combined with incremental iterative analysis, combining the advantages of both methods. An incremental iterative analysis is performed and once the limit stress is reached somewhere, the stiffness of that element is reduced and the load is set to the level where the stress is just below the limit. From that point on, a new increment is performed until the maximum stress is reached somewhere else. Combinations of SLA and NLFEA are not further considered in this thesis.

3.3   General theory

In Sections 1.1 and 3.2, the general principles of SLA have been described. In this section, the procedure is described in more detail. In NLFEA, the space is discretized in space via finite elements and the load is discretized in load steps. In SLA, the space is still discretized with the aid of finite elements. However, instead of discretizing the load, the constitutive material law is discretized using a saw-tooth curve and the load is computed based on a scaling technique. Furthermore, regular SLA is based on a fixed smeared crack model (as mentioned by many authors, e.g. [21, 63, 66]), meaning that the crack direction is fixed upon initiation. Also, the only applied failure criteria is the tensile stress and influences of shear and compressive failure are not considered in regular SLA (they are included in extended versions of SLA). The SLA-procedure as applied in this thesis for a cycle j is listed below. For now, it is assumed that the loading is proportional, meaning that all loads on the structure are depending on a factor λ. In Section 3.5, non-proportional loading is discussed.

- **Apply a reference load**
  Single or multiple loads can be put on the structure, as long as they can all be scaled with a factor λ.

- **Calculate the principal stresses in all integration points through a linear elastic analysis**
  In this step, the element stiffness matrices and external load vectors are assembled and the system $f = ku$ is solved. For undamaged integration points, the constitutive law is elastic isotropic and given by Equation 2.6 and for damaged integration points, an orthotropic formulation is used as given by Equation

2.8. Both equations are based on the fixed crack model with the possibility of secondary (or perpendicular) cracking. In the first SLA models [63], only a primary crack was able to form. Later, the possibility to have a crack perpendicular to the primary crack was included. By allowing the formation of a secondary crack, the number of potential damages is doubled as the stress in the perpendicular direction might also induce damage. In Equations 2.6 and 2.8, the stiffnesses E_n and E_t follow a certain tension-softening law (e.g. linear, exponential or nonlinear). From the solution, the principal stress field is found, being a function of the factor λ.

- **Determine the critical integration point in the structure and determine the critical load multiplier $\lambda_{crit}^{(j)}$**
  Assuming proportional loading, the critical integration point is the point in which the ratio between the maximum principal tensile stress and the current strength is the highest. For uncracked integration points, the current strength in the considered direction is f_t, where for cracked points, the current strength in the considered direction is the reduced strength $f_{t,i}$ at the current cycle j according to the tension-softening law. The critical load multiplier of an integration point i is found by

$$\lambda_{crit,i}^{(j)} = \frac{f_{t,i}^{(j)}}{\sigma_{princ}} \tag{3.1}$$

  in which σ_{princ} can be either σ_1 and σ_2, as the concrete can crack in two directions. When a certain direction is considered, also the corresponding current strength should be used. The critical load multiplier of the complete structure, assuming that the tensile stress is the only failure criteria, is given by

$$\lambda_{crit}^{(j)} = \min\left(\lambda_{crit,i}^{(j)}\right) \quad \text{for all } \lambda_{crit,i}^{(j)} > 0 \tag{3.2}$$

- **Scale the reference load proportionally with $\lambda_{crit}^{(j)}$ and determine the stress- and strain fields again**
  This step is required for post-processing, such that the actual forces, displacements, stresses and strains of each cycle can be followed and analyzed. The reference load on the structure and the displacements are found by multiplication with λ_{crit}, as a linear analysis has been performed. From the displacement field, the stresses and strains can be found.

- **Increase the damage in the critical integration point by reducing the stiffness and strength according to the saw-tooth constitutive curve**
  The stiffness and strength are reduced to simulate the increase of structural damage and follow a certain tension softening curve. In Figure 3.3, a linear tension softening constitutive law has been drawn. In the same figure, an example of a discretized saw-tooth curve is shown. The continuum material law is replaced by a piecewise saw-tooth curve. How the saw-tooth curve is generated, will be discussed in Section 3.4. Once the critical stress $f_{t,i}$ is reached, a damage increment is applied, meaning that the next secant stiffness E_{i+1} and strength $f_{t,i+1}$ are used for the subsequent cycle. The reduction of stiffness is permanent, meaning that unloading also takes place following the secant stiffness. For the next cycle, only the part related to the critical integration point changes in the stiffness matrix. All other terms remain the same.

- **Repeat this cycle of steps until the damage has reached a user-specified state**
  The reference load is put on the structure and a new cycle with the damaged integration point is performed. The sequentially linear analysis keeps on running until all integration points are fully damaged or a certain state that is specified by the user is reached (e.g. a state with 100 damage steps).

3.4   Stepwise secant material law

Within the framework of sequentially linear analysis, nonlinear constitutive laws are approximated with the aid of stepwise secant materials laws, in literature often called saw-tooth diagrams. During the last two decases, different type of saw-tooth formulations have been developed, as shown by Figure 3.4. In this section, these different formulations are discussed for the case of linear tension softening.

In the first version of SLA, proposed by Rots [63], two types of saw-tooth laws are considered. Firstly, a stepwise reduction of the tensile strength from f_t to 0 in N equal steps is suggested. This results in a constant stress decrement Δf_t determined by

$$\Delta f_t = \frac{f_t}{N} \tag{3.3}$$

with N a user-defined number of saw-teeth. The constant stress decrement saw-tooth curve is shown by (1) in Figure 3.4. In this approach, the stress never exceeds the continuum tension softening law. Secondly, a stepwise reduction of the Young's modulus via a constant factor a is proposed. The reduced stiffness is in this approach found by

$$E_i = \frac{E_{i-1}}{a} \quad \text{for } i = 1..N \tag{3.4}$$

in which a is larger than 1. This approach is visualized by curve (2). Compared to curve (1), curve (2) has more branches in the later stages of crack development. As mentioned by Rots and Invernizzi [66], the fracture energies of both curves (1) and (2), which is the area underneath the curve divided by the crack band h, is dependent on the number of saw-teeth N. For a small N, less fracture energy than the case with large N is obtained. Furthermore, the fracture energies of curves (1) and (2) are always lower than the continuum fracture energy. It is aimed to develop an approximation technique that maintains objectivity with respect to the number of saw-teeth. Rots and Invernizzi mentioned three possibilities to solve this problem:

- Increase the tensile strength f_t with a factor c

- Increase the ultimate strain ϵ_u with a factor c

- Increase both the tensile strength and the ultimate strain with a factor c

All three approaches are applied in combination with Equation 3.4. The factor c should be chosen such that the fracture energy of the continuum constitutive law is maintained. Using the first approach, results objective with respect to N were obtained. However, the peak load was significantly overestimated. The second approach also led to objective results. In this case, the peak load was underestimated. The third approach worked out to be the best option, since the peak load could be properly estimated. This approach is shown by curve (3). For linear tension softening, a closed form expression for c is found [66].
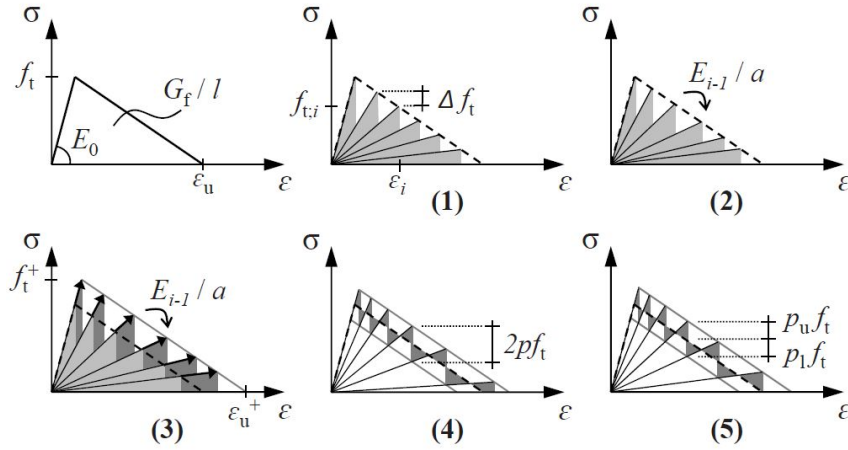
FIGURE 3.4: Different saw-tooth curve approximation techniques,
taken from [71]

Rots, Belletti and Invernizzi [64] came up with a more general concept called
the *Ripple band* saw-tooth curve. This approach is generally applicable, meaning
that it can be straightforwardly applied to nonlinear constitutive laws. In the ripple
band approach, a strength range is set as a percentage p of the maximum tensile
strength. Two imaginary curves are drawn: one $+pf_t$ above and one $-pf_t$ below
the continuum constitutive curve, as shown in (4) of Figure 3.4. First, the point
of intersection $\epsilon_{t,i}$ between the secant elastic branch with stiffness E_i and the upper
curve is determined. The corresponding stress is called $f_{t,i}^+$. Then, the tensile strength
$f_{t,i}^-$ on the bottom curve for the same strain $\epsilon_{t,i}$ is calculated and based on that, the
new reduced secant stiffness E_{i+1} for the next tooth is obtained by

$$E_{i+1} = \frac{f_{t,i}^-}{\epsilon_{t,i}} \tag{3.5}$$

with

$$f_{t,i}^- = f_{t,i}^+ - 2pf_t \tag{3.6}$$

This procedure is repeated until a stress free state is reached, equivalent to a fully
developed crack. The number of saw-teeth N follows from the procedure and de-
pends on the width of the ripple band $2pf_t$. In this way, both linear and nonlinear
tension and compression constitutive laws for concrete and yielding of steel can be
considered [64]. Invernizzi et al. [37] showed that a slightly adapted version of the
ripple band concept can be used to simulate local linear constitutive snap back be-
haviour, meaning that the ultimate strain ϵ_u is smaller than the elastic strain ϵ_t. The
dark triangles above the continuum curve (see Figure 3.4) represent an overestima-
tion and the dark triangles below the continuum curve represent an underestimation
of the fracture energy. As for linear tension softening these triangles are equal in size,
Rots et al. [64] concluded that the fracture energy of the ripple band concept is ob-
jective with respect to the number of saw-teeth. For nonlinear constitutive laws, the
ripple band concept is assumed to be approximately objective as the triangles are
not exactly equal in size anymore.

Van de Graaf [29] mentioned that these conclusions do not completely hold.
Firstly, the number of triangles above the continuum curve exceeds the number of
triangles below the continuum curve by one. Secondly, the last area before the stress

free state is not by definition a triangle, as the ultimate strain found by the ripple band might differ from the continuum ultimate strain. Thirdly, for nonlinear constitutive relations, the triangles above and below the continuum curve are not equal anymore and therefore do not drop out against each other. These three observations lead to a small deviation of the fracture energy with respect to the continuum law. Therefore, Van de Graaf developed the improved ripple band concept, which is shown by curve (5). In this concept, the ripple band of $2pf_t$ is replaced by an upper band of $p_u f_t$ and a lower band of $p_l f_t$. The parameters p_u and p_l are determined by an iterative procedure, which takes as input the number of saw-teeth N. This iterative procedure solves p_u and p_l such that 1) the area enclosed by the saw-tooth curve equals the continuum fracture energy and 2) the ultimate strain of the saw-tooth equals the continuum ultimate strain. In an adapted way, the improved ripple band can be applied to linear constitutive snap back. For nonlinear snap back, the saw-tooth curve might intersect the continuum constitutive law. For this case, no solution has been found.

3.5   Application issues

In order to make sequentially linear analysis applicable in practice, some challenges are still remaining. In this section, four application issues are discussed, namely non-proportional loading, crack closure during stress reversal, the assumption of fixed cracking possibly leading to stress locking and application of SLA to 3D-problems, possibly including non-proportional loading.

Non-proportional loading
Until now, the loading is assumed to be proportional. In this section, also non-proportional loading is considered in order to make SLA applicable in practice, where combinations of initial constant loading (e.g. self weight) and reference loading (e.g. traffic on a bridge) are rather a standard than an exception. Although for non-proportional loading the same principles of Section 3.3 can be applied, the identification of the critical integration point and its load multiplier is not that straightforward anymore. DeJong et al. [21] developed a strategy to handle non-proportional loading. For this purpose, the loading is subdivided in an initial load A and a subsequent proportional load B. Taking this into consideration, the stresses at any integration point can be written as

$$\begin{aligned}
\sigma_{xx} &= \sigma_{xx,A} + \lambda \sigma_{xx,B} \\
\sigma_{yy} &= \sigma_{yy,A} + \lambda \sigma_{yy,B} \\
\sigma_{xy} &= \sigma_{xy,A} + \lambda \sigma_{xy,B}
\end{aligned} \tag{3.7}$$

where λ is the load multiplier that is sought for. The applied failure criteria is the tensile stress in the principal directions. Furthermore, it is assumed that the initial loading A does not result in damage. From Equation 3.7, the principal stresses are found to be

$$\sigma_{1,2} = \frac{1}{2}(\sigma_{xx} + \sigma_{yy}) \pm \sqrt{\frac{1}{4}(\sigma_{xx} - \sigma_{yy})^2 + \sigma_{xy}^2} \tag{3.8}$$

The principal stresses are set equal to the current tensile strength and the load multipliers are solved accordingly from the quadratic equation. Furthermore, the principal directions are determined. The difficulty of non-proportional loading is the selection of the critical load multiplier. DeJong et al. found that selecting the

lowest positive λ_{crit}, just like is done for proportional loading, is not appropriate anymore as this might lead to not allowable stress states. The following selection procedure is proposed [21]:

- In each integration point and in each principal direction, the scaled normal stresses due to the proportional load B should be checked for either tension or compression.

- In case of tension, load B has a crack opening effect. The lowest load multiplier λ^t_{min} that results in a total tensile stress (including load A) equal to the current tensile strength should be taken, in line with SLA for proportional loads.

- In case of compression, load B has a crack closing effect. The compressive stresses must be such that the tensile stresses following from initial load A together with the compressive stresses from load B do not exceed the current tensile strength. When compressive stress B is lower than the required stress, the tensile strength is exceeded. Therefore, the critical load multiplier is found by the highest load multiplier λ^c_{max}, as this is the first to have damage. When a lower load multiplier would be used, other integration points have already exceeded their tensile strength.

- If $\lambda^t_{min} > \lambda^c_{max}$, there is a critical load multiplier for which all integration points obtain admissible stresses and a damage increment is performed for the corresponding critical element. However, if $\lambda^t_{min} < \lambda^c_{max}$, there is no critical load multiplier leading to admissible stresses for all integration points. Irrespective of the applied load multiplier, the tensile strength will be exceeded somewhere. It is assumed that $\lambda_{crit} = \lambda^c_{max}$ and the corresponding integration point is damaged. The analysis continues without reaching equilibrium.

In the approach of DeJong et al. it is not considered whether the redistribution of stresses after the damage increment does not immediately induce new events elsewhere in the model, leading to an 'avalanche' type of behaviour. In order to overcome this issue, Eliáš et al. [23] came up with the force-release (F-R) method. In their approach, not only the material properties are updated via damage increments at the critical integration point, but also the unbalance forces following from the damage increment are added to the nodal forces. These unbalance forces lead to a stress redistribution, which may intermediately trigger more events. Once such an event occurs, the same procedure is repeated for the same load as the previous event and the residual unbalance forces are redistributed again (which again might lead to a new event). By gradually reducing the unbalance forces to zero, the earlier mentioned avalanche type of behaviour can be captured and only admissible stress states are obtained (where DeJong's approach allows non admissible states). The load can be increased once the disbalance forces completely vanished. As unbalance loads are added to the nodes and gradually redistributed, the approach is in fact a combination of an incremental and SLA type of strategy.

Lately, Van de Graaf [29] developed a strategy, inspired by the work of DeJong et al., that makes use of a constrained maximization. In this approach, each integration point puts one or more constraints on the load multiplier. The goal is to find a load multiplier that fulfills all the constraints using the procedure of constrained maximization. In case it is not possible to find a suitable load multiplier, a double load multiplier strategy is applied in which the last successful combination of initial load A and proportional load B is scaled, resulting in a possible reduction of the initial
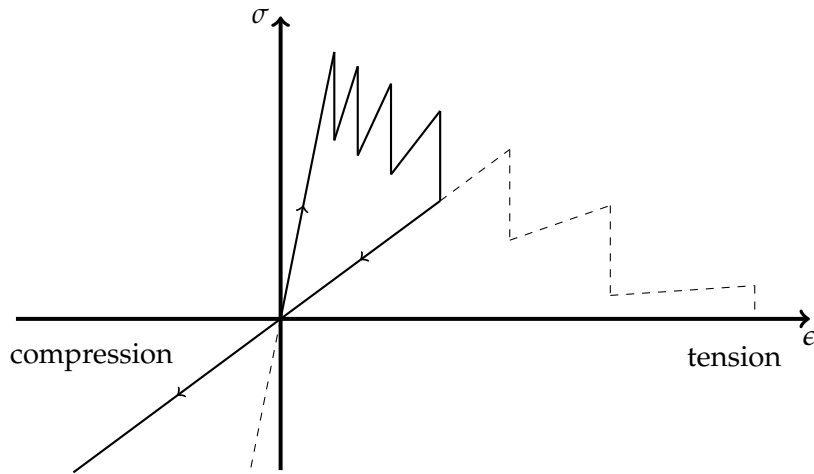
FIGURE 3.5: Visualization of a stress cycle with secant unloading
from the tension to compression regime

load. This reduction on the initial load is needed to not violate one of the constitutive laws of the integration points.

Very recently, Alfaiate and Sluys [1] proposed a slightly different strategy to cope with non-proportional loading, which is claimed to be an improved strategy compared to the double load multiplier strategy by Van de Graaf. Instead of explicitly reducing the last successful combination of constant load and variable load with the aid of a constant load multiplier, Alfaiate and Sluys implicitly incorporate the stress redistribution in their strategy by slightly redefining the definition of λ. For more information, the reader is referred to the paper. It is noted that the proposed strategy is only tested for academic cases and validation studies are required to demonstrate the effectiveness and correctness of the proposed strategy.

Stress reversal
One of the core assumptions of SLA is secant loading and unloading [32], meaning that unloading always passes through the origin and that cracks are assumed to close completely during unloading. During stress reversal in an integration point (in this case the transition from the tensile to the compressive regime), the damaged secant stiffness is maintained and the original stiffness is not regained, as mentioned by Pari et al. [58]. The problem of stress reversal is exemplified by Figure 3.5: after a certain amount of damage increments, the integration point unloads and enters the compressive regime, where it should regain its original stiffness as the concrete properties in compression are not damaged. Unloading/stress reversal can be the result of cyclic loading or stress redistribution and with the current SLA framework, it is not possible to capture these effects. In order to overcome these issues, a possible solution would be to implement status parameters which check the reversal of stresses during the calculation [58].

Stress locking
As discussed in Section 2.3.2, fixed smeared cracking models suffer from a type of stress locking as a result of the spurious (shear) stresses in the plane of cracking. Due to the crack not co-rotating with the principal stresses, unrealistic stresses are found in the cracking plane (e.g. a high shear retention value might lead to large shear stresses for a completely developed crack, which is stress-free). Furthermore, stresses larger than the tensile strength can occur unnoticed as only the stresses in

the fixed crack direction are monitored (where the current principal stress direction should be monitored). The current framework of sequentially linear analysis is based on a fixed smeared cracking approach (Section 3.3) and therefore also suffers to this type of stress locking. The formation of spurious stresses can be counteracted by using a smeared rotating crack model, which is further outlined in Chapter 4.

3-Dimensional problems

Up until now, only the background theory regarding 2D SLA has been described. However, for practical implementation expansion to 3D structural behaviour is required, as most problems in the physical reality are subdued to multi-dimensional stress states. To this end, this section briefly considers the implementation of 3D stress states in SLA. Up until cracking, the concrete behaves isotropic. During the process, three (3D) instead of two (2D) principal stress components are monitored and compared with the allowable stress. Once the undamaged concrete reaches its maximum stress, the crack direction and thereby the axis of orthotropy are fixed perpendicular to the maximum principal stress direction, following a fixed cracking approach. The global $x - y - z$ coordinate system is replaced by a local $n - s - t$ coordinate system, where the n-axis is aligned normal to the crack. Upon crack initiation, the primary, secondary and tertiary crack directions are fixed and damage increments are performed following the same procedure as listed in Section 3.3.

The orthotropic compliance matrix C, describing the strain-stress relation $\epsilon = C \sigma$, changes due to the 3D stress state to

$$
\begin{bmatrix} \epsilon_{nn} \\ \epsilon_{ss} \\ \epsilon_{tt} \\ \gamma_{ns} \\ \gamma_{st} \\ \gamma_{tn} \end{bmatrix} = \begin{bmatrix} \dfrac{1}{E_n} & -\dfrac{\nu_{ns}}{E_s} & -\dfrac{\nu_{nt}}{E_t} & 0 & 0 & 0 \\ -\dfrac{\nu_{sn}}{E_n} & \dfrac{1}{E_s} & -\dfrac{\nu_{st}}{E_t} & 0 & 0 & 0 \\ -\dfrac{\nu_{tn}}{E_n} & -\dfrac{\nu_{ts}}{E_s} & \dfrac{1}{E_t} & 0 & 0 & 0 \\ 0 & 0 & 0 & \dfrac{1}{G_{ns}} & 0 & 0 \\ 0 & 0 & 0 & 0 & \dfrac{1}{G_{st}} & 0 \\ 0 & 0 & 0 & 0 & 0 & \dfrac{1}{G_{tn}} \end{bmatrix} \begin{bmatrix} \sigma_{nn} \\ \sigma_{ss} \\ \sigma_{tt} \\ \sigma_{ns} \\ \sigma_{st} \\ \sigma_{tn} \end{bmatrix} \tag{3.9}
$$

where the Poisson's moduli, shear moduli and stiffness moduli are found in the same manner as for 2D (a full description for 3D is given in Chapter 8), simulating the propagation of damage by damage increments. As mentioned by Pari et al. [57], fixation of the secondary and tertiary crack directions could be postponed until damage is obtained in a secondary direction, allowing a more realistic improved description of the cracking process.

The first expansion of SLA to 3D has been developed by Voormeeren [80], however limited to merely proportional loading. In this study, it was concluded that SLA is able to properly describe 3D quasi-brittle fracture behaviour with solid elements. Furthermore, it was found that the determination of the crack band h is not as straightforward anymore for 3D solid elements, since cracks can potentially deviate from the mesh lines in multiple directions, hence causing significant deviations from the theoretical crack band $h = \sqrt[3]{V}$. Computational efforts were found to increase considerably as a result of the solid elements.

The implementation of non-proportional loading in the context of 3D sequentially linear analysis is a topic of current research. In the approach of DeJong et al.

for 2D [21], a set of load multipliers is solved based on the quadratic Equation 3.8, which is a function of the constant and proportional parts of the loading. For 3D, a cubic equation has to be solved in order to find load multipliers. Pari et al. [57] developed two approaches to implement non-proportional loading for 3D stress states in SLA: 1) the cubic function is analytically solved for with the aid of trigonometric solutions or the Cardano method and 2) the cubic function is solved by using a constrained optimization approach, invoking the load multiplier as a function of the inclination of a damage plane, in line with the approach of Van de Graaf [29]. In their research, studies on a prestressed skewed notched beam and reinforced concrete slab failing in shear are performed, both indicating that the 3D failure process is properly captured within the framework SLA. As has been substantiated by DeJong et al. [20], it is also possible for some cases to make use of shell elements instead of computationally more heavy solid elements. Especially for structures that can be considered as thin in one dimension, such that trough thickness stresses can be neglected, the application of shell elements becomes tempting. The applied shell elements are in fact layered membrane elements over the thickness of the considered element, neglecting the influence of through thickness stresses. Hence, the compliance matrix of Equation 3.9 reduces to

$$
\begin{bmatrix} \epsilon_{nn} \\ \epsilon_{ss} \\ \epsilon_{tt} \\ \gamma_{ns} \\ \gamma_{st} \\ \gamma_{tn} \end{bmatrix} = \begin{bmatrix} \dfrac{1}{E_n} & -\dfrac{\nu_{ns}}{E_s} & 0 & 0 & 0 & 0 \\ -\dfrac{\nu_{sn}}{E_n} & \dfrac{1}{E_s} & 0 & 0 & 0 & 0 \\ 0 & 0 & 0 & 0 & 0 & 0 \\ 0 & 0 & 0 & \dfrac{1}{G_{ns}} & 0 & 0 \\ 0 & 0 & 0 & 0 & \dfrac{1}{G_{st}} & 0 \\ 0 & 0 & 0 & 0 & 0 & \dfrac{1}{G_{tn}} \end{bmatrix} \begin{bmatrix} \sigma_{nn} \\ \sigma_{ss} \\ \sigma_{tt} \\ \sigma_{ns} \\ \sigma_{st} \\ \sigma_{tn} \end{bmatrix} \tag{3.10}
$$

which results after inverting in a constitutive law that is similar to the 2D membrane formulation of Equation 2.8, with additional shear effects following from out of plane behaviour. Shell elements only have primary and secondary crack directions and therefore, the non-proportional algorithm for 2D suffices. In this way, facades and other thin structures can be considered without the use of solid elements and a complex non-proportional loading algorithm, resulting in far less computational expenses [20]. However, one should be aware of the limitations.

Chapter 4

The Sublayer Model

In this chapter, the Sublayer Model as proposed by Hendriks and Rots [31] is further elaborated. First, an introductory example in which cracked concrete is modelled using a parallel set of springs is discussed in Section 4.1. Secondly, alternative models from literature to capture rotating cracks within a sequentially linear analysis are mentioned in Section 4.2, followed by a thorough elaboration of the theory behind the sublayer model in Section 4.3. Lastly, the limit case of an infinite number of sublayers is discussed in Section 4.4 for different loading cases.

4.1 Example 2: modelling cracked concrete with springs

As discussed in Section 3.1, concrete loses a certain amount of stiffness and strength when cracking starts and propagates. In fact, the start of cracking means the formation of micro-cracks in the fracture zone, according to the fictitious crack model (see Section 2.1). The formation of micro-cracks gradually reduces the strength and stiffness of the cross-section, leading to a so-called tension softening effect. Physically speaking, tension softening can be interpreted as a gradual reduction of the cross-section, as the micro-cracks continue to grow. This inspired Hendriks and Rots [31] to develop the *Sublayer Model* (in their paper called the 'fraction model'). The main concept of the sublayer model is exemplified using the following example of a parallel set of springs in tension. The single spring of the example in Section 3.1, called 'Example 1' from now on, is replaced by an equivalent set of N parallel springs with stiffnesses $k_i = \beta_i k$, with $\sum_{i=1}^{N} \beta_i = 1$ such that the same initial stiffness k of example 1 is obtained. A set of 5 parallel springs (so $N = 5$) is shown by Figure 4.1.

Just like for example 1, the springs are responding elastically up until their capacity $\alpha_i F_m$ is reached. Once the capacity of a specific spring i is reached, the considered
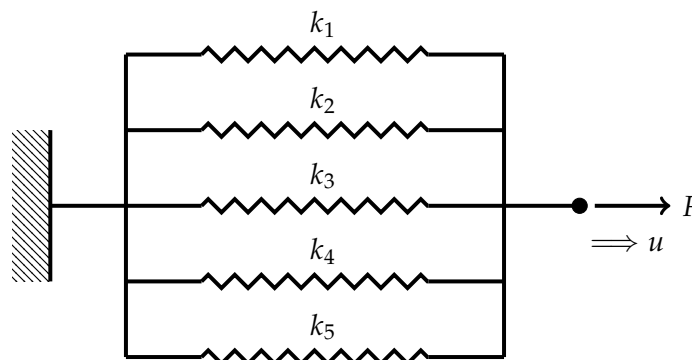

FIGURE 4.1: Model of a set of parallel springs (N=5) with stiffness k_i loaded by a tensile load F

spring fails and is not able to transfer load anymore. The total maximum strength of the springs should be F_m in order to agree with example 1. How to choose factors α_i and β_i to obtain the same results, will be discussed in a later section. Instead of replacing the single spring from example 1 by a weaker spring, a parallel configuration is used to obtain equivalent behaviour. In this parallel configuration, the simulation of damage is obtained by a superposition of sequential failures of the individual springs. The factors α_i and β_i are chosen such that spring 1 is the first spring to fail and spring N is the last the fail. After failure of a specific spring, a load drop is obtained, similar to example 1, until the last spring fails and the complete load carrying capacity is lost.

For the case with 5 parallel springs, the total load displacement curve is given by Figure 4.2 (A) and the contributions of the 5 individual springs are shown in Figures 4.2 (B) till (F). The relation between curves (A) and (B) till (F) is straightforwardly given by

$$(A) = (B) + (C) + (D) + (E) + (F) \tag{4.1}$$

When comparing Figures 3.2 and 4.2 (A) it is evident that both the approaches of examples 1 and 2 can result in the same load-displacement curve, when parameters α_i and β_i are chosen correctly (where α_i and β_i of both the approaches do not necessarily have to be the same). The following relation forces the maximum load of example 2 to be equal to F_m

$$(\beta_1 + \beta_2 + \beta_3 + \beta_4 + \beta_5)k \cdot u_1 = F_m \tag{4.2}$$

with

$$u_1 = \frac{\alpha_1 F_m}{\beta_1 k} \tag{4.3}$$

Again, up until the first load drop, uncracked concrete behaviour is obtained and past this point, tension softening behaviour of cracked concrete is simulated using a parallel set of springs. Following this line of thinking, the concept of the sublayer model has been developed, as will be discussed later in this chapter.

4.2   Alternative models

Regular sequentially linear analysis makes use of a fixed smeared cracking approach. A major shortcoming of fixed crack models is the inability to capture the influence of rotating principal stress directions, hence leading to stress locking, as discussed in Section 3.5. When principal stresses rotate, a shear force in generated within the cracking plane and non-admissible stress states might be obtained. To account for rotation of principal stresses, one could adapt the shear retention relation to have less locking, as mentioned by Vorel and Boshoff [81]. However, this leads to more complex material laws and additional, often unknown, parameters. Therefore, it is aimed to develop an approach that includes rotational cracking without the need for additional complex material laws and parameters. In this context, the sublayer model has been developed. Before this model is further elaborated, alternative approaches to include rotational cracking by Slobbe [72], Vorel and Boshoff [81] and Cook et al. [17] are discussed respectively.
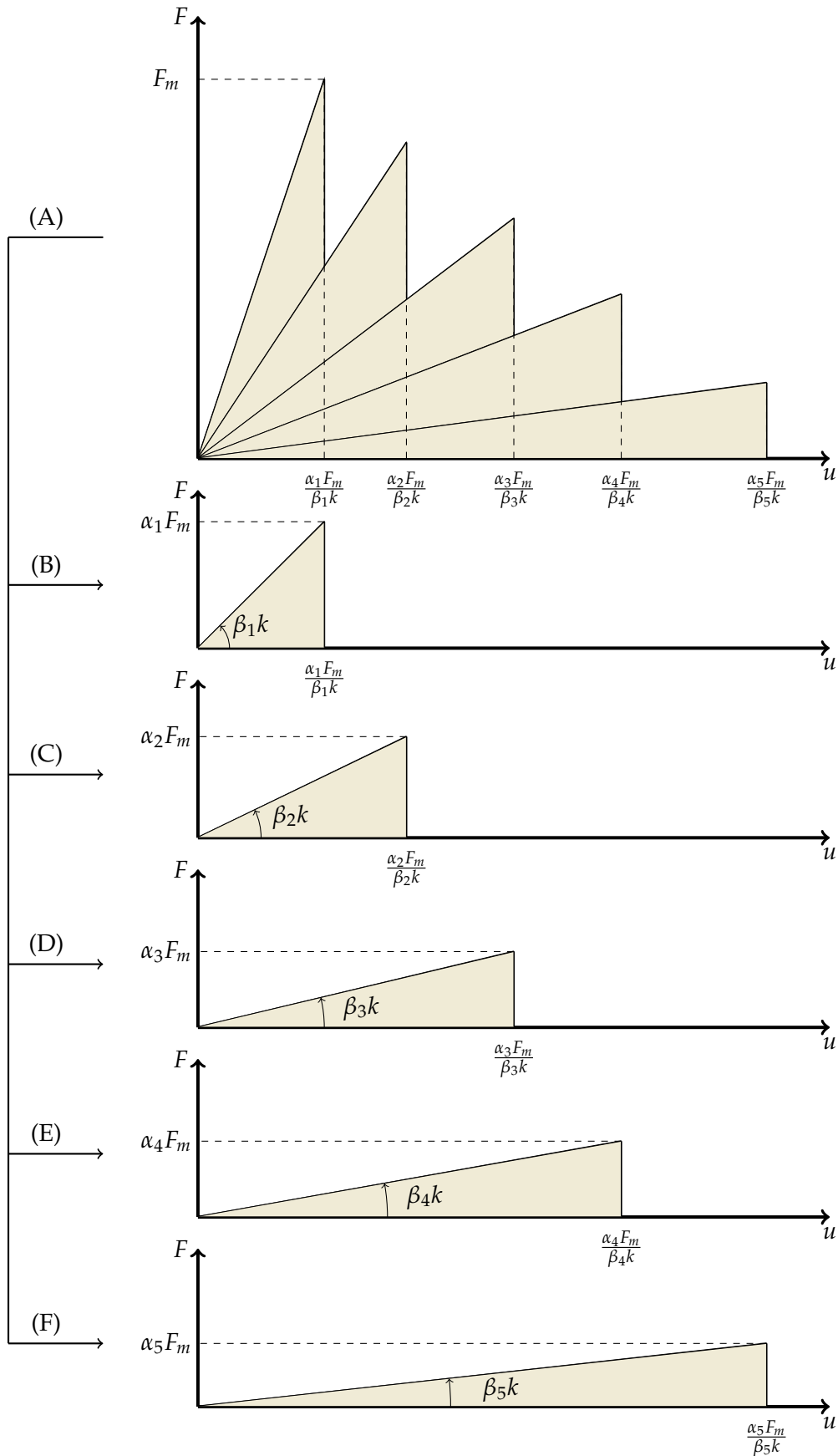
FIGURE 4.2: (A) Total load-displacement curve of parallel spring configuration and (B)-(F) load-displacement curves individual springs

4.2.1   Rotating crack as an event

One way of implementing rotational cracking within the framework of SLA is to define a new type of event: the rotation of a crack (only for cracked integration points). This approach has been elaborated by Slobbe [72] in his Master's thesis assuming only proportional loading on the structure. In his version of SLA, not only damage increments but also crack rotations are performed during the analysis, allowing for the simulation of rotating principal stress states due to changing load conditions or local stress redistributions. As a continuous change of crack direction, defined in absolute sense by $|\Delta\gamma|$, would lead to an undesirable number of events, a certain threshold angle α is defined. If the change in crack direction in a specific cracked integration point is larger than α, this is considered as an event and the crack direction is updated. In fact, the stiffness is also changed by updating the crack direction, as the cracked material is assumed to be orthotropic (material properties are direction dependent). If $|\Delta\gamma|$ in a cracked integration point is smaller than α, the usual SLA procedure is followed to find the critical integration point. However, the crack direction in the critical integration point is updated simultaneously. To summarize, Slobbe distinguished two types of action:

- If one or more cracked or fully cracked integration points require a change in crack direction $|\Delta\gamma| > \alpha$, the largest $|\Delta\gamma_{max}|$ is taken and the crack direction of the corresponding element is updated.

- If no cracked or fully cracked integration points require a change in crack direction $|\Delta\gamma| > \alpha$, the critical un-cracked or cracked integration point is searched for, a damage increment is performed for that specific point and if cracked, the crack direction of the specific point is updated.

It is recommended to take the threshold angle α not too small, because this will lead to an unfavourable large number of events. After a damage increment or crack rotation, the stresses redistribute and other crack rotations are likely to follow. For a real rotating crack model, the crack directions for each cracked integration point should be constantly updated. The nature of SLA entails that only one integration point can be updated at a time, meaning that the proposed concept is a combination of fixed and rotating cracking, where all integration points except the critical one follow the fixed cracking model. Only the critical integration point follows the rotating crack concept. For that reason, it is still necessary to define a shear retention factor, potentially inducing spurious stresses. Therefore, it is not sure whether this approach leads to a robust model to capture the influences of rotational cracking. Furthermore, it must be mentioned that the added event of crack rotation results in a significant increase of computational costs as the crack rotation might be subdued to large deviations during the calculations. Local stress redistributions take place after a change in stiffness, and therefore it is likely that a so-called 'snowball-effect' is obtained (the updated crack direction leads locally to changes of crack direction, which, after they are updated, also lead to other changes of crack directions etc.).

4.2.2   Rotating crack as a force-release strategy

Following a different path, Vorel and Boshoff [81] developed a rotating crack model that can be used within the framework of SLA to analyze the behaviour of composites. As a starting point, the Force-Release (F-R) approach by Eliáš et al. [23] is utilized. In F-R, as described in Section 3.5, disbalance forces at the nodes are generated after the damage increment of the stiffness. Subsequently, the disbalance forces
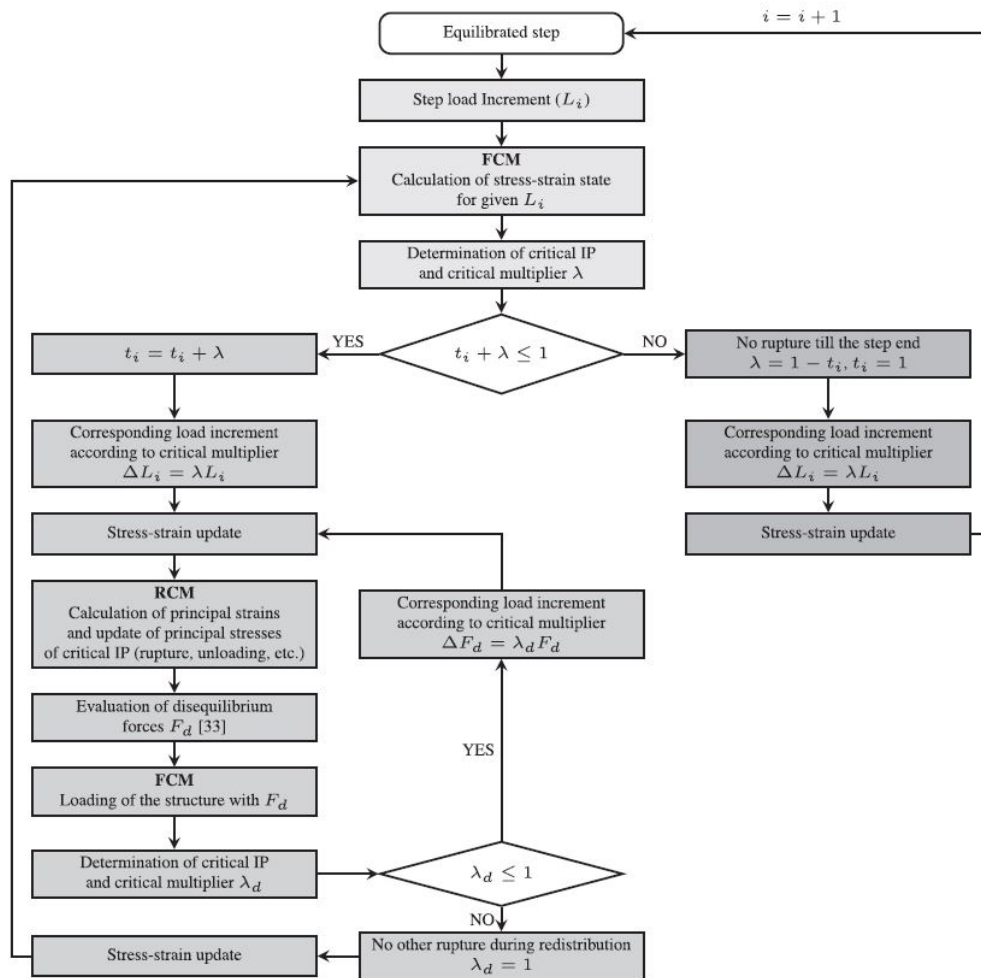
FIGURE 4.3: Sequentially linear analysis for rotating crack models in
the framework of the Force-Release concept, taken from Vorel and
Boshoff [81]

are gradually redistributed, with the possibility to induce another event meanwhile.
In the approach by Vorel and Boshoff, the principal direction of the critical integration point is updated after each stress redistribution. This step is highlighted by
RCM (rotating crack model) in the flowchart, which is taken from [81] and shown by
Figure 4.3. As the rotation of the principal directions is not known beforehand and
depends on the scaling factor, it is assumed that the load multiplier can be evaluated
with respect to the last equilibrated principal direction of the considered integration point. When the principal directions do not change within one increment, the
procedure is exact. By invoking the flowchart of Figure 4.3, the crack directions of
the critical integration points are updated during the calculations. However, in line
with the approach by Slobbe [72] taking a rotating crack as an event, the approach by
Vorel and Boshoff only resembles a rotating crack model for the critical integration
point and can therefore only be partly labeled as a rotating crack model.

It must be mentioned that the proposed solution is not merely a secant linear
analysis anymore, as the disbalance forces are redistributed with the aid of load increments, hence following an incremental type of approach. However, as also mentioned by Vorel and Boshoff, the incremental nature of the algorithm is required to
capture the non-linear nature of rotational cracking. The method has been applied

to a three-point bending test in shear failure and in bending failure. For both cases, the adapted version of SLA including rotational cracking gave similar load displacement curves as the experiment and nonlinear finite element analysis with smeared rotating crack elements.

4.2.3   Rotating crack as multi-directional cracking

Lately, another approach to simulate rotational cracking was developed by Cook et al. [17]. Although the approach is developed for a different field of application, namely heterogeneous brittle materials on a micro scale (aggregate grain level), it is also applicable for computational modelling of concrete structures. The approach of Cook et al. is in fact a multi-directional smeared fixed crack approach. The main idea is that each element is split in a certain amount of potential cracking planes (in the paper each element has 180 planes). With the aid of a sequentially linear analysis, the critical potential crack plane is searched and damage increments are performed according to certain saw-tooth laws. The approach differs from SLA as a critical pre-defined crack plane instead of a critical integration point is searched for. By allowing multiple fixed cracks to form within one element, a rotating crack can be simulated and stress locking effects are released. The number of potential crack planes is limited with the aid of a crack tracking algorithm, such that stress locking and mesh direction bias are reduced. Using the developed crack algorithm, cracks are only allowed to form in so-called user defined 'isolated' elements and can only propagate in so-called 'intersected' elements, which are elements that share an edge with a 'cracked' element, being an element in which a potential cracking plane already has been activated. In this way, spurious cracks somewhere else in the structure are not allowed to form and the effects of stress locking are reduced.

The approach is developed for anisotropic behaviour, but can be reduced to isotropic material behaviour by inserting homogeneous material properties. Just like for regular SLA, material properties in the direction perpendicular to the considered cracking plane are damaged. Considering one specific element, all potential crack planes have a different orientation and therefore a different crack band. In the proposed model, crack bands are calculated with the aid of a simple orthographic projection method, under the assumption that all finite elements are constant strain (linear) triangular elements. In the paper, it is shown that element size dependency and directional bias effects are reduced with the aid of double-edge notched (DEN) specimen test. Furthermore, the proposed model is applied to a square heterogeneous concrete (stiffness and strength vary in space) sample and is shown to be able of predicting realistic and useable results.

4.3   Sublayer model theory

In an attempt to mimick the effects of rotational cracking within sequentially linear analysis, Hendriks and Rots [31] developed the *Sublayer model*. In two-dimensional space, this model subdivides each element in a set of N parallel sublayers k, as visualized in Figure 4.4 (A). Each of these sublayers is elastic-perfectly brittle with tensile strength $f_{t,k}$, compressive strength $f_{c,k}$, stiffness E_k and thickness Δt_k, chosen such to represent the continuum constitutive material law as accurate as possible. The Poisson's ratio ν_k is the same for all layers and equal to the inputted material property ν. The sublayer model follows the same line of thinking as the parallel spring system of Example 2 (see Section 4.1), in which the individual spring properties can be
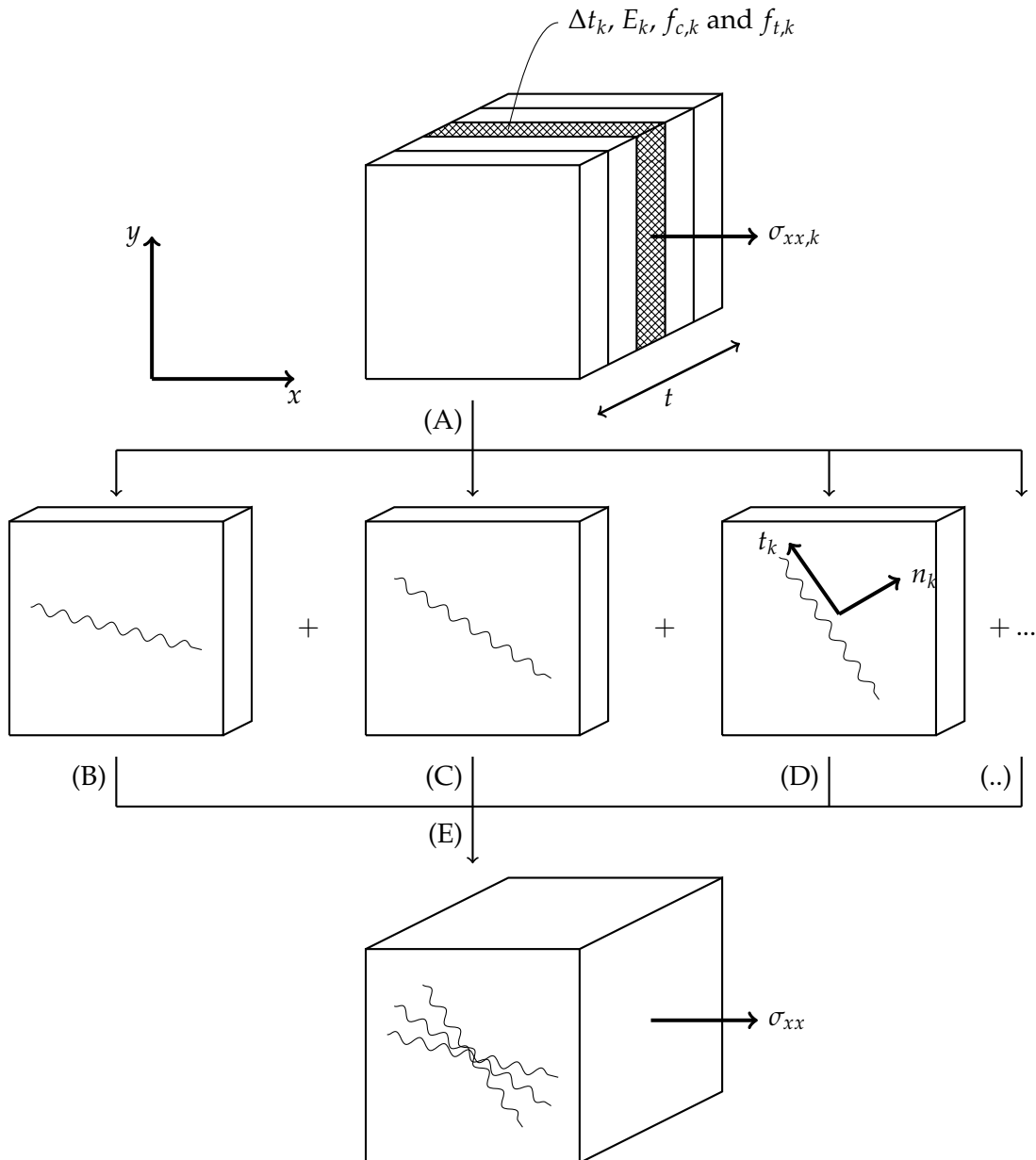
FIGURE 4.4: (A) Single element sublayer model with definitions of
layer properties, (B)-(C)-(D)-(..) sublayers with each their own fixed
crack direction and (E) the total element mimicking a rotating crack

chosen such to follow a certain saw-tooth-like load-displacement curve, as appears
from Figure 4.2. The total behaviour is found by the superposition of the stresses
and strains of the perfectly brittle sublayers, just like the total response of parallel
springs is found by superposition of the individual springs. Each of the sublayers is
allowed to have its own crack direction θ_k and therefore, the global crack direction
might rotate. In other words, the model utilizes a fixed cracking model per layer
and mimics a rotating crack on element level. This process is depicted by Figure
4.4, where (B)-(D) are the fixed crack sublayers and (E) is the mimicked rotating
crack. Because the crack on element level is allowed to rotate, the proposed sublayer
model might potentially reduce stress locking effects which are described in Section
3.5.

As mentioned by Hendriks and Rots, the model describes softening as a gradual reduction of the cross-sectional area. In fact, this is a more physically justified approach compared to regular SLA, as the formation of micro-cracks in the fracture zone, according to the fictitious crack model of Hillerborg et al. [35] (described in Section 2.1), is equivalent to a reduction of the effective material cross-section. The theory behind the sublayer model is explained with the aid of three levels from local to global: *sublayer level*, *element level* and *structural level*.

Sublayer level
On sublayer level, represented by Figures 4.4 (B)-(D), the constitutive behaviour is governed by a fixed cracking approach. Therefore, the theory as discussed in Section 2.3 can be applied straightforwardly. For a sublayer k, the elastic-perfectly brittle material behaviour is shown by Figure 4.5. Up until either the compressive or tensile strength is reached, the layers behave isotropic according to Equation 2.6

$$\begin{bmatrix} \sigma_{xx} \\ \sigma_{yy} \\ \sigma_{xy} \end{bmatrix}_k = \frac{E_k}{1 - \nu_k^2} \begin{bmatrix} 1 & \nu_k & 0 \\ \nu_k & 1 & 0 \\ 0 & 0 & \frac{1-\nu_k}{2} \end{bmatrix} \begin{bmatrix} \epsilon_{xx} \\ \epsilon_{yy} \\ \gamma_{xy} \end{bmatrix} \tag{4.4}$$

where E_k and ν_k are the layers' stiffness and Poisson's ratio respectively. The strain vector does not have an index k as the strain is the same for all sublayers. Once the tensile or compressive strength is reached in direction n_k (the maximum stress is obtained in the principal stress direction), a completely developed crack perpendicular to the failure stress in direction t_k is formed and the stiffness $E_{n,k} = 0$ is completely lost, introducing orthotropic material behaviour. The principal stresses $\sigma_{nn,k}$ and $\sigma_{tt,k}$ are found with the aid of Mohr's circle:

$$\sigma_{nn,tt,k} = \frac{\sigma_{xx,k} + \sigma_{yy,k}}{2} \pm \sqrt{\left(\frac{\sigma_{xx,k} - \sigma_{yy,k}}{2}\right)^2 + \sigma_{xy,k}^2} \tag{4.5}$$

The crack direction θ_k is fixed to the principal stress and strain directions just before cracking, which coincide due to the isotropic behaviour prior to cracking. From Mohr's circle follows

$$\tan(2\theta_k) = \frac{2\sigma_{xy,k}}{\sigma_{xx,k} - \sigma_{yy,k}} = \frac{\gamma_{xy}}{\epsilon_{xx} - \epsilon_{yy}} \tag{4.6}$$

where the stresses and strains prior to crack formation are used. As the stiffness $E_{n,k}$ is completely lost, the Poisson's ratio ν_{tn} reduces according to Equation 2.9 to 0. The crack is completely developed, meaning that no shear stresses should be transmitted within the cracking plane. Equation 2.13 gives $G_{red} = 0$, meaning that zero shear retention is obtained. Hence, the orthotropic fixed smeared crack formulation of Equation 2.8 reduces to

$$\begin{bmatrix} \sigma_{nn} \\ \sigma_{tt} \\ \sigma_{nt} \end{bmatrix}_k = \begin{bmatrix} 0 & 0 & 0 \\ 0 & E_{t,k} & 0 \\ 0 & 0 & 0 \end{bmatrix} \begin{bmatrix} \epsilon_{nn} \\ \epsilon_{tt} \\ \gamma_{nt} \end{bmatrix}_k \tag{4.7}$$

The strain vector now includes index k, as the axes of orthotropy n_k and t_k differ per sublayer. Once the tangential stress $\sigma_{tt,k}$ reaches the compressive or tensile strength of the sublayer, a secondary crack is allowed to form. After the formation of this second crack, the complete capacity of the considered sublayer is lost.
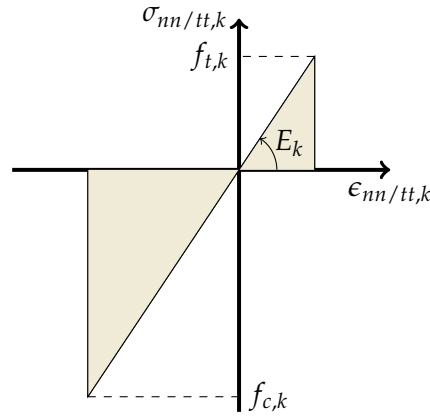
FIGURE 4.5: Constitutive elastic-perfectly brittle material behaviour
for a sublayer k

Element level

The stresses and strains on element level, which is represented by Figure 4.4 (A), are found by superposition of the stresses and strains in the individual sublayers. In this way, the element stress vector σ is obtained by

$$\sigma(\epsilon) = \frac{1}{t} \sum_{k=1}^{N} \sigma_k(\epsilon) \Delta t_k \quad \text{with} \quad t = \sum_{k=1}^{N} \Delta t_k \tag{4.8}$$

Once a sublayer cracks, the considered layer starts behaving orthotropic rather than isotropic and the crack direction of that layer is fixed. The transition of a sublayer from isotropic to orthotropic influences the stresses and strains on element level: the summation of cracks is changed due to the formation of another crack and eventually, the direction of the crack on element level might change, hence mimicking a rotating crack. As each element is subdivided in a set of N layers, the number of integration points increases and the computational expenses increase accordingly. The element stiffness matrix K_e of a plane stress element is given by [9]

$$K_e = \int_\Omega B^T D B \, d\Omega \tag{4.9}$$

in which matrix B transfers the displacement field at the nodes to strains at the integration points, matrix D is the elements' constitutive material law and Ω is the domain or volume of the considered element, such that the stiffness matrix is integrated over the complete element. As an element of the sublayer model consists of a set of N parallel sublayers, the stiffness matrix $K_{e,k}$ is elaborated for each layer by Equation 4.9 and summation of $K_{e,k}$ results in the element stiffness matrix K_e. Because the strain field is the same for all parallel sublayers, the B-matrix is the same for all sublayers; the only changing part is the stiffness matrix D due to changing stiffness and strengths over the layers.

In sequentially linear analysis, the constitutive continuum law is discretized to a saw-tooth or stepwise secant material law (for example Figure 3.3). The properties of each elastic-perfectly brittle sublayer can be chosen such that the superposition of sublayers results in a specific saw-tooth curve, which is in agreement with example 2. How the sublayer properties should be chosen to simulate a saw-tooth curve will be discussed in Chapter 5.
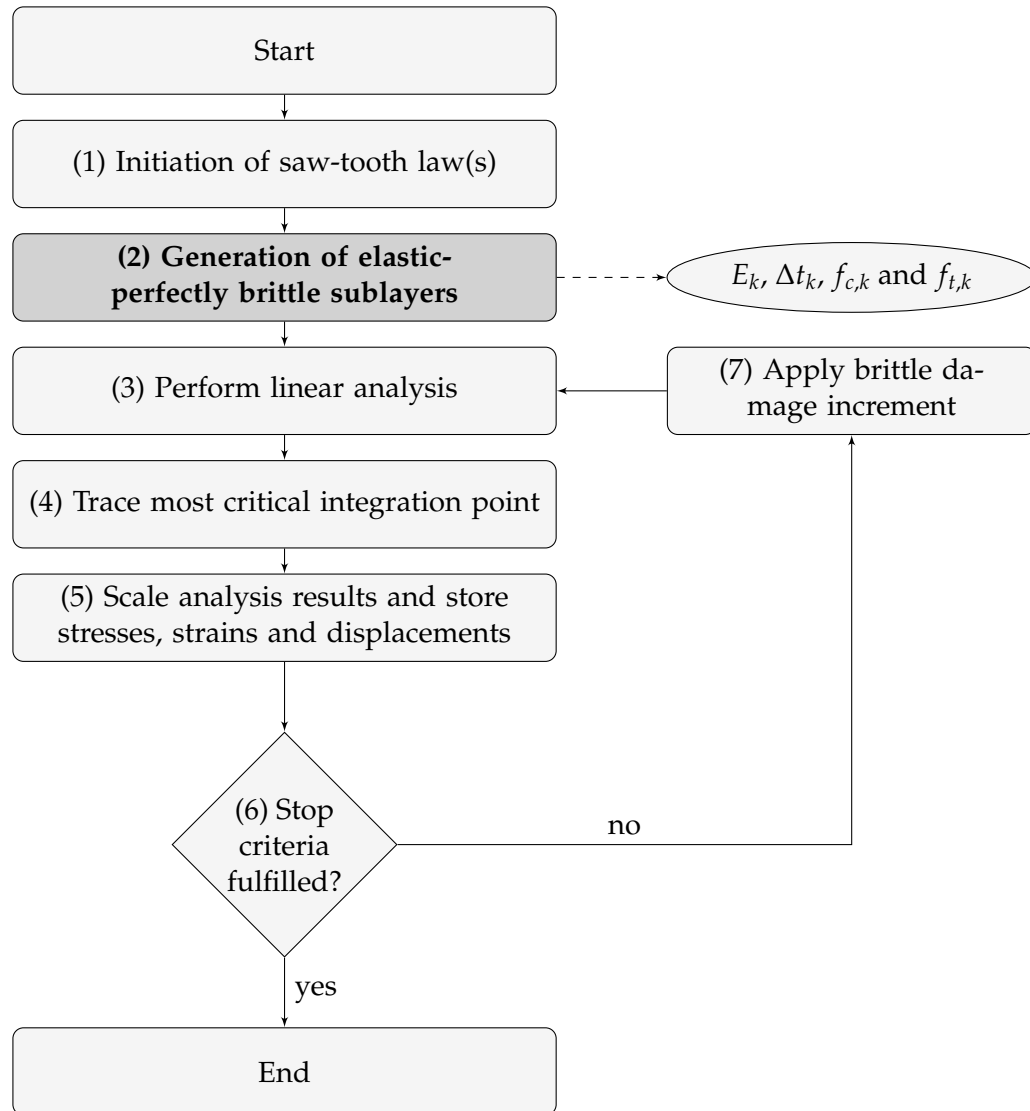
FIGURE 4.6: Flowchart of the sublayer model within the framework of sequentially linear analysis, with extra step for sublayer model highlighted

Structural level

On a structural level, the sublayer model fits well within the framework of regular sequentially linear analysis. Figure 4.6 presents the flowchart of the model, where the additional step in the algorithm compared to regular SLA is highlighted. First, the saw-tooth law(s) is (are) generated in step (1) based on for example the Ripple band approach (see Section 3.4) and a specific continuum law (e.g. linear tension softening as described in Section 2.3). As the continuum law in a smeared crack formulation depends on the crack band h, and since not all elements do necessarily have the same crack band, the initiation of multiple saw-tooth laws might be required. Based on the saw-tooth curve, elastic-perfectly brittle sublayers are generated in step (2) such that on element level the same constitutive material behaviour is found. The output of this step are strength, stiffness and thickness properties for each of the sublayers. The general description of this transition is given in Chapter 5. Step (2) is an extra step that is required for the sublayer model. However, this step fits well within the framework of regular SLA, as can be seen in the flowchart. Next,

a linear analysis is performed in step (3), the most critical integration point is traced in step (4) and the analysis results are scaled with the critical load multipier in step (5). The SLA procedure is stopped in step (6) once a specific user-defined damage state is reached (e.g. a maximum number of damage increments). If the stop criteria is not fulfilled, a brittle damage increment is applied in step (7) and the stiffness perpendicular to the formed crack is set to 0.

Within the flowchart of Figure 4.6, steps (1) and (2) take place on an element level, steps (3) till (6) occur on a structural level and step (7) is performed on sublayer level. As mentioned before, the sublayer model utilizes a fixed cracking approach on sublayer level and mimicks a rotating crack on element level. On a structural level, a damage increment is applied to only 1 critical integration point at a time. Therefore, the crack direction can only rotate at the considered critical element and the other elements are forced to follow a fixed cracking approach. When interpreting the sublayer model as merely rotational cracking for the critical element, similarities with the approaches of Slobbe [72], taking a rotating crack as an event, and Vorel and Boshoff [81], updating the principal directions of the critical integration point after each stress redistribution, become evident. Instead of updating the crack rotation on element level for a critical element like Slobbe, a damage increment on sublayer level is performed, representing a crack rotation on the critical element level. Where the approach of Slobbe considers damage increments and crack rotations separately, the sublayer model simulates crack rotations by applying damage increments, marking a clear fundamental difference between the two approaches. Instead of requiring an incremental iterative stress redistribution to redistribute stresses after a damage increment like Vorel and Boshoff, the sublayer model is a purely sequentially linear approach, where redistribution takes place in the subsequent steps. On top of that, crack directions are fixed upon initiation on sublayer level, where Vorel and Boshoff update the crack directions on element level during the remainder of the analysis for the critical integration points.

The sublayer model also shows similarities with the approach of Cook et al. [17]. In the sublayer model, sublayers are predefined with potentially each their own crack direction. Following the same line of thinking, the model of Cook et al. simulates a rotating crack as a multidirectional crack with predefined cracking planes, having each their own predefined crack direction. The most critical plane (instead of sublayer) is sought for and a damage increment is performed. However, where the model of Cook et al. requires a large amount of predefined cracking planes on element level, each sublayer of the sublayer model is allowed to crack in any direction, depending on the principal stress direction, and therefore, a wide spectrum of cracks can be simulated without the need to predefine a large amount of cracking planes a priori.

Recently, a study by Liu [49] has been published, proposing a so-called *subelement* strategy, in which an element is discretized into elastic-perfectly brittle overlay elements. Although the author seems to be not aware of this, clear similarities with the sublayer model are found. However, the sub-element model by Liu is more or less applied as a lattice model (see Section 3.2) and no attention is paid to the crack direction. The main purpose of the sub-element model by Liu was to offer an alternative to incremental iterative analysis and regular SLA, although it is fundamentally similar to the sublayer model and could have been used to mimick a rotating crack model as well.

4.4   Continuous approach

In this section, a theoretical background of the sublayer model will be given by considering a uniaxially loaded element with an infinite number of sublayers with a infinitesimal size. Within this framework, the strength $f_{t/c,k}$ and stiffness E_k properties of the layers are described by a continuous function. For this purpose, the discrete index k is replaced by a continuous parameter $\phi = [0..1]$, describing the fraction of the elements area that is already cracked, in line with the approach of Hendriks and Rots [31]. For $\phi = 0$, no sublayers are cracked and for $\phi = 1$, all sublayers are cracked and the element has completely failed. The stiffness is given by function $E(\phi)$ and the strength by function $f_{t/c}(\phi)$. Both uniaxial tension and compression are considered. Before the first layer cracks, the total homogenized stiffness of the element is equal to E_0, which is for discrete sublayers found by

$$E_0 = \frac{1}{t} \sum_{k=1}^{N} E_k \Delta t_k \tag{4.10}$$

and for the continuous case with an infinite number of sublayer equal to

$$E_0 = \int_0^1 E(\phi)\, d\phi \tag{4.11}$$

During cracking, at a moment that fraction $\phi_{cr} > 0$ of the element is cracked, the momentary stiffness $E(\phi_{cr})$ of the element is the stiffness of the uncracked fraction of the cross-section, which is found using Equation 4.11 to be

$$E(\phi_{cr}) = \int_{\phi_{cr}}^1 E(\phi)\, d\phi \tag{4.12}$$

4.4.1   Uniaxial tension

For the case of uniaxial tension, two types of softening curves will be considered in this section. First, reciprocal tension softening as derived by Hendriks and Rots [31] is elaborated. On top of that, this thesis extended the continuous approach to linear tension softening.

Reciprocal softening
In the following paragraph, it is shown that a reciprocal tension softening curve is obtained for continuous functions $E(\phi)$ and $f_t(\phi)$ given by

$$\begin{aligned} E(\phi) &= 2E_0(1-\phi) \\ f_t(\phi) &= 2f_t \end{aligned} \tag{4.13}$$

where E_0 and f_t are assumed to be the stiffness and strength of the standard isotropic uncracked material. From Equation 4.13 follows that the stiffness reduces for increasing cracked fraction ϕ, hence simulating softening effects. Applying Equation 4.12 results in the momentary stiffness

$$\begin{aligned} E(\phi_{cr}) &= \int_{\phi_{cr}}^1 2E_0(1-\phi)\, d\phi \\ &= E_0(1-\phi_{cr})^2 \end{aligned} \tag{4.14}$$

The momentary uniaxial strain ϵ is derived from $\epsilon = f_t(\phi)/E(\phi)$, leading after substitution of Equations 4.13 to
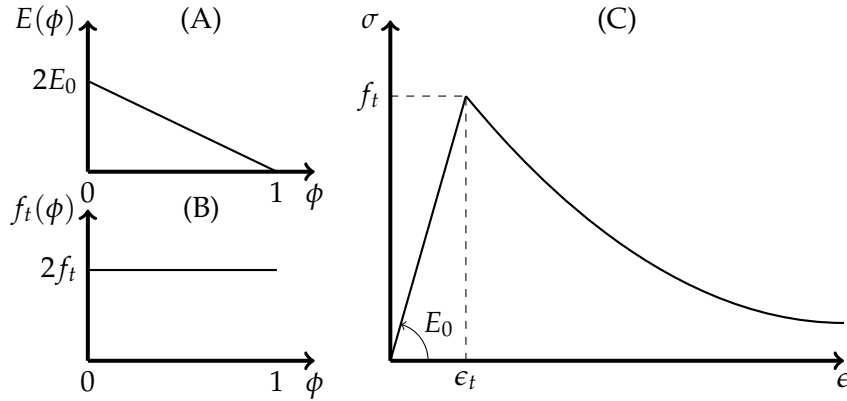
FIGURE 4.7: Visualization of (A) function $E(\phi)$, (B) function $f_t(\phi)$ and (C) the resulting reciprocal tension softening curve for uniaxial tension

$$\epsilon = \frac{2f_t}{2E_0(1-\phi)} \tag{4.15}$$

which can be rewritten to

$$\frac{f_t}{E_0 \, \epsilon} = (1-\phi) \tag{4.16}$$

The stress at the moment that a fraction ϕ_{cr} is cracked, is now straightforwardly found by $\sigma(\phi_{cr}) = E(\phi_{cr}) \, \epsilon$, which reduces after substitution of Equation 4.14 to

$$\sigma(\phi_{cr}) = E_0(1-\phi_{cr})^2 \epsilon \tag{4.17}$$

and substitution of Equation 4.16 gives

$$\sigma(\phi_{cr}) = E_0 \left(\frac{f_t}{E_0 \, \epsilon}\right)^2 \epsilon = \frac{f_t^2}{E_0 \, \epsilon} \tag{4.18}$$

Equation 4.18 describes a reciprocal softening relation and is valid for $\epsilon > f_t/E_0$. For strains smaller than the elastic strain ϵ_t, $\phi_{cr} = 0$. However, ϕ_{cr} is only defined for values larger than 0, since at $\phi_{cr} = 0$ no fractions are cracked yet. Furthermore, from Equation 4.18 also follows that E_0 and f_t are indeed the initial uncracked homogenized material properties. Figure 4.7 gives a visualization of the applied strength and stiffness function and the resulting reciprocal softening curve.

Linear softening
In this thesis, the application of the continuous approach is extended to linear tension softening behaviour. In the following paragraph, it is shown in the same manner as for reciprocal tension softening that a linear tension softening curve is obtained for continuous functions $E(\phi)$ and $f_t(\phi)$ described by

$$\begin{aligned} E(\phi) &= E_0 \, a \, \exp\left(-b\phi\right) \\ f_t(\phi) &= c \, f_t \end{aligned} \tag{4.19}$$

For now, coefficients a, b and c are undefined. Later on, a physical meaning is given to these coefficients. The momentary stiffness is found using Equation 4.12

$$
\begin{aligned}
E(\phi_{cr}) &= \int_{\phi_{cr}}^{1} E_0\, a \, \exp\left(-b\phi\right) d\phi \\
&= \tfrac{a}{b} E_0 \left[\exp\left(-b\phi_{cr}\right) - \exp\left(-b\right)\right]
\end{aligned}
\tag{4.20}
$$

The momentary strain ϵ is derived in the same manner as for reciprocal tension softening, giving

$$
\epsilon = \frac{c f_t}{E_0\, a \, \exp\left(-b\phi\right)}
\tag{4.21}
$$

which is rewritten to

$$
E_0\, a \, \exp\left(-b\phi\right) = \frac{c f_t}{\epsilon}
\tag{4.22}
$$

The momentary stress $\sigma(\phi_{cr})$ is found by substitution of Equations 4.20 and 4.22 in $\sigma(\phi_{cr}) = E(\phi_{cr})\,\epsilon$

$$
\begin{aligned}
\sigma(\phi_{cr}) &= \tfrac{a}{b} E_0 \left[\exp\left(-b\phi_{cr}\right) - \exp\left(-b\right)\right]\epsilon \\
&= \tfrac{c}{b} f_t - \tfrac{a}{b} E_0 \exp\left(-b\right)\epsilon
\end{aligned}
\tag{4.23}
$$

It can already be seen from Equation 4.23 that a linear dependency to ϵ is obtained with the chosen stiffness and strength functions. As the linear tension curve should pass the point $(\epsilon_t = f_t/E_0, f_t)$, there is a restriction on the coefficients a, b and c.

$$
\sigma(\epsilon_t) = \frac{c}{b} f_t - \frac{a}{b} E_0 \exp\left(-b\right)\frac{f_t}{E_0} = f_t
\tag{4.24}
$$

All terms in Equation 4.24 are a multiplication of f_t and hence, it can be further reduced to

$$
\frac{c}{b} - \frac{a}{b} \exp\left(-b\right) = 1
\tag{4.25}
$$

from which coefficient a is solved

$$
a = (c - b) \, \exp\left(b\right)
\tag{4.26}
$$

Substitution of coefficient a, as given by Equation 4.26, in Equation 4.23 results in a linear tension softening curve description

$$
\sigma = \frac{c}{b} f_t - \frac{E_0(c - b)}{b}\epsilon \quad \text{for} \quad \epsilon > \frac{f_t}{E_0}
\tag{4.27}
$$

Figure 4.8 visualizes the stiffness and strength functions $E(\phi_{cr})$ and $f_t(\phi_{cr})$ respectively, together with the resulting tension softening curve. Next, the physical background of coefficients b and c is investigated. The second brand of a linear tension softening law is described by

$$
\sigma = D(\epsilon_t - \epsilon) + f_t \quad \text{with} \quad D = \frac{f_t}{\epsilon_u - \epsilon_t}
\tag{4.28}
$$

Extracting the terms that are independent of ϵ from Equations 4.27 and 4.28 results in the following equality:
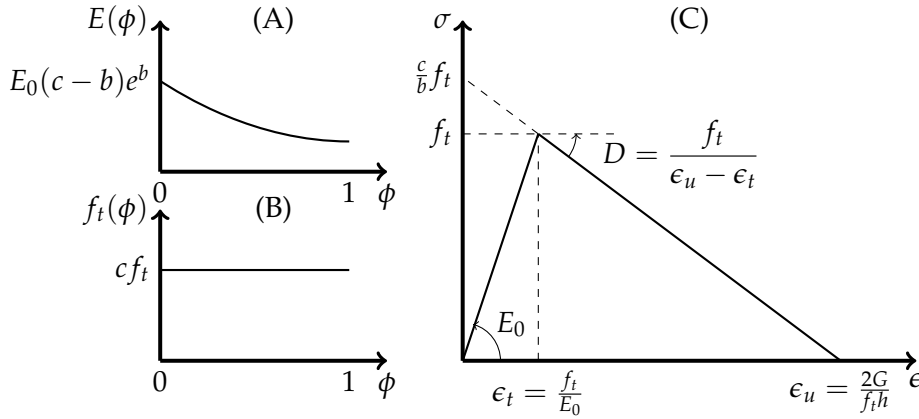
$$
\frac{c}{b} f_t = D\epsilon_t + f_t
\tag{4.29}
$$

FIGURE 4.8: Visualization of (A) function $E(\phi)$, (B) function $f_t(\phi)$ and (C) the resulting linear tension softening curve for uniaxial tension with definitions

from which the factor $f_t c/b$ can now be physically understood to be the crossing point with the vertical axis, as depicted by Figure 4.8 (C). As the slope D of the second branch is negative, the crossing point with the vertical axis is always larger than f_t, adding the restriction $c/b > 1$. In the same manner, the terms that are dependent of ϵ are extracted from Equations 4.27 and 4.28, resulting in

$$\frac{E_0(c - b)}{b} = D \tag{4.30}$$

Apparently, coefficients b and c relate the stiffness E_0 of the first branch to the negative stiffness D of the second branch of the tension softening curve. Solving Equations 4.29 and 4.30, and substituting D from Equation 4.28, one obtains a relation for coefficient b:

$$b = c \left(1 - \frac{\epsilon_t}{\epsilon_u}\right) \tag{4.31}$$

in which c is a variable that should be predefined, the elastic strain $\epsilon_t = f_t/E_0$ and the ultimate strain $\epsilon_u = 2G/f_t h$. Assuming that no constitutive snap-back occurs, ϵ_u is by definition larger than ϵ_t. From Equation 4.31 can be concluded that the restriction $c/b > 1$ is automatically fulfilled. For this reason, the continuous approach as described in this paragraph is not applicable for constitutive snap-back. For $c = 1$, the coefficients a and b and the stiffness and strength functions $E(\phi_{cr})$ and $f_t(\phi_{cr})$ respectively are given by:

$$a = \frac{\epsilon_t}{\epsilon_u} \exp\left(1 - \frac{\epsilon_t}{\epsilon_u}\right)$$
$$b = 1 - \frac{\epsilon_t}{\epsilon_u}$$
$$c = 1 \tag{4.32}$$
$$E(\phi) = E_0 \frac{\epsilon_t}{\epsilon_u} \exp\left[(1 - \phi)\left(1 - \frac{\epsilon_t}{\epsilon_u}\right)\right]$$
$$f_t(\phi) = f_t$$

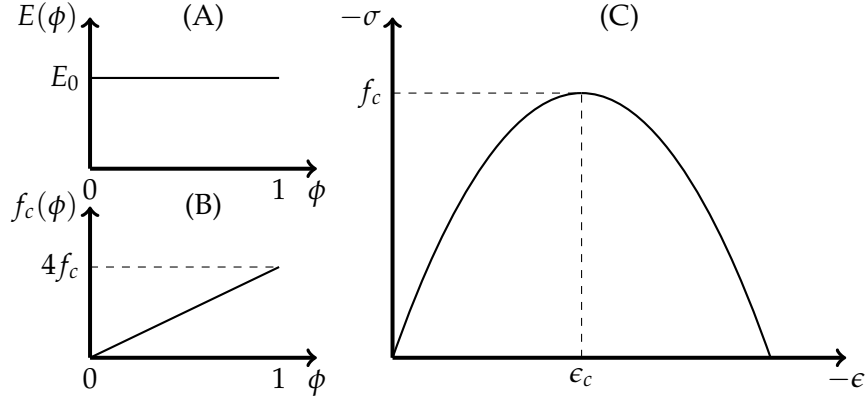With the aid of Equations 4.32, a continuous representation has been found which

FIGURE 4.9: Visualization of (A) function $E(\phi)$, (B) function $f_c(\phi)$ and (C) the resulting parabolic compressive hardening/softening curve for uniaxial compression

can be used to apply the sublayer model for linear tension softening in a continuous manner, using an infinite number of sublayers with infinitesimal size.

4.4.2   Uniaxial compression

For the case of uniaxial compression, two types of constitutive curves will be considered in this section. First, the parabolic hardening/softening curve as derived by Hendriks and Rots [31] is considered. Secondly, this thesis extended the approach to ideal constant crushing (linear until the strength is reached and then a horizontal plateau until the ultimate strain ϵ_u is reached).

Parabolic hardening/softening
In the following, it is shown that a parabolic hardening/softening curve can be described by

$$\begin{array}{rcl} E(\phi) & = & E_0 \\ f_c(\phi) & = & 4f_c\,\phi \end{array} \tag{4.33}$$

where E_0 and f_c are assumed to be the stiffness and strength of the considered material. As the approach for a parabolic curve is the same as for reciprocal softening, only the main steps are described. The momentary stiffness is found by

$$E(\phi_{cr}) = E_0(1 - \phi_{cr}) \tag{4.34}$$

The momentary uniaxial strain $\epsilon = f_c(\phi)/E(\phi)$, in which Equations 4.33 are substituted. From the resulting expression, ϕ_{cr} is solved

$$\phi_{cr} = -\frac{E_0}{4f_c}\epsilon \tag{4.35}$$

which can be used to reduce $\sigma(\phi_{cr}) = E(\phi_{cr})\,\epsilon$ to

$$\sigma(\phi_{cr}) = E_0\left(1 + \frac{E_0}{4f_c}\epsilon\right)\epsilon \tag{4.36}$$

Equation 4.36 describes a parabolic constitutive softening/hardening relation for $-4f_c/E_0 \leq \epsilon \leq 0$. Figure 4.9 gives a visualization of the functions for the strength
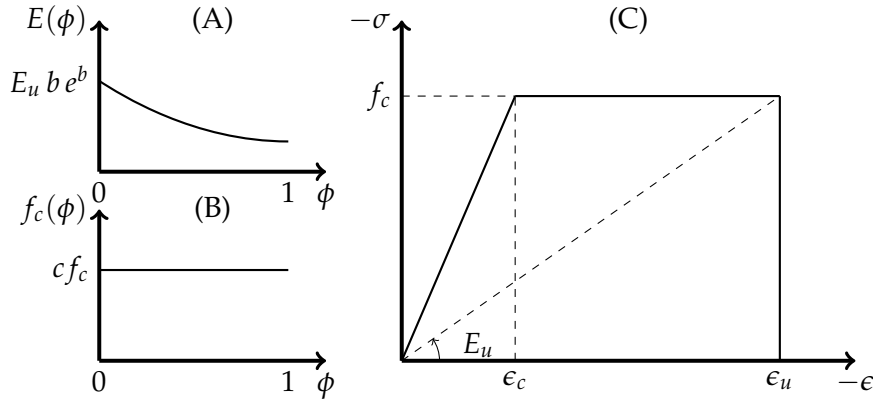
FIGURE 4.10: Visualization of (A) function $E(\phi)$, (B) function $f_c(\phi)$ and (C) the resulting ideal constant crushing curve for uniaxial compression

and stiffness and the resulting constitutive behaviour. The obtained parabolic curve is in line with the Hognestad parabola [36].

Ideal constant crushing
The constitutive curve for ideal constant crushing increases linearly until the strength is reached. The second branch is a horizontal plateau with constant stress f_c, until the maximum strain ϵ_u is reached and the stress drops abruptly to 0. The ideal constant curve is the most simple way to describe the nonlinear process of compressive failure of concrete. Because the second branch of both the linear tension softening and ideal constant curves are linear, the continuous approach for this case follows the same path as linear tension softening and the same functions $E(\phi)$ and $f_c(\phi)$ as given in Equations 4.19 can be applied. However, special attention must be paid to the coefficients a, b and c, as these are found in a slightly different way. From Figures 4.8 (C) and 4.10 (C) follows that the ratio c/b must be 1 such that a constant stress plateau is found at f_c, and hence $b = c$. However, this results in $a = 0$, following Equation 4.26, causing the function $E(\phi)$ to be 0 for all ϕ, giving a non-usable and non-physical solution. Therefore, a different approach has to be followed.

The stiffness and strength properties of all sublayers with infinitesimal size can be described with functions $E(\phi)$ and $f_c(\phi)$, except the last layer to crack (corresponding to $\phi = 1$). This layer cracks at the ultimate strain ϵ_u. Because at this point, a major stress drop takes place and the linearity of the second branch is lost, functions $E(\phi)$ and $f_c(\phi)$ are not valid anymore. This specific layer contributes with a stiffness E_u and strength f_c, as depicted by Figure 4.10 (C). As this last layer can not be described by $E(\phi)$ and $f_c(\phi)$, the expression to determine the momentary stiffness $E(\phi_{cr})$ changes to

$$
\begin{aligned}
E(\phi_{cr}) &= \int_{\phi_{cr}}^1 E_0\, a\, \exp\left(-b\phi\right) d\phi + E_u \\
&= \tfrac{a}{b} E_0 \left[\exp\left(-b\phi_{cr}\right) - \exp\left(-b\right)\right] + E_u
\end{aligned}
\tag{4.37}
$$

with

$$
E_u = \frac{f_c}{\epsilon_u}
\tag{4.38}
$$

The change in momentary stiffness does not alter Equation 4.22. The expression for the momentary stress $\sigma(\phi_{cr}) = E(\phi_{cr})\,\epsilon$ becomes

$$
\begin{aligned}
\sigma(\phi_{cr}) &= \tfrac{a}{b}E_0\left[\exp\left(-b\phi_{cr}\right) - \exp\left(-b\right)\right]\epsilon + E_u\epsilon \\
&= \tfrac{c}{b}f_c - \tfrac{a}{b}E_0\exp\left(-b\right)\epsilon + E_u\epsilon
\end{aligned}
\tag{4.39}
$$

Equation 4.39 must cross $\epsilon = \epsilon_c$ and $\sigma = f_c$. From this requirement, the coefficient a is solved straighforwardly:

$$
a = \left(c - b + \frac{E_u}{E_0}\right)\exp\left(b\right)
\tag{4.40}
$$

Now, the differences between the approaches for linear tension softening and ideal constant crushing become clear by Equations 4.26 and 4.40. Substitution of Equation 4.40 in Equation 4.39 gives

$$
\begin{aligned}
\sigma(\phi_{cr}) &= \tfrac{c}{b}f_c - \tfrac{E_0}{b}\left(c - b + \tfrac{E_u}{E_0}b\right)\epsilon + E_u\epsilon \\
&= \tfrac{cf_c}{b} + \tfrac{E_0(c-b)}{b}\epsilon \quad \text{for} \quad -\epsilon > \tfrac{f_c}{E_0}
\end{aligned}
\tag{4.41}
$$

Although a different approach is used, Equations 4.27 and 4.41 are exactly the same. The horizontal plateau requires a restriction, as a horizontal curve can only be obtained when coefficients b and c are equal to each other (the ϵ term drops out of Equation 4.41). After substitution of Equation 4.38 and $\epsilon_c = f_c/E_0$, the coefficient a and functions $E(\phi)$ and $f_c(\phi)$ are now given by

$$
\begin{aligned}
a &= \frac{E_u}{E_0}b\,\exp\left(b\right) = \frac{\epsilon_c}{\epsilon_u}b\,\exp\left(b\right) \\
b &= c \\
E(\phi) &= E_0\,\frac{\epsilon_c}{\epsilon_u}b\,\exp\left[(1-\phi)b\right] \\
f_c(\phi) &= b\,f_c
\end{aligned}
\tag{4.42}
$$

where coefficient b is an undefined scaling parameter, which can take any value > 0. For simplicity, one could take $b = 1$, leading to

$$
E(\phi) = E_0\,\frac{\epsilon_c}{\epsilon_u}\exp\left[(1-\phi)\right]
\tag{4.43}
$$

With the aid of Equations 4.42, a continuous representation has been found which can be applied to all infinitesimal sublayers, except the last layer to crack. The functions $E(\phi)$ and $f_c(\phi)$ and the resulting stress-strain curve are shown in Figure 4.10.

Chapter 5

General transition saw-tooth law SLA to sublayer properties

In this chapter, the general transition from regular SLA to the sublayer model is formulated. First, the concept of the general transition is discussed in Section 5.1, followed by a thorough formal derivation in Section 5.2, resulting in formulations to obtain sublayer properties based on a saw-tooth curve. Next, constitutive snap-back is considered in Section 5.3, followed by an elaboration of three examples in Section 5.4. In Section 5.5, the general transition is extended to cases where the constitutive laws in both tension and compression are considered. Lastly, some final notes and a brief outline for the remainder of this thesis are discussed in Section 5.6. It is noted that in this chapter both the damaged stiffness corresponding to a saw-tooth and the stiffness of a sublayer are used together. To be absolutely clear which one is used, the upper index L (abbreviation of 'layer') is added to sublayer properties. In this way, E_i is the damaged stiffness of a saw-tooth and E_i^L the stiffness of an elastic-perfectly brittle sublayer.

5.1 Concept general transition

As mentioned in Section 4.3, the sublayer model fits well within regular sequentially linear analysis. In this chapter, more attention will be given to the transition from a continuum saw-tooth SLA formulation to a set of elastic-perfectly brittle sublayers (step (2) in the flowchart of Figure 4.6). Before a formal derivation of the general transition from saw-tooth law to sublayer properties is given in Section 5.2, the general concept is discussed. Figure 5.1 contains a flowchart, in which the principal idea is schematized. An arbitrary stress-strain continuum softening/hardening law (e.g. linear tension softening or Thorenfeldt compressive crushing, see Chapter 2) is taken as input. In step (1), a stepwise secant material law or so-called saw-tooth law is set up with the aid of a specific saw-tooth formulation, for example the ripple band approach, as discussed in Section 3.4. Discretization of the continuum law results in a set of N saw-teeth, all having their own specific reduced stiffness E_i and strength $f_{t/c,i}$. Once the strength of a specific saw-tooth is reached, a damage increment is performed and lower stiffness and strength are attributed to the critical element.

The gap between SLA and the sublayer model is bridged by step (2) of Figure 5.1. The strains $\epsilon_{t/c,i}$ (t in case tension is considered and c for compression) belonging to damage increments are found based on the strength and stiffness of the saw-teeth

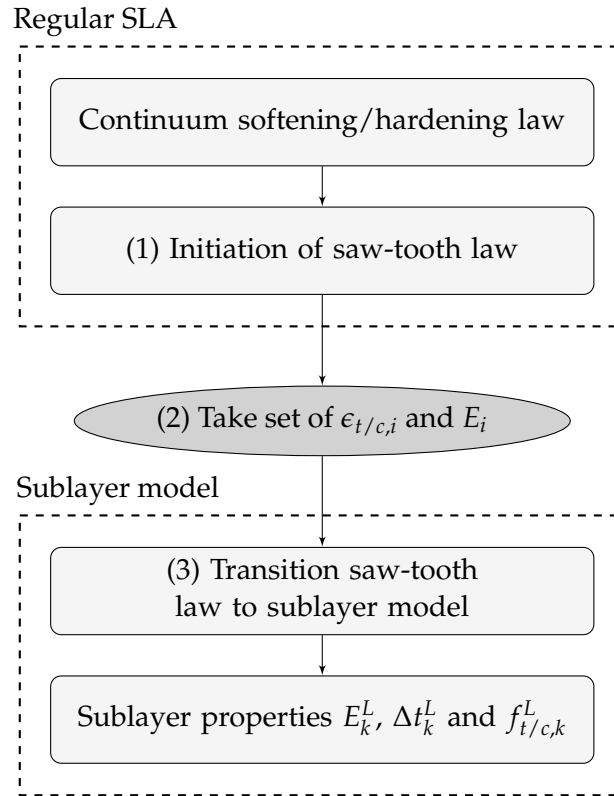$$\epsilon_{t/c,i} = \frac{f_{t/c,i}}{E_i} \tag{5.1}$$

Regular SLA

FIGURE 5.1: Flowchart of concept general transition from saw-tooth
law to sublayer (material) properties

Furthermore, in step (2) the collection of damaged stiffnesses E_i is extracted from
the saw-tooth law. The transition from a saw-tooth law formulation to the sublayer
model in step (3) takes as input the set of strains $\epsilon_{t/c,i}$ and damaged stiffnesses E_i.
As will be shown in Section 5.2, the properties of sublayer k can be derived straight-
forwardly with the aid of these two inputs. Since all sublayers of a certain element
are subdued to the same strain field, the saw-tooth strain on element level equals
the strain on sublayer level. The output of step (3) are the sublayer stiffness E_k^L,
thickness Δt_k^L and strength (either tensile or compressive depending on the load-
ing) $f_{t/c,k}^L$. With this flowchart, a method is proposed that generates a saw-tooth law
based on the framework of regular SLA, which is subsequently transformed to sub-
layer properties within the '*Sublayer model*' block of the flowchart. Step (2) can be
seen as a coupling agent between the regular SLA as discussed in Chapter 3 and the
sublayer model as proposed in Chapter 4.

5.2   Formal derivation

In this section, the concept as explained in Section 5.1 is theoretically substanti-
ated for stress-strain continuum laws without constitutive snap-back, as constitutive
snap-back is discussed in Section 5.3. The derivation is split in two parts. Firstly, step
(1) of Figure 5.1 is elaborated and secondly, step (3) is formally derived. Arbitrarily, a
linear tension softening continuum law is used for this derivation (other continuum
laws can be used as well following the same approach). Furthermore, for demonstra-
tion purposes the ripple band concept as proposed by Rots, Belletti and Invernizzi
[64] is used, where also the more advanced improved ripple band concept by Van
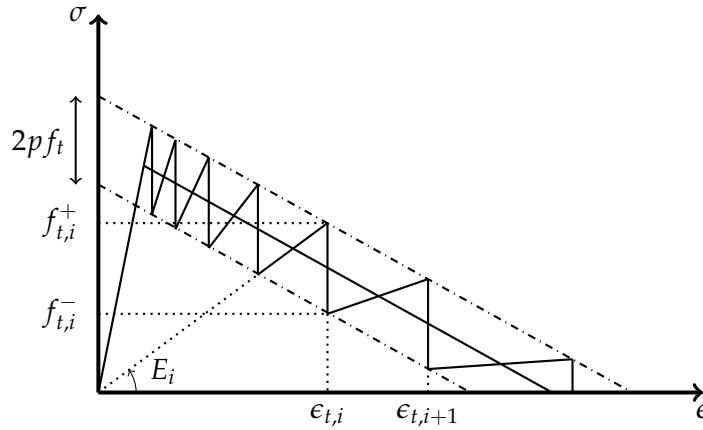
FIGURE 5.2: Schematization of step (1): initiation of saw-tooth law for linear tension softening continuum law using the ripple band concept

de Graaf [29] could have been applied. The main contribution of this thesis to SLA is found in step (3) and therefore, most attention is paid to this step and step (1) is not made more complicated by using the advanced improved ripple band concept which requires an iterative solution procedure.

Step (1): initiation of saw-tooth law
Following the work of [64], the saw-tooth curve is obtained using the ripple band concept. Figure 5.2 depicts the transition from a linear tension softening smeared cracking continuum law to a saw-tooth law. The first branch is linear elastic with stiffness E_0 up until the strength f_t is reached. The second branch has a negative slope D, which is found by

$$D = \frac{f_t}{\epsilon_u - \epsilon_t} \quad \text{with} \quad \epsilon_u = \frac{2G_f^I}{f_t h} \quad \text{and} \quad \epsilon_t = \frac{f_t}{E_0} \tag{5.2}$$

Considering a specific saw-tooth i, where $i = 1..N$ and N the total number of saw-teeth, the point of intersection $\epsilon_{t,i}$ between the secant elastic branch with stiffness E_i and the upper ripple band is sought for. The upper ripple curve is given by

$$\sigma = D(\epsilon_t - \epsilon) + (1 + p)f_t \tag{5.3}$$

and hence, the point of intersection with the secant elastic branch is found for

$$\epsilon_{t,i} = \frac{D\epsilon_t + (1 + p)f_t}{D + E_i} \tag{5.4}$$

Next, the tensile strength on the upper curve $f_{t,i}^+ = \epsilon_{t,i} E_i$ is further elaborated with the aid of Equation 5.4 and by substitution of $\epsilon_u = \epsilon_t + f_t/D$, leading to [64]

$$f_{t,i}^+ = E_i \left(\epsilon_u + \frac{pf_t}{D} \right) \frac{D}{D + E_i} \tag{5.5}$$

and

$$f_{t,i}^- = f_{t,i}^+ - 2pf_t \tag{5.6}$$

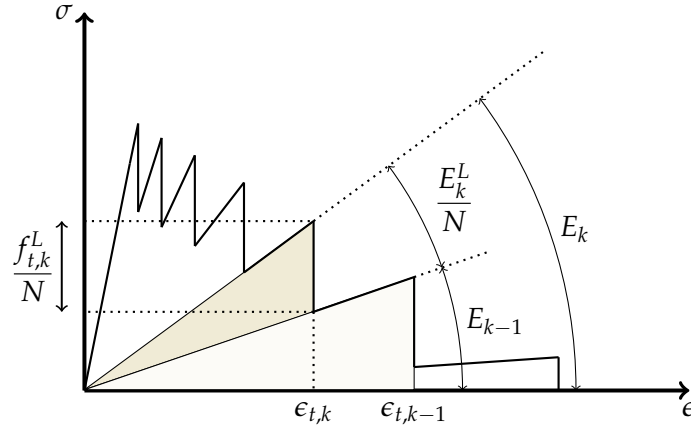Lastly, the stiffness of the next saw-tooth is found by substitution of Equations 5.4 and 5.6 in

FIGURE 5.3: Schematization of step (3): transition saw-tooth law to sublayer model properties

$$E_{i+1} = \frac{f_{t,i}^-}{\epsilon_{t,i}} \tag{5.7}$$

and the process is repeated until $f_{t,i}^+ < 2pf_t$, meaning that the last branch is reached. The total number of saw-teeth N mainly depends on the ripple band parameter p and is unknown beforehand. The transition from a saw-tooth curve to the sublayer model takes the collection of $\epsilon_{t,i}$ and E_i, as input. Step (2) takes these two quantities as output from step (1) and inputs them in step (3).

Step (3): transition saw-tooth law to sublayer model
In step (3), the saw-tooth curve of Figure 5.2 is simulated with the aid of N parallel sublayers, following the ideas behind example 2 in Section 4.1. The core idea behind the transition is very simple: the remaining stress at a specific moment is the superposition of the stresses of the uncracked sublayers. Starting from the last layer to crack (with the largest ultimate strain), the sublayer properties can be determined in a backwards manner, using the elements stress-strain saw-tooth law as already defined in step (1). As the sublayer properties are determined starting from the last layer ($i = N$), a new index

$$k = N - i + 1 \tag{5.8}$$

is introduced, which takes value 1 for $i = N$ and N for $i = 1$. In this way, the layer with the largest strain $\epsilon_{t/c,i}$ has index $k = 1$.

For the determination of the sublayer properties, either the thickness Δt_k^L or stiffness E_k^L should be predefined, in order to prevent an infinite number of solutions (for each thickness distribution, a solution can be found). As a starting point, it is assumed that all layers have the same thickness $\Delta t_k^L = t/N$. By doing so, the contribution of the stress of the considered sublayer to the total element behaviour is σ_k^L/N. The stress is averaged over the total element thickness t. On top of that, the same holds for the sublayer stiffness.

The given collection of damaged stiffnesses E_k from the saw-tooth curve are used to determine the sublayer stiffnesses E_k^L according to Figure 5.3. As both damaged stiffnesses E_k and E_{k-1} are known, and the difference between the both of them is the stiffness contribution of sublayer k with respect to the complete element thickness E_k^L/N, the following equality can be set up

$$E_k = \frac{E_k^L}{N} + E_{k-1} \tag{5.9}$$

The physical meaning of Equation 5.9 is visualized in Figure 5.3; both the left hand side and right hand side should give the same total stiffness. From Equation 5.9 E_k^L is solved, giving

$$E_k^L = N(E_k - E_{k-1}) \tag{5.10}$$

With the aid of Equation 5.10, the stiffness of a specific sublayer k can be derived from the damaged stiffnesses following from the saw-tooth law in step (1). In Figure 5.3, the two filled areas represent two separate sublayers. The tensile strength $f_{t,k}^L$ of sublayer k is obtained by

$$\frac{f_{t,k}^L}{N} = \frac{E_k^L}{N} \epsilon_{t,k} \quad \text{so} \quad f_{t,k}^L = E_k^L \epsilon_{t,k} \tag{5.11}$$

Invoking Equations 5.10 and 5.11, all properties of a sublayer k have been determined: thickness Δt_k^L, stiffness E_k^L and tensile strength $f_{t,k}^L$. Based on step (3), input collections $\epsilon_{t/c,i}$ and E_i can be transferred to the sublayer model. The choice of a specific continuum law and saw-tooth set-up law only influences the procedure of step (1); Equation 5.4 is specifically valid for linear tension softening with a ripple band approach. Hence, for different continuum and saw-tooth set-up laws, the procedure and output of step (1) will definitely change. However, the procedure of step (3) does not change at all since the choice of continuum and saw-tooth set-up laws is embedded in the input damaged stiffness E_i and strain $\epsilon_{t/c,i}$ from step (2). The procedure of step (3) is completely decoupled from the chosen continuum and saw-tooth set-up law and therefore, the transition from saw-tooth law to sublayer model is considered to be a *general transition*. One could for example apply the improved ripple band concept. By doing so, step (1) becomes an iterative procedure to determine the upper and lower ripple band width, leading to a specific saw-tooth curve that can be described by a collection E_i and $\epsilon_{t/c,i}$. Step (3) takes these two quantities as input and determines the sublayer properties with Equations 5.10 and 5.11. With this general transition, the sublayer model is directly linked to regular SLA.

In this section, it was assumed that all sublayers have the same thickness. This assumption has been made in order to have a more straightforward calculation of element stresses and stiffnesses (dividing by N, instead of scaling with the thickness of the considered sublayer relative to the total thickness). In Appendix A, the approach assuming the same stiffness for all sublayers and different thickness is elaborated. Furthermore, it is shown that both the approaches are equivalent. The approach assuming the same thickness will be used throughout the remained of this thesis for the aforementioned reason.

5.3 Constitutive snap-back

In this section, constitutive snap-back for a linear tension softening continuum law is discussed. Constitutive snap-back occurs for very brittle materials with low fraction energies. For a smeared crack formulation, the ultimate strain $\epsilon_u = 2G_f^I/f_t h$ might become smaller than the elastic tensile strain $\epsilon_t = f_t/E_0$ (for example for the continuum law shown in Figure 5.4). In that case, the procedure as described in Section 5.2
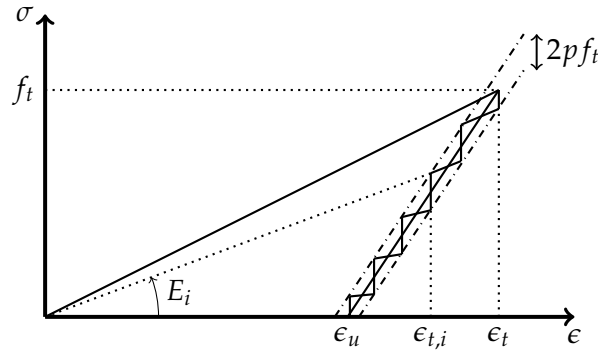
FIGURE 5.4: Saw-tooth law generation for constitutive snap-back

should be slightly adapted. The occurrence of constitutive snap-back can be steered with the crack band h and takes place for

$$h > \frac{2G_f^I E_0}{f_t^2} \tag{5.12}$$

For h not fulfilling Equation 5.12, a negative tangent stiffness is obtained in NLFEA, leading to numerical instabilities, as discussed in Section 2.3. SLA does not have these numerical issues and Invernizzi et al. [37] have shown that SLA is able to handle constitutive snap-backs. In their paper, the initiation algorithm for constitutive snap-back is derived. As the derivation of step (1) for the case of constitutive snap-back is conceptually the same as performed in Section 5.2, it will not be repeated here and the reader is referred to [37]. The only notable difference for constitutive snap-back is found in the first saw-tooth, which has only a stress decrement of pf_t instead of $2pf_t$, to prevent a significant strain overshoot here. Figure 5.4 depicts the generation of a saw-tooth law for the case of constitutive snap-back. Furthermore, steps (2) and (3) do not change, as snap-back is implemented in the set of strains $\epsilon_{t/c,i}$ and stiffnesses E_i.

However, constitutive snap-back within the sublayer model requires an additional measure. The sublayer model inherently generates N decoupled sublayers, where SLA generates N coupled saw-teeth. Consider the case of uniaxial loading. For SLA, the loading can be increased until the first saw-tooth strength is reached. Then, a damage increment is performed and the element loaded is again loaded until the second saw-tooth strength. The sublayer model encounters some trouble here; due to the uncoupled nature of the sublayers, the layer with the smallest ultimate strain is the first to crack. For regular cases, this would suffice. However, for constitutive snap-back, the layer with the largest cracking strain should be the first to crack instead of the layer with the smallest ultimate strain. Without any measures, all sublayers are cracked by the time the maximum stress f_t is reached. Therefore, a cracking order should be added to the sublayer model in case of constitutive snap-back: a sublayer k is only able to crack if sublayer $k+1$ is already cracked. In this way, a conditional strength is implemented, which allows the sublayer model to follow the same stress-strain path as the saw-tooth curve.

For regular concrete structures, constitutive snap-back does not take place. The problem is more relevant for extremely brittle materials like glass. As this thesis is mainly focussed on the analysis of quasi-brittle (and not extremely brittle) concrete structures, constitutive snap-back behaviour is not further considered. It is however discussed in this section for the sake of completeness.

Quantity		Value	Unit
Tensile strength	f_t	3.0	N/mm^2
Initial stiffness	E_0	20000	N/mm^2
Fracture energy	G_f^I	0.1	N/mm
Crack bandwidth	h	20	mm
Ripple band parameter	p	0.14	-

TABLE 5.1: Properties example exponential tension softening

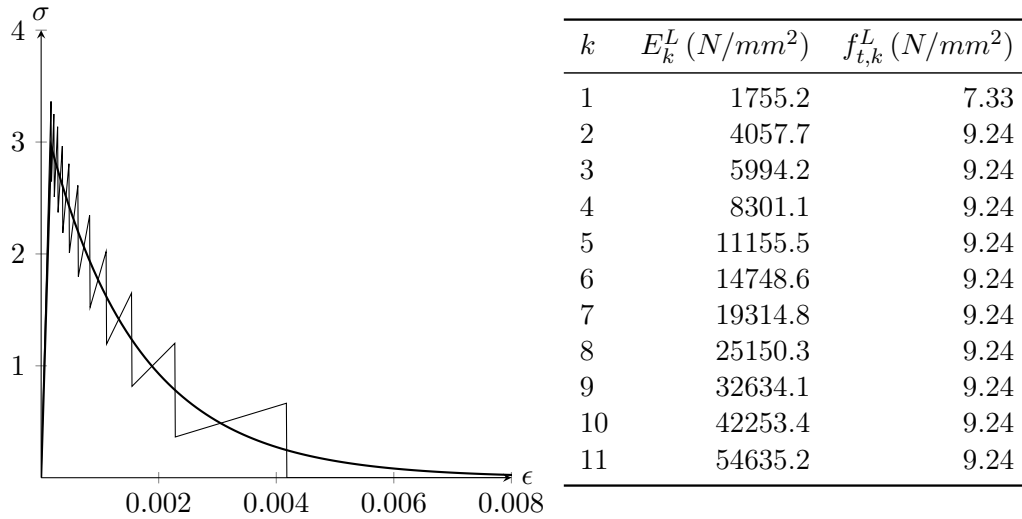| k	E_k^L (N/mm^2)	$f_{t,k}^L$ (N/mm^2)
1	1755.2	7.33
2	4057.7	9.24
3	5994.2	9.24
4	8301.1	9.24
5	11155.5	9.24
6	14748.6	9.24
7	19314.8	9.24
8	25150.3	9.24
9	32634.1	9.24
10	42253.4	9.24
11	54635.2	9.24

FIGURE 5.5: Example exponential tension softening with the corresponding sublayer properties

5.4 Examples

With the aid of Equations 5.10 and 5.11, all properties of a sublayer k can be determined, assuming all sublayers have the same thickness Δt_k^L. To exemplify the application and correctness of these equations, this section considers three example cases: 1) exponential tension softening, 2) Thorenfeldt compressive crushing and 3) linear tension softening. The latter is compared with the continuous formulation as has been derived in Section 4.4.

5.4.1 Exponential tension softening

The first example considers exponential tension softening. The smeared cracking continuum law for this case is given by Equation 2.11. Table 5.1 entails the applied (material) properties. A ripple band parameter $p = 0.14$ is used for the transition from the continuum law to a saw-tooth curve (step (1) of the general transition), resulting in $N = 11$ saw-teeth, which are plotted by Figure 5.5. If needed, the last saw-tooth should be limited to the strain where 98% of the fracture energy is released in order to prevent non-proportionally large cracking strains. However, for this case, this limitation is not needed since the last saw-tooth does not reach the strain corresponding to 98% energy dissipation. The strains $\epsilon_{t,i}$ and stiffnesses E_i are extracted from the saw-tooth curve in step (2) and translated to sublayer properties E_k^L and $f_{t,k}^L$ in step (3), assuming all sublayers having the same thickness t/N. The resulting material properties are listed by Figure 5.5. For increasing k (and hence

Quantity		Value	Unit
Compressive strength	f_c	-35	N/mm^2
Initial strain	ϵ_0	-0.002	-
Initial stiffness	E_0	26914.6	N/mm^2
Fracture energy	G_c^I	6.91	N/mm
Crack bandwidth	h	50	mm
Ripple band parameter	p	0.10	-

TABLE 5.2: Properties example Thorenfeldt compressive crushing

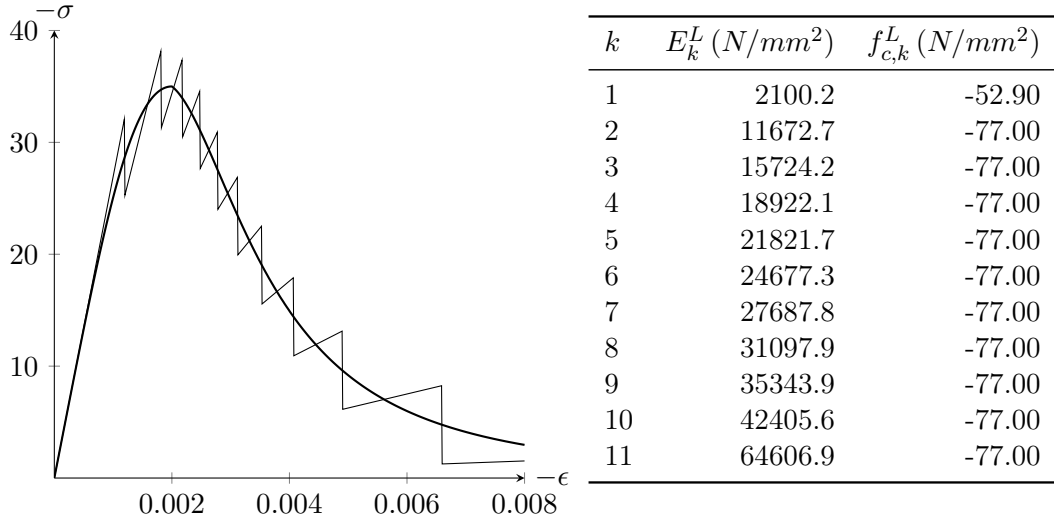| k	$E_k^L\ (N/mm^2)$	$f_{c,k}^L\ (N/mm^2)$
1	2100.2	-52.90
2	11672.7	-77.00
3	15724.2	-77.00
4	18922.1	-77.00
5	21821.7	-77.00
6	24677.3	-77.00
7	27687.8	-77.00
8	31097.9	-77.00
9	35343.9	-77.00
10	42405.6	-77.00
11	64606.9	-77.00

FIGURE 5.6: Example Thorenfeldt compressive crushing with the corresponding sublayer properties

decreasing $\epsilon_{t,k}$), increasing stiffnesses E_k^L are found, following the secant stiffness of the continuum law. As a direct result of the ripple band approach, all stress drops except the last one are the same and therefore, all sublayers except sublayer $k = 1$ have the same strength $f_{t,k}^L = 9.24\,N/mm^2$. The strength directly follows from the magnitude of the ripple band multiplied by the number of sublayers to correct for the influence of a single sublayer on the total element:

$$f_{t,k}^L = 2p\,f_t\,N = 2 \cdot 0.14 \cdot 3.0 \cdot 11 = 9.24N/mm^2 \tag{5.13}$$

Furthermore, sublayer $k = 1$ has a different strength, since the last stress drop in the saw-tooth curve is smaller than $2pf_t$. In the uncracked stage, all sublayers contribute to the total stiffness, which should be equal to the stiffness of the continuum material. Summation of the stiffness contribution E_k^L/N over all sublayers $k = 1..N$ indeed leads to an uncracked stiffness of $E_0 = 20000N/mm^2$ and hence, the correctness of the general transition is shown.

5.4.2 Thorenfeldt compressive crushing

The next example considers Thorenfeldt compressive crushing, which is described by Equations 2.22 and 2.23. The influence of lateral tensile cracks according to Vecchio and Collins [77] is neglected for this example, so $\alpha = \epsilon$. The Thorenfeldt formulation makes use of an initial strain $\epsilon_0 = -0.002$. The initial stiffness E_0 is derived

Quantity		Value	Unit
Tensile strength	f_t	5.0	N/mm^2
Initial stiffness	E_0	26914.6	N/mm^2
Fracture energy	G_f^I	0.15	N/mm
Crack bandwidth	h	50	mm
Ripple band parameter	p	0.11	-

TABLE 5.3: Properties example linear tension softening

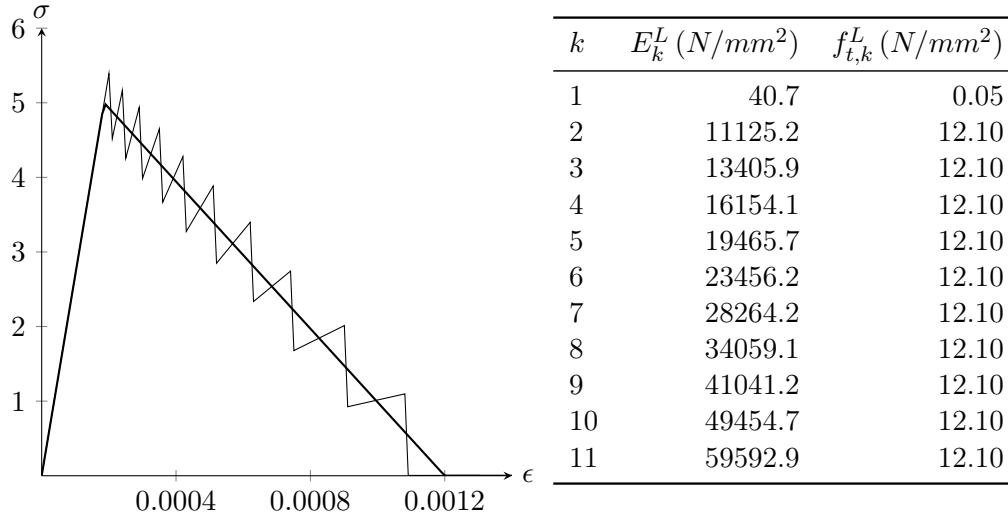| k	$E_k^L\ (N/mm^2)$	$f_{t,k}^L\ (N/mm^2)$
1	40.7	0.05
2	11125.2	12.10
3	13405.9	12.10
4	16154.1	12.10
5	19465.7	12.10
6	23456.2	12.10
7	28264.2	12.10
8	34059.1	12.10
9	41041.2	12.10
10	49454.7	12.10
11	59592.9	12.10

FIGURE 5.7: Example linear tension softening with the corresponding sublayer properties

by taking the derivative of Equation 2.22 at $\epsilon = 0$, leading to

$$E_0 = \left.\frac{d\sigma}{d\epsilon}\right|_{\epsilon=0} = \frac{f_c}{\epsilon_0}\frac{n}{n-1} \tag{5.14}$$

Using the material properties as listed in Table 5.2, initial stiffness $E_0 = 26914.6$ N/mm^2. The fracture energy G_c^I is found by integration over the compressive domain. Invoking a ripple band parameter $p = 0.10$, $N = 11$ saw-teeth and sublayers are obtained, as shown by Figure 5.6. The material properties of sublayers $k = 1..N$ are found in the same figure, which are determined following the same procedure as the first example. Again, the strength $f_{c,k}^L$ directly follows from

$$f_{c,k}^L = 2p\,f_c\,N = 2 \cdot 0.10 \cdot (-35) \cdot 11 = -77.0\,N/mm^2 \tag{5.15}$$

Again, sublayer $k = 1$ deviates from the other sublayers for the aforementioned reasons. Since the Thorenfeldt formulation reveals asymptotic behaviour, the saw-tooth formulation uses a cut-off for 98% fracture energy dissipation.

5.4.3 Linear tension softening: discrete versus continuous

The third and last example considers the case of linear tension softening and compares the discrete formulation of Chapter 5 with the continuous formulation of Chapter 4. Table 5.3 lists the applied (material) properties. The same stiffness E_0 as the Thorenfeldt-example is used. Figure 5.7 entails the obtained saw-tooth curve and
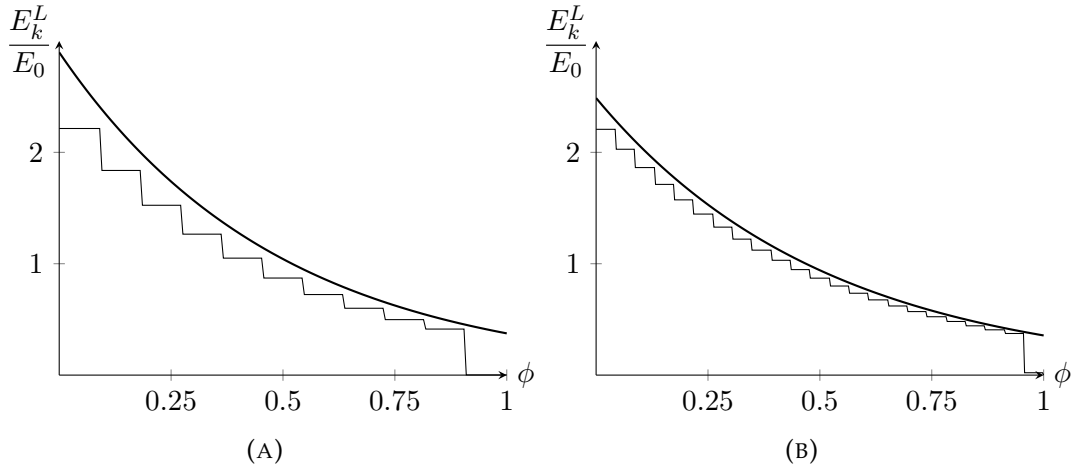
FIGURE 5.8: Comparison continuous and discrete formulations for a
linear tension softening law with (A) $p = 0.11$ and (B) $p = 0.05$

the sublayer properties derived using the proposed general transition for a ripple band parameter $p = 0.11$. In Section 4.4, expressions are derived to describe the strength and stiffness for the limit case of an infinite number of sublayers:

$$
\begin{aligned}
a &= (c - b) \, \exp{(b)} \\
b &= c \left(1 - \frac{\epsilon_t}{\epsilon_u} \right) \\
E^L(\phi) &= a \, \exp{(-b\phi)} \\
f_t^L(\phi) &= c \, f_t
\end{aligned}
\tag{5.16}
$$

in which ϕ is related to sublayer index k via

$$
\phi = \frac{N - k}{N}
\tag{5.17}
$$

All sublayers have strength $f_{t,k}^L = 12.10 N / mm^2$ and hence

$$
c = \frac{f_{t,k}^L}{f_t} = \frac{12.10}{5} = 2.420
\tag{5.18}
$$

Furthermore, the elastic strain $\epsilon_t = 1.858 \cdot 10^{-4}$ and the ultimate strain $\epsilon_u = 12 \cdot 10^{-4}$, from which $b = 2.045$ and $a = 2.899$ are found according to Equations 5.16. Figure 5.8a compares the discrete formulation for $N = 11$ sublayers with the continuous formulation. The discrete and continuous curves do not exactly match, although both curves seem to follow the same trend. Especially for $\phi < 0.5$, significant differences are found. However, differences between the discrete and continuous formulations can be understood when realizing the following: a discretization of the continuous formulation for sublayer stiffnesses does not by definition result in a saw-tooth curve according to the ripple band concept, since the continuous formulation is by definition completely decoupled from the ripple band concept (for the limit case of a continuum, the ripple band is in fact not required as $p = 0$). Conversely, the generated stiffnesses using the ripple band saw-tooth law do not by definition follow the continuous formulation for the sublayer stiffnesses and therefore, differences are obtained. However, for very small p, the ripple band saw-tooth curve approximates the continuum formulation and therefore, smaller differences are found for smaller

p. This statement is supported by Figure 5.8b, which is based on a ripple band parameter $p = 0.05$, generating 23 sublayers. For this case, $f_{t,k} = 11.50 N/mm^2$ and therefore $c = 2.300$, $b = 1.944$ and $a = 2.488$. Compared to Figure 5.8a, differences between the discrete and continuous curves significantly decreased. For the limit case of an infinitesimal *p*, the theoretical continuous formulation is obtained. With this example, the similarity between the continuous and discrete formulations is shown.

5.5 Transition for tension and compression

Until now, only cases considering either tensile or compressive constitutive laws are elaborated. In these cases, a saw-tooth law is set up with the aid of a specific concept (e.g. the ripple band concept) and translated to sublayer material properties using the general transition Equations 5.10 and 5.11. When both tensile and compressive constitutive laws are required, some trouble is encountered for the sublayer model. In regular SLA, the saw-tooth curves in tension and compression are uncoupled regarding the strength and stiffness reductions (they are coupled in the sense that a stiffness reduction in tension will reduce the stiffness in compression after stress reversel, this case is however not considered in this section). For example, it is possible in regular SLA to have 15 saw-teeth in tension and 30 in compression. Furthermore, during the determination process of the saw-tooth curve (step (1) in the flowchart of Figure 5.1), the damaged stiffnesses and strengths in tension and compression do not depend on each other.

When making use of the sublayer model, stiffness and strengths in tension and compression do depend on each other, marking a clear difference between regular SLA and the sublayer model. The nature of the sublayer model requires a different approach, as the stiffness E_k^L of a certain sublayer *k* in tension and compression is by definition the same, where in SLA different reduced stiffnesses in tension and compression are found for a certain saw-tooth *i*. As the sublayer stiffness in both tension and compression is the same, the sublayer strengths $f_{t,k}^L$ and $f_{c,k}^L$ in tension and compression respectively are depending on each other. Only one stiffness can be allocated to a specific sublayer, where performing the general transition process as described in Section 5.2 for both tension and compression separately would lead to two different stiffness values for one specific sublayer *k*, which is not possible. Each sublayer behaves according to Figure 4.5, showing the same stiffness in tension and compression.

For the purpose of this thesis, it is decided to determine the sublayer stiffness E_k^L based on the saw-tooth law in tension, as for concrete and the considered test cases in this thesis, failure in tension is most often governing. However, one could also turn the process around and take the saw-tooth curve in compression to determine the sublayer stiffness. First, the tensile branch of the constitutive law is transferred to sublayer properties according to Section 5.2, resulting in a set of sublayer properties E_k^L and $f_{t,k}^L$. Next, assuming that a ripple type of saw-tooth generation is applied, the crossing point between the secant curve $E_k^L \epsilon$ and the upper compressive ripple band is searched for to determine the compressive strength $f_{c,k}^L$. Contrary to the sublayer properties in tension, all compressive strengths can be different, as the stiffnesses E_k^L are not determined based on the ripple band concept for compression, but for tension instead. To clearify the described process, an example is elaborated. In this example, the constitutive laws of the examples on linear tension softening and
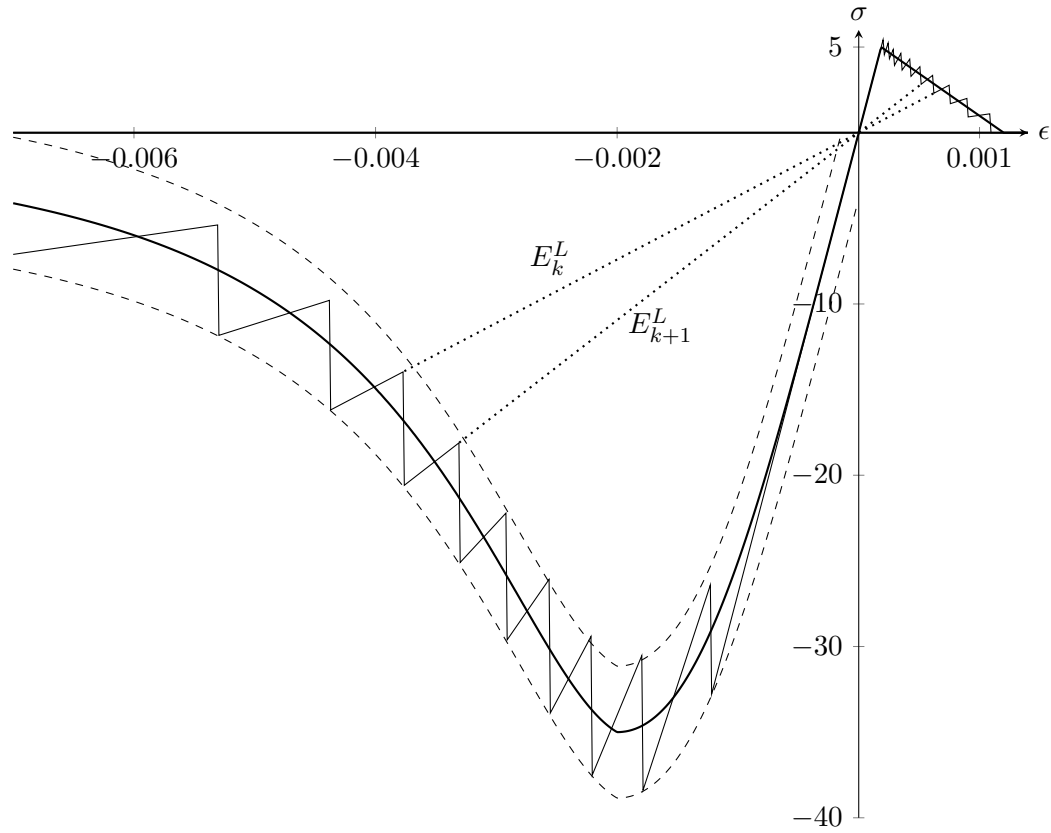
FIGURE 5.9: Example combined linear tension softening and Thoren-
feldt compressive crushing based on tension softening ripple band

k	$E_k^L \, (N/mm^2)$	$f_{t,k}^L \, (N/mm^2)$	$f_{c,k}^L \, (N/mm^2)$	$\Delta 2 p_c \, (\%)$
1	40.7	0.05	-42.35	-19.9
2	11125.2	12.10	-81.97	-3.2
3	13405.9	12.10	-71.14	-16.0
4	16154.1	12.10	-70.71	-16.5
5	19465.7	12.10	-73.41	-13.3
6	23456.2	12.10	-77.61	-8.4
7	28264.2	12.10	-82.47	-2.6
8	34059.1	12.10	-87.22	+3.0
9	41041.2	12.10	-90.66	+7.0
10	49454.7	12.10	-88.48	+4.5
11	59592.9	12.10	-72.96	-13.9

TABLE 5.4: Properties example combined linear tension softening
and compressive Thorenfeldt crushing

Thorenfeldt compressive crushing from Section 5.4 are combined. Material properties as given in Tables 5.2 and 5.3 are applied, where the ripple band parameter $p = 0.11$ is taken from the tensile branch. First, the general transition is performed for the linear tension softening branch (Figure 5.7). Next, the compressive branch is considered and the stiffness E_k^L is used to find the crossing point with the upper ripple band, where $p = 0.11$ is used according to the tension softening law. In this way, for each sublayer the stiffness and strengths in tension and compression are determined. Figure 5.9 depicts the described process for this example. The tensile part is exactly equal to Figure 5.7. The compressive part however differs from Figure 5.6, as the used sublayer stiffnesses are derived from the tensile branch instead of the compressive branch. It can be seen from Figure 5.9 that the ripple band in compression is quite well approximated, even when using different sublayer stiffnesses. Table 5.4 lists the obtained material properties. Constant tensile strength $f_{t,k}^L$ are found, according to

$$f_{t,k}^L = 2p\,f_t\,N = 2 \cdot 0.11 \cdot 5.0 \cdot 11 = 12.10\,N/mm^2 \qquad (5.19)$$

Furthermore, the constant compressive strength $f_{c,k}^L$ following from the ripple band saw-tooth law should be

$$f_{c,k}^L = 2p\,f_c\,N = 2 \cdot 0.11 \cdot (-35.0) \cdot 11 = -84.70\,N/mm^2 \qquad (5.20)$$

However, the sublayer compressive strengths $f_{c,k}^L$ differ from this value due to the stiffness being determined based on the tensile branch. These differences also follow from Figure 5.9, where the ripple band compressive stress drops are found to be unequal to $2pf_c$. The last column of Table 5.4 lists the deviation of the obtained ripple band for the case of combined tension and compression compared to the theoretical ripple band of $2pf_c$ via

$$\Delta 2p_{c,k} = \left.\frac{2pf_{c,+/-}^L - 2pf_{c,-}^L}{2pf_{c,-}^L}\right|_k = \left.\frac{f_{c,+/-}^L - f_{c,-}^L}{f_{c,-}^L}\right|_k \qquad (5.21)$$

Although the sublayer model for combined tensile and compressive constitutive formulations is not able to exactly reproduce the formulations of regular SLA, the method as described in this section results in a reasonable approximation, as has been exemplified for an example with combined linear tension softening and compressive Thorenfeldt crushing.

5.6 Discussion

In this chapter, the general transition from regular sequentially linear analysis to the sublayer model has been made. A continuum law is transferred to a saw-tooth law, which is subsequently translated to sublayer material properties, assuming all sublayers having the same thickness. This general transition can be applied to continuum laws describing merely the tensile or compressive branch, as well as to continuum laws describing both of the branches, as has been discussed in Section 5.5. Furthermore, the case of constitutive snap-back can be considered by implementing a sequence of failure within the general transition formulation.

The proposed general transition bridges the gap between regular SLA and the sublayer model. Within the framework of SLA, the contribution of this chapter can be seen as *pre-processing*, which takes place prior to the cycle of performing linear

analyses and applying damage increments (conform the flowchart of Figure 4.6). In the next phase of the thesis, the general transition formulation will be applied to generate sublayer material properties for single element cases, fundamental cases and full-scale experimental cases.

It is noted that the general transition is a procedure on element level. When all elements of a finite element model are equal (same size and material properties), the general transition can be performed on structural level. However, when different element sizes, causing different crack bands h, or different material properties are used, the constitutive law for a smeared crack formulation differs per element. Hence, this case requires the transition from continuum law to sublayer properties to be performed on element level. The same holds for regular SLA.

Lastly, the number of sublayers for a certain element depends on the ripple band parameter p. As the sublayer model requires the generation of N sublayers, the number of integration point increases by a factor N and hence, the computational efforts compared to regular SLA significantly increase. One could reduce these efforts by increasing p. Furthermore, an optimization can be performed that allocates different ripple band parameters for different elements to reduce the computation time, while maintaining a high level of detail in zones where rotational cracking is expected to occur.

Chapter 6

Verification and understanding on element level

This chapter entails the verification of the proposed sublayer model on element level and focuses on physically understanding the behaviour, such that later on, the extension to structural behaviour can be made. First, Section 6.1 gives an overview of the considered cases and their learning goals. Next, 5 cases are further elaborated: uniaxial loading (Section 6.2), biaxial loading (Section 6.3), shear with non-proportional loading (Section 6.4), tension shear loading (Section 6.5) and shear with non-proportional loading reconsidered (Section 6.7). Lastly, the conclusions of this chapter and an outlook to structural tests are discussed in Section 6.8.

6.1 Introduction

The goal of this chapter is twofold: 1) verification of the sublayer model for some single element cases by comparison with regular SLA and NLFEA and 2) thorough understanding of the behaviour, which can best be captured with basic single element tests. The testing cases are chosen such that each of the cases contributes to the physical understanding of the sublayer model on a specific subject, making sure that at the end of this chapter, the fundamentals of the sublayer model are completely understood. Table 6.1 gives an overview of the considered cases and the corresponding learning goals. The cases in this chapter are academic and therefore not practical. However, the obtained knowledge from these simple tests is required to correctly apply the sublayer model to realistic structural cases.

Appendix B describes how the algorithm of the sublayer model is practically implemented in the available software. First, the saw-tooth initiation and general transition are performed in Maple. Then, a Matlab-script automatically generates an input file for DIANA Finite Element Analysis, in which sublayer properties are allocated to specific overlay elements. All finite element analyses are performed with the software DIANA.

Case	Loading	Used to understand
1	uniaxial loading	Poisson effects
2	biaxial loading	higher order element effects
3	shear and non-proportional loading (a)	cracking angle
4	tension-shear loading (Willam)	shear retention factor
5	shear and non-propertional loading (b)	deviations compared to NLFEA

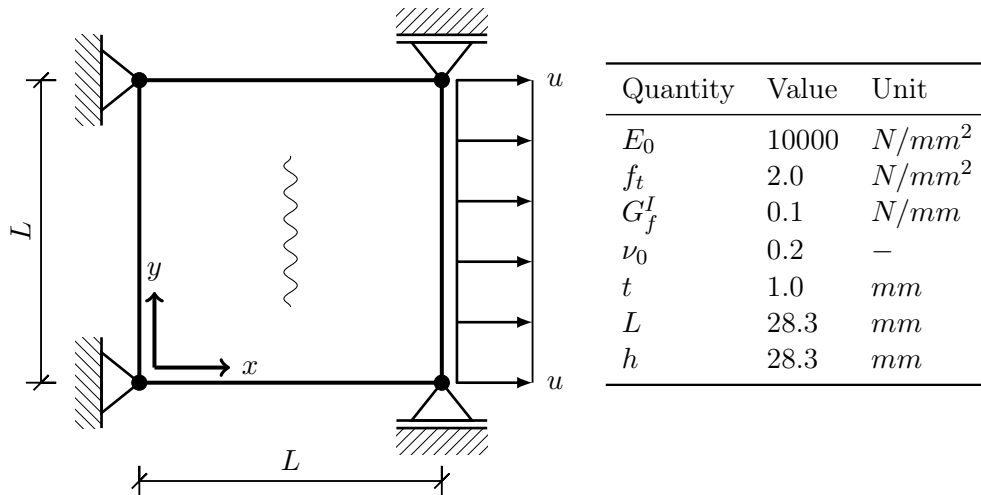TABLE 6.1: Overview of considered cases and the learning goals

FIGURE 6.1: Geometry, crack direction and properties of case 1: single
element in uniaxial tension

6.2   Case 1: uniaxial loading

The first case considers uniaxial tensile displacement controlled loading on the single square element that is shown by Figure 6.1. The applied properties are listed in the same figure. Since the complete element is subjected to a homogeneous stress and strain state, a Gaussian reduced integration scheme with only 1 integration point is applied. The element is uniaxially loaded and therefore, a tensile crack perpendicular to the loading is expected. Vertical deformations are restrained by vertical supports. In this section, two cases are distinguished: uniaxial loading with and without Poisson effects.

No Poisson effect: $\nu_0 = 0$
When setting the Poisson's ratio $\nu_0 = 0$, coupling between the directions vanishes. Therefore, the response in the load-direction is expected to follow the applied continuum tension softening law. The element is modelled with a linear Q8MEM-element and loaded along mesh lines and hence, a cracking band $h = L = 28.3\,mm$ is assumed. Two types of softening laws are considered: linear tension softening with $p = 0.10$ ($N = 16$) and exponential tension softening with $p = 0.05$ ($N = 30$). A smaller ripple band parameter is applied for the latter one to make sure that the asymptotic last part of the exponential continuum curve is captured properly. The ripple band approach by Rots, Belletti and Invernizzi [64] is used to generate the saw-tooth curve and the general transition as described in Chapter 5 is applied to obtain sublayer properties. Figure 6.2 captures the stress-strain output for the x-direction (direction of loading) for both linear and exponential tension softening, together with the corresponding continuum laws. The found stresses are slightly larger than the constitutive stresses as a result of the ripple band concept; this concept overshoots the stress by pf_t. Each dot in the graph represents a brittle damage increment of a critical sublayer. Since the element is uniaxially loaded and $\nu_0 = 0$, no vertical stresses σ_{yy} are found.

Included Poisson effect: $\nu_0 = 0.2$
A sequentially linear analysis is also performed for the case with linear tension softening, $p = 0.10$ and $\nu_0 = 0.2$. Since the Poisson ratio is non-zero, a so-called *Poisson's*
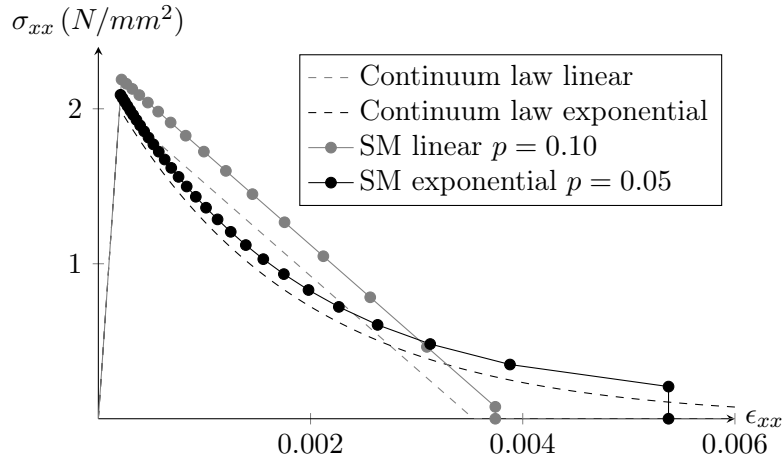
FIGURE 6.2: Stress-strain diagram in load-direction x continuum laws and output sublayer model (SM) analysis for $\nu_0 = 0$
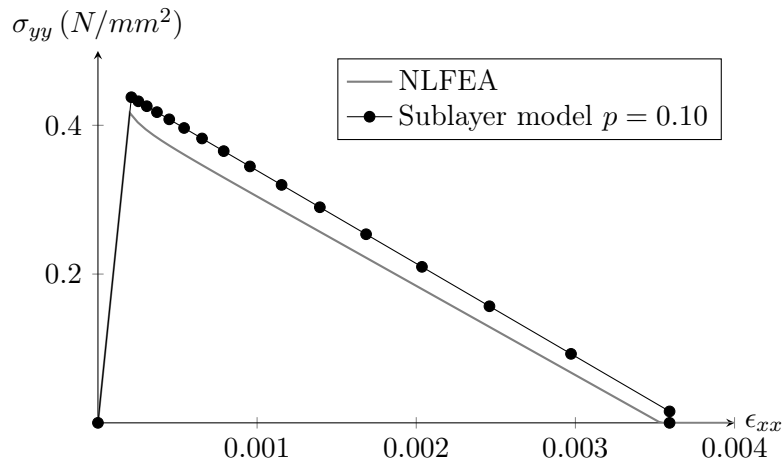

FIGURE 6.3: Vertical stress σ_{yy} versus strain ϵ_{xx} for NLFEA and the sublayer model due to Poisson's effect

effect is encountered, meaning that the element wants to deform in the y-direction due to the applied displacements in x-direction. Deformations in the y-direction are restrained, generating tensile stresses in the y-direction. These vertical tensile stresses are plotted in Figure 6.3 as a function of the strain ϵ_{xx} ($\epsilon_{yy} = 0$) for both the sublayer model and NLFEA. For NLFEA, damage based reduction of Poisson's ratio is used and the displacement is applied incrementally. The maximum vertical stress is found by $f_t \cdot \nu_0$ and reduces gradually to 0 for the completely cracked state. The results of NLFEA and the sublayer model are similar. Larger vertical stresses are found for the sublayer model due to the applied ripple band concept. Furthermore, the Poisson's effect does not influence the behaviour in x-direction, as vertical deformations are restrained.

After initiation of the first crack, a reduced Poisson's ratio ν_{yx} should be obtained according to Equations 2.9, as a result of increasing damage. The reduced ν_{xy} can be calculated based on Equation 2.8, as the following orthotropic formulation holds after cracking:

$$\sigma_{yy} = \frac{1}{1 - \nu_{xy}\nu_{yx}}(\nu_{yx}E_y\,\epsilon_{xx} + E_y\,\epsilon_{yy}) \tag{6.1}$$
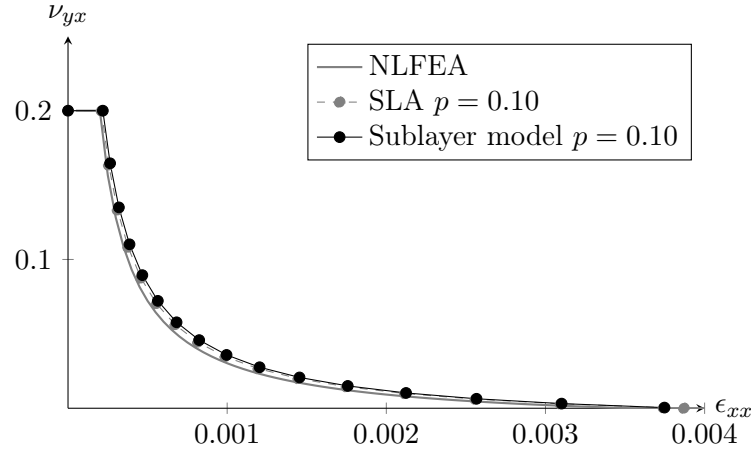
FIGURE 6.4: Reduction of Poisson's ratio ν_{yx} against strain ϵ_{xx} for NLFEA, regular SLA and the sublayer model

from which ν_{yx} is solved, leading to

$$\nu_{yx} = \frac{\sigma_{yy} - E_y\,\epsilon_{yy}}{E_y\,\epsilon_{xx} + \sigma_{yy}\nu_{xy}} \tag{6.2}$$

Furthermore, the vertical strain $\epsilon_{yy} = 0$, the Poisson's ratio $\nu_{xy} = \nu_0$ and $E_y = E_0$, as the element is not damaged in the y-direction. Therefore, Equation 6.2 reduces to

$$\nu_{yx} = \frac{\sigma_{yy}}{E_0\,\epsilon_{xx} + \sigma_{yy}\nu_0} \tag{6.3}$$

With the aid of Equation 6.3 and the results of Figure 6.3, the reduced Poisson's ratio ν_{yx} of the element can be calculated. This analysis is performed for NLFEA, regular SLA and the sublayer model and the results are shown by Figure 6.4. For increasing load, damage increases and ν_{yx} decreases gradually to 0 for a completely developed crack, following Equations 2.9. Insignificant differences between the methods are found. This is an important observation, as the sublayer model is now proved to be able to mimick damage based reduction of the Poisson's ratio on element level by brittle damage increments of $\nu_{yx,k}^L$ on sublayer level. Once a sublayer k cracks, its Poisson's ratio changes from ν_0 to $\nu_{yx,k}^L = 0$. The superposition of sublayers is able to represent the element behaviour correctly and therefore, it can be concluded that the sublayer model is able to accurately represent damaged based reduction of Poisson's ratio.

6.3   Case 2: biaxial loading

The second case considers biaxial tensile displacement controlled loading on an eight-noded quadratic CQ16M element, which is shown by Figure 6.5. The vertical tensile loading is proportional to the horizontal tensile load by a factor B. As the element is quadratic, a crack band $h = \sqrt{L \cdot L} = 20.0\,mm$ is assumed. The different h results in a different saw-tooth curve: $p = 0.10$ gives $N = 17$ sublayers. The quadratic element uses a 2x2 Gaussian integration scheme. In each of the integration points two perpendicular tensile cracks are formed as a result of the biaxial tensile loading. For scaling factor $B < 1$, the first damage increments are performed for the stiffness in x-direction and later on, damage increments are performed in both x-
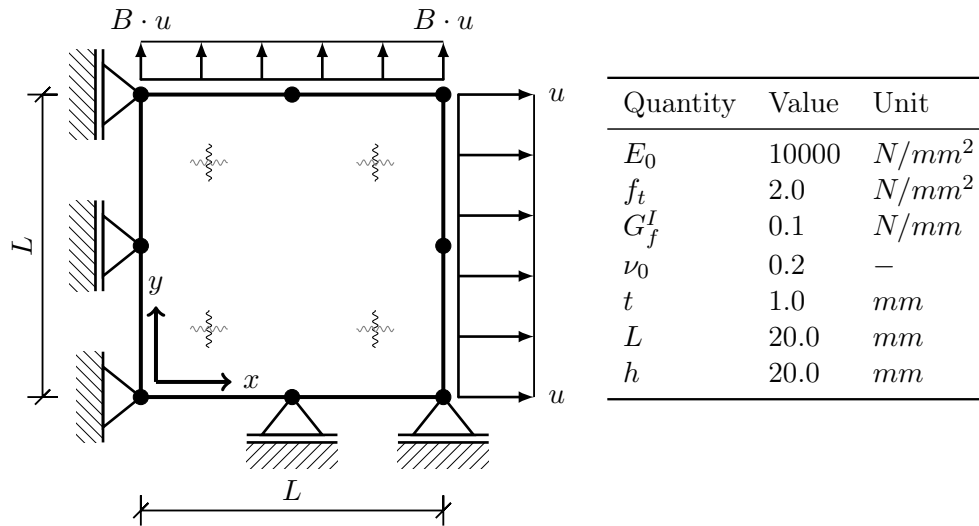
FIGURE 6.5: Geometry, crack direction and properties of case 2: single element in biaxial tension

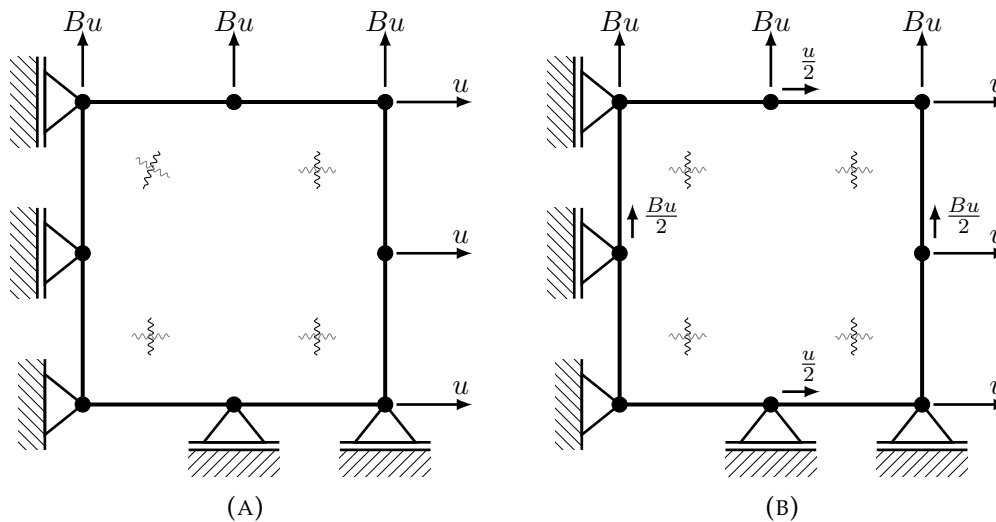| Quantity	Value	Unit
E_0	10000	N/mm^2
f_t	2.0	N/mm^2
G_f^I	0.1	N/mm
ν_0	0.2	–
t	1.0	mm
L	20.0	mm
h	20.0	mm

FIGURE 6.6: Comparison of (A) incorrect and (B) correct load application for higher order elements

and y-directions alternately. This case focuses on the effects of applying higher order elements. These effects are demonstrated by using two different load applications (A) and (B), as defined by Figure 6.6.

For load application (B), the displacements of all nodes are prescribed and a constant strain field over the element is obtained. The constant strain field ensures that a damage increment is performed for all 4 integration points of the critical sublayer consecutively. After any 4 damage increments, a uniform damaged state is obtained and therefore, correct results are found. The analysis stops after 136 load steps, meaning that all integration points are completely damaged in both directions ($4 \cdot 2 \cdot 17 = 136$). The contrary holds for load application (A). The load is now only put on the outer nodes and displacements of mid-side nodes are not prescribed. At the moment of the first damage increment, stiffness reduction of the critical integration point results in an asymmetric stiffness matrix. For load application (B) this is not a problem, since all deformations are prescribed. For (A), this is a problem: the

asymmetric stiffness matrix and the non-prescribed nodes allow for a non-uniform strain field. Ultimately, localization in the right half of the element is observed and, after the damage in this part is fully developed, unrealistic crack directions are found due to the asymmetry of the strain field. When considering single higher order element cases, one must be aware of this phenomena.

Problems of incorrect load application on single higher order elements are inherently found for SLA-type of procedures: in each load step, only 1 single damage increment is performed, allowing for asymmetric strain fields (if restraints are not properly prescribed). These problems are not found for incremental iterative approaches. In NLFEA, all integration points are updated at the same time and therefore, no asymmetric strain fields are generated. For multi-element structural cases, the aforementioned problems are not found for SLA and the sublayer model, since adjacent elements restrain the deformations of mid-side nodes and thereby indirectly 'prescribe' deformations.

6.4   Case 3: shear loading with non-proportional loading

Case 3 considers a single linear element under displacement controlled shear loading u combined with vertical tensile non-proportional loading $u_{nonprop}$, as shown by Figure 6.7. The same saw-tooth law as for case 1 is obtained ($p = 0.10$ and $N = 16$) since the same crack band $h = \sqrt{2 \cdot L^2} = 28.3\,mm$ is found for $L = 20\,mm$. The lateral shear loading results in a tensile tie and compressive strut perpendicular to each other under $45°$. In this case, only tensile damage is accounted for and compressive damage propagation is not considered. The non-proportional loading requires the algorithm as has been discussed in Section 3.5, in which the loading is subdivided in a proportional and non-proportional part. The non-proportional displacement controlled loading induces rotating principal strain directions and consequently, differences between regular SLA and the sublayer model are expected.

First, the case without non-proportional loading is analyzed and the $\sigma_{xy} - \gamma_{xy}$ results for both SLA and the sublayer model are plotted in Figure 6.8a, invoking $p = 0.10$. For SLA, variable shear retention according to Equation 2.13 is applied. As the loading on the single element is proportional, no crack rotations are obtained

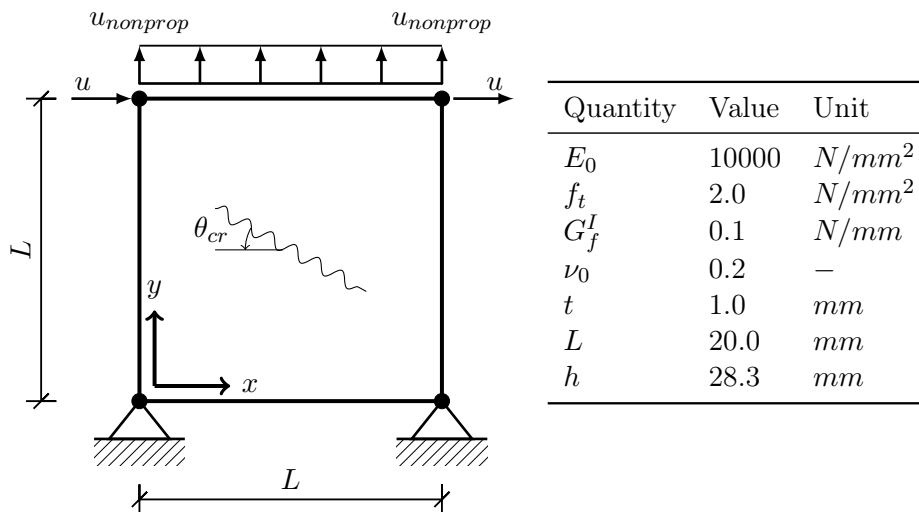| Quantity	Value	Unit
E_0	10000	N/mm^2
f_t	2.0	N/mm^2
G_f^I	0.1	N/mm
ν_0	0.2	$-$
t	1.0	mm
L	20.0	mm
h	28.3	mm

FIGURE 6.7: Geometry, crack direction, definition θ_{cr} and properties of case 3: shear with non-proportional loading
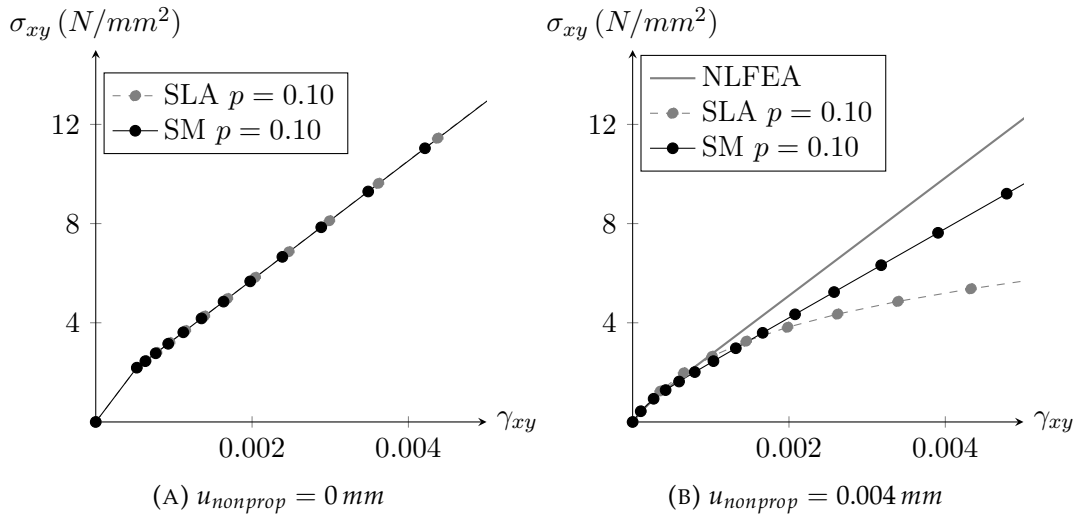
FIGURE 6.8: Shear stress σ_{xy} versus shear strain γ_{xy} for cases with and without non-proportional loading for NLFEA, regular SLA and the sublayer model

and all sublayers crack for an angle $\theta_{cr} = 45°$. Both SLA and the sublayer model give the same results, because the fixed crack formulation of regular SLA suffices for this case (the crack does not rotate).

Next, the case with non-proportional loading is considered. A vertical constant tensile load of $u_{nonprop} = 0.004\,mm$ is applied on top of the element. In the first load step, the constant load is put on the element, not causing any damage. In the next load steps, the proportional shear load is applied to the element, while maintaining the constant vertical loading. Due to this non-proportional loading, the stress-strain path significantly changes, as can be seen in the $\sigma_{xy} - \gamma_{xy}$ plot in Figure 6.8b. For both SLA and the sublayer model, the first damage increment takes place for $u = 2.07 \cdot 10^{-3}\,mm$. At this specific moment, the principal stress and strain directions are found by $\theta_{cr} = 13.7°$. For SLA, the crack direction is fixed at the initiation of damage. On the contrary, the sublayer model allows for crack rotation, as only the crack direction of the stiffest layer is fixed upon initiation and other sublayers are free to crack in any direction. Therefore, significant differences are found between both methods for increasing damage, as can be seen in Figure 6.8b. Both methods are compared with a rotating crack NLFEA, in which the crack directions are by definition equal to the principal strain directions, with damage based reduction of the Poisson's ratio. The sublayer model leads to a better approximation of a rotating crack compared to regular SLA, which becomes especially clear for larger shear strains. The superposition of fixed cracking sublayers mimics a rotating crack and therefore, more realistic shear stresses are found.

The last statement is supported by Figure 6.9, which exemplifies the fundamental advantage of the sublayer model over regular SLA. Where regular SLA proceeds with the crack direction of (A) ($\theta_{cr} = 13.7°$), the sublayer model simulates a rotating crack in steps (B)-(E), leading to a typical shear crack of $\theta_{cr} = 45°$. For increasing load, the sublayer model slowly corrects its crack direction by the consecutive cracking of individual sublayers, each having their own $\theta_{cr,k}$. Although a more accurate description is obtained, diffences with NLFEA are noted. In NLFEA, the crack direction for the complete element is updated; in the sublayer model, only the crack direction of the critical sublayer is updated. The previously cracked sublayers have outdated crack directions, while they are still contributing to the element behaviour.

(A) $u = 2.07 \cdot 10^{-3}\, mm$ (B) $u = 1.19 \cdot 10^{-2}\, mm$ (C) $u = 2.64 \cdot 10^{-2}\, mm$

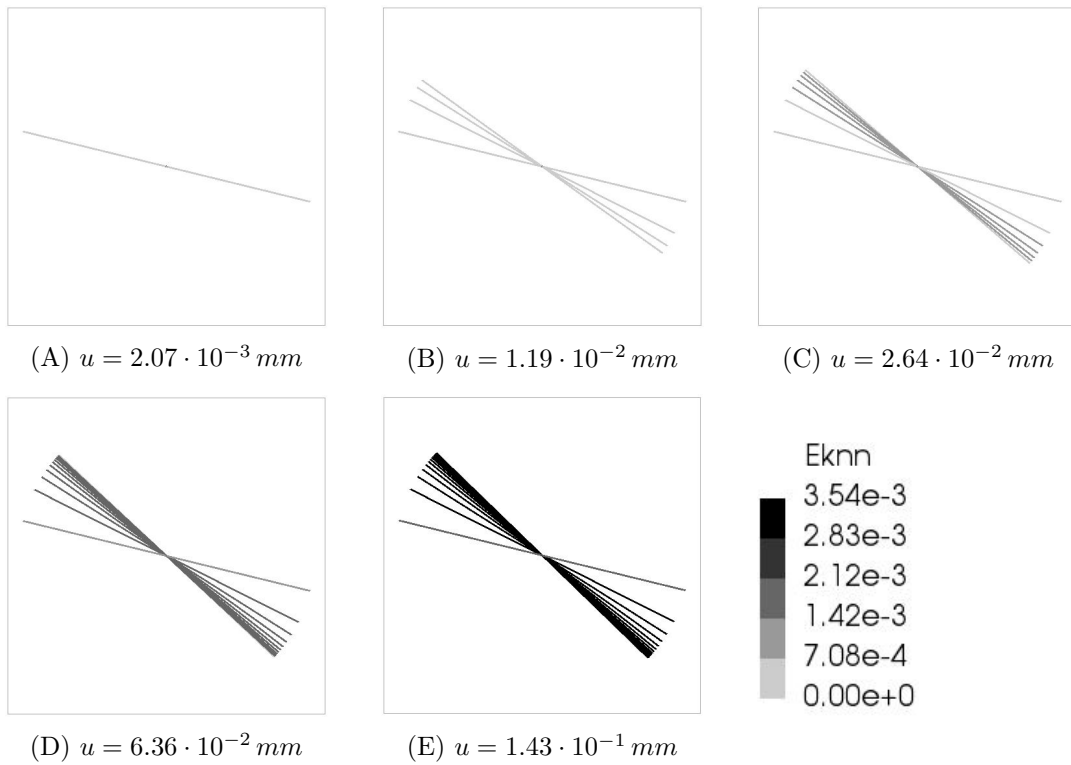(D) $u = 6.36 \cdot 10^{-2}\, mm$ (E) $u = 1.43 \cdot 10^{-1}\, mm$

FIGURE 6.9: Crack development for specific u, mimicking a rotating crack with *Eknn* the normal strain in a crack ($\epsilon_u = 3.54 \cdot 10^{-3}$)
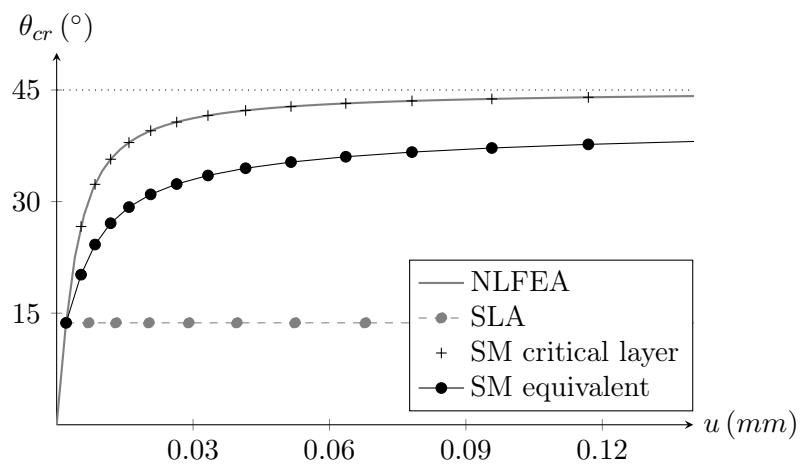

FIGURE 6.10: Crack direction for NLFEA, regular SLA, the last cracked layer of the SM and the averaged crack direction of the SM

For that reason, differences with the rotating crack model are reduced but not completely resolved. Or in other words, for each specific load step, the principal strain direction $\theta_{cr,k}$ of the critical sublayer k corresponds exactly with NLFEA results, but for the consecutive load step with critical sublayer $k - 1$, the fixed crack direction $\theta_{cr,k}$ of the same sublayer k might deviate from the updated principal strain direction $\theta_{cr,k-1}$. Only when for all k holds that $\theta_{cr,k} = \theta_{cr,k-1}$, which is the case for $u_{nonprop} = 0$, the sublayer model is exactly equal to NLFEA.

Since each of the cracked sublayers has its own crack direction, a unique definition of the elements total crack angle is hard to achieve. The total crack angle can be used to compare the sublayer model on element level with NLFEA. For this thesis, the elements total equivalent crack angle is defined as the principal 'cracked element stress' direction. The cracked element stress σ_{cr} is found by superposition of stresses in the cracked sublayers, while not considering the stress contributions of uncracked layers. In this way, a total equivalent crack direction is retrieved from the sublayer model, according to

$$\tan(2\theta_{cr}) = \frac{2\sigma_{xy,cr}}{\sigma_{xx,cr} - \sigma_{yy,cr}} \tag{6.4}$$

from which θ_{cr} is solved. Figure 6.10 compares the equivalent total crack direction of the sublayer model with NLFEA and regular SLA. The following conclusions can be drawn:

1. As mentioned, the crack direction of the critical sublayer is exactly equal to the crack direction of NLFEA (at that specific moment).

2. The crack direction of regular SLA is fixed upon initiation and leads to large differences in crack direction with NLFEA ($45°$ versus $13.7°$), hence explaining the results of Figure 6.8b.

3. The total equivalent crack direction, which is based on all cracked sublayers, approximates NLFEA significantly better than regular SLA ($45°$ versus $35°$), although differences with NLFEA are still found.

6.5 Case 4: tension-shear problem

This section entails the analysis of a tension-shear problem, in literature often referred to as the Willam [83] problem, which is visualized by Figure 6.11. A single element is considered, with stiffness $E_0 = 10000\,N/mm^2$, Poisson's ratio $\nu_0 = 0.2$, tensile strength $f_t = 1.0\,N/mm^2$, mode I fracture energy $G_f^I = 0.15 \cdot 10^{-3}N/mm$ and crack band $h = 1\,mm$. The continuum law is described by a linear tension softening relation with ultimate strain $\epsilon_u = 3.00 \cdot 10^{-4}$. Two loading stages are prescribed:

- Loading stage (A): the element is loaded by tensile straining $\Delta\epsilon_{xx}$ combined with vertical compressive straining $\Delta\epsilon_{yy} = -\nu_0\Delta\epsilon_{xx}$ to simulate Poisson's effects in the y-direction, as shown by Figure 6.11a. A tensile crack perpendicular to the tensile load is formed.

- Loading stage (B): at the onset of cracking, the loading is changed to stage (B). The element is loaded by combined biaxial tension and shear loading according to: $\Delta\epsilon_{xx} : \Delta\epsilon_{yy} : \Delta\gamma_{xy} = 0.5 : 0.75 : 1$, resulting in a rotating crack, as shown by Figure 6.11b. The loading of stage (A) remains on the element during stage (B), hence non-proportional loading is obtained.
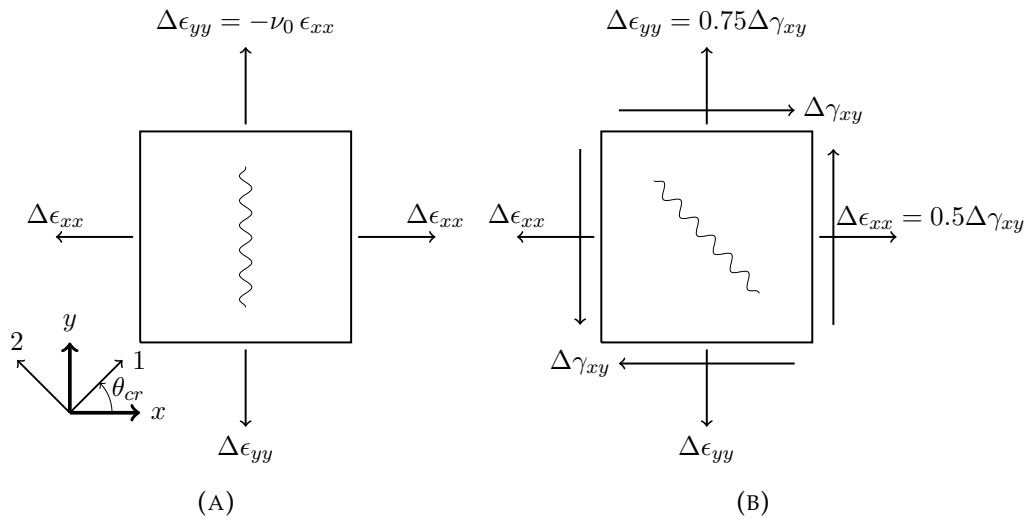
FIGURE 6.11: Loading stages of the tension-shear problem: (A) tensile loading up until first damage and (B) tension-shear loading

(A) $\gamma_{xy} = 0$ (B) $\gamma_{xy} = 3.04 \cdot 10^{-5}$ (C) $\gamma_{xy} = 8.53 \cdot 10^{-5}$

(D) $\gamma_{xy} = 1.12 \cdot 10^{-4}$ (E) $\gamma_{xy} = 2.08 \cdot 10^{-4}$

FIGURE 6.12: Crack development for specific γ_{xy}, mimicking a rotating crack with *Eknn* the normal strain in a crack ($\epsilon_u = 3.00 \cdot 10^{-4}$)

FIGURE 6.13: Shear stress σ_{xy} versus shear strain γ_{xy} per sublayer and for total element, with $p = 0.05$ and $N = 17$

The single element is modelled with the aid of a linear Q8MEM element with unit thickness $t = 1\,mm$ and 1 integration point. The displacement of the bottom left node is fixed to zero and the displacement of the other three nodes are prescribed such that the element follows the applied strain fields for both loading stages. A very small ripple band parameter $p = 0.01$ is applied, leading to $N = 83$ sublayers, in order to ap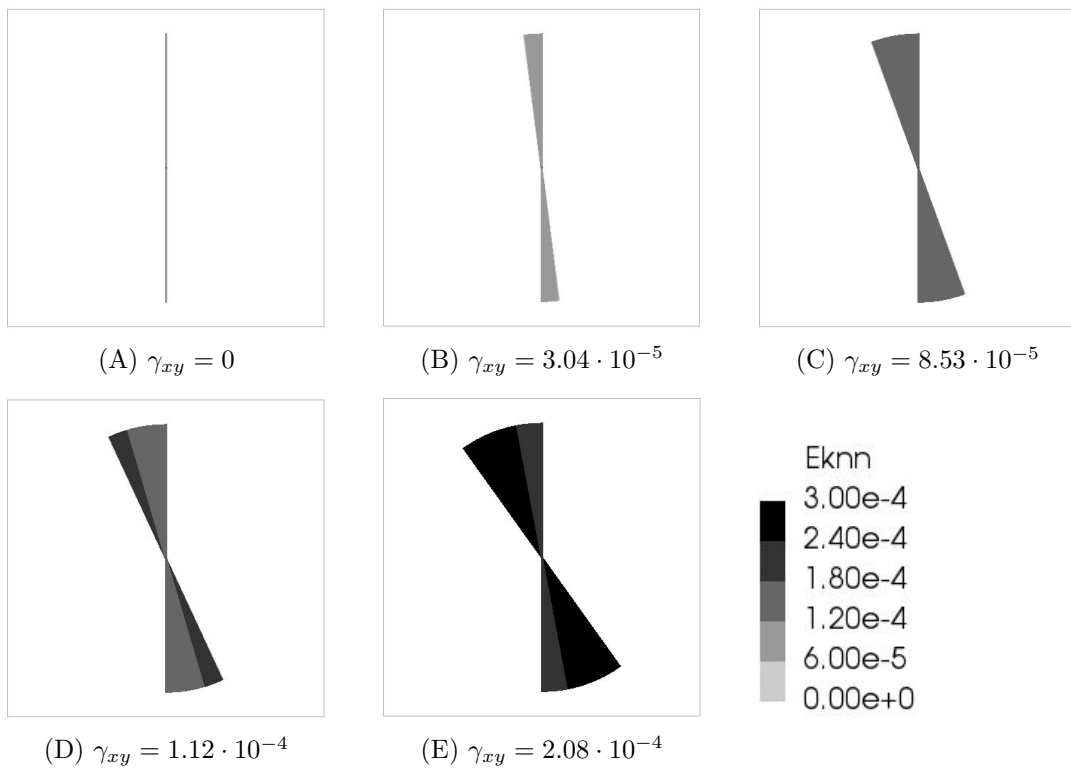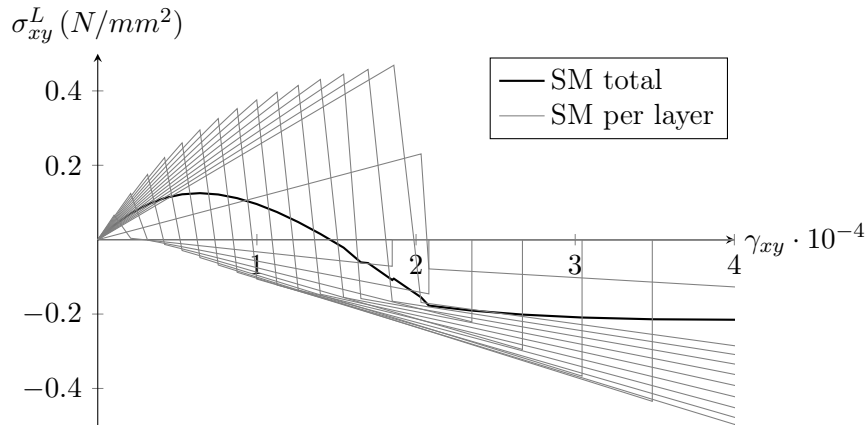proximate a continuous solution that allows for a one-to-one comparison. Figure 6.12 entails a graphical representation of the cracking process. After damage initiation in step (A), the loading is changed to stage (B) and a rotating crack is obtained in steps (B)-(E), following from the non-proportional loading on the element. At step (E), for $\gamma_{xy} = 2.08 \cdot 10^{-4}$, in all sublayers a primary crack is formed and the ultimate strain is reached normal to the crack. From this point on, secondary cracks form as the remaining uncracked part of the element is still capable of carrying some load. At any moment, the primary crack angle of the critical sublayer is equal to the principal strain direction and therefore, this specific sublayer has the same crack angle as a rotating crack NLFEA (as discussed in Section 6.4).

For the case of $p = 0.05$ and $N = 17$, the contributions of all sublayers are plotted in Figure 6.13 (it is interesting to observe the similarities with Figure 4.2). Here, it can also be observed that around $\gamma_{xy} = 2.08 \cdot 10^{-4}$ all primary cracks are formed. Each sublayer shows two brittle stress drops corresponding to primary and secondary cracking respectively. After scaling to thickness and superposition of all sublayer contributions, the total stress on element level is found.

Three types of analyses are performed: 1) NLFEA based on a rotating crack model with damage based reduction of the Poisson's modulus, 2) SLA with variable shear retention according to Equation 2.13 and $p = 0.01$ and 3) the sublayer model with elastic perfectly brittle sublayers and $p = 0.01$. The shear response $\sigma_{xy} - \gamma_{xy}$ of all three analyses is plotted in Figure 6.14. When comparing regular SLA with NLFEA results, clear differences are observed in the shear behaviour as SLA is prone to significant stress locking effects. After damage initiation, the crack angle of SLA is fixed vertically and a rotation of principal stresses is not followed. Stresses are only monitored within the fixed cracking plane, while stresses exceeding the capacity might take place in a different direction and therefore, spurious stresses are obtained. Since these spurious stresses exceed the capacity of the material, they are often referred to as stress locking or stiffening effects. These stiffening effects are clearly observed in the shear stress response of SLA. Oppositely, the sublayer model entails much less pronounced stress locking effects and approximates the rotating
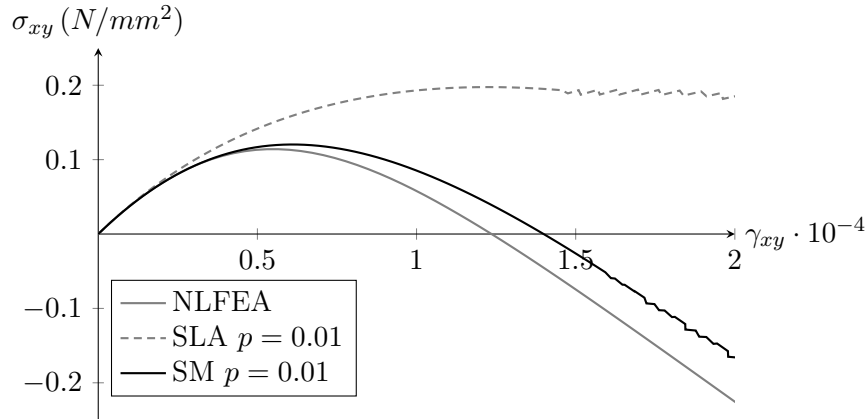
FIGURE 6.14: Shear stress σ_{xy} versus shear strain γ_{xy} for NLFEA, SLA
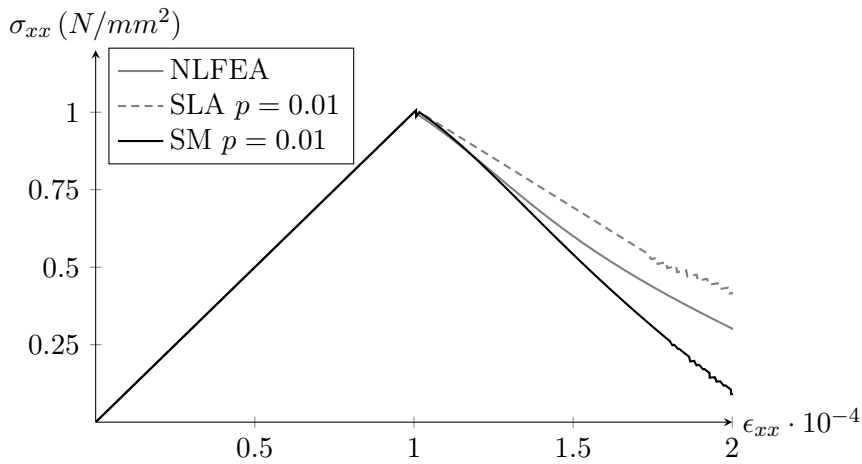and the sublayer model

FIGURE 6.15: Normal stress σ_{xx} versus strain ϵ_{xx} for NLFEA, SLA
and the sublayer model

crack NLFEA better. No significant shear stress overshoot is obtained and a simi-
lar trend as the rotating crack model is followed. It is noted that some differences
are still found due to the influence of earlier cracked sublayers with crack directions
deviating from the current principal stress direction (see Section 6.4 and Figure 6.10).

Figure 6.15 shows the response in x-direction for all three methods. Rots [62] also
considered the tension-shear problem and mentioned that for this case, fixed crack-
ing models replicate the inputted linear tension softening law due to the vertically
fixed crack (which is basically the same as Case 1). Regular SLA is based on a fixed
cracking model and therefore, the linear tension softening law is followed. For a
rotating crack model, the principal direction deviates from the x-direction, causing
the stress-strain relation to deviate from the linear tension softening law, which is ob-
served for both the sublayer model and NLFEA. Especially for ϵ_{xx} between $1.0 \cdot 10^{-4}$
and $1.5 \cdot 10^{-4}$ the sublayer model approximates NLFEA properly. For larger strains,
differences are found for the same reasons as for σ_{xy}.

The elements response in y-direction is captured by Figure 6.16 for all three meth-
ods. Negative ϵ_{yy} are found as a result of the Poisson's contraction in loading stage
(A). In line with σ_{xx}, the vertical stresses following from regular SLA reproduce the
linear tension softening law, although slightly influenced by Poisson's effects from
loading in the x-direction. The vertical crack is fixed and strength degradation takes
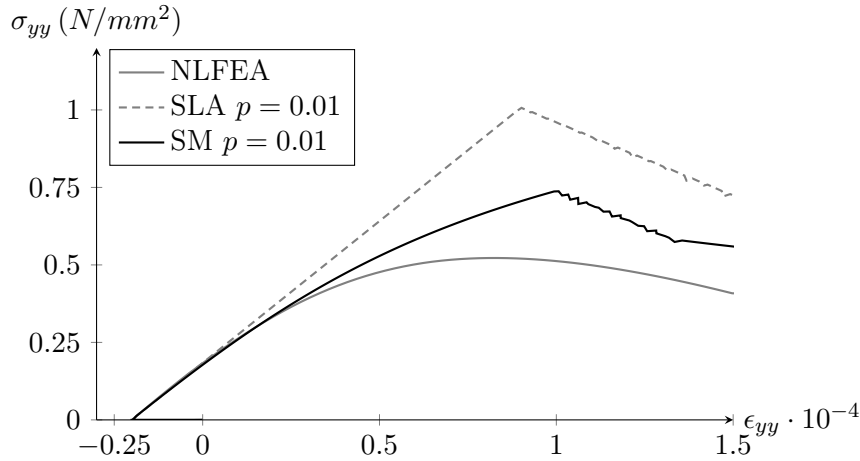
FIGURE 6.16: Normal stress σ_{yy} versus strain ϵ_{yy} for NLFEA, SLA and the sublayer model

place by perpendicular secondary cracking. Rots [62] mentions that fixed smeared cracking approaches are observed to suffer from excessive orthogonal cracking, according to studies by Leibengood et al. [45]. As a fixed crack is not able to co-rotate with the principal stresses, orthogonal cracking is the only way for an element to 'compensate' for the crack direction. This effect is also observed for regular SLA. Since crack rotation is simulated by the sublayer model, the effects of orthogonal secondary cracking are much less pronounced, resulting in a better approximation of the rotating crack NLFEA.

In the context of the sublayer model, the principal stresses and their directions are left undetermined. Every sublayer has its own crack direction and therefore, there is no single definition of principal directions 1 and 2 possible. Consider for example the principal crack strain within a crack ϵ_1^{cr}, which is defined normal to the crack. For each layer a different crack strain axis is found and comparing these results on element level does not make sense.

Lastly, the shear retention factor β, which is used to determine the reduced shear modulus $G_{red} = \beta G_0$, is considered. In regular SLA, a shear retention factor is required as the fixed crack inherently causes the presence of significant shear stresses within the crack plane after rotation of principal stresses. For regular SLA the reduction on the shear modulus is determined by Equation 2.13. Reduction factor $\beta = G_{red}/G_0$, where

$$G_0 = \frac{E_0}{2(1 + \nu_0)} = 4166.7 \, N/mm^2 \tag{6.5}$$

For a rotating crack model, the shear retention factor is used to enforce coaxiality between the principal stress and strain directions and is described by Equation 2.19. The elastic perfectly brittle damage increments of the sublayer model reduce the shear retention factor on sublayer level to $\beta = 0$, as discussed in Section 4.3 and according to Equation 2.13. Hence, after crack initiation, no shear stresses are obtained within the crack plane of that specific sublayer, while principal stress rotations occur and therefore, shear stresses within the cracking plane should be generated. To that end, one could argue that the sublayer model does not allow for a correct representation of the gradual shear stiffness degradation on element level. However, shear
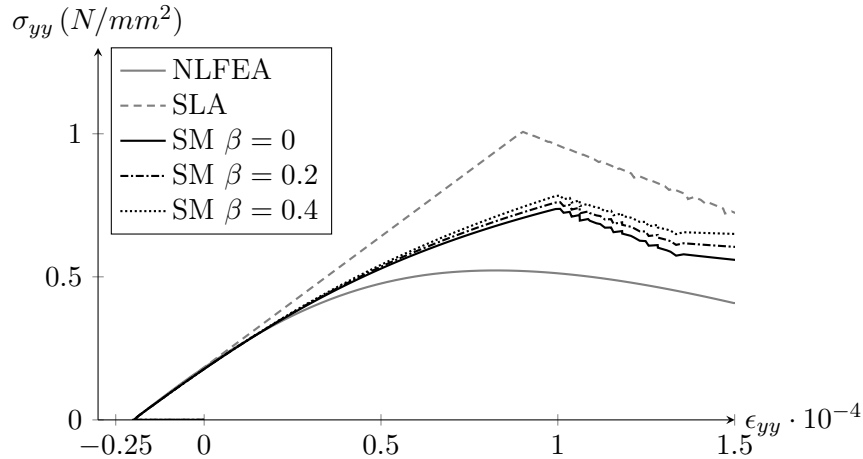
FIGURE 6.17: Influence of the shear retention factor β on the vertical stresses of the sublayer model for $\beta = [0, 0.2, 0.4]$

retention occurs implicitly as a consequence of the rotating crack plane over the different sublayers. In fact, previously cracked sublayers generate shear stresses within the cracking plane of consecutively cracked sublayers, thereby indirectly introducing a shear retention effect. Within a single fixed crack, significant shear stresses develop due to a misfit with the principal stress directions. However, for the sublayer model, a gradual global crack rotation is obtained and therefore, smaller shear stresses are found within the cracking planes of sublayers. The latter statement is supported by Figure 6.17, where the response for different shear retention factors is plotted (the y-component is used since differences are most notable here). Varying β does not lead to a notable variance of the stress state, indicating that only small shear stresses are found within the cracking planes. Furthermore, nonzero β even leads to larger deviations compared to rotating crack NLFEA, supporting the statement that the sublayer model implicitly describes shear retention behaviour on element level by brittle damage increments ($\beta = 0$ after crack initiation) on sublayer level.

As a matter of fact, when comparing the sublayer model with the discussed approaches by Rots [62] (fixed/rotating/multidirectional crack), similarities are found with the multidirectional cracking model which allows for multiple cracks to form within one integration point, where the angle between two consecutive cracks is controlled by treshold angle α. The superposition of sublayer cracks can be interpreted as a multidirectional crack. Furthermore, in line with the multidirectional crack model, coaxiality between principal strains and stresses is not maintained for the sublayer model, which is supported by the difference in principal strain direction and equivalent crack direction in Figure 6.10. The previously cracked sublayers ensure that the elements principal stress direction does not match the principal strain direction.

6.6   Theoretical intermezzo: understanding deviations

In this section, a theoretical framework is introduced that can be used to explain the nature of stress state deviations between NLFEA and the sublayer model in a qualitative manner. Once the origin of deviations is understood, the theoretical framework can be used to qualitatively predict deviations. Consider an elastic perfectly brittle element, that is cracked under an angle θ_{cr}. As the element is brittle, no normal
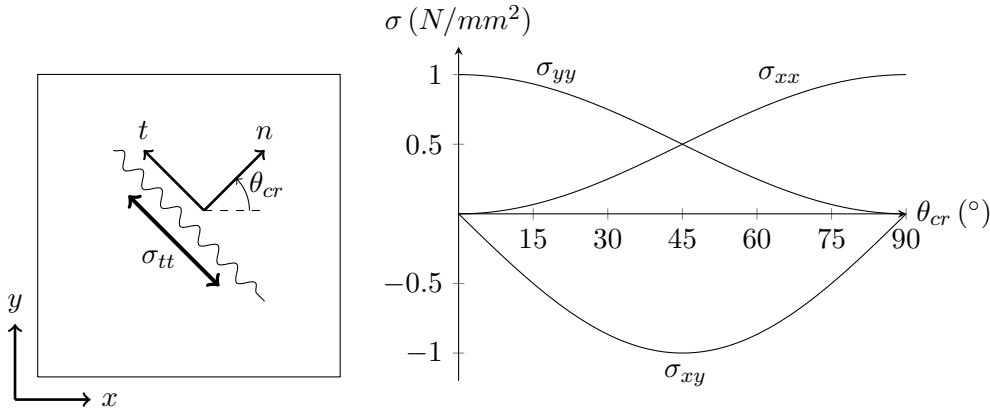
FIGURE 6.18: Transition from a local unit stress $\sigma_{tt} = 1$ after cracking
to global stresses as function of θ_{cr}

and shear stresses can be transmitted across the crack and only tangential stresses
are allowed. Assuming that the tangential stress in the crack is a unit stress, the local
stress vector $\bar{\sigma}_{nt}$ is given by

$$\bar{\sigma}_{nt} = \begin{bmatrix} \sigma_{nn} \\ \sigma_{tt} \\ \sigma_{nt} \end{bmatrix} = \begin{bmatrix} 0 \\ 1 \\ 0 \end{bmatrix} \tag{6.6}$$

Generally, stresses are considered in a global coordinate system. The local stresses
are transformed to global stresses with the aid of rotation matrix T, leading to

$$\bar{\sigma}_{xy} = T^{-1} \bar{\sigma}_{nt} \tag{6.7}$$

Substitution of Equations 2.16 and 6.6 results in

$$\bar{\sigma}_{xy} = \begin{bmatrix} \sigma_{xx} \\ \sigma_{yy} \\ \sigma_{xy} \end{bmatrix} = \begin{bmatrix} \sin(\theta_{cr})^2 \\ \cos(\theta_{cr})^2 \\ -2\sin(\theta_{cr})\cos(\theta_{cr}) \end{bmatrix} \tag{6.8}$$

The components of the global stress vector $\bar{\sigma}_{nt}$ as a function of θ_{cr} and the global
and local axes definitions are visualized by Figure 6.18. For $\theta_{cr} = 0°$ and $\theta_{cr} = 90°$,
only stresses in the y-direction and x-direction respectively are found. In between,
a combination of normal and shear stresses is observed. For example for a crack
direction $\theta_{cr} = 45°$, normal stresses $\sigma_{xx} = \sigma_{yy} = 0.5\,N/mm^2$ and shear stress $\sigma_{xy} = -1\,N/mm^2$ are found.

With the aid of these considerations, differences between NLFEA and the sub-
layer model can be understood. Under the assumption that in each cracked sublayer
a unit tangential stress is present (which is not true, but assumed for the sake of il-
lustration and understanding), a one-to-one comparison between the global stresses
of NLFEA and the sublayer model can be performed. The local stresses on sublayer
level are transformed to global stresses and can be compared with the rotating crack
NLFEA global stresses. The main ideas of this approach are explained with the aid
of Case 4 with $p = 0.05$. In Figure 6.19, the fixed crack directions of all $N = 17$ sub-
layers k are plotted within the global stress plot of Figure 6.18. The last and first layer
to crack are found for $k = 1$ and $k = N$ respectively. As concluded in Section 6.4,
the crack direction and the corresponding stress state of sublayer $k = m$ is exact at
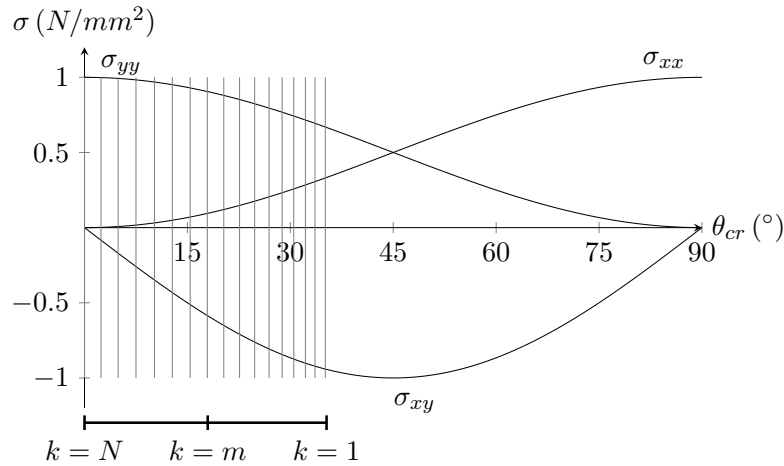the moment of cracking. At that specific moment, stronger sublayers $k = 1..(m-1)$

FIGURE 6.19: Visualization of crack directions of sublayers k, where
$k = N$ belongs to first cracked layer (Chapter 5) and all vertical bars
represent brittle cracking of a layer, for $p = 0.05$

are not cracked yet and weaker sublayers $k = (m+1)..N$ are already cracked (see Figure 6.19 for visualization of sublayer index k). Based on the comparison of the stresses in all cracked layers, which are found by the graph of Figure 6.19, with the exact stress state of sublayer m, a qualitative estimation of the difference between NLFEA and the sublayer model can be made.

For any cracked sublayer $k = (m+1)..N$, lower stresses σ_{xx} are found compared to sublayer $k = m$, resulting in an underestimation of the stresses on element level in x-direction compared to NLFEA, which is observed in Figure 6.15. Following the same line of thinking, for any cracked sublayer $k = (m+1)..N$, higher stresses σ_{yy} are found compared to sublayer $k = m$, resulting in an overestimation of the stresses in y-direction compared to NLFEA, as can be seen in Figure 6.16. For the shear stresses, less negative stresses σ_{xy} are found in the cracked layers compared to sublayer m, leading to less negative total shear stresses for the sublayer model, which also follows from Figure 6.14. Furthermore, for the tension-shear problem only small deviations in σ_{xy} are found, where relatively larger deviations are obtained for σ_{xx} and σ_{yy}. This phenomena can also be explained by Figure 6.19: the slope of the global stress curve σ_{xy} is steep for $\theta_{cr} < 15°$, causing the relative error of the first cracked layers (with cracking angles differing significantly from the actual crack angle) to reduce quite quickly. On the contrary, for global stress curves σ_{xx} and σ_{yy}, the slope for $\theta_{cr} < 15°$ is very low (almost zero), causing the relative error of the cracked layers to reduce quite slowly, and larger errors compared to the shear component are expected.

Following this line of thinking, deviations of the sublayer model compared to rotating crack NLFEA can be explained based on the set of crack directions of the sublayers. In this way, an effective theoretical tool is created to predict the quality of the sublayer model for specific cases. No quantitative results are provided by this theoretical approach, as the assumption of unit tangential stresses in all sublayers does not hold. Furthermore, secondary cracking is not included in this consideration. After the formation of a secondary crack, the contribution of a sublayer is completely lost and thereby does not cause any deviations. Besides, this framework only considers deviations on element level. In a structure, the behaviour of an element depends on adjacent elements and therefore, a small deviation might lead to crack path deviations that are not captured by this theoretical framework.
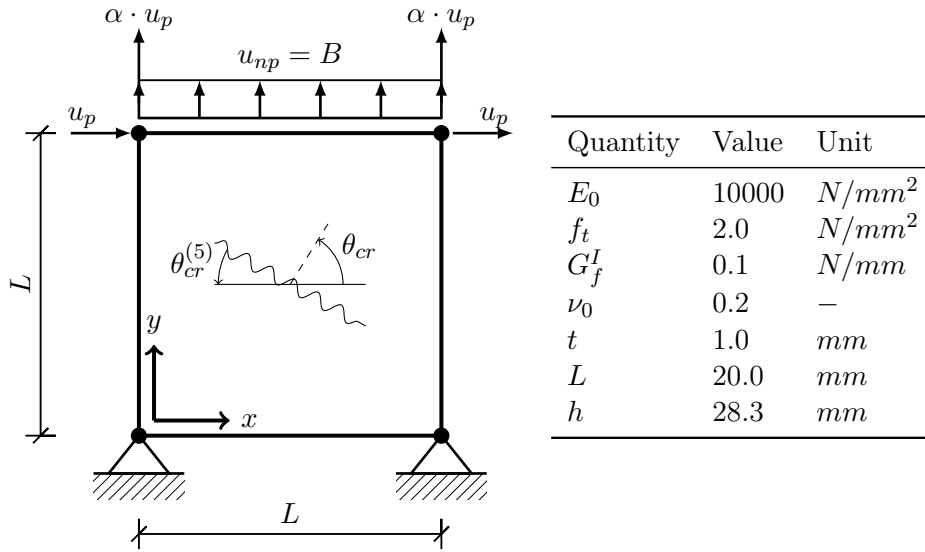
FIGURE 6.20: Geometry, crack direction definition and properties of
case 5: case 3 reconsidered $((n)p$=(non-)proportional load)

6.7   Case 5: case 3 reconsidered

In this section, the geometry of case 3 is reconsidered in order to exemplify the the-
oretical framework as proposed in Section 6.6. The proportional part of the load-
ing is extended by a vertical load $\alpha \cdot u_p$, as shown by Figure 6.20. In this figure,
the definition of crack angle θ_{cr} is in line with Section 6.6. However, for this case
$\theta_{cr}^{(5)} = 90° - \theta_{cr}$ is a more appropriate definition. Coefficients α and B are defined
such that the crack rotates over the following rotation intervals:

- Rotation interval A: $\theta_{cr}^{(5)} = 0 \ldots 15°$

- Rotation interval B: $\theta_{cr}^{(5)} = 15 \ldots 30°$

- Rotation interval C: $\theta_{cr}^{(5)} = 30 \ldots 43°$

Rotation interval C differs from the others as it only runs till $43°$ instead of $45°$. Due
to the definition of α and B, reaching the limit state of crack angle $45°$ is not possible
without crack closure (in fact, the non-proportional loading should be counteracted
by a negative α to reach a perfect shear crack). For the purpose of this section (un-
derstanding), this inconsistency is accepted. The strain state of the element is given
by

$$\epsilon_{xx} = 0 \quad \text{and} \quad \epsilon_{yy} = \frac{\alpha u_p + B}{L} \quad \text{and} \quad \gamma_{xy} = \frac{u_p}{L} \tag{6.9}$$

Furthermore, the crack angle is obtained from

$$\theta_{cr}^{(5)} = \frac{1}{2} \arctan\left(\frac{u_p}{\alpha u_p + B} \right) \tag{6.10}$$

and the principal strain by

$$\epsilon_1 = \frac{\epsilon_{xx} + \epsilon_{yy}}{2} + \sqrt{\left(\frac{\epsilon_{xx} - \epsilon_{yy}}{2} \right)^2 + \left(\frac{\gamma_{xy}}{2} \right)^2} \tag{6.11}$$

(A) $\theta_{cr}^{(5)} = 0 \ldots 15°$ (B) $\theta_{cr}^{(5)} = 15 \ldots 30°$ (C) $\theta_{cr}^{(5)} = 30 \ldots 43°$
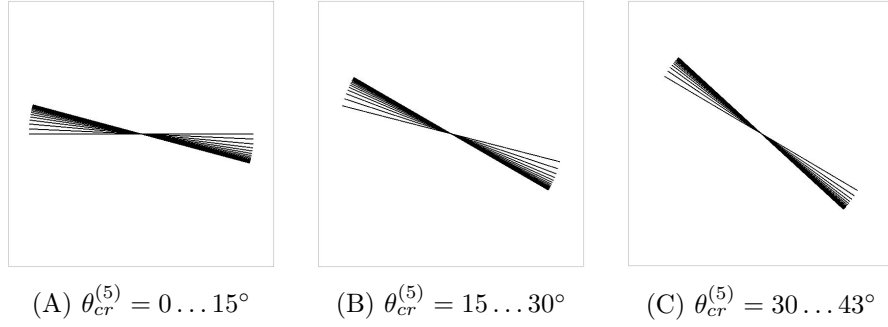
FIGURE 6.21: Representation rotation intervals A, B and C of case 5
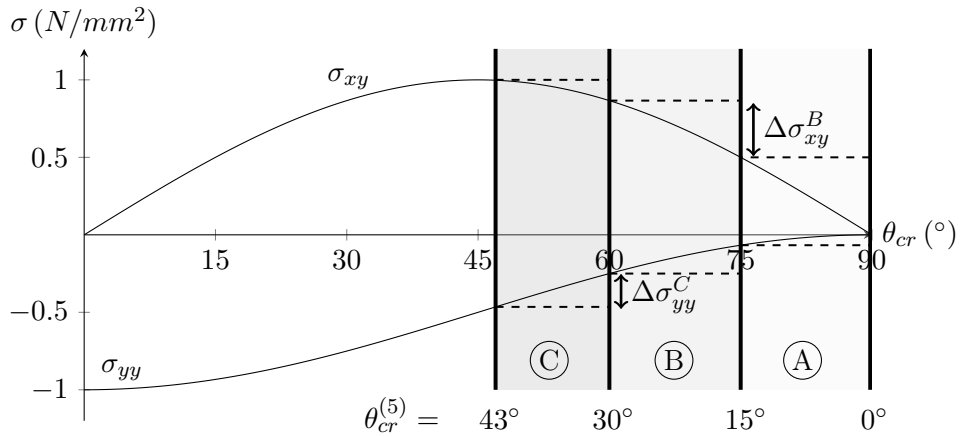
FIGURE 6.22: Visualization of understanding deviations compared to
NLFEA of rotation intervals A, B and C

Equations 6.10 and 6.11 are solved for α and B such that at crack initiation, the principal strain $\epsilon_1 = \epsilon_t$ and at ultimate limit state, $\epsilon_1 = \epsilon_u$, where the crack directions at crack initiation and ultimate limit state are prescribed by the rotation interval. It must be noted that ϵ_t and ϵ_u corresponding to NLFEA are slightly different compared to the sublayer model, as NLFEA is based on the continuum law and the sublayer model is based on the ripple band. For that purpose, slightly different α and B values are used for both cases. Figure 6.21 depicts the obtained output: the crack indeed rotates over the specified rotation intervals.

With the aid of crack rotation intervals A, B and C, a study is performed to exemplify the theoretical framework to understand deviations. In order to adapt the framework of Section 6.6, a slight change is required. The tangential stress σ_{tt} corresponding to this loading case is negative instead of positive, since the stress in line with the crack is in fact the compressive strut. Therefore, the local stress vector after cracking $\bar{\sigma}_{nt}$ is now given by

$$\bar{\sigma}_{nt} = \begin{bmatrix} \sigma_{nn} \\ \sigma_{tt} \\ \sigma_{nt} \end{bmatrix} = \begin{bmatrix} 0 \\ -1 \\ 0 \end{bmatrix} \tag{6.12}$$

and as a result of that, the signs of the global stresses change. Figure 6.22 visualizes the global shear stress σ_{xy} and normal stress σ_{yy} as a function of the cracking angle θ_{cr} (and thereby implicitly as a function of $\theta_{cr}^{(5)}$). Stress σ_{xx} is not considered because strain in this direction is restrained. Rotation intervals A, B and C are shown in the same figure. For example for rotation interval A, the first sublayer cracks for an

angle $\theta_{cr} = 90°$ and the last sublayer cracks for angle $\theta_{cr} = 75°$. At the moment that the last sublayer cracks, the stress state in this sublayer exactly matches the stress state of rotating crack NLFEA, as previously discussed. The difference in stress state between the first and last layer to crack can be used as a qualitative measure to estimate deviations compared to NLFEA. For example for interval B, considering σ_{xy}, the difference $\Delta\sigma_{xy}^B$ is defined by Figure 6.22 and can be used to understand deviations compared to NLFEA. Based on this figure, the following two statements are made:

$$\Delta\sigma_{xy}^C < \Delta\sigma_{xy}^B < \Delta\sigma_{xy}^A \tag{6.13}$$

$$\Delta\sigma_{yy}^A < \Delta\sigma_{yy}^B < \Delta\sigma_{yy}^C \tag{6.14}$$

From Equation 6.13 follows that for σ_{xy} the largest deviations are expected for rotation interval A, as the difference between sublayer stress states is largest, and the smallest deviations for interval C. Furthermore, all cracked sublayers within an interval have a lower shear stress than the last layer to crack (for example in interval B, all crack angles result in a lower shear stress than obtained for $\theta_{cr} = 60°$) and therefore, an undershoot compared to NLFEA is expected. Following the same line of thinking, from Equation 6.14 is concluded that for σ_{yy} largest deviations are expected for interval C and smallest deviations for interval A, which is exactly the opposite as for σ_{xy}. As all cracked sublayers within an interval have a less negative stress compared to the last layer to crack, an overshoot compared to NLFEA is expected (in this context, overshoot means a stress state that lies above NLFEA in the stress-strain diagram).

The output of both the sublayer model wit $p = 0.10$ and rotating crack NLFEA are shown by Figure 6.23 and the following observations are made:

- The shear stress σ_{xy}, plotted in subfigures (A), (C) and (E), is underestimated by the sublayer model.

- The difference in shear stresses σ_{xy} between NLFEA and the sublayer model is smallest for rotation interval C and largest for rotation interval A.

- The normal stress σ_{yy}, plotted in subfigures (B), (D) and (F), is overestimated by the sublayer model.

- The difference in stresses σ_{yy} between NLFEA and the sublayer model is smallest for rotation interval A and larger for rotation intervals B and C. As interval C is limited to 43°, a one-to-one comparison can not be made.

All observations are in line with the aforementioned expected deviations. Therefore, the applicability of the theoretical framework to properly understand and predict deviations between rotating crack NLFEA and the sublayer model is proved by this case.

6.8 Discussion

In this chapter, the sublayer model has been applied to several single element cases. Each of the test cases focused on a different learning / understanding goal, in order to obtain a complete understanding of the advantages and downsides of the model. The following conclusions are drawn in this chapter:

(A) $\theta_{cr}^{(5)} = 0\ldots 15°$

(B) $\theta_{cr}^{(5)} = 0\ldots 15°$

(C) $\theta_{cr}^{(5)} = 15\ldots 30°$

(D) $\theta_{cr}^{(5)} = 15\ldots 30°$

(E) $\theta_{cr}^{(5)} = 30\ldots 43°$
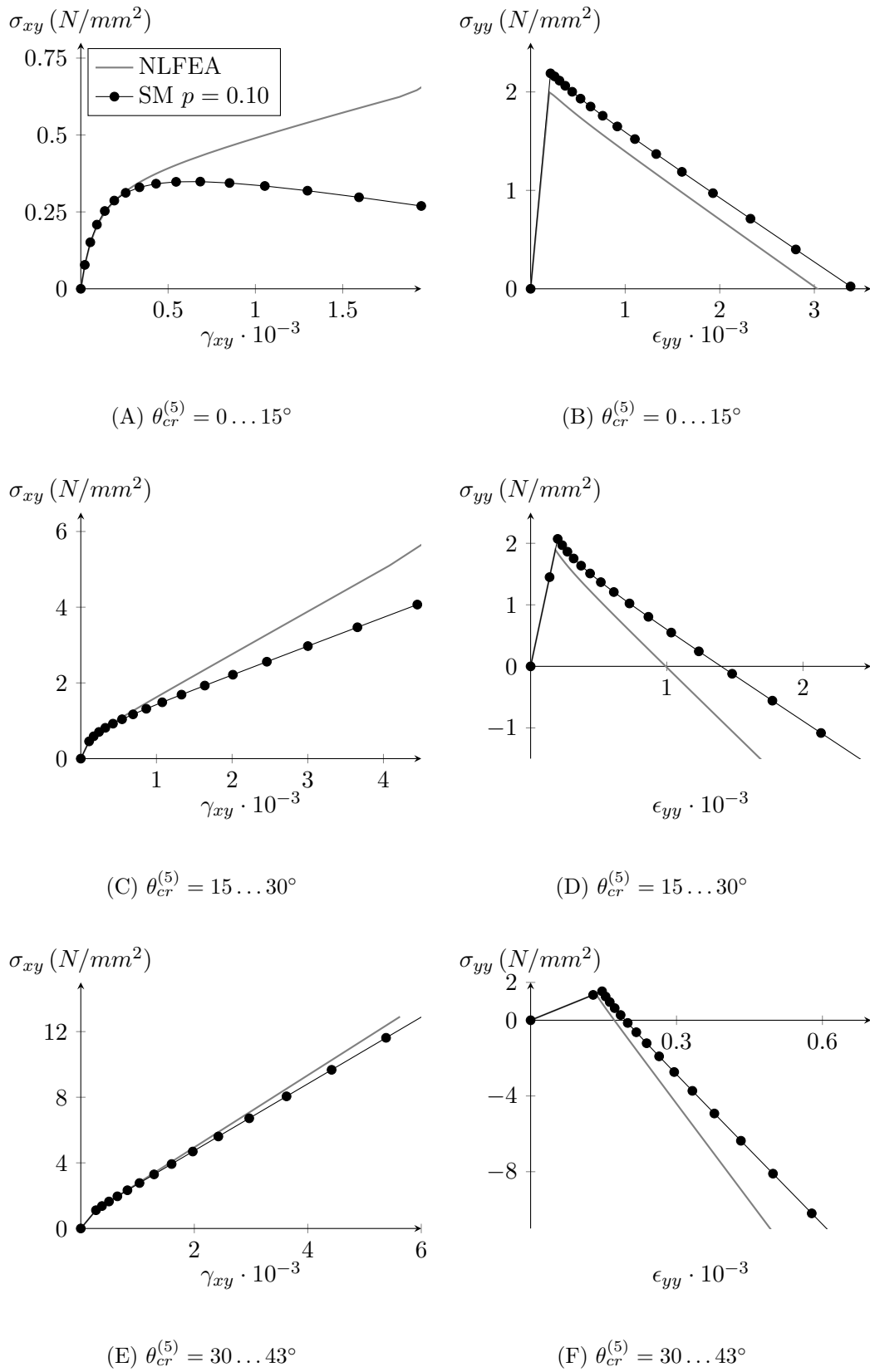
(F) $\theta_{cr}^{(5)} = 30\ldots 43°$

FIGURE 6.23: Stresses σ_{xy} and σ_{yy} for different rotation intervals $\theta_{cr}^{(5)}$ for both NLFEA and the sublayer model with $p = 0.10$

- The superposition of sublayers is able to mimick gradual damaged based reduction of the Poisson's ratio on element level by perfectly brittle damage increments on sublayer level.

- For single element cases with higher order elements, one should be aware of the incorrect occurrence of asymmetric strain fields and localization effects. However, in structural cases all nodes are restrained by adjacent elements, preventing these incorrect effects.

- With the aid of the sublayer model, the stress path of a rotating crack is better approximated compared to regular SLA and a rotating crack is mimicked by the superposition of sublayers with each their own crack direction.

- At the moment of cracking, the stress and strain state of the considered sublayer is exactly equal to NLFEA. However, on element level, differences are found between the crack angle of NLFEA and the total equivalent crack angle of the sublayer model due to the contribution of previously cracked sublayers that have outdated crack directions, which explains deviations in stress states.

- Within the sublayer model, shear retention occurs implicitly as a consequence of the rotating crack plane over the different sublayers. In fact, previously cracked sublayers generate shear stresses within the cracking plane of consecutively cracked sublayers, thereby indirectly introducing a shear retention effect.

- A theoretical framework is proposed which can be used to qualitatively understand deviations between rotating crack NLFEA and the sublayer model. Application of this framework is exemplified by a test case.

The results on single element tests are promising and indicate that a rotating crack is simulated quite well. The sublayer model proves to be more accurate compared to regular SLA, especially for cases with significant crack rotations. With the acquired knowledge in mind, structural test cases will be considered in the following chapter. All mentioned findings are valid on single element level. On structural level, interaction between adjacent elements takes place and therefore, deviations and error propagation do not solely depend on the single elements crack angles, but on the structural behaviour as a total. However, the fundamental knowledge of this chapter can be used as a measure to qualitatively understand what is happening within the considered structure. Furthermore, problems regarding mesh directional bias, stress locking and spurious stresses come to mind when considering structural problems. These problems are not considered yet and will be further addressed in Chapter 7.

Chapter 7

Verification on structural level

This chapter entails the verification of the proposed sublayer model on structural level and mainly focuses on differences that are found between regular SLA and the sublayer model. First, Section 7.1 gives an overview of the considered cases and lists some of their properties. Next, 5 cases are considered: the notched beam (Section 7.2, the shear notched beam (Section 7.3), the double-edge-notched beam (Section 7.4), a full scale facade (Section 7.5) and a concrete dam (Section 7.6). To conclude, Section 7.7 gives an overview of this chapter and compares the results.

7.1 Introduction

Up until now, the model has only been tested on element level in Chapter 6. The goal of this chapter is to verify the proposed sublayer model on structural level with the aid of several cases. An overview of the considered cases with their corresponding loading (proportional or non-proportional) and crack pattern is given by Table 7.1. With the selected cases, a wide variety of structures is considered in order to obtain a clear insight in the pros and cons of the sublayer model compared to regular sequentially linear analysis. Furthermore, these cases are used to provide an understanding of when to use which method and where to expect differences between both methods. If relevant, the results are compared to NLFEA. When performing tests on structural level, mesh-related problems are inherently generated (e.g. mesh directional bias), which did not pop up for single elements. On top of that, multiple element types with different integration schemes can be applied, potentially leading to significant differences. In this chapter, these effects are all considered and discussed if relevant for the considered case. To this end, another goal of this chapter is to compare the suitability of different type of elements to different type of cases (proportional versus non-proportional loading and straight versus curved crack patterns). In this chapter, all linear quadrilateral element invoke selective reduced integration by default, ensuring a constant shear strain over the element.

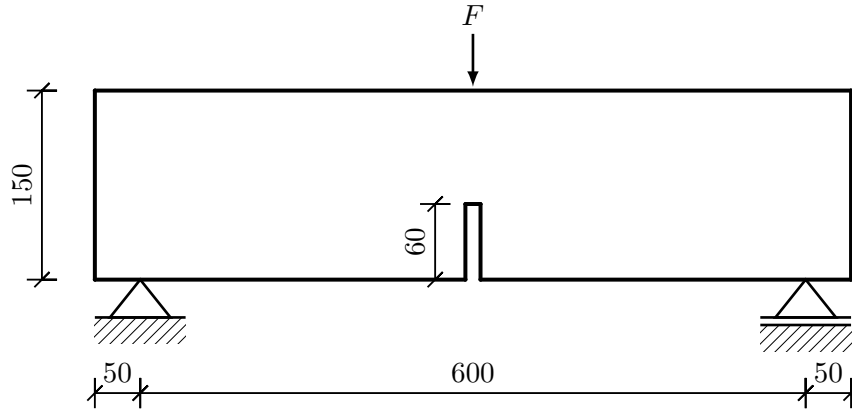| Case		Loading	Crack pattern
1	notched beam	proportional	straight
2	shear notched beam	proportional	curved
3	double-edge-notched beam	non-proportional	curved
4	full scale facade	non-proportional	diffuse
5a	scaled concrete dam	proportional	curved
5b	Koyna dam	non-proportional	curved

TABLE 7.1: Overview of considered cases, loads and crack patterns

FIGURE 7.1: Geometry of case 1 with all dimensions in mm

Quantity		Value	Unit
Tensile strength	f_t	3.78	N/mm^2
Initial stiffness	E_0	16000	N/mm^2
Poisson's modulus	ν_0	0.15	-
Fracture energy	G_f	0.30	N/mm

TABLE 7.2: Material properties of the notched beam specimens, taken
from [29] based on the experimental program by Zhao et al. [44, 85]

7.2   Case 1: notched beam

The first case that is considered is the notched beam, also known as the three point
bending beam, which is used by many authors (for example [29, 62, 66, 71]) as a
benchmark test to study the performance of finite element models regarding crack-
ing and localization behaviour in quasi-brittle materials. For this study, the geome-
try as shown by Figure 7.1 and experimental results are taken from the experimental
program performed by Zhao et al. [44, 85]. Beam specimen SG2-B1 of the mentioned
experimental program is examined in this thesis. The thickness of specimen SG2-B1
is $t = 120\,mm$. Material properties as presented in Table 7.2 are retrieved from Van
de Graaf [29], who slightly adapted the material properties as presented in [85] to
better fit the experimental data. A mode I tensile fracture mode is observed above
the notch as a result of tensile bending stresses. The size of the notch is taken equal
to the size of a single finite element.

For both regular SLA and the sublayer model, six analyses (A till F) are per-
formed: linear plane stress elements with reduced integration, linear plane stress
elements with 2 x 2 Gaussian integration and quadratic plane stress elements with
as well 2 x 2 Gaussian integration, all performed for element sizes L of 10 and 5 mm.
Two types of softening laws are applied: linear and exponential tension softening.
Detailed information on the applied saw-tooth laws and finite element models for
analyses (A) till (F) can be found in Table C.1. For all analyses, the crack band h is
equal to the localization width of the crack in line with the notch, for linear elements
equal to the element size L and for quadratic elements 0.5L.

The load-displacement graphs for both regular SLA and the sublayer model for
all six analyses are presented in Figure 7.2. Furthermore, the corresponding crack
patterns for regular SLA and the sublayer model based on linear tension softening
for a mid-span displacement of 1 mm are depicted in Figures 7.3 and 7.4 respectively.

(A) Q8MEM - 1 IP - 10 mm

(B) Q8MEM - 2x2 IP - 10 mm

(C) CQ16M - 2x2 IP - 10 mm

(D) Q8MEM - 1 IP - 5 mm

(E) Q8MEM - 2x2 IP - 5 mm

(F) CQ16M - 2x2 IP - 5 mm
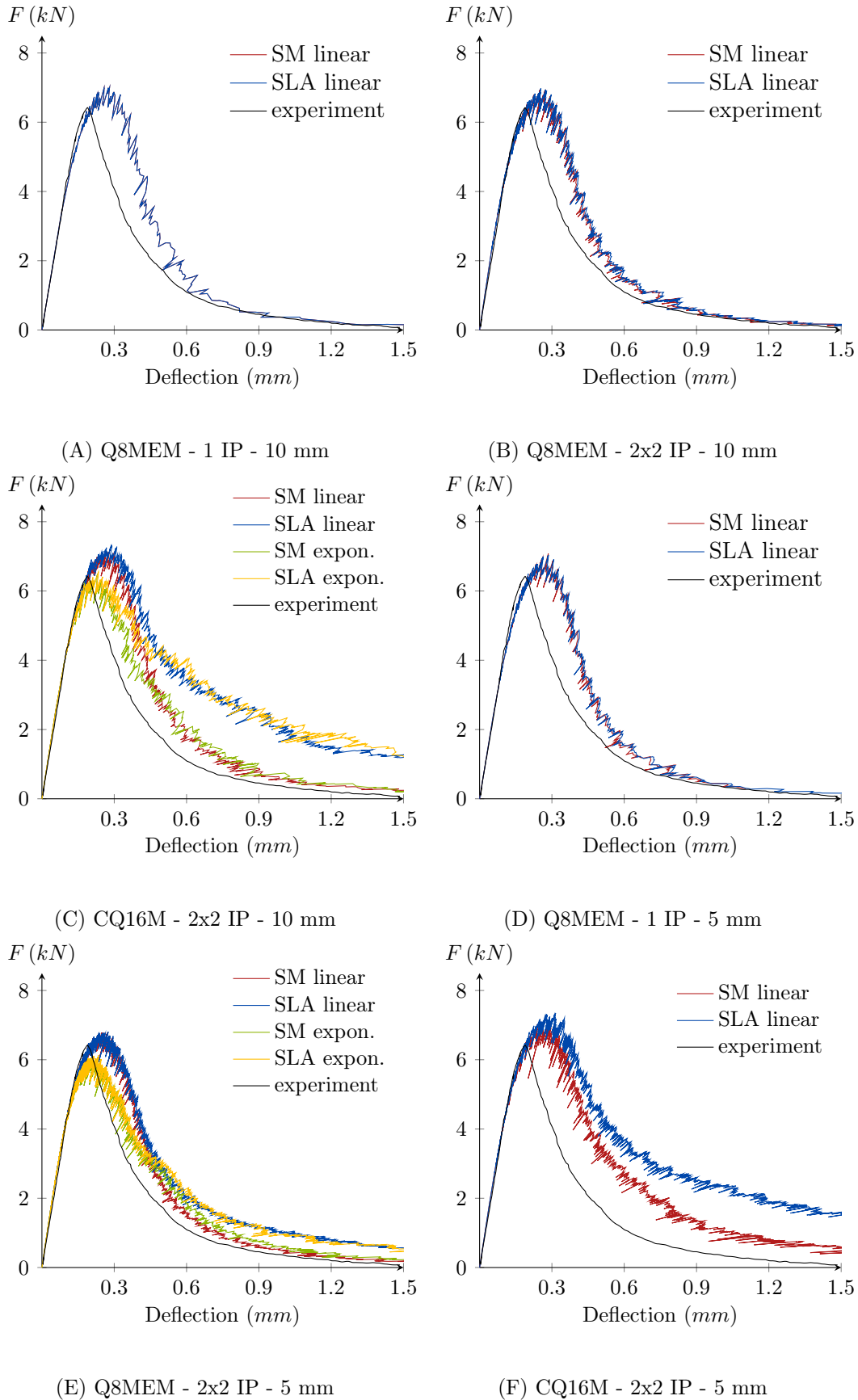
FIGURE 7.2: Load versus displacement at mid-span for the considered cases, based on both linear and exponential tension softening

(A) Q8MEM - 1 IP - 10 mm   (B) Q8MEM - 2x2 IP - 10 mm   (C) CQ16M - 2x2 IP - 10 mm

(D) Q8MEM - 1 IP - 5 mm   (E) Q8MEM - 2x2 IP - 5 mm   (F) CQ16M - 2x2 IP - 5 mm

FIGURE 7.3: Crack strain plots regular SLA for cases (A)-(F) of the notched beam for a mid-span deflection of 1.0 *mm* and linear tension softening

(A) Q8MEM - 1 IP - 10 mm   (B) Q8MEM - 2x2 IP - 10 mm   (C) CQ16M - 2x2 IP - 10 mm

(D) Q8MEM - 1 IP - 5 mm   (E) Q8MEM - 2x2 IP - 5 mm   (F) CQ16M - 2x2 IP - 5 mm

FIGURE 7.4: Crack strain plots sublayer model for cases (A)-(F) of the notched beam for a mid-span deflection of 1.0 *mm* and linear tension softening

Before the results are discussed, the reader is referred to Section 2.3.4, discussing the existence of spurious stresses causing stress locking. In this section, two types of spurious stresses that are relevant for the purpose of this thesis are distinguished:

- *Incorrectness of the crack direction*: due to the crack not co-rotating with the principal stresses for fixed crack models, unrealistic stresses might be found in the considered element, as the maximum stress might be found outside the fixed crack plane (only stresses in the fixed crack plane are monitored). Therefore, stresses exceeding the elements capacities are allowed, leading to a stiffer response. These effects have been widely observed in the single element tests in Chapter 6 and appear to be significantly reduced by the sublayer model.
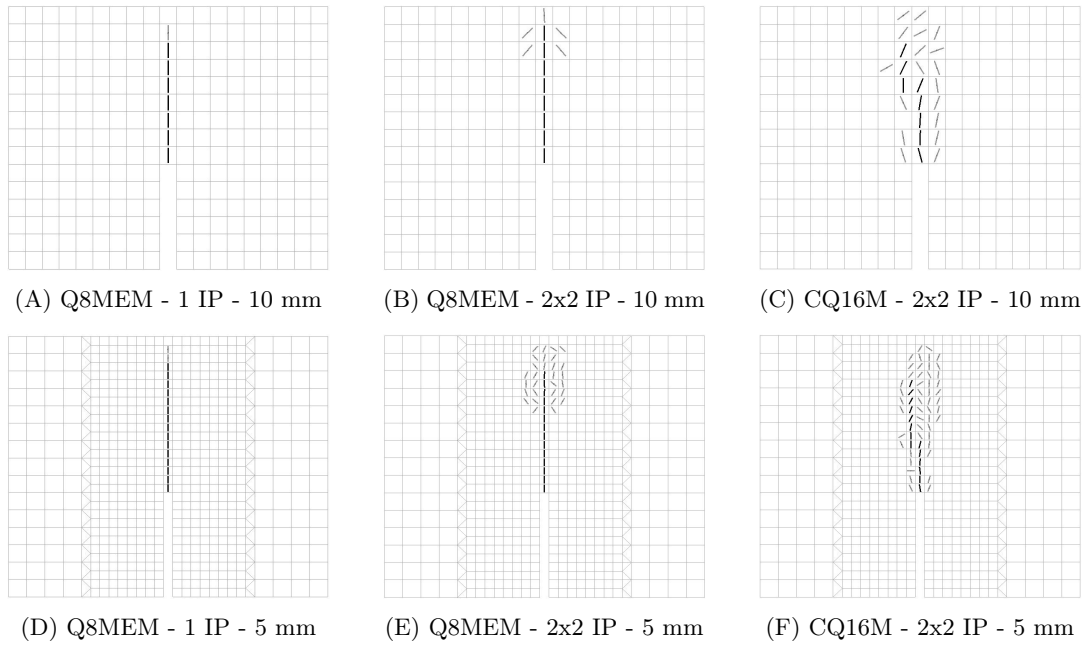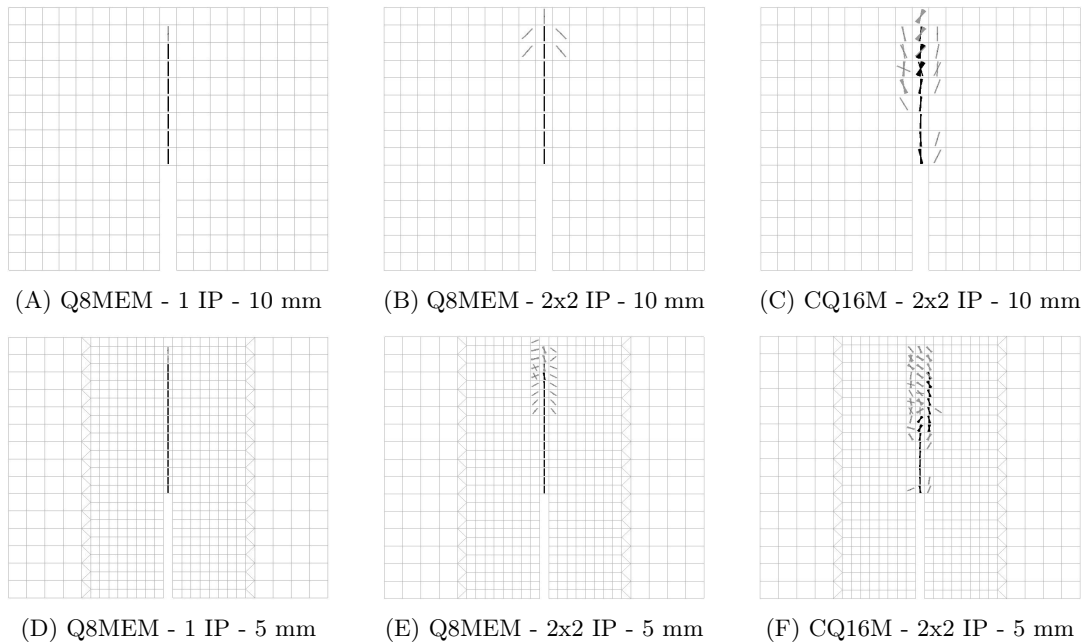
- *Inability to follow discontinuous nature of displacement field*: when large localized deformations take place in a specific element, surrounding elements inherently are subjected, to some extend, to deformations as well. As mentioned by Rots [62], neighbouring elements are connected to the cracked element and can not be truly separated from each other in the smeared cracking concept (contrary to discrete cracking), potentially causing significant straining in these elements as well. Subsequently, localization in a cracked element might induce neighbouring elements to be subjected to stresses exceeding the elements capacity. In this way, spurious stresses and cracks are generated, since these neighbouring elements are not really cracked in the physical sense, but crack as a result of their inability to follow the discontinuous nature of the displacement field, as also described by Jirasek and Zimmermann [39].

In Figures 7.3 and 7.4, black lines represent fully developed cracks and gray lines depict cracks that are initiated but still in development. For plane stress Q8MEM elements with reduced integration, analyses (A) and (D), a perfectly straight crack path is obtained without the occurrence of any spurious stresses. Hence, no differences are found between the load-deflection curves of regular SLA and the sublayer model. The crack simulates the formation of a discrete crack that ultimately leads to zero capacity. For this simple case, no spurious stresses and cracks are found for elements with reduced integration. As will be discussed later on, regular 2x2 integration does result in spurious stress states. A possible explanation for this difference can be found in the integration scheme. For reduced integration, the strain state of the complete element is in fact averaged in a single point, where for regular integration, each integration point belongs to a specific part of the element. Spurious stresses due to the discontinuous nature of the displacement field are mainly present on the side facing the cracked element. With regular integration, a large part of the area belonging to an integration point (on the side facing the cracked element) is subjected to severe straining, while for reduced integration, a relatively smaller part of the area belonging to the integration point is subjected to straining. In other words, the spurious behaviour is in fact averaged over the complete element for reduced integration and therefore, the influence of spurious stresses is less severe for reduced integration for this case and hardly any or even zero spurious stresses are generated.

For regular plane stress Q8MEM elements with a size of $10\,mm$ in analysis (B), some spurious stresses are observed at the top of the crack. However, the influence on the total load-deflection curves is rather small and hardly any differences between SLA and the sublayer model are found. It is noted that per element only the maximum absolute crack strain is plotted instead of the crack strain per integration point (this option is not allowed within the software anymore). Therefore, the
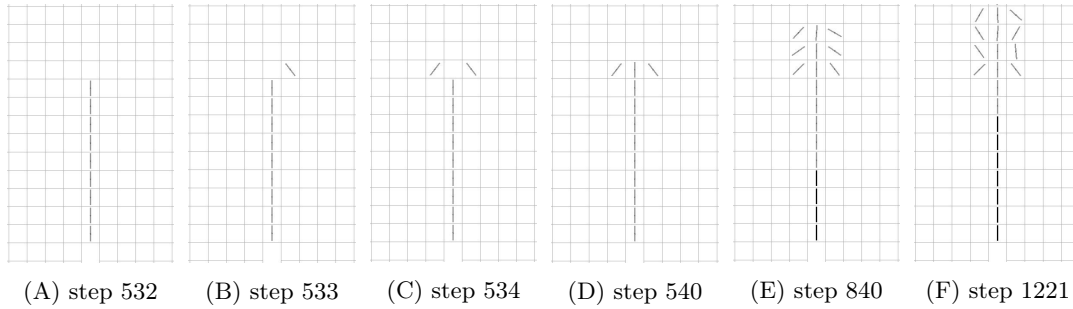
(A) step 532   (B) step 533   (C) step 534   (D) step 540   (E) step 840   (F) step 1221

FIGURE 7.5: Zoomed in crack development of regular SLA for analy-
sis (E) with linear tension softening, showing generation of asymmet-
ric (spurious) stress states

total elements crack direction might rotate when its integration points sequentially crack. However, this rotation does not represent crack rotation, which takes place on integration point level. As discussed by Van de Graaf [29], more spurious stresses and a higher energy dissipation are found for more refined meshes. This phenomena is also observed for regular plane stress Q8MEM elements with a size of 5 *mm* in analysis (E), showing severe spurious stresses. For smaller elements, the deformation with respect to the element size increases and much bigger strains are found. Therefore, the imposed straining on neighbouring elements increases and spurious stresses are more likely to occur in these elements.

The development of spurious stresses is explained with the aid of Figure 7.5, showing the crack pattern for different load steps for regular SLA. In step 533 of the analysis, the first spurious crack is formed as a result of the large deformation at the crack left underneath the element. For a sequentially linear analysis, only 1 event can occur per step and therefore, an asymmetric crack pattern is found for this step. As a result of this asymmetry, an asymmetric stress state is found and in step 534, the other spurious crack left from the crack path is formed. However, the asymmetric stress state enforces this crack to have a slightly, yet not notable, different crack angle compared to the spurious crack right from the crack path. Since the asymmetry stays intact, the center-line crack that forms in step 540 is not perfectly vertical anymore. This process is repeated several times, until in step 840 the first notable difference in crack direction can be observed. In fact, a non-stable process of increasing asymmetry has been initiated and spurious stresses due to incorrect crack directions are formed as a result of asymmetric generation of spurious stresses due to the inability of the elements to follow the discontinuous nature of the displacement field. Both regular SLA and the sublayer model reveal the development of spurious stresses due to the inability to follow the discontinuous displacement field. However, where an increasing asymmetric state is observed for regular SLA, the sublayer model is able to correct its crack direction by sequential cracking of the different sublayers with each their own crack direction. Hence, spurious stresses and cracks due to incorrect crack directions for the sublayer model are limited and a less wide localization band is observed in Figure 7.4E. In the same figure, significant crack rotations are observed at the top of the crack, where Figure 7.3E reveals an incorrect crack direction here. The advantage of SLA to follow asymmetric failure modes and overcome bifurcations, as mentioned by Rots et al. [67], comes with the disadvantage of potentially enforcing locally asymmetric failure modes for symmetric problems. The sublayer model is still able to overcome bifurcations by following asymmetric failure modes, but is meanwhile able to correct itself when the asymmetric failure mode is
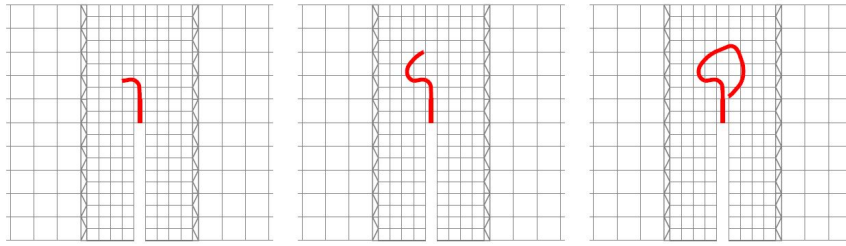
FIGURE 7.6: The development of a so-called U-turn for quadratic elements, where the crack path is marked in red and taken from Slobbe et al. [74]

undesired (e.g. for symmetric cases). Due to the aforementioned reasons, differences between the load-deflection curves of regular SLA and the sublayer model are found for analysis (E): the reduction of spurious stresses results in less energy dissipation and therefore a less stiff response of the sublayer model compared to regular SLA, especially in the post-peak regime.

Another problem that comes with regular SLA is that spurious stresses fix the crack direction of the surrounding elements, while for the sublayer model only the weakest layer(s) is (are) fixed. The other layers are not influenced by the spurious crack direction, while for regular SLA the crack direction of the entire integration point is fixed based on a spurious crack. For the notched beam, this is no problem since there is a clear difference between the central elements where the straight crack propagates and the spurious crack elements. However, for cases where crack propagation passes elements that already have encountered some spurious cracks, the fixed crack regular SLA is not able to adapt itself and the crack propagation will be based on the incorrect crack angle that formed as a result of spurious stresses.

Lastly, quadratic plane stress CQ16M elements with 2x2 integration, as used by analyses (C) and (F), are discussed. The crack localizes within half of the element, which is included in the applied crack band. According to Slobbe [71], when using higher order elements, stress fields become highly disturbed due to strain localization within an element and an increase of spurious stresses is expected. The crack plots corresponding to analyses (C) and (F) support this statement: a wide band of spurious cracks is obtained. In a paper by Slobbe et al. [74] on a delayed crack path fixation approach, so-called *U-turns* of the crack paths in the notched beam were observed for quadratic elements, manifesting themselves in sudden and unrealistic sharp changes of crack paths, as shown by Figure 7.6 (which is taken from the paper). The crack bends sideways and then turns around. Similar cracking paths are observed in this study in Figures 7.3C and F for quadratic meshes for regular SLA, as the crack also bends sideways and some near horizontal cracks are found at the top of the crack. However, a plot of the cracks per integration point is required to prove this statement. Unfortunately, such a plot can not be made with the current software. For analysis (C), the sublayer model seems to resolve the appearance of a U-turn: the crack path stays at the center-line column of elements instead of diverging to a different column of elements, although significant crack rotation is required in the top elements for this purpose. For analysis (F), the crack can not be kept within the center-line column of events, but further development of a U-turn seems to be restrained and a smaller localization band compared to regular SLA is found. The reduction of spurious stresses indicates that the underlying reason for the occurrence of U-turns must be sought for in the fixed crack assumption that is the basis for regular SLA. The latter statement is supported by the load-deflections curves of analyses
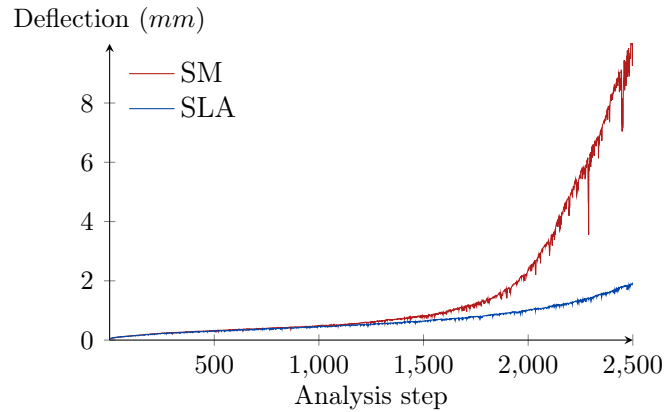
FIGURE 7.7: Deflection at mid-span versus analysis step number of
analysis (F) with linear tension softening for both the sublayer model
and SLA

(C) and (F): very pronounced differences are found in the post-peak responses of regular SLA and the sublayer model as a result of the restrained U-turn and reduction of spurious stress development. Much stiffer behaviour is obtained when using regular SLA, which is clearly not in line with the experimental results, showing a rather flexible reduction to zero load bearing capacity. The results of the sublayer model show much better agreement with the experimental results, although application of quadratic elements for this case is not recommended: quadratic elements are more suitable for complex cases with more complex deformation modes, rather than cases with straight crack paths, for which the application of linear plane stress elements is more appropriate.

In the delayed crack path fixation approach of Slobbe et al. [74], the crack-path is fixed once a certain amount of damage has taken place. In this way, the occurrence of U-turns is resolved. Following this line of thinking, the sublayer model can in fact also be seen as a type of delayed crack path fixation, since the crack path direction is not directly fixed after initiation, but is gradually fixed once damage increases and more sublayers are cracked, which can be interpreted as a 'delayed' type of crack path fixation.

In Figure 7.7, the deflection at mid-span is plotted versus the analysis step number of analysis (F) for both regular SLA and the sublayer model. Since less spurious stresses are found when using the sublayer model, the total number of events is reduced. Regular SLA requires roughly 2500 steps to reach a deflection of 2 mm, where the sublayer model requires approximately 2000 steps to reach the same deflection, a reduction of 20% compared to regular SLA.

For analyses (C) and (E), both linear and exponential tension softening are applied. From the load-deflection curves in Figure 7.2 is found that exponential tension softening better suits the experimental results. Ultimately, the same response is found, but the peak-load is lower and more flexible post-peak response is observed for exponential tension softening, caused by the larger slope in the continuum constitutive law after reaching the materials strength. While invoking a different tension softening law, the same differences are found between both models.
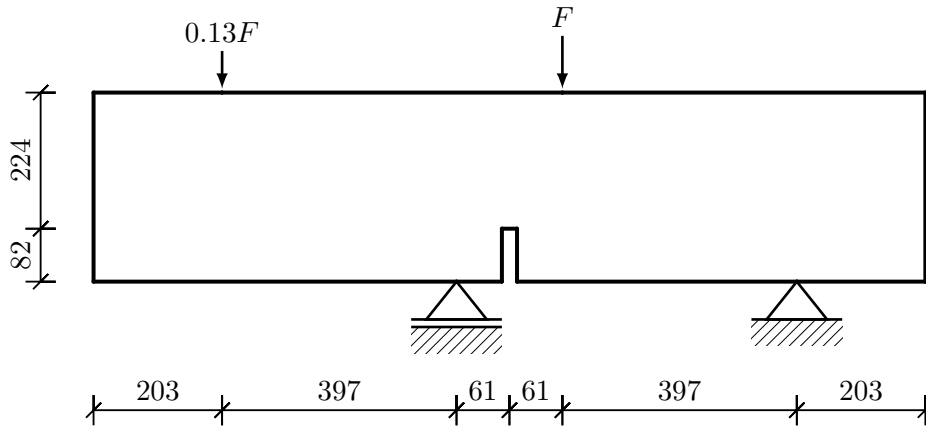
FIGURE 7.8: Geometry of case 2 with all dimensions in mm

Quantity		Value	Unit
Tensile strength	f_t	2.80	N/mm^2
Initial stiffness	E_0	24800	N/mm^2
Poisson's modulus	ν_0	0.18	-
Fracture energy	G_f	0.15	N/mm

TABLE 7.3: Material properties of the shear notched beam specimens, all properties except G_f are taken from Rots [62]

7.3 Case 2: shear notched beam

The second case that is considered is the shear notched beam, also known as the four-point shear test. The curved crack pattern, that is found right above the notch and propagates towards the load F, has been used by many authors (e.g. [7, 11, 14, 38, 46, 56, 62, 71]) to study the performance of a wide variety of smeared and discrete crack models in mixed-mode crack propagation. In this study, the geometry and the experimental results of Series C of the research program performed by Arrea and Ingraffea [2] are used. The beam specimens have a thickness $t = 156\,mm$ and a geometry as shown by Figure 7.8. For serie C, three beams were tested, of which only two were considered to be valid. For that reason, some significant scatter is observed in the results as well as in the material properties of the specimens. In the experimental program, only the compressive strength, stiffness and Poisson's ratio were measured and information on the tensile strength and fracture energy is missing. In this study, the tensile strength f_t, stiffness E_0 and Poisson's ratio ν_0 are taken from Rots [62], which are frequently used by other references as well. Regarding the fracture energy G_f, values between 0.075 and 0.2 N/mm are found in the given references and $G_f = 0.15\,N/mm$ is applied for this study to be somewhere in the middle. Table 7.3 lists the applied material properties.

The shear notched beam is a combined mode I and mode II fracture, although mainly governed by mode I tensile crack development above the notch: the generation of mode II shear cracks is rather limited. According to Rots and De Borst [65], the shear notched beam releases the mode I fracture energy much quicker than the mode II fracture energy. Although an analysis considering only mode I fracture is therefore justified for the purpose of this thesis, it is noted that in reality no pure mode I fracture is obtained and one should consider mode II shear fracture patterns as well for a complete description of this case.

(A) Undeformed mesh

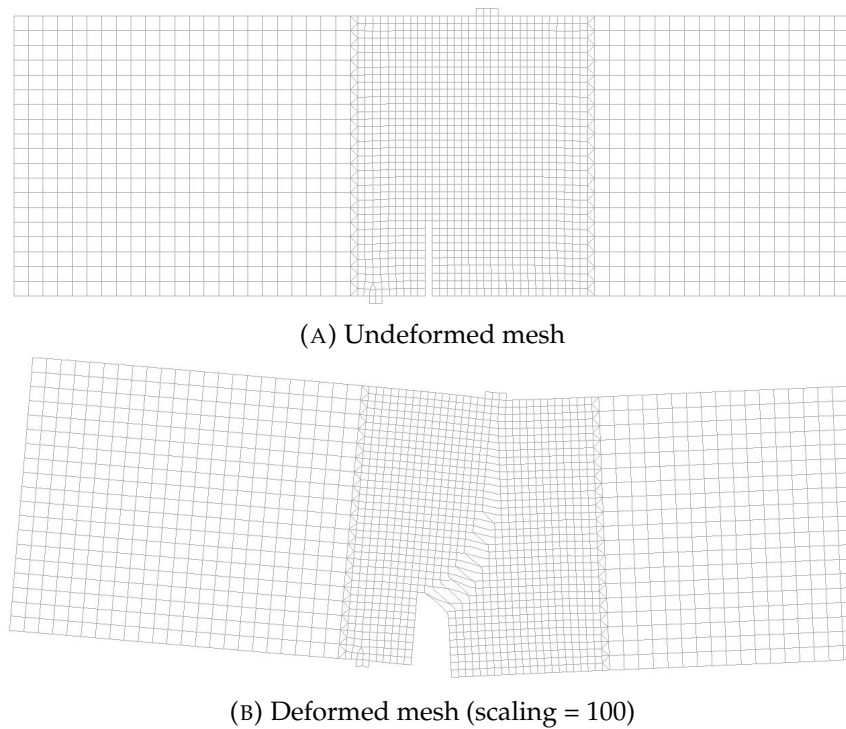

(B) Deformed mesh (scaling = 100)

FIGURE 7.9: Finite element model of case 2 where on both sides the
outer 203 mm is not modelled, in (A) undeformed and (B) deformed
configuration

The specimen is modelled using quadrilateral elements. Figure 7.9 entails both
the deformed and undeformed finite element meshes. Around the notch, nonlinear
material behaviour following Hordijk tension softening (see Section 2.3) is assumed.
Nonlinear material behaviour is only allocated to the relevant part of the beam to re-
duce computational efforts. Furthermore, the outer 203 *mm* of the beam in Figure 7.8
is not modelled for the same reasons. Around the notch, smaller elements are used
compared to the rest of the beam, 8 *mm* and 16 *mm* respectively, to have a sufficient
level of detail. The loading and support close to the notch are both modelled with an
extra row of elements, to prevent influence of the load introduction on the response.
For the shear notched beam, three analyses (A)-(C) are performed: Q8MEM with
reduced integration, Q8MEM with regular integration and CQ16M with regular in-
tegration. Crack bands are chosen according to a zig-zag propagation pattern [62].
All details on analyses (A)-(C) can be found in Table C.2. The width of the notch is
taken equal to the size of a single element.

During the analyses, the crack mouth sliding displacement (CMSD) is moni-
tored, defined as the difference in vertical displacement between the two sides of the
notch, considered at the height of the supports. The CMSD-load curves for all three
cases and the experimental results [2] are shown by Figure 7.10. The corresponding
crack patterns for a CMSD of 0.20 *mm* for both regular SLA and the sublayer model
are depicted by Figures 7.11 and 7.12 respectively.

For plane stress linear Q8MEM-elements with reduced integration in analysis
(A), a semi-curved crack pattern is observed for both regular SLA and the sublayer
model. The crack is described as semi-curved, since the obtained crack curve is in
fact a collection of straight parts that are in line with the mesh, where only the first
part of the crack path is found under roughly 45 degrees. Starting from the notch,
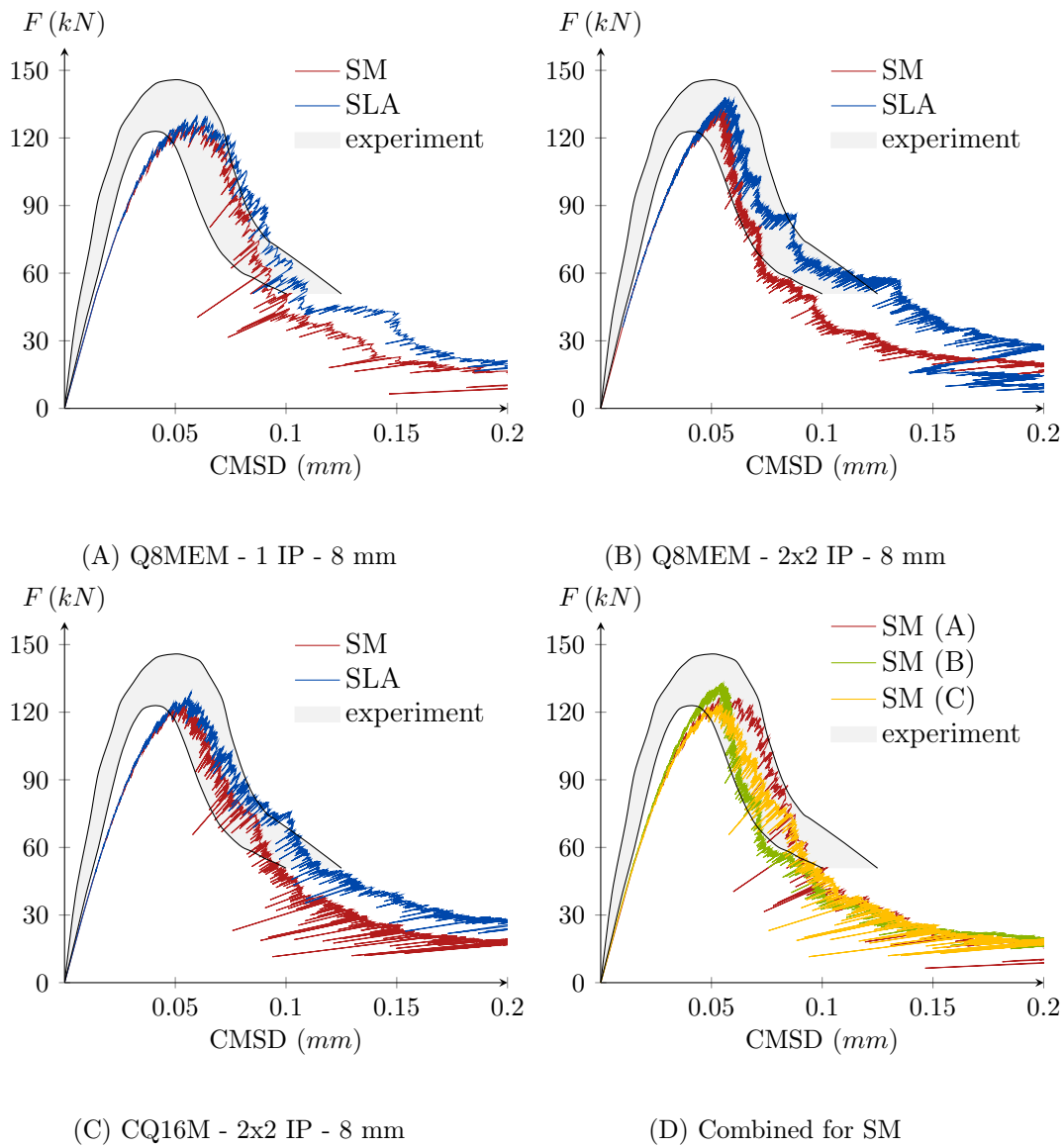
(A) Q8MEM - 1 IP - 8 mm

(B) Q8MEM - 2x2 IP - 8 mm

(C) CQ16M - 2x2 IP - 8 mm

(D) Combined for SM

FIGURE 7.10: Load on the shear notched beam versus crack mouth sliding displacement (CMSD) for the considered cases (A) till (C) and all combined
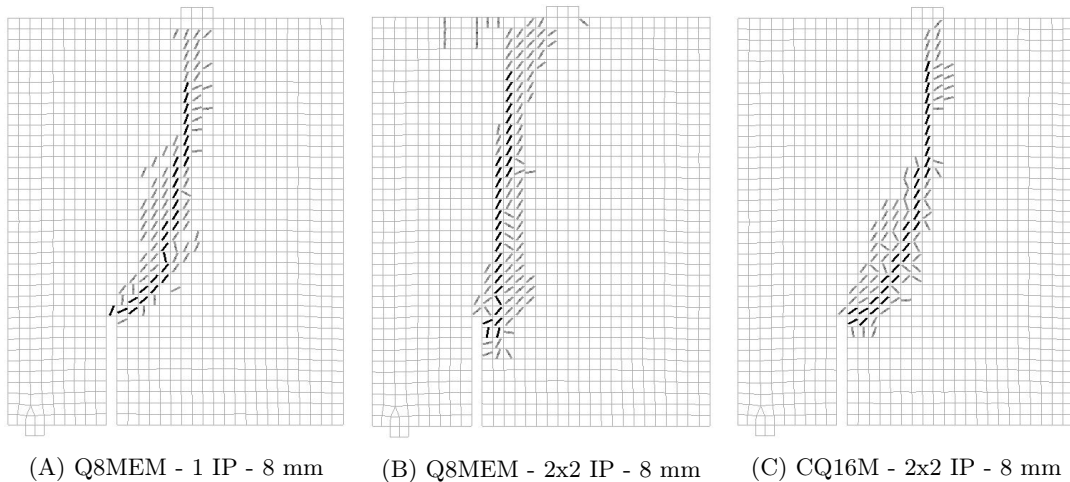
(A) Q8MEM - 1 IP - 8 mm   (B) Q8MEM - 2x2 IP - 8 mm   (C) CQ16M - 2x2 IP - 8 mm

FIGURE 7.11: Crack strain plots regular SLA for cases (A)-(C) of the
shear notched beam for a CMSD of 0.20 mm

(A) Q8MEM - 1 IP - 8 mm   (B) Q8MEM - 2x2 IP - 8 mm   (C) CQ16M - 2x2 IP - 8 mm
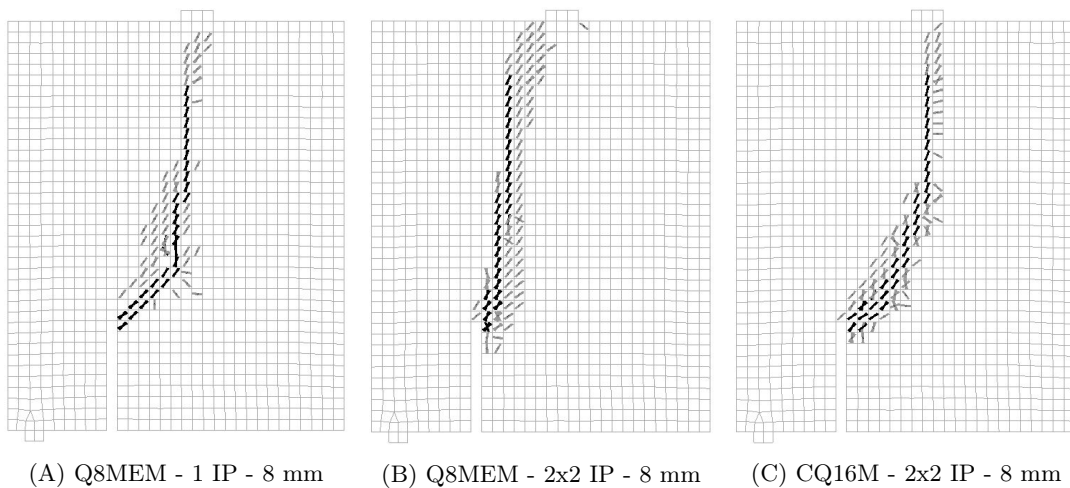
FIGURE 7.12: Crack strain plots sublayer model for cases (A)-(C) of
the shear notched beam for a CMSD of 0.20 mm

the crack gradually propagates towards the point of load application. Using the sub-
layer model, pronounced crack rotations are observed around the notch (the point of
crack initiation), since the curved crack pattern causes the local stress state to change
here. Furthermore, crack rotations seem to take place at points where the crack shifts
to another column of elements in order to 'smoothen' the crack path. Crack rota-
tions influence the structural response in two ways: on single element level and on
structural level. The influence on single element level has been widely discussed in
Chapter 6: a more up-to-date crack angle is obtained and less spurious stresses are
observed within the element, as the stresses are monitored in a plane that is more
in line with the critical plane and the occurrence of stresses exceeding the elements
capacity is reduced (which is not the case for the fixed crack model). Secondly, over-
stiff behaviour on single element level induces the generation of spurious stresses
in neighbouring elements as well. Due to stiffening, larger stresses are accepted for
the cracked element, causing surrounding elements to crack while the considered
element should crack, generating spurious cracks. When comparing the crack pat-
terns of regular SLA and the sublayer model for analysis (A), a smaller localization

(A) Q8MEM - 1 IP - 8 mm   (B) CQ16M - 2x2 IP - 8 mm

FIGURE 7.13: Comparison of crack paths analyses (A) and (C) with experimental bounds for a CMSD of 0.20 mm

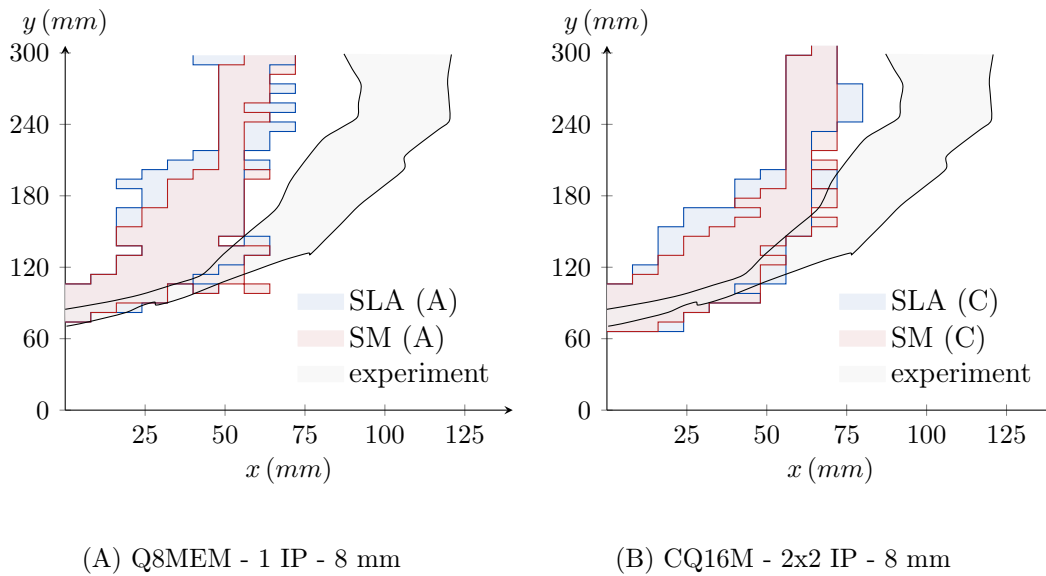band is found on structural level for the sublayer model due to the more flexible behaviour on element level. In Figure 7.13A, the cracks patterns at a CMSD of 0.20 mm are compared with the experimental crack band, as reported by Cendon et al. [14]., supporting the smaller localization band of the sublayer model. The coordinate center is defined at the right bottom corner of the notch. Quite substantial deviations are found compared to the experimental crack patterns, especially in the vertical branch of the crack, which is probably the result of the mesh following tendency, better known as mesh directional bias. Instead of having a small curvature near the end, the crack propagates vertically. When comparing the CMSD-load curves of both methods, more flexible behaviour is obtained using the sublayer model in the post-peak regime, supporting previous findings. The results are in good agreement with experimental results. According to Rots [62], prediction of genuine separation and softening down to zero load is desired. In his study, it was observed that smeared crack approaches were not able to fulfill these requirements. Both regular SLA and the sublayer model tend to predict an ultimate softening down to zero, although the sublayer model seems to reach this state quicker.

For plane stress linear Q8MEM-elements with regular 2x2 Gaussian integration in analysis (B), a different crack path is found. A more or less straight crack is obtained for both regular SLA and the sublayer model. Apparently, full integration of linear elements enforces a straight crack path for this case. The same phenomena has been observed for regular linear plane stress elements by Slobbe [71] for regular SLA and by Bhattacharjee [7] for a coaxial rotating crack model in NLFEA. Apparently, the straight incorrect crack pattern is found for other analyses as well and therefore, the reason for this discrepancy must be sought for in the finite element geometry and element type rather than the model: the sublayer model is not able to resolve the problem, but is also not the underlying reason of the problem. For this case, linear elements with reduced integration perform better than regular integration, which is a remarkable finding. A possible explanation is that shear-related behaviour might be better captured with reduced integration, allowing for a constant shear stress over the element, meanwhile averaging troubling spurious stresses over the complete element size and reducing their effect. When comparing the crack patterns of both

methods, a slightly smaller localization band is observed for the sublayer model. Furthermore, the crack pattern of the sublayer model reaches the third column right from the notch earlier than regular SLA, suggesting that the crack path is somehow slightly corrected. Despite the incorrect crack pattern, reasonable CMSD-load curves are found, again marking over-stiff behaviour of regular SLA.

Lastly, quadratic CQ16M-elements are considered in analysis (C). With quadratic elements, the curved crack path is better described and seems to be less dependent on the mesh direction for both methods. Quadratic elements allow for a more complex crack pattern, such as the shear notched beam, where linear elements are more convenient for straight crack patterns, as was already observed for the notched beam in Section 7.2. The suitability of quadratic elements for this case becomes clear by Figure 7.13B, which shows that the experimental curved path is better approximated by both methods compared to analysis (A). On top of that, the crack pattern that is found by the sublayer model exhibits a smaller localization band compared to regular SLA, indicating a reduction of spurious cracks and stresses, in line with analyses (A) and (B). The CMSD-load curve shows that excellent agreement is found with experimental results, and clear differences are found between both methods: at a CMSD of 0.20 mm, the sublayer model finds a load of 17.7 kN, while regular SLA results in 26.5 kN, being 49.7% higher compared to the sublayer model. From this can be concluded that significant differences are found between both methods and that the sublayer model outperforms the sublayer model regarding the requirements as posed by Rots [62], as the model quicker converges to zero loading.

When looking in more detail to Figure 7.10, it is observed that bigger snap-backs are found for the sublayer model, which becomes especially clear for the quadratic analysis (C). In order to understand this difference, it is first explained why snap-backs occur for regular SLA according to Van de Graaf [29]. Stress jumps occur when multiple neighbouring elements are almost loaded up to their tensile strength. In this case, a damage increment can only be performed for the most critical integration point, after which a stress distribution takes place that relieves the critical integration point. The surrounding elements are not able to take over the released stress and the only way to distribute these additional stresses is by reducing the load factor, thereby causing a snap-back. This process is repeated several times until the surrounding elements allow for recovery of the load factor. The large snap-backs of both regular SLA and the sublayer model are found at roughly the same places in the CMSD-load curve, meaning that the underlying cause for snap-backs is the same for the sublayer model. However, the snap-backs are bigger compared to regular SLA, which is most likely the result of a fundamental difference between the two models. For regular SLA, the critical integration points are often already cracked and therefore considered in the fixed crack direction, meaning that not by definition the direction with biggest stresses is monitored. For the sublayer model with brittle damage increments, the critical sublayer is most often uncracked (except for perpendicular cracking) and stresses are considered in the maximum direction. As a result, the monitored stresses in the surrounding elements are potentially even closer to the tensile strength for the sublayer model, since regular SLA monitors the stresses in the surrounding elements not in the maximum direction. Since the surrounding elements have higher stresses, the released stress after a damage increment becomes even more difficult to distribute and the loading should be reduced even further, causing bigger snap-backs to occur for the sublayer model compared to regular SLA. In fact, the more exact description of stresses by the sublayer model, with therefore higher stresses in the surrounding elements, requires bigger snap-backs.
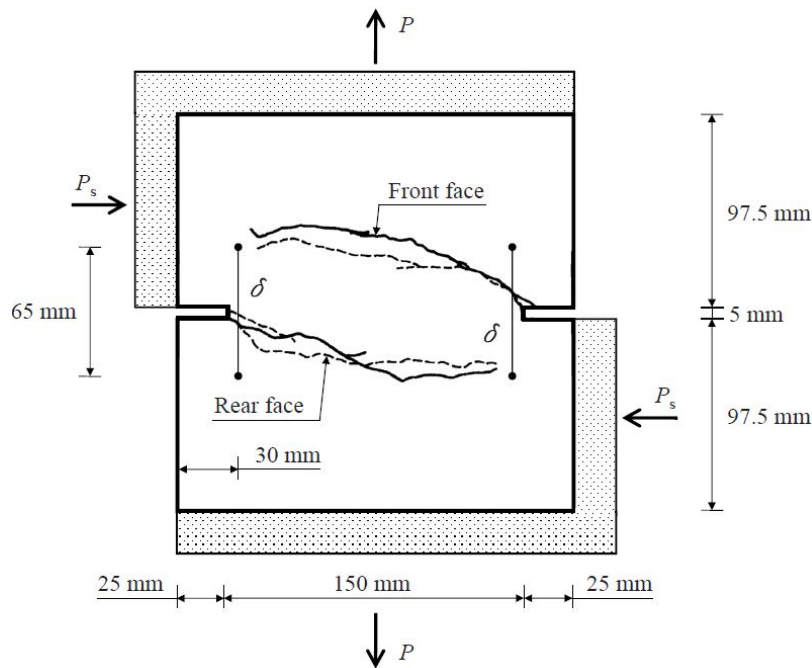
FIGURE 7.14: Geometry of case 3 with all dimensions in mm together with experimental crack pattern and definition of δ, figure taken from Slobbe [71]

Quantity		Value	Unit
Tensile strength	f_t	3.00	N/mm^2
Initial stiffness	E_0	30000	N/mm^2
Poisson's modulus	ν_0	0.20	-
Fracture energy	G_f	0.10	N/mm

TABLE 7.4: Material properties of the double-edge-notched beam specimens, all properties except tensile strength f_t are taken from Nooru-Mohamed [55]

7.4 Case 3: double-edge-notched beam

The next case to be considered is the double-edge-notched beam, often abbreviated by DEN-beam, which has been subjected to several tests with a wide range of load paths by Nooru-Mohamed [55] to study the mixed-mode fracture behaviour of concrete in more detail. In this thesis, the specimens with label '46-05' and '47-01' are studied, which are loaded by non-proportional load-path '4b'. The curved crack pattern of this specific load-path has been used by many authors (e.g. [11, 15, 17, 21, 52, 56, 61, 71]) to validate their approaches. The geometry of the considered specimens is depicted by Figure 7.14 and applied material properties are listed by Table 7.4. The stiffness E_0, Poisson's modulus ν_0 and the mode I fracture energy G_f are taken from Nooru-Mohammed. Following the material properties of most references, a tensile strength $f_t = 3.00\,N/mm^2$ is adopted, which is slightly lower than the tensile strength of $3.80\,N/mm^2$ that is used by Nooru-Mohamed. All specimens have a thickness of $50\,mm$. The combined non-proportional loading and pronounced curved crack path makes load-path '4b' an interesting case to study the differences between the sublayer model and regular SLA, since rotating principal stress states
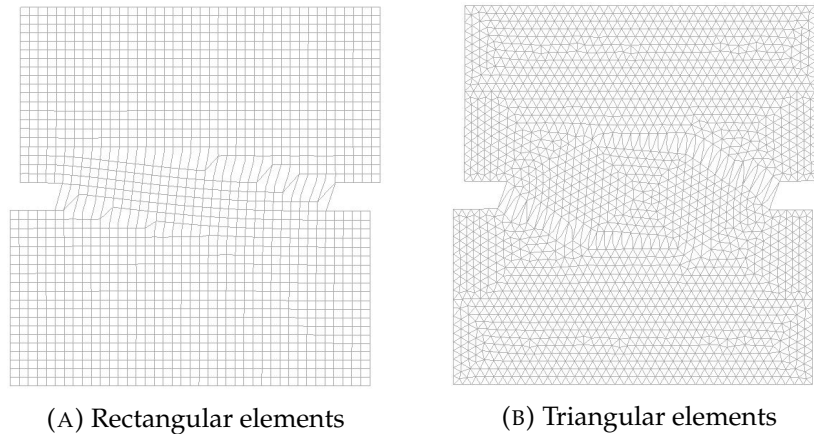
(A) Rectangular elements   (B) Triangular elements

FIGURE 7.15: Finite element model for (A) rectangular elements and
(B) triangular elements in deformed configuration (scaling = 100) cor-
responding to analyses (C) and (E) respectively

are encountered during non-proportional loading. Furthermore, the curved crack pattern also allows for the study of issues related to mesh-directional bias.

During the experiments, loading on the specimens was applied in two stages. In the first stage, a lateral shear loading was applied in displacement control until a load $P_s = 10\,kN$ was reached. Meanwhile, vertical deformations were allowed and therefore $P = 0\,kN$ during the first stage. After reaching a shear load $P_s = 10\,kN$, the lateral load was changed from displacement control to load control, in order to maintain a constant shear load, while increasing the tensile load P under displacement control. During the second load stage, the constant shear load is non-proportional. For modelling purposes, the simplifications as described by Slobbe [71], and later on invoked by Cook et al. [17], are used. The displacement controlled vertical loading requires vertical constraints to the finite element model. However, these restraints are also applied during the first loading stage since it is not possible to change boundary conditions during the analysis, which is obviously not in line with the applied loading during the experiment. Slobbe justifies this simplification by stating that negligible vertical deformations are observed in the experiment during application of the first load stage, such that the influence of the vertical restraints in the first load stage is rather small. The used finite element models are shown by Figure 7.15. The bottom and bottom-right edge are supported and the top-left and upper edge are required to remain planar to simulate the experimental loading as accurate as possible. The lateral shear load is applied as a line load over the top-left edge and the axial displacement controlled load is applied over the full top edge.

Three analyses (A)-(C) with quadrilateral elements and two analyses (D)-(E) with triangular elements are performed, all with element size 5 mm. Three types of integration schemes are considered: reduced integration with linear elements (only for quadrilaterals) and regular integration with both linear and quadratic elements. Hordijk tension softening is applied and crack bands according to a zig-zag crack propagation are used [62]. A detailed overview of all analysis properties can be found in Table C.3. During the experiments, the vertical deformations were measured at specific places. As a quantitative measure, the deformation δ, as defined in Figure 7.14, is averaged over both notches, resulting in $\delta_{average}$. Figure 7.16 entails the vertical load P versus $\delta_{average}$ graphs for all five analyses and experimental bounds. This figure also contains a combined plot of all outputs from the sublayer model, which is compared with a band of NLFEA solutions. This band corresponds

(A) Q8MEM - 1 IP - 5 mm

(B) Q8MEM - 2x2 IP - 5 mm

(C) CQ16M - 2x2 IP - 5 mm

(D) T6MEM - 1 IP - 5 mm

(E) CT12M - 3 IP - 5 mm

(F) Combined for SM
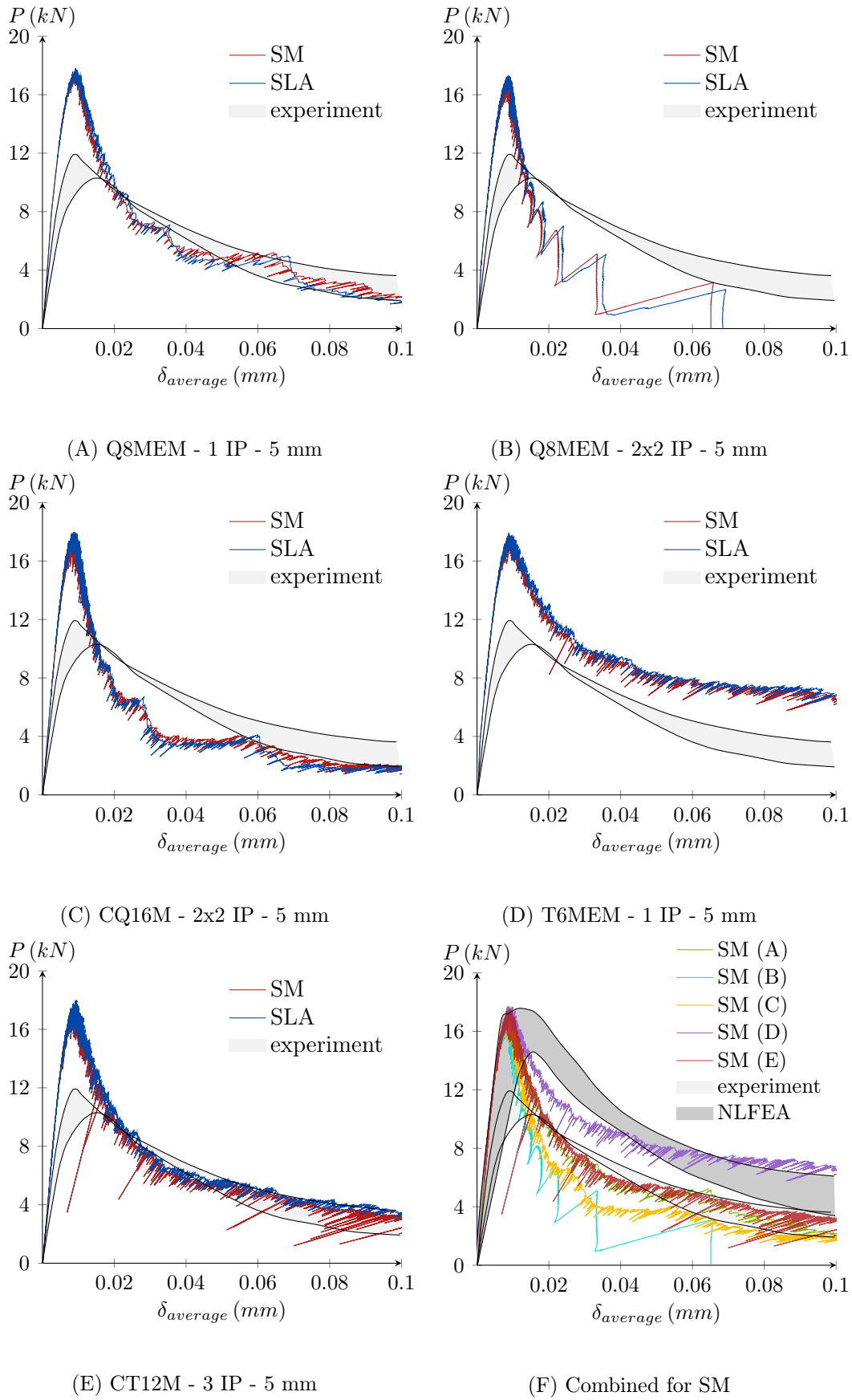
FIGURE 7.16: Load P versus average displacement $\delta_{average}$ for the considered cases (A) till (E) and all combined

(A) SLA: Q8MEM - 1 IP - (A)   (B) SLA: Q8MEM - 2x2 IP - (B)   (C) SLA: CQ16M - 2x2 IP - (C)

(D) SM: Q8MEM - 1 IP - (A)   (E) SM: Q8MEM - 2x2 IP - (B)   (F) SM: CQ16M - 2x2 IP - (C)

FIGURE 7.17: Crack strain plots for both regular SLA and sublayer
model for cases (A)-(C) of the DEN-beam for $\delta_{average} = 0.1\,mm$

(A) SLA: T6MEM - 1 IP - (D)   (B) SLA: CT12M - 3 IP - (E)

(C) SM: T6MEM - 1 IP - (D)   (D) SM: CT12M - 3 IP - (E)

FIGURE 7.18: Crack strain plots for both regular SLA and sublayer
model for cases (D)-(E) of the DEN-beam for $\delta_{average} = 0.1\,mm$

(A) step 701   (B) step 1201   (C) step 1501   (D) step 2101
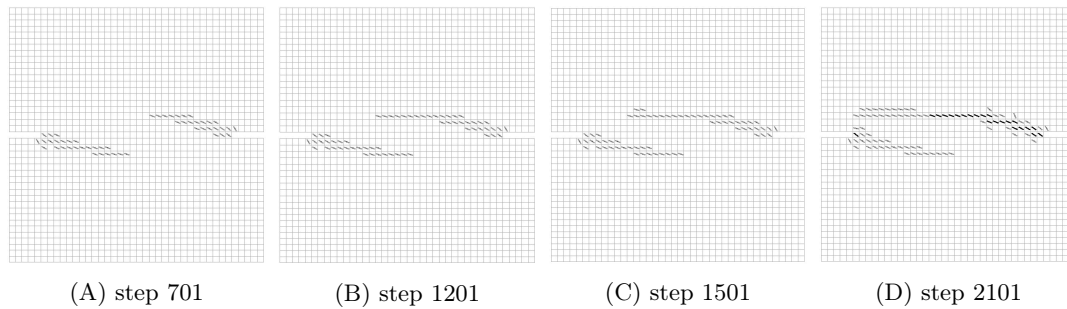
FIGURE 7.19: Zoomed in crack development of regular SLA for analysis (C), showing the development of an asymmetric crack pattern

to the range of solutions that are found by De Borst and Pamin [11] using a continuum plasticity based approach, by Roth et al. [61] based on extended finite element analysis (XFEM) with a crack-tracking algorithm and by Meschke and Dumstorff [52] based on XFEM with energy-based criteria for both the crack propagation and direction, all based on (approximately) the same material properties. The resulting crack patterns for $\delta_{average} = 0.1\,mm$ for both regular SLA and the sublayer model are shown by Figures 7.17 and 7.18. For all analyses, no damage is obtained during the application of the shear load.

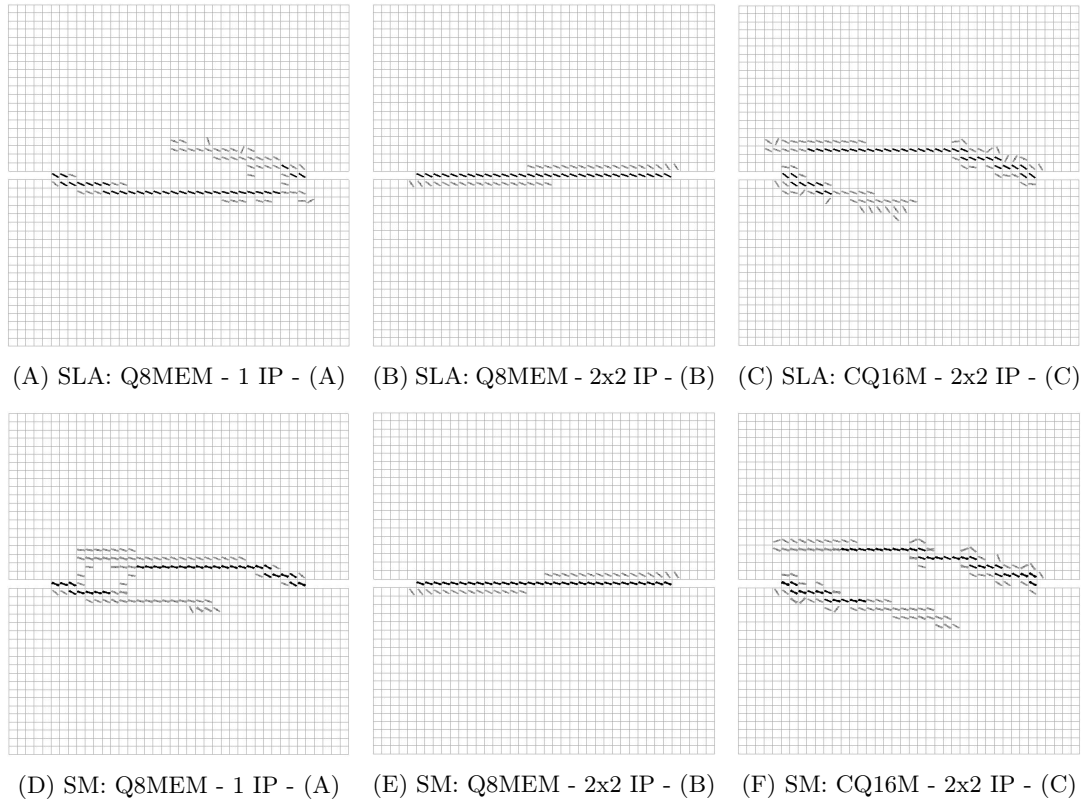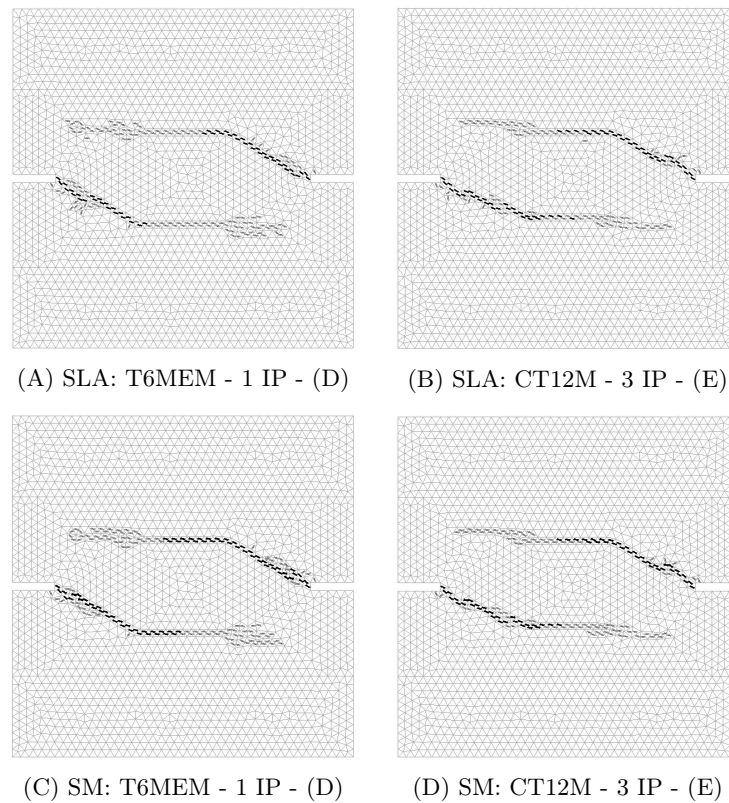The crack patterns of both regular SLA and the sublayer model reveal that linear quadrilateral Q8MEM elements with regular integration, as performed in analysis (B), do not suffice for non-proportional curved crack propagation, in line with the findings for the shear notched beam in Section 7.3. Severe mesh-directional bias seems to cause an incorrect crack path for this type of elements for this case, which was also concluded by DeJong et al. [21], who introduced a random triangular mesh to minimize mesh alignment in the crack pattern. Slobbe et al. [74] concluded as well that linear quadrilateral elements with regular integration are less capable to handle the force transmission along curved and non-aligned cracks and that quadratic elements are more suitable. Using linear quadrilateral elements with reduced integration in analysis (A), effects of mesh-directional bias are reduced and a slightly curved crack pattern is observed, in line with analysis (A) of the shear notched beam. However, a very asymmetric crack pattern develops during crack propagation and a single crack becomes dominant, which is clearly not in line with the experimental crack path that is show by Figure 7.14. Although the sublayer model reduces the level of asymmetry, no proper crack path is found using reduced integration. The simplicity of single integration point elements comes with the inability to accurately describe complex curved crack patterns.

With the aid of quadratic CQ16M elements, a significantly better crack pattern with less asymmetry is obtained for both regular SLA and the sublayer model. The influence of mesh-directional bias seems to be limited by application of quadratic elements. Before further discussion of the differences, the origin of the assymmetric crack pattern is discussed. Figure 7.19 shows the crack development of regular SLA for analysis (C). During the first stage of the analysis, an almost symmetric crack pattern is observed. As discussed in Section 7.2, damage increments can only be performed at one place at a time, leading to asymmetric stress states, potentially causing the gradual development of asymmetric crack patterns. For this case, the same phenomena is observed: the initially symmetric crack path is subjected to small asymmetries that arise inherently for SLA-type of approaches (crack propagation can only take place at one of the notches at a time) and subsequently,
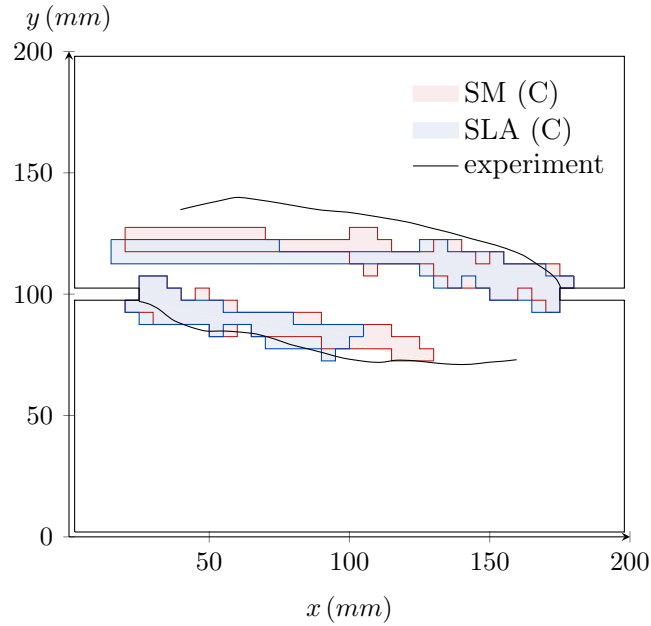
FIGURE 7.20: Comparison of crack paths analysis (C) for $\delta_{average} = 0.1\,mm$ with average experimental crack path [11]

the asymmetry increases during the analysis. The fixed crack model does not allow for any correction of the crack path after the initiation of damage. On the contrary, the sublayer model does allow for rotation of the crack after initiation and in fact counteracts the formation of incorrect asymmetric crack paths for symmetric cases by sequential cracking of the different sublayers with each their own crack direction. Since cracks on sublayer level are fixed, the sublayer model is not able to completely resolve the problems of asymmetric crack development. Figure 7.20 gives a detailed comparison of the crack paths corresponding to analysis (C), including the experimental crack path that is averaged over the front and back of the specimen, taken from [11]. With the aid of the sublayer model, a more symmetric crack path is observed compared to regular SLA, especially in the bottom crack. Furthermore, better agreement with the experimental crack path is found in the upper crack for the sublayer model. The non-proportional loading causes the crack at both notches to show severe rotation, since these cracks were initiated for a shear-dominated load, while a later stage of the analyses is dominated by the axial load. On top of that, slight rotations are observed along the entire crack path.

For analyses (D) and (E), linear and quadratic triangular elements are applied respectively. The triangular mesh is generated such that the experimental crack path is simulated well and very localized crack paths are found for both analyses. In fact, since the mesh is almost in line with the experimental crack, the effects of mesh-directional bias become advantageous for the results, since they force the crack to follow the experimental path (does only make sense when the path is known a priori). With the triangular mesh, hardly no crack rotations and spurious stresses are found and the crack paths of regular SLA and the sublayer model do not show notable differences. Meshes that better suit the crack path seem to reduce differences between both models. Vice versa, worse meshes (e.g. quadrilaterals suffering to mesh-directional bias) seem to increase differences between both models. Since in practice, most meshes are structured and therefore prone to issues related to mesh-directional bias, the latter statement is a very promising feature of the sublayer model.

When quantitatively comparing all load-displacement curves of Figure 7.16, the following is observed:

- All analyses overshoot the experimental peak load, which has also been noted by Slobbe [71] and other references. Some authors therefore reduced some of the properties. When comparing the results with the band of NLFEA-solutions that make use of approximately the same material properties, the same overshoot is obtained. The shape of the NLFEA-band is not followed by both regular SLA and the sublayer model, which might be attributed to the applied Hordijk softening law (the applied NLFEA solutions are based on different internal material laws).

- The incorrect crack pattern of analysis (B) comes with an incorrect load displacement curve as well.

- Analysis (C) is less stiff compared to analysis (A). The crack is better represented by quadratic elements and therefore shows less energy dissipation for both models.

- Analysis (E) shows much more flexible post-peak behaviour than analysis (D), which is the result of a wide localization band in the crack tip for analysis (D) that is not found for analysis (E).

- For all analyses, hardly no differences are found between regular SLA and the sublayer model, despite the pronounced differences in crack paths. The total energy dissipation in the double-edge-notched beam is the superposition of energy dissipation in the two individual cracks. Regular SLA shows 1 fully developed crack and 1 hardly developed crack. The sublayer model more or less shows 2 semi-developed crack. In this way, the total energy dissipation for both regular SLA and the sublayer model is approximately the same and hardly no differences are found in the load-displacement curves. However, the crack paths corresponding to the sublayer model better approximate physical reality.

- In line with the findings of Section 7.3, bigger snap-backs are found for the sublayer model compared to regular SLA, which becomes very clear for analysis (E).

7.5   Case 4: full scale facade

Next, the full scale masonry building that has been tested by Maganes et al. [50] is studied. The building consists of four walls: walls A + B + C, which are connected by an interlocking brick pattern around the corner and should be modelled as a total using 3D or shell elements, and wall D, which is disconnected from perpendicular walls A and C, such that it can be simulated with merely 2D elements. The building, as shown by Figure 7.22A, has been used by several researchers as a benchmark study to investigate the seismic response of masonry buildings [12, 26]. Since SLA is not suitable for cyclic seismic loadings, DeJong et al. [20] performed sequentially linear analyses with monotonically increasing lateral loads using shell elements to capture 3D-effects. In this study, the two-dimensional wall D, with geometry as shown by Figure 7.21, is considered. The masonry facade is 6 meters wide, 6.4 meters high, has a thickness of 0.25 m and represents two stories. The facade is tested

FIGURE 7.21: Geometry of case 4 with all dimensions in cm

Quantity		Value	Unit
Tensile strength	f_t	0.1	N/mm^2
Compressive strength	f_c	-3.0	N/mm^2
Initial stiffness	E_0	1410	N/mm^2
Poisson's modulus	ν_0	0.2	-
Fracture energy tension	$G_{f,t}$	0.05	N/mm
Fracture energy compression	$G_{f,c}$	10.0	N/mm

TABLE 7.5: Material properties of the full scale masonry facade, all
tensile properties are taken from DeJong et al. [20]

and modelled on full scale. Loading on the facade consists of two stages. First, the
floors are loaded by a distributed load of $10\,kN/m^2$, resulting in total vertical loads
of $248.4\,kN$ and $236.8\,kN$ at the first and second floor respectively. The floors rest
on beams, which are connected to walls B and D, such that half of the floor load is
carried by each facade. In the second load stage, the building is loaded by a mono-
tonically increasing lateral load P_c at both floors to simulate the static equivalence of
seismic action (in the analysis of DeJong both forces have the same magnitude in line
with a mass-proportional pushover analysis, contrary to a modal pushover analysis,
in which the dominant eigen-mode is followed). Meanwhile, the vertical floor load
is maintained and hence, non-proportional loading is applied.

    The masonry is modelled on macro-scale, meaning that the masonry is treated
as a continuum. Tensile properties, stiffness and Poisson's modulus are taken from
DeJong et al. [20]. They obtained a stiffness of 1410 MPa by an iterative process
of linear elastic analyses to determine the stiffness which provides a response that
intersects the experimental cyclic envelope at 75% of the maximum base shear force.
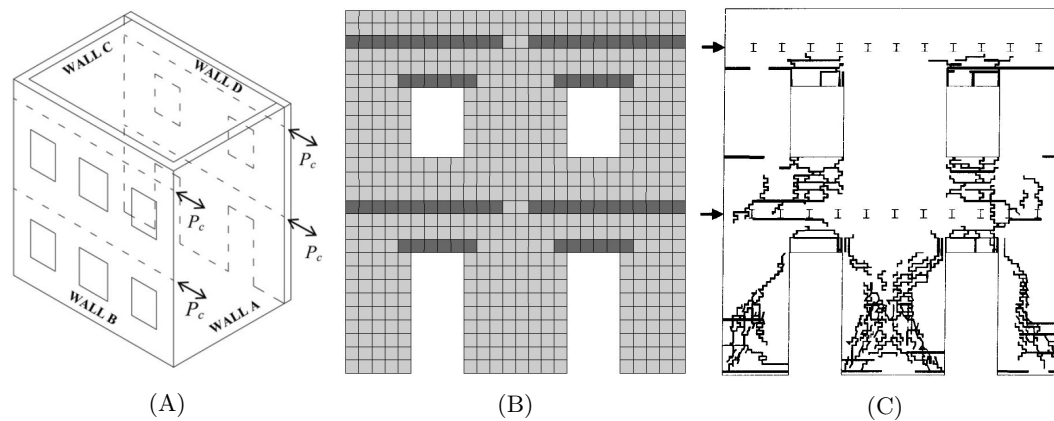Furthermore, they obtained the tensile strength from the average mortar shear and

FIGURE 7.22: Finite element model of (A) wall D of total building with (B) elastic zones (dark gray) in areas where no cracks were observed in (C) experiment at ultimate displacement (23 mm) [50]

tensile strengths, as cracks are expected to grow in the weakest link, being the mortar. In line with the study of DeJong, linear tension softening is assumed. In this study, the facade is loaded till its ultimate state and therefore, compressive crushing is expected at the right pillar. To that end, the masonry wall is given a compressive strength of 3.0 MPa, compressive fracture energy of 10.0 N/mm (the exact properties are not of interest for this rather qualitative study) and compressive hardening according to Feenstra (Section 2.3.5) is applied. The framework of Section 5.5 is used: sublayer properties are generated based on the ripple-band saw-tooth law in tension and subsequently, compressive strength properties of the generated sublayers are determined based on the tensile sublayer stiffnesses.

The facade is modelled using quadrilateral elements with an element size of 230 mm, as can be seen in the finite element mesh in Figure 7.22B. Crack bands are applied according to a zig-zag pattern [62]. Vertical loads are applied as line loads along the height of the two stories. Above the openings, lintels were placed in the facade and hence, no cracks are expected here. Furthermore, no cracks were observed along the floor supports at the facade. For that purpose, some parts of the model are assigned linear material behaviour (dark gray in the shown finite element model), in line with DeJong et al. Linear elastic behaviour is desirable at points of loading to limit spurious cracks due to load introduction. The facade is supported at the bottom in both horizontal and vertical direction.

Three analyses (A)-(C) are performed for both regular SLA and the sublayer model: linear elements with reduced integration and linear and quadratic elements with regular integration. Detailed information on all analyses can be found in Table C.4. The top displacement is monitored and plotted against the base shear force V, which is twice the lateral load P_c, for all analyses in Figure 7.23. In the experiment, the facade was loaded by an increasing cyclic load. For the purpose of qualitative comparison, the backbone curve of the cyclic envelope is shown as well. For analysis (A), the crack pattern at the moment that the base shear force reduced to $V = 10\,kN$ is shown by Figure 7.24. For analyses (B) and (C), the crack patterns are given in Figures 7.25 and 7.26 respectively for 1) the moment that the top displacement reaches $23\,mm$, in line with the ultimate displacement of the experiment, and 2) the moment that the shear force reduced to $10\,kN$. The states corresponding to the crack strain snap-shots are marked within the load-displacement curves with green dots for the sublayer model and yellow dots for regular SLA.
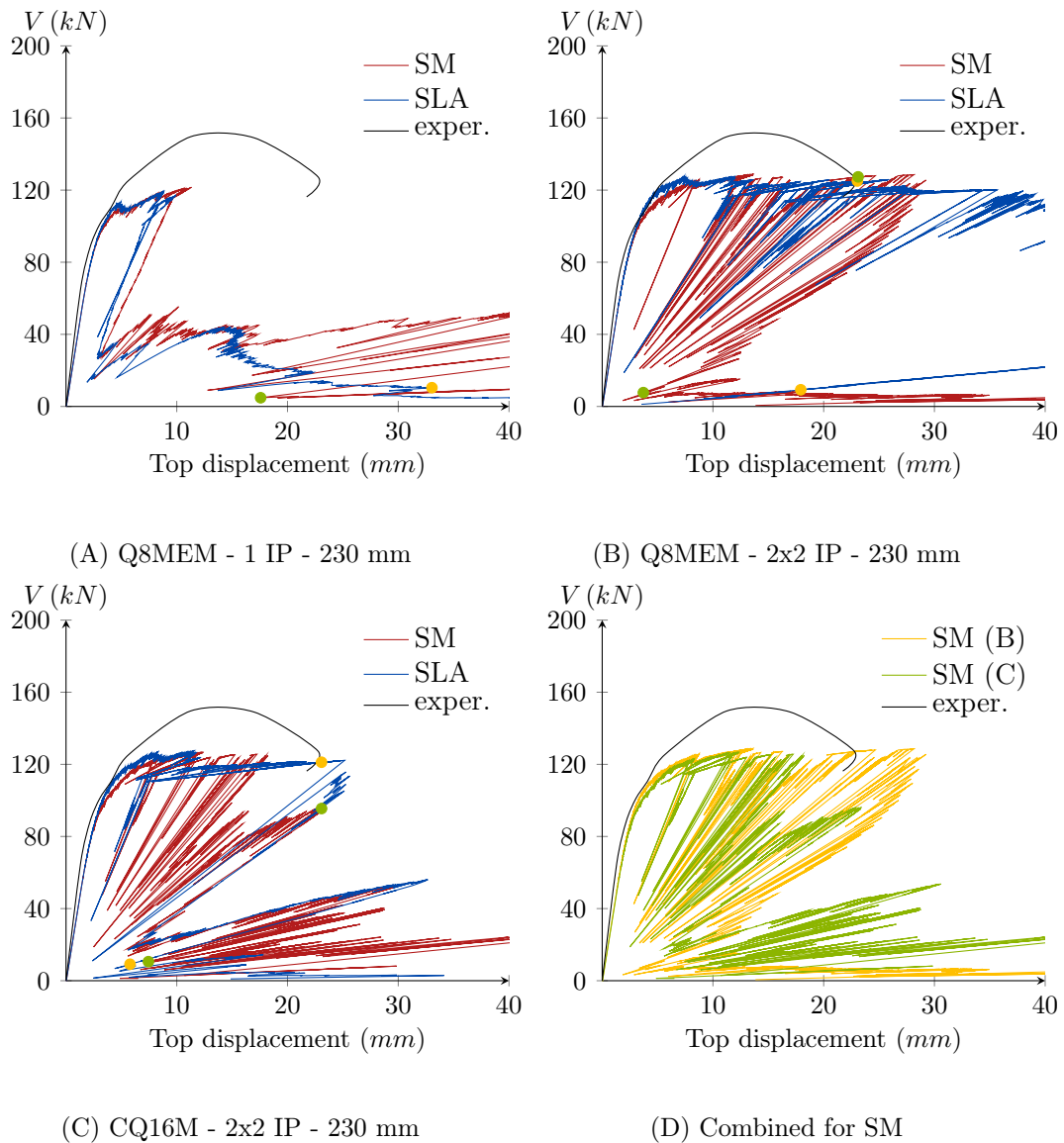
(A) Q8MEM - 1 IP - 230 mm

(B) Q8MEM - 2x2 IP - 230 mm

(C) CQ16M - 2x2 IP - 230 mm

(D) Combined for SM

FIGURE 7.23: Total base shear force *V* versus the top displacement for the considered cases (A) till (C) and all combined. Crack strain snap-shots are given for locations with green and yellow dots, corresponding to the sublayer model and regular SLA respectively
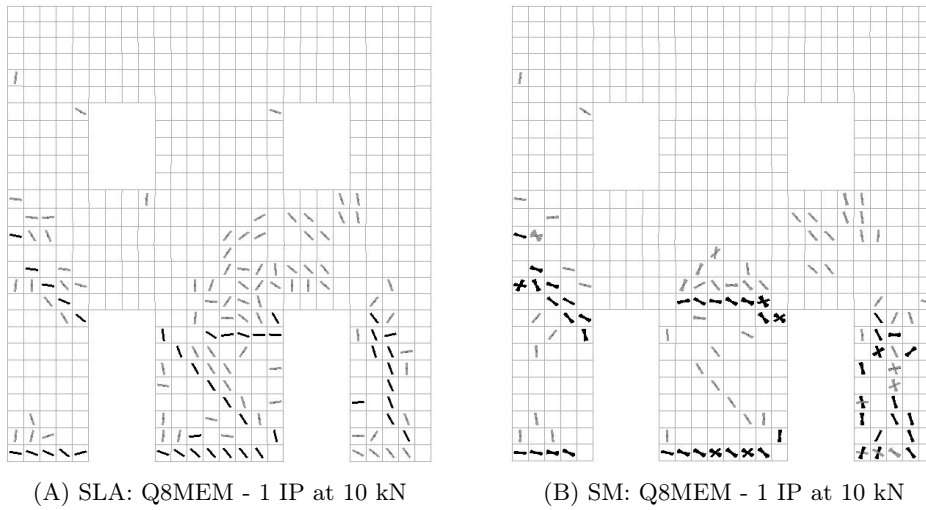
(A) SLA: Q8MEM - 1 IP at 10 kN   (B) SM: Q8MEM - 1 IP at 10 kN

FIGURE 7.24: Crack strain plots for analysis (A) for both regular SLA
and the sublayer model

(A) SLA: Q8MEM - 2x2 IP at 23 mm   (B) SM: Q8MEM - 2x2 IP at 23 mm

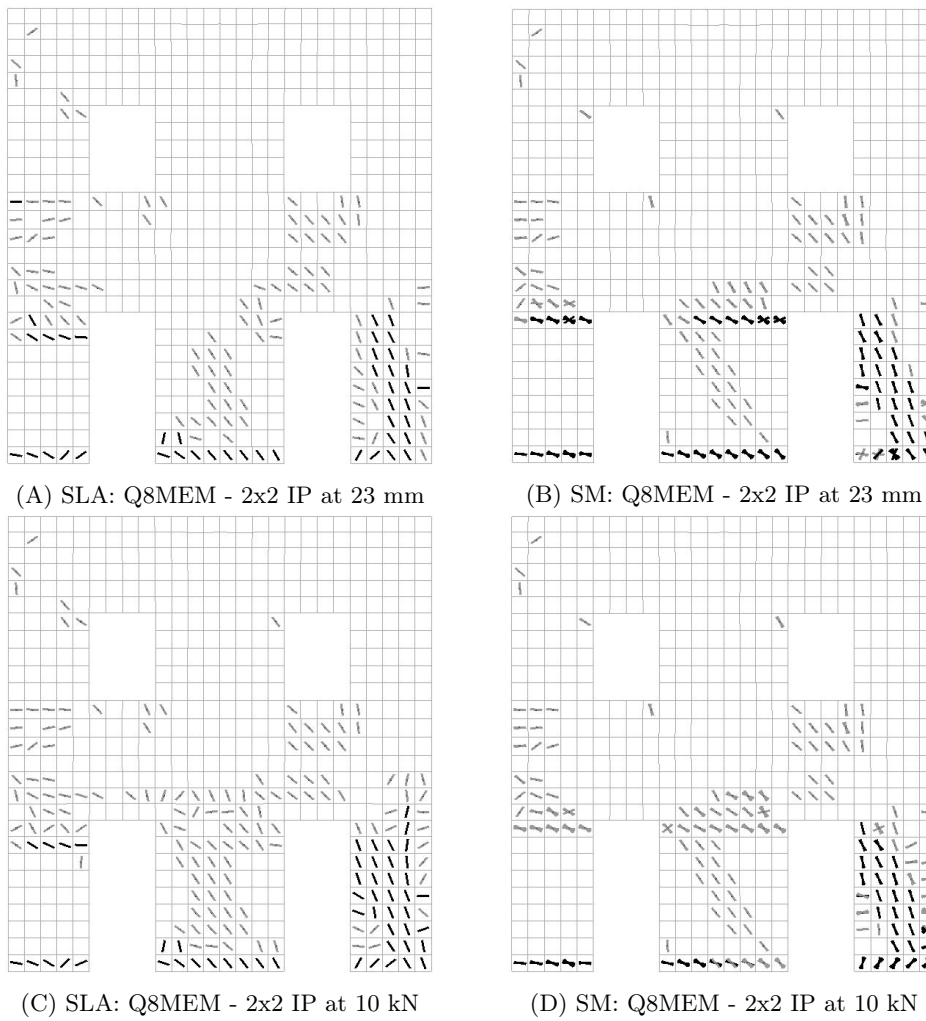(C) SLA: Q8MEM - 2x2 IP at 10 kN   (D) SM: Q8MEM - 2x2 IP at 10 kN

FIGURE 7.25: Crack strain plots for analysis (B) for both regular SLA
and the sublayer model at a top displacement of 23 mm and at a base
shear force of 10 kN

(A) SLA: CQ16M - 2x2 IP at 23 mm

(B) SM: CQ16M - 2x2 IP at 23 mm

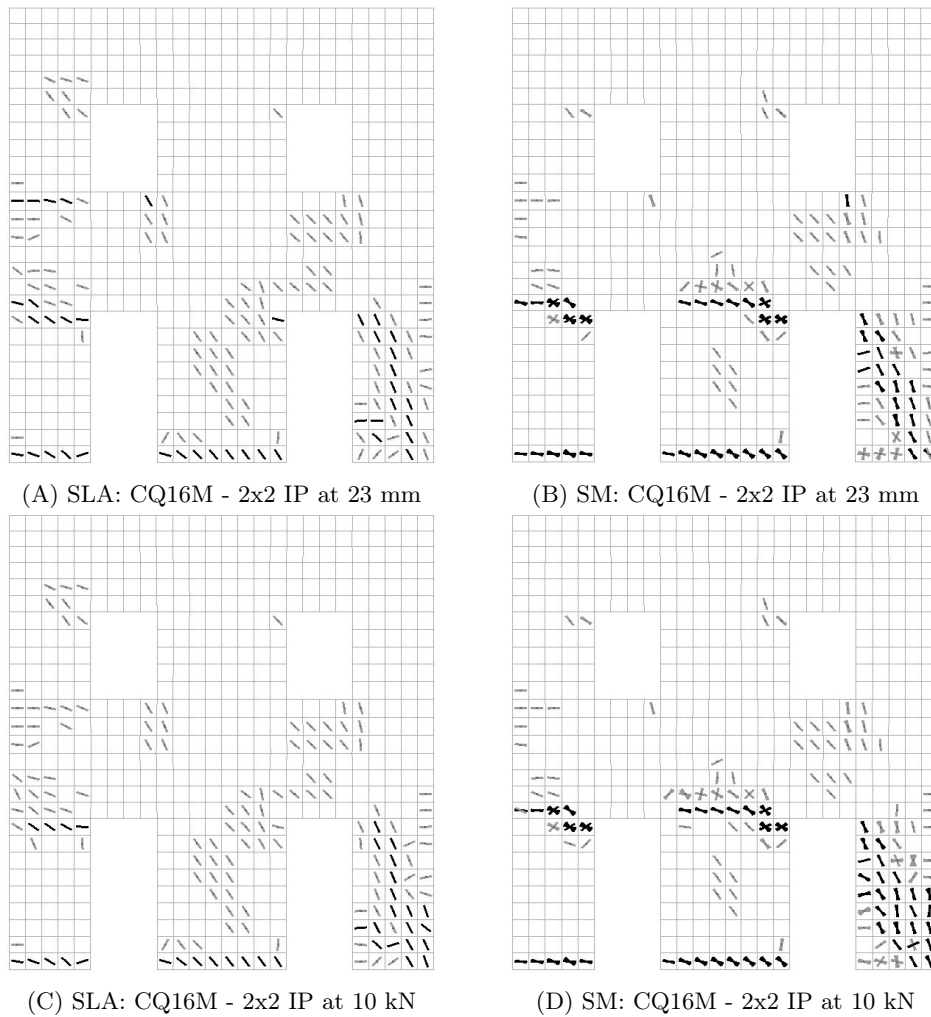(C) SLA: CQ16M - 2x2 IP at 10 kN

(D) SM: CQ16M - 2x2 IP at 10 kN

FIGURE 7.26: Crack strain plots for analysis (C) for both regular SLA
and the sublayer model at a top displacement of 23 mm and at a base
shear force of 10 kN

From the results can be concluded that linear elements with reduced integration, as performed in analysis (A), do not suffice for this rather complex case. Premature failure is found at the left pillar, which is clearly not in line with the experimental crack path. Furthermore, an incorrect load-displacement curve is found for both regular SLA and the sublayer model. Apparently, elements with reduced integration are too simple and do not allow for an accurate description of diffuse crack patterns. It is however noted that the sublayer model generates less spurious cracks, especially in the center part above the doors.

Next, the results of analyses (B) and (C) are discussed by a stepwise description of the crack propagation. During the first load stage, no damage occurs. After application of the lateral loading, cracks start to open at the left bottom corner of the building and at the left top corners of the doors. Shear cracks develop in the center pillar between the doors and the left corner cracks at the doors further propagate. For the sublayer model, the left corner crack of the right door tends to localize and follow the mesh for both analyses (B) and (C), where a completely different crack is observed for regular SLA and during the experiment (see Figure 7.22C). The lateral load results in a rocking type of deformation and tensile damage is observed along

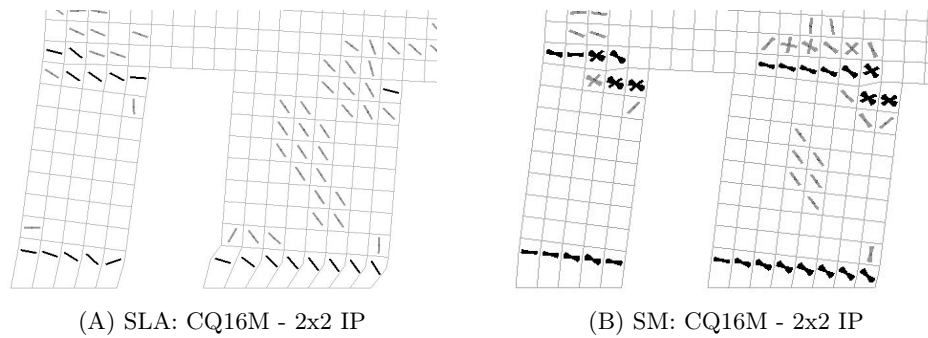(A) SLA: CQ16M - 2x2 IP   (B) SM: CQ16M - 2x2 IP

FIGURE 7.27: Detailed view on different deformed state regular SLA
compared to sublayer model for a top displacement of 23 mm

the entire bottom row of elements for the left and center pillar. Furthermore, compressive damage is found at the right bottom corner of the building and at the right bottom element of the center pillar for both regular SLA and the sublayer model. Subsequently, the complete load carrying capacity is taken over by the right pillar, as the other two pillars are effectively disconnected from the supports. A shearing type of deformation is observed in the right pillar, causing the development of a tension tie and compressive strut. For the sublayer model, secondary perpendicular compressive cracks are found along the compressive strut, after the formation of primary tensile cracks along the tension tie. On the contrary, the fixed crack model of regular SLA does not allow for development of compressive cracks here, since the fixed tensile cracks are directed almost vertically (where the sublayer model gradually rotates here), restraining the development of secondary perpendicular compressive cracks as the perpendicular crack direction is not in line with the compressive strut. Ultimately, the tensile tie further develops and the complete load-carrying capacity of the facade is released. The obtained crack pattern is qualitatively in line with the experimental results when only considering the cracks that follow from a lateral load pushing to the right. The tensile tie at the outer pillar and the shear cracks in the center pillar are correctly predicted. Furthermore, most cracks around doors and windows are predicted as well.

Despite the similarities between the crack patterns and load-displacement curves of regular SLA, the sublayer model and the experiment, some severe differences are obtained. Relevant differences are mentioned and briefly discussed below:

- During the first 7-8 mm of the load-displacement graphs, small differences are found: the base shear force of the sublayer model is roughly 5% lower than for regular SLA, as a result of local crack rotation. This rotation is mainly observed in the bottom row of elements and at the left top corners of the doors. In line with Chapter 6, more flexible behaviour is obtained with the sublayer model, although the differences are rather small.

- Pronounced differences between the two models are found at the center pillar between the doors. Figure 7.27 entails a close-up view on the deformed structure for analysis (C) for both models. The deformation in the bottom row of elements is a combination of bending (lateral loads causing a bending moment) and shearing (transmission of shear load to the support). For regular SLA, this deformation seems to be shear-dominated and for the sublayer model, deformation of the bottom row seems to be bending-dominated. Based on the crack rotation, it is concluded that at crack initiation, shear deformation is dominant and that during crack development, bending deformation becomes dominant.

The fixed crack model of regular SLA does not allow for this changing stress state, while the sublayer model does allow for this. The bending deformation of the sublayer model at the bottom row requires the formation of a localized crack at the top left edge of the right door (due to severe rotation of the center pillar), which is not observed for regular SLA.

- As a result of the different crack pattern at the left corner of the right door, significant differences are found in the load-displacement graphs. For linear elements with regular integration in analysis (B), differences become most clear. Instead of damage propagation in the right pillar leading to ultimate failure, the damage propagates at the left corner of the right door for regular SLA, leading to unrealistic top displacements up to 120 mm.

- The diffuse crack pattern combined with the non-proportional loading make this case very susceptible to stress-reversal and crack closure. In load - displacement curves, crack closure effects are revealed by sharp snap-backs with a stiffness deviating significantly from the secant stiffness (even an almost horizontal snap-back is possible). When reviewing the load-displacement curves of Figure 7.23, clear crack closure effects are observed, especially for SLA. The fixed crack direction seems to cause issues when combined with diffuse crack patterns and non-proportional loading. The sublayer model offers much more adaptability, since consecutive sublayers can adapt to changing stress states. In this way, the effects of crack closure are reduced (but not resolved) when making use of the sublayer model.

- For analysis (C), different ultimate collapse mechanisms are generated, as can be seen in Figures 7.26C and D. The right pillar ultimately fails very abruptly due to a horizontal crack near the support for regular SLA, where the sublayer model results in a fully developed diagonal band of tensile fracture causing ultimate collapse, which is more in line with physical reality. The fixed crack model can not adapt itself to develop a diagonal tensile band, in line with the inability to develop a strut with compressive damage. The severe crack rotations in Figure 7.26D indicate that significant crack rotations took place. During the final stage, no constitutively allowable stress state can be reached without reduction of the non-proportional constant vertical load. Therefore, the last successful combination of non-proportional and proportional loading is reduced by a constant load multiplier λ_{const}, which has been discussed in Section 3.5. Figure 7.28 plots the constant load multipliers for analyses (B) and (C). For analysis (C), a more gradual reduction of the constant load factor is found for the sublayer model due to the gradual development of the diagonal crack band. For SLA, abrupt failure is found due to locked-in and stiff behaviour. It is noted that the graphs are hard to compare, since the analyses show different failure mechanisms.

- In general, more localization effects are observed for the sublayer model, which is in the nature of the model. During crack propagation, the crack direction can be corrected for and therefore, very narrow banded crack bands are found. However, for cases with diffuse crack patterns (e.g. with multiple macro cracks and wide localization zones), this is not necessarily favourable, since the nature of the sublayer model does not really allow for the development of local diffuse crack patterns, marking a clear contradiction. Furthermore, influence of mesh-directional bias seems to be more pronounced for the sublayer model for this case, which can for example be observed at the left corners of the doors.

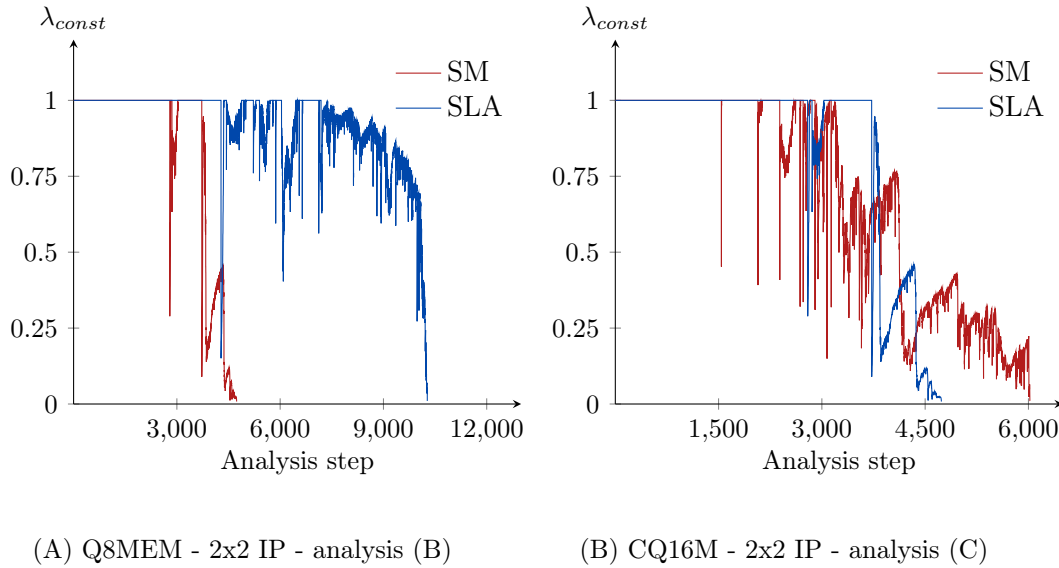(A) Q8MEM - 2x2 IP - analysis (B) (B) CQ16M - 2x2 IP - analysis (C)

FIGURE 7.28: Comparison of constant load factor λ_{const} for analysis (B) and (C) for both regular SLA and sublayer model

From this case study it can be concluded that the sublayer model locally encounters difficulties with diffused crack patterns, since the model inherently results in localization. On top of that, it is even questionable whether crack rotation takes place within the small lines of mortar between bricks. Diffused crack patterns seem to be better described by regular SLA. However, both analyses (B) and (C) showed that globally, regarding the collapse mechanism, crack-closure effects and non-proportional loading, the sublayer model offers more flexibility and adaptability to changing stress states. For both analyses, regular SLA predicted an unrealistic collapse mechanism, while for the sublayer model the collapse mechanisms for both analyses were in good agreement with each other and with physical reality. Compared to the results of DeJong et al. [20], the crack patterns qualitatively agree, although lower peak base shear loads are found in this study.

7.6 Case 5: concrete dam

In this section, the application of SLA and the sublayer model to simulate the behaviour of unreinforced concrete gravity dams is studied. First, a scaled concrete dam with proportional loading is considered in Section 7.6.1, followed by the full scale Koyna Dam under non-proportional loading in Section 7.6.2.

7.6.1 Case 5a: scaled concrete dam with proportional loading

During the years, the experiments performed by Carpinteri et al. [13] have been simulated by many authors (e.g. [7, 27, 46, 61]). In the experimental program, two scaled down 1:40 models of a concrete gravity dam, with geometry as shown in Figure 7.29, were subjected to lateral loading, representing a hydrostatic pressure along the upstream side of the dam. Initially, the goal of the experimental program was to include a certain multiplier of the self-weight (to account for scale-effects) as well in the loading. However, a test including simulation of self-weight had to be stopped prematurely. Hence, the scaled concrete dam is loaded by a proportional load. In this study, 'test 3' with a notch/depth ratio of 0.2 is simulated. The specimen
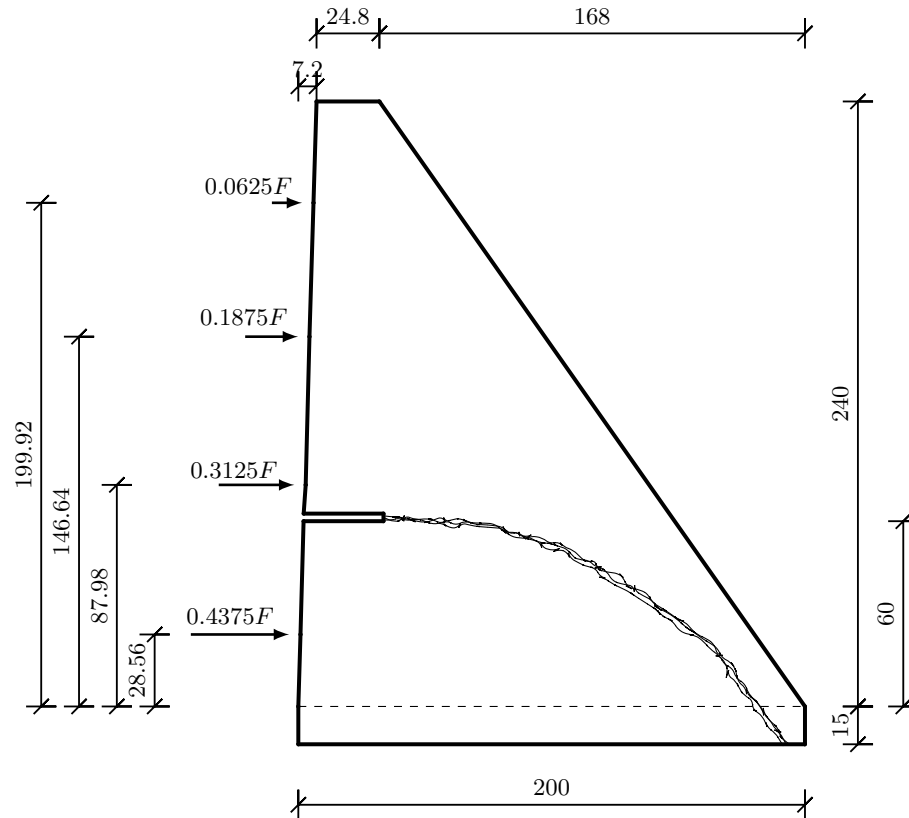
FIGURE 7.29: Geometry of case 5a with all dimensions in cm

Quantity		Value	Unit
Tensile strength	f_t	3.6	N/mm^2
Initial stiffness	E_0	35700	N/mm^2
Poisson's modulus	ν_0	0.10	-
Fracture energy	G_f	0.184	N/mm

TABLE 7.6: Material properties of the scaled concrete dam, taken from
the experiments by Carpinteri et al. [13]

has a thickness of 30 *cm* and material properties are taken from Carpinteri et al. and
listed in Table 7.6. In an attempt to simulate the experiment as accurate as possible,
Hordijk tension softening is assumed. During the experiment, a curved crack path
propagating towards the downstream bottom side of the dam is observed according
to Figure 7.29.

In line with the given references, the hydrostatic pressure at the dam is simulated
with the aid of 4 equivalent lateral point loads, such that *F* equals the integrated hy-
drostatic pressure over the height of the dam. Lateral and vertical displacements
are restrained at the bottom of the specimen. Figure 7.30 entails the four types of
meshes that are used: quadrilaterals with element sizes 30 and 60 mm and trian-
gular elements with sizes 30 and 60 mm as well. In order to reduce computational
efforts, nonlinear material behaviour is only assigned to the light-gray part of the
meshes. Following the trend of previous cases, an analysis is performed with linear
Q8MEM elements with reduced integration. As can be seen in Figure 7.31, spurious
kinematic modes are found below the notch immediately: rectangular elements with

(A) Quadrilat. 60 mm   (B) Quadrilat. 30 mm   (C) Triangular 60 mm   (D) Triangular 30 mm
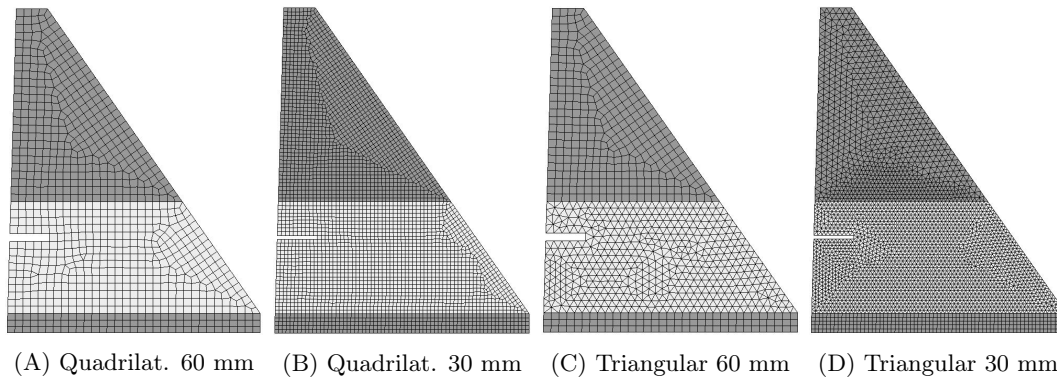
FIGURE 7.30: Overview of the meshes with quadrilateral/triangular elements with size 60/30 mm
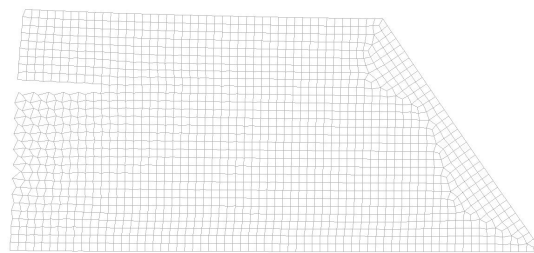

FIGURE 7.31: Spurious kinematic mode that is obtained for Q8MEM elements with reduced integration (element size 30 mm)

a single integration point are not able to correctly describe the vertical and horizontal deformations of all four nodes for certain cases. Apparently, the element type allows for this specific case for the generation of a spurious kinematic mode. Since the concrete dam has a small slope on the left edge, no perfectly rectangular elements are found in the mesh, probably also contributing to the inconvenient results for reduced integration.

For all four meshes, analyses with linear and quadratic elements are performed, leading to a total of eight analyses (A)-(H). Detailed information on all analyses can be found in Table C.5. The crack mouth opening displacement (CMOD) is monitored and plotted against the lateral load *F* for quadrilateral analyses (A)-(D) and triangular analyses (E)-(G) in Figures 7.32 and 7.34 respectively. In these figures, two bands of NLFEA solutions are also shown for comparison: 1) the band of results by Ghrib and Tinawi [27], obtained with the aid of both isotropic and anisotropic damage smeared crack formulations and 2) the band of results by Roth et al. [61] obtained by XFEM analyses with a crack-tracking algorithm. Both studies are based on the same material properties that are used in this study. Furthermore, the experimental results are included as well [13]. The corresponding crack-strain plots for a CMOD of 2 mm for analyses (A)-(D) and (E)-(G) are found in Figures 7.33 and 7.35 respectively.

First, the results obtained by quadrilateral elements in analyses (A)-(D) are discussed. For a coarse mesh with linear elements in analysis (A), two crack tips are found for regular SLA. Although the sublayer model restricts the formation of a second crack path, both models fail to accurately describe the crack path: both paths are mainly dominated by the mesh alignment. In line with the shear notched beam and double-edge-notched beam, severe issues related to mesh-directional bias are observed for linear elements with regular integration. Although the finer mesh of
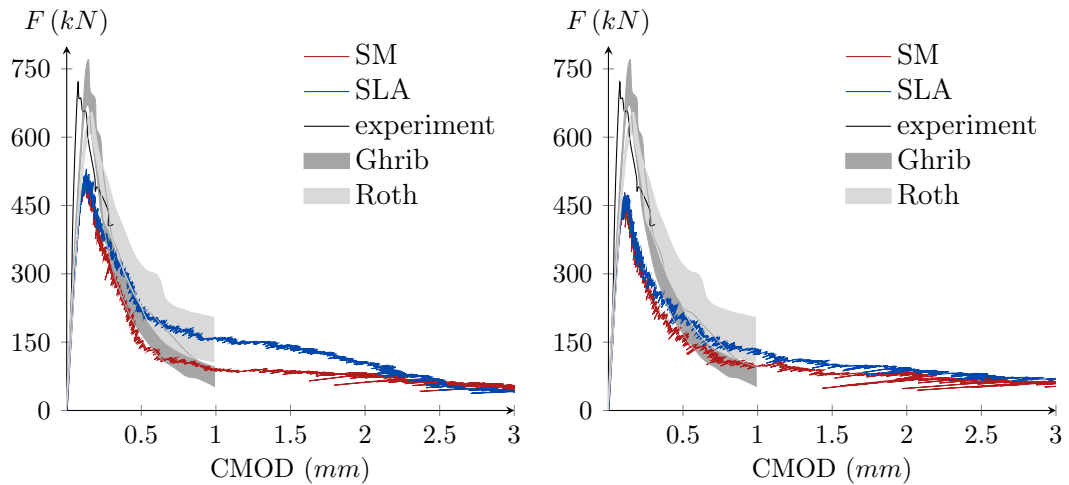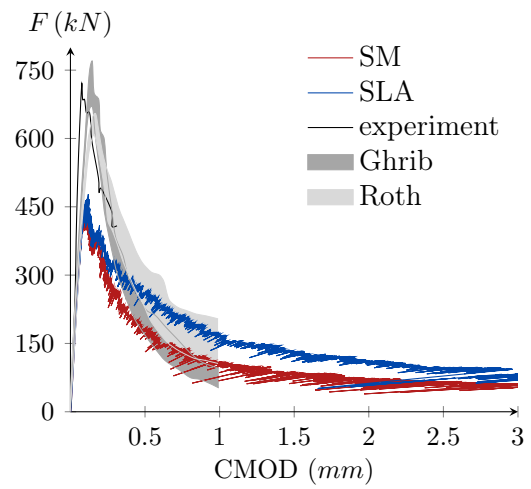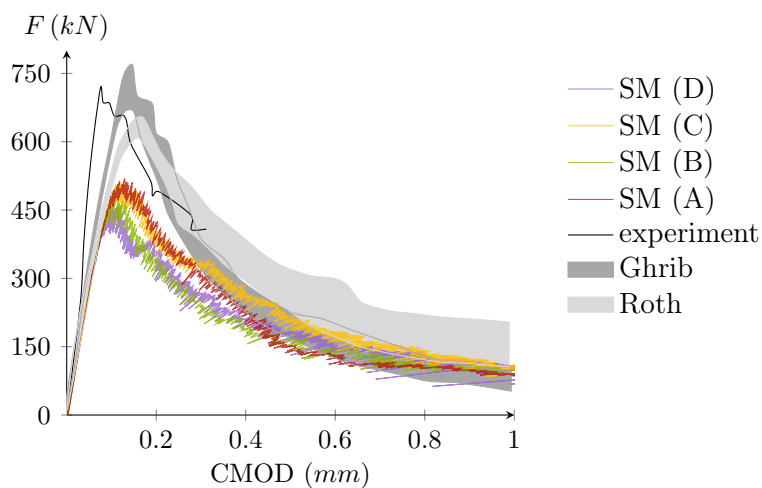
(A) Q8MEM - 60 mm - analysis (A)

(B) CQ16M - 60 mm - analysis (B)
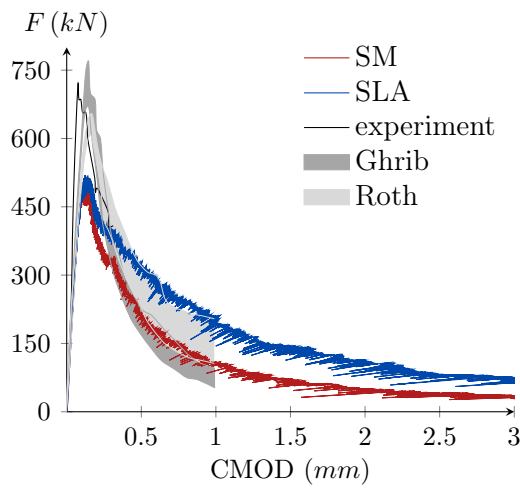
(C) Q8MEM - 30 mm - analysis (C)

(D) CQ16M - 30 mm - analysis (D)

(E) Combined for SM

FIGURE 7.32: Load F versus CMOD for the considered cases (A) till
(D) and all combined

(A) SLA: Q8MEM - 60 mm - analysis (A)

(B) SM: Q8MEM - 60 mm - analysis (A)

(C) SLA: CQ16M - 60 mm - analysis (B)

(D) SM: CQ16M - 60 mm - analysis (B)

(E) SLA: Q8MEM - 30 mm - analysis (C)

(F) SM: Q8MEM - 30 mm - analysis (C)

(G) SLA: CQ16M - 30 mm - analysis (D)

(H) SM: CQ16M - 30 mm - analysis (D)

FIGURE 7.33: Crack strain plots for analysis (A)-(D) for both regular SLA and the sublayer model at a crack mouth opening displacement (CMOD) of 2 mm

(A) T6MEM - 60 mm - analysis (E)

(B) CT12M - 60 mm - analysis (F)

(C) T6MEM - 30 mm - analysis (G)

(D) CT12M - 30 mm - analysis (H)

(E) Combined for SM

FIGURE 7.34: Load F versus CMOD for the considered cases (E) till (H) and all combined

(A) SLA: T6MEM - 60 mm - analysis (E)

(B) SM: T6MEM - 60 mm - analysis (E)

(C) SLA: CT12M - 60 mm - analysis (F)

(D) SM: CT12M - 60 mm - analysis (F)

(E) SLA: T6MEM - 30 mm - analysis (G)

(F) SM: T6MEM - 30 mm - analysis (G)

(G) SLA: CT12M - 30 mm - analysis (H)
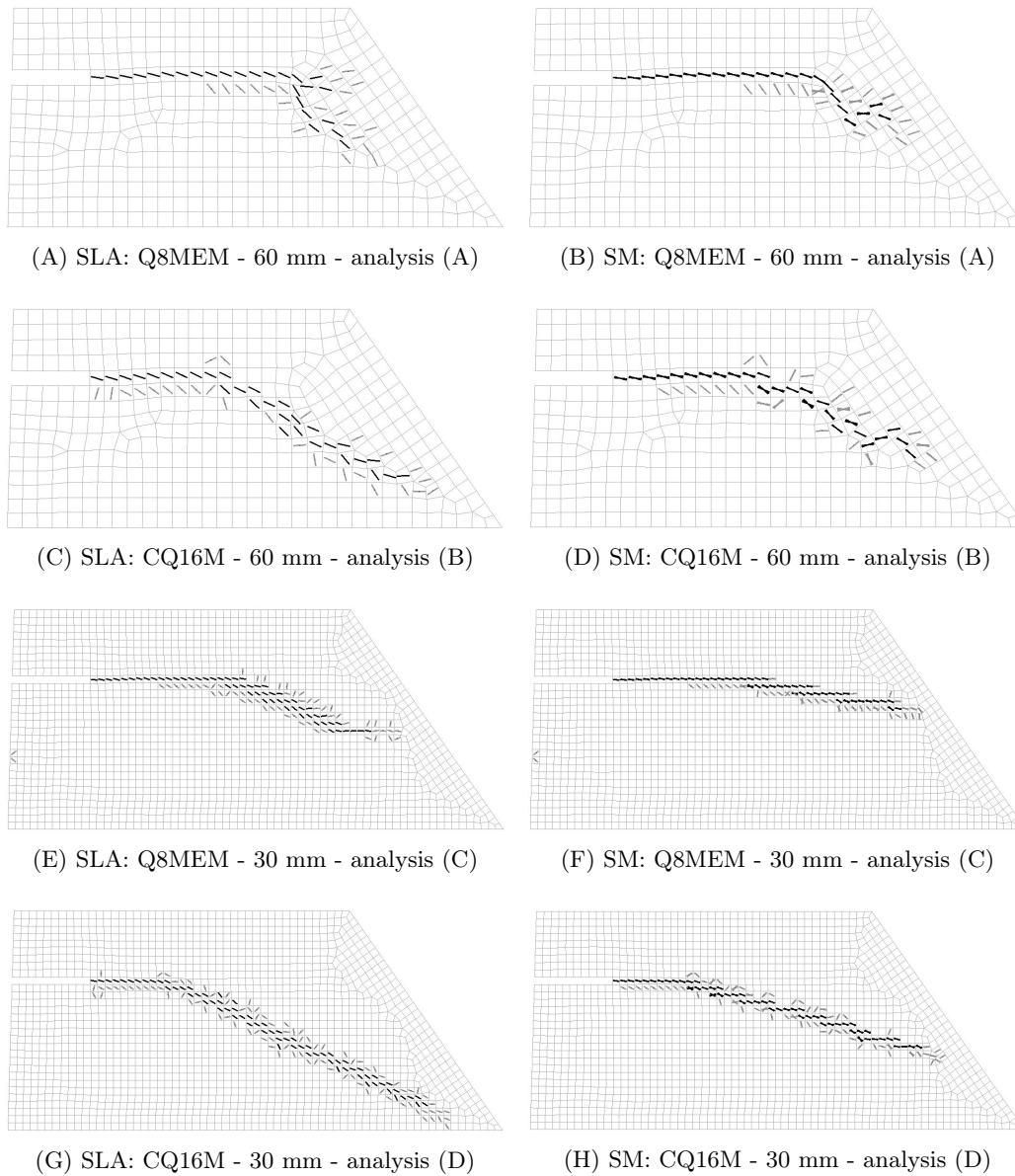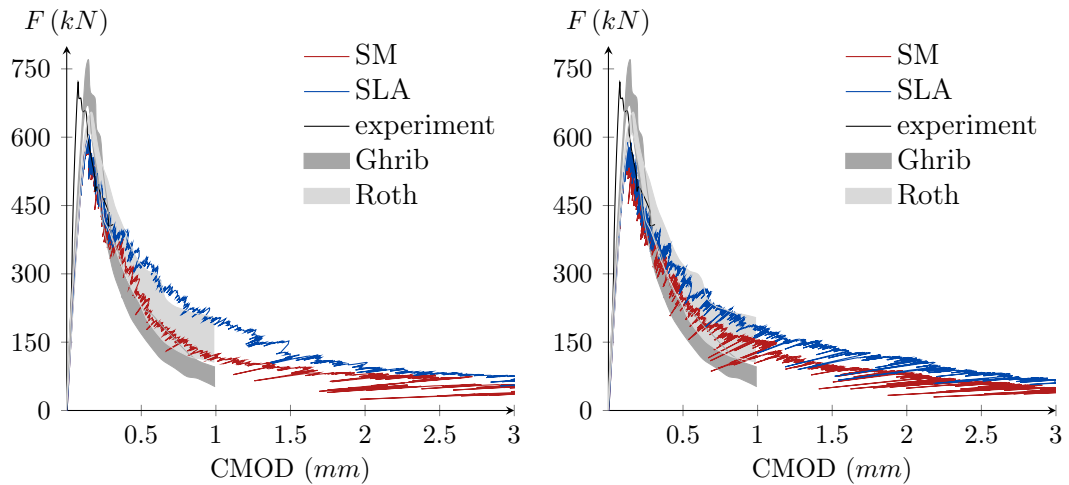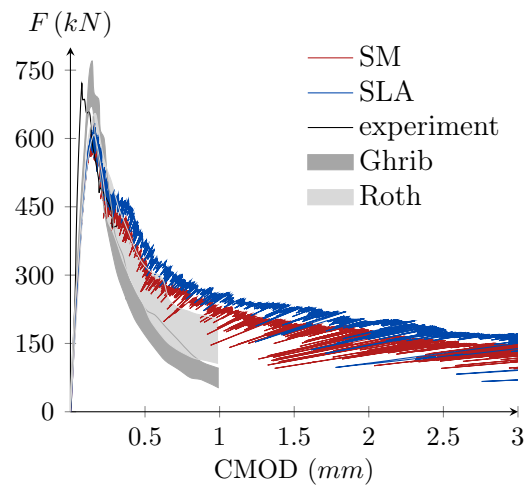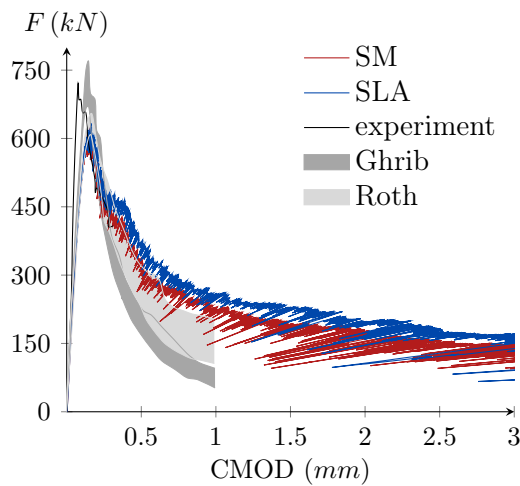
(H) SM: CT12M - 30 mm - analysis (H)

FIGURE 7.35: Crack strain plots for analysis (E)-(H) for both regular
SLA and the sublayer model at a crack mouth opening displacement
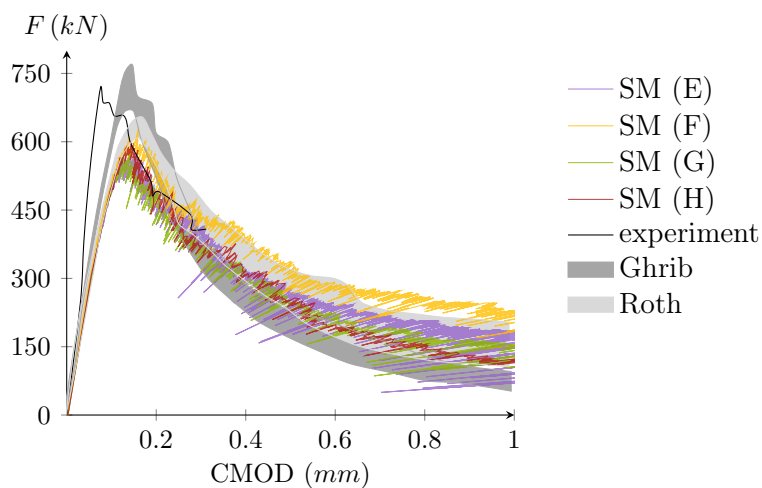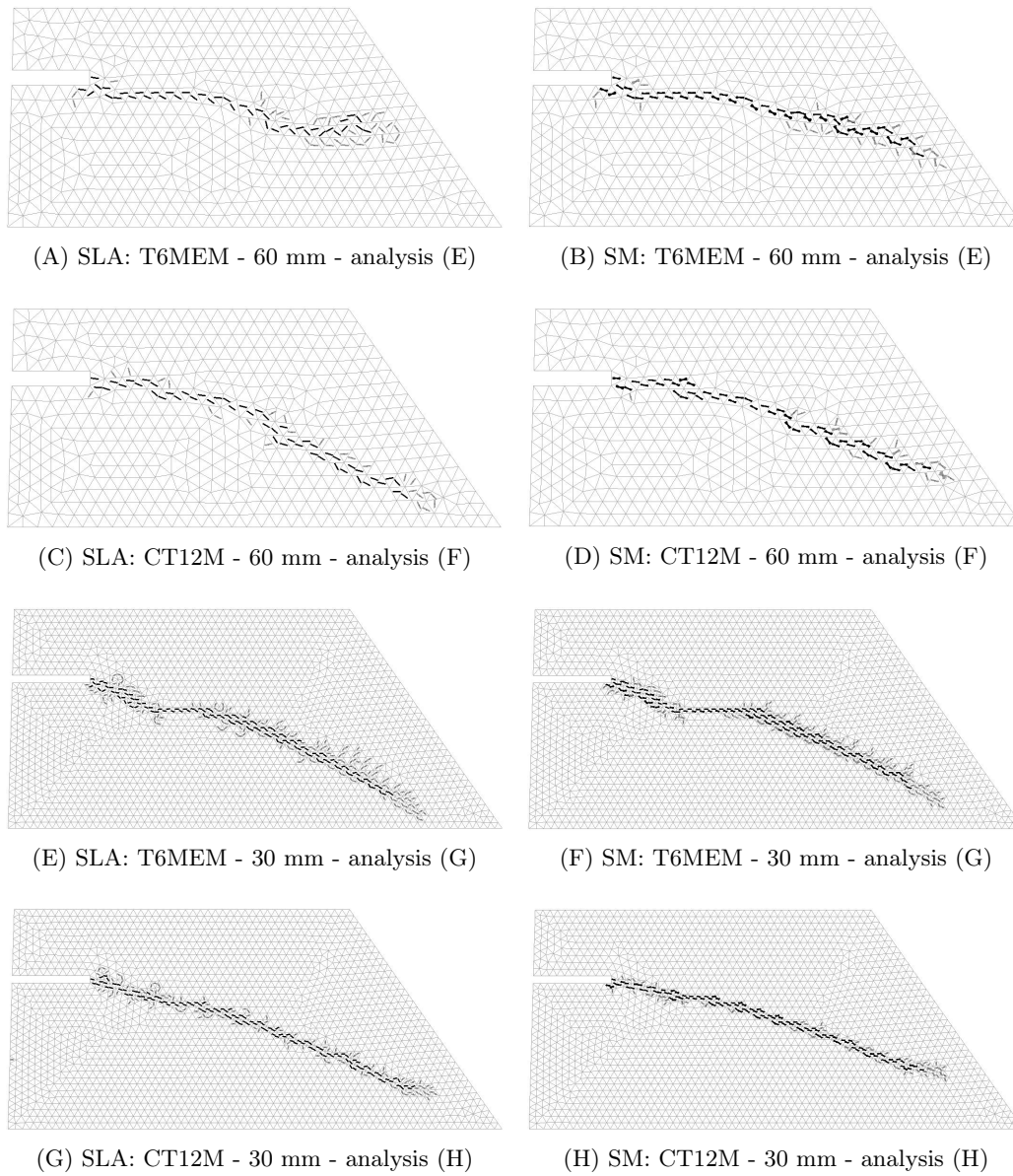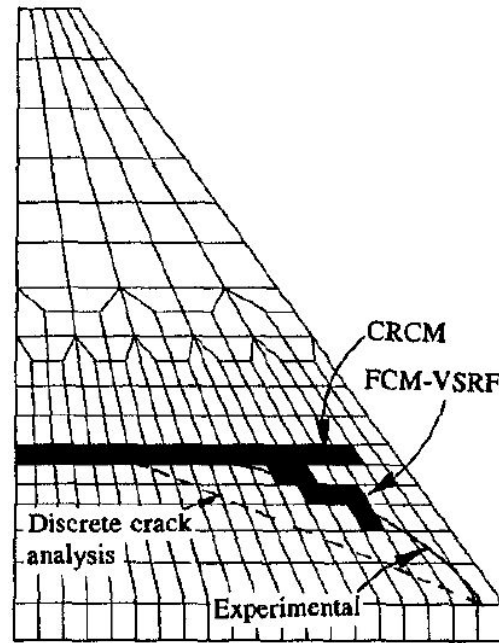(CMOD) of 2 mm

FIGURE 7.36: Crack propagation in the concrete dam for RCM and
FCM, figure taken from Bhattacharjee and Léger [7]

analysis (C) seems to reduce effects of the mesh alignment, the crack is for both models not able to reach the downstream bottom side of the concrete dam. For quadratic elements with a fine mesh in analysis (D), significant differences are obtained between both methods. Regular SLA is able to reach the downstream bottom of the dam, indicating that the influence of mesh-directional bias is reduced when making use of quadratic elements. However, as can be clearly seen in Figure 7.32H, the sublayer model suffers to severe mesh-directional bias effects and hence, the bottom of the concrete dam is not reached. Apparently, instead of propagating further downwards, the sublayers correct the crack direction to maintain mesh alignment. In a study by Bhattacharjee and Léger [7], two types of analyses were performed on the scaled concrete dam:

1. *Fixed Crack Model with Variable Shear Resistance Factor (FCM-VSRF)*, in line with the fixed cracking model that is the basis of regular SLA. The crack path that is found by FCM-VSRF is shown by Figure 7.36. Excellent agreement with the experimental crack path is revealed.

2. *Coaxial Rotating Crack Model (CRCM)*, in line with the rotating crack model that is mimicked by the sublayer model. Contrary to the fixed crack model, the rotating crack model seems to be unable to overcome the restraining effects of mesh alignment, as can be seen in Figure 7.36. Bhattacharjee and Léger concluded that the stress locking that is developed due to a fixed crack direction probably induces high internal forces that are able to overcome issues related to mesh-directional bias. With the aid of a rotating crack model, these high internal forces do not develop since the crack direction is able to correct itself and hence, a straight crack path is obtained (for a very rough mesh).

Ghrib and Tinawi [27] came to the same conclusions: the rotating crack model follows the horizontal mesh lines and does not suffice for this case. They advised to make use of a fixed crack model instead. Since the sublayer model tries to mimick a

(A) Complete crack pattern, marking considered part

(B) Step 701

(C) Step 901

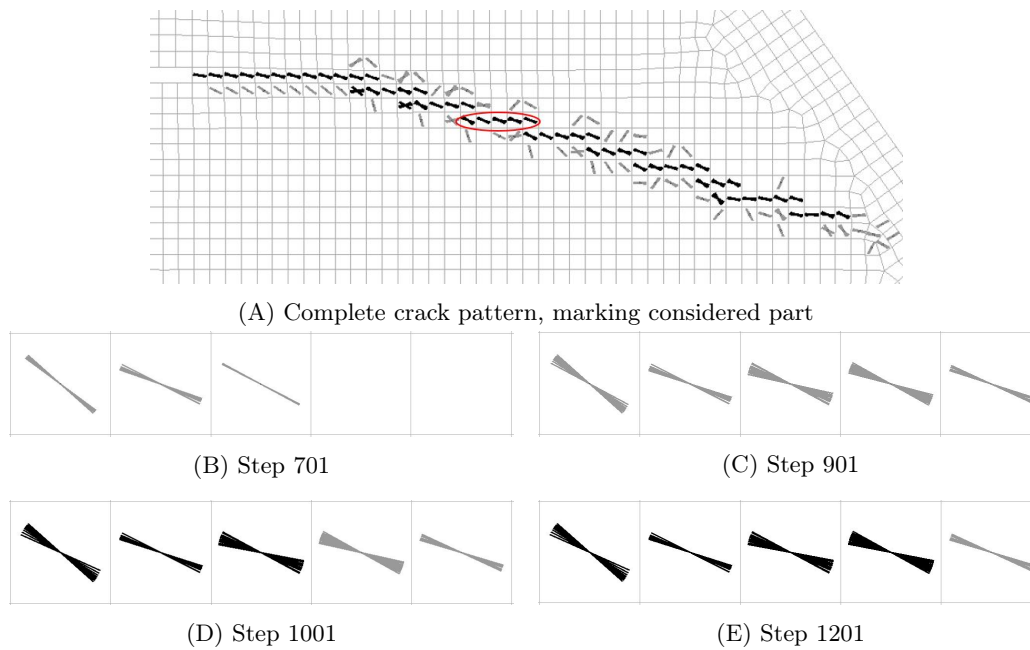(D) Step 1001

(E) Step 1201

FIGURE 7.37: Visualization of sublayer model correcting crack angle
to follow horizontal lines of the mesh for analysis (D)

rotating crack model, the issues that are encountered for a rotating crack model are
to a certain extend also found for the sublayer model (possibly less severe issues,
since on sublayer level, the crack is fixed). The advantage of a rotating crack model
comes with the disadvantage of possibly correcting the crack direction to maintain
a mesh-following tendency. For analysis (D), these 'correcting' effects are shown for
a small straight part of the mesh in Figure 7.37. After damage initiation, the cracks
of consecutive sublayers gradually rotate to align with the horizontal mesh lines, as
can be observed when taking a closer look to steps 701 and 1201. This 'correcting'
type of behaviour is not found for regular SLA and for this specific case, the stress
locking of regular SLA leads to correct results and mimicking of a rotating crack is
undesirable. Although the sublayer model does not suffice for this specific case for
quadrilateral meshes, this case again confirms that the sublayer model does indeed
mimic a rotating crack model.

Next, the results obtained with triangular elements in analyses (E)-(H) are stud-
ied. Compared to quadrilateral elements, better agreement with the experimental
crack path is found since much less problems related to mesh-directional bias are
observed. For analysis (E), the crack path is not able to propagate for regular SLA,
as the crack tip seems to be lost in spurious stresses. With the aid of the sublayer
model, the crack is able to propagate, marking a clear difference between both meth-
ods. For finer meshes, differences are less pronounced. Although the influence of
mesh alignment is reduced, analysis (G) shows that the influence is still present for
linear triangular elements: especially around the notch and along the horizontal part
of the crack path, cracks are aligned with the mesh. When comparing the crack paths
of analyses (G) and (H) for both models, less spurious stresses and therefore smaller
localization bands are found for the sublayer model. The latter statement is sup-
ported by Figure 7.38, which shows zoomed-in snap-shots of the same part of the
mesh for both models for analysis (G). This figure evidently shows the fundamental
differences between regular SLA and the sublayer model. For regular SLA, a trian-
gular mesh gives a zig-zag type of crack propagation, which is on element level not

(A) Analysis (G) - SLA at CMOD of 2 mm   (B) Analysis (G) - SM at CMOD of 2 mm
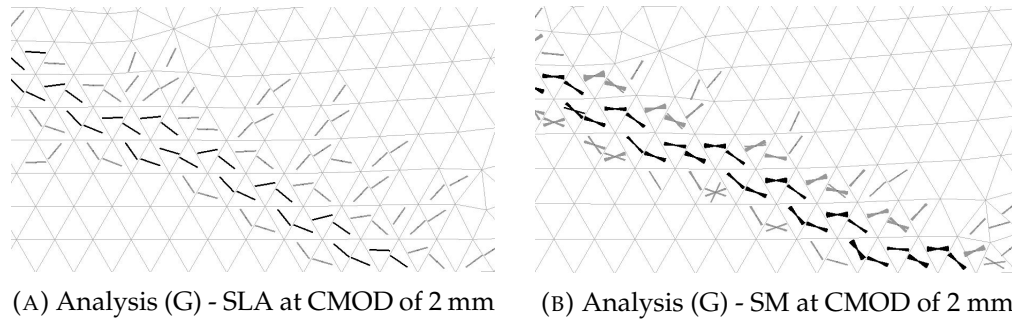
FIGURE 7.38: Crack propagation through a triangular mesh for both
regular SLA and the sublayer model explaining spurious stresses

in line with the global crack propagation direction. To this end, spurious stresses are generated along the crack path, which can be clearly observed in Figure 7.38a. For the sublayer model, damage is initiated along the same zig-zag path. However, consecutive sublayers are able to adapt their crack direction to be in line with the global crack propagation direction. As can be seen in Figure 7.38b, quite large rotations are found along and next to the crack path to correct for the zig-zag type of crack propagation. As a result, less spurious stresses are found along the path. Ultimately, the crack is smoothened and a more realistic crack path is observed that is less dependent on the finite element mesh.

For both quadrilateral and triangular meshes, more accurate crack paths are observed for quadratic elements. Since quadrilateral elements are more prone to influences of mesh-directions bias, application of quadratic triangular elements is recommended for this case. In line with previous cases (shear notched beam, double-edge-notched beam etc.), linear elements with regular integration prove to be inadequate. Hence, the full scale concrete Koyna Dam that is considered in Section 7.6.2, will solely be modelled with quadratic triangular CT12M elements.

Lastly, the load-CMOD curves of Figures 7.32 and 7.34 are discussed. In line with the crack paths, best agreement with experimental results is obtained with triangular elements. Quadrilateral elements result in a lower peak load, which can be possibly attributed to the incorrect crack band assumption: a zig-zag crack path is assumed, while the actual crack path is directed more or less in line with the mesh. All curves reveal that a more flexible response is obtained for the sublayer model compared to regular SLA, in line with previous cases. Biggest differences are found for analyses (A) and (E), in line with the previously described crack path differences. Apparently, differences are most pronounced for coarse meshes with linear elements. For triangular elements, the load-CMOD curves of the sublayer model better suit the NLFEA solutions by [27, 61], indicating that the more flexible response is desirable. The curves for quadrilateral elements are difficult to compare: the sublayer model gives a more flexible response, but the crack patterns that are found by regular SLA for analyses (C) and (D) are more correct, indicating that the stiffer curves resulting from regular SLA are more accurate for these cases.
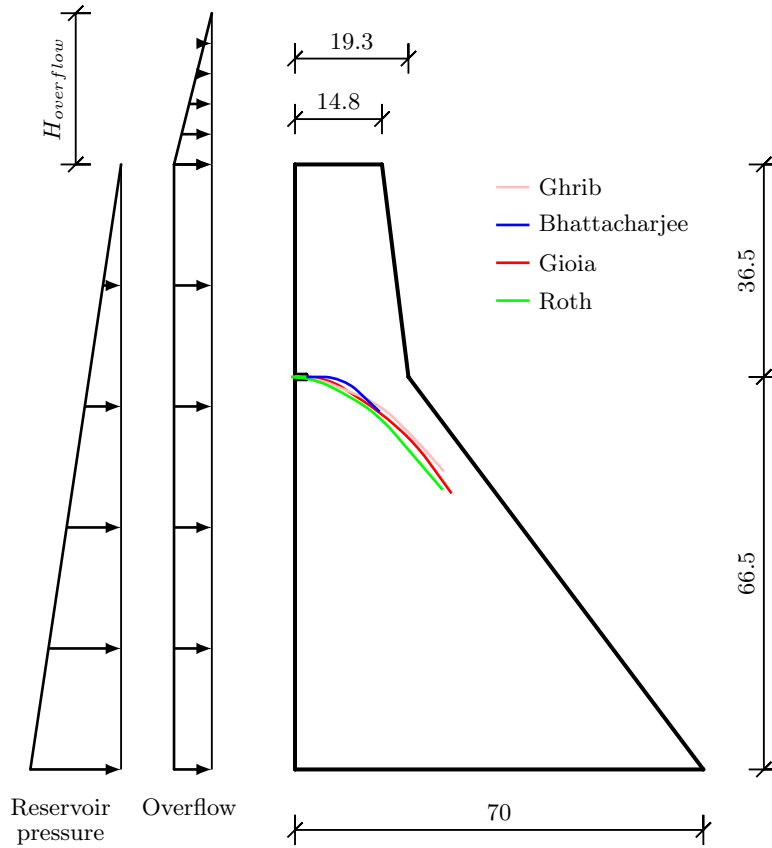
FIGURE 7.39: Geometry of case 5b with all dimensions in meter together with loading and crack paths that are found in references

Quantity		Value	Unit
Tensile strength	f_t	1.0	N/mm^2
Initial stiffness	E_0	25000	N/mm^2
Poisson's modulus	ν_0	0.20	-
Fracture energy	G_f	0.10	N/mm
Density	ρ	2450	kg/m^3

TABLE 7.7: Material properties of the full scale Koyna Dam taken from Roth et al. [61]

7.6.2 Case 5b: Koyna Dam with non-proportional loading

The Koyna Dam is a 103-m-high concrete gravity dam in India, that has been widely used as a benchmark test case for numerical modelling of the seismic performance of full scale concrete structures. With the aid of SLA-type of approaches, seismic behaviour can not be studied. However, some authors (e.g. [7, 27, 28, 46, 61]) considered the Koyna Dam in a static analysis, ultimately resulting in a relation describing the crest (top) displacement versus the overflow height of the dam. In this thesis, the static case study is used to validate the sublayer model and compare its results with regular SLA and several NLFEA results by Bhattacharjee and Léger [7] based on a rotating smeared crack model, Ghrib and Tinawi [27] with a damage mechanics based rotating smeared crack model, Gioia et al. [28] making use of plasticity theory and Roth et al. [61] based on XFEM. The geometry of the dam, together with the

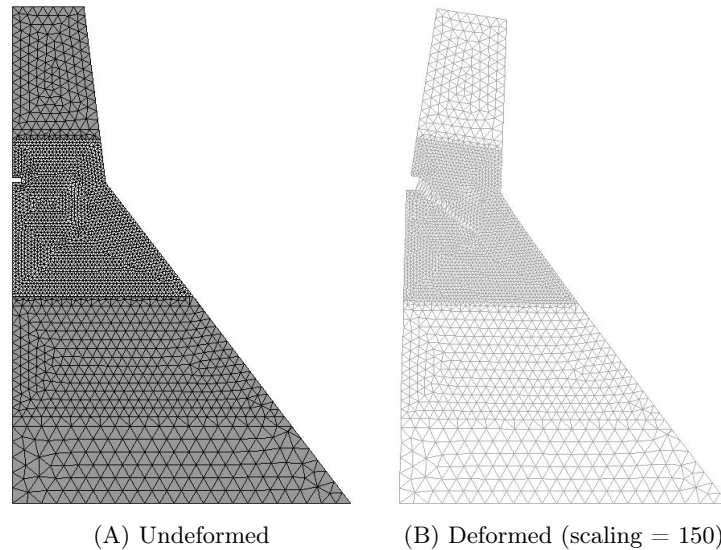(A) Undeformed   (B) Deformed (scaling = 150)

FIGURE 7.40: The applied mesh in A) undeformed state with nonlinear properties assigned to bright parts and B) deformed state

load definition and crack paths that are found in the given references are shown by Figure 7.39. The notch to depth ratio for this case equals 0.1, such that a notch with length 1.93m is created. In an extensive case study, Gioia et al. considered multiple notch locations and concluded that an imperfection at the upstream side at the elevation of the downstream change of slope has most critical effects. In this study, the height of the notch equals the size of a single finite element. A unit thickness of the dam of 1m is considered. Initially, the dam is loaded by its self-weight and by a full reservoir pressure, linearly increasing from $\rho_w g H_{dam}$ at the bottom to 0 at the top. Next, overflow-pressure is applied as a uniformly distributed load $\rho_w g H_{overflow}$ over the height of the dam, while maintaining the self-weight and full reservoir pressure, such that non-proportional loading is obtained. For the sake of simplicity and in line with the given references, water pressure within the cracks is neglected.

Material properties are retrieved from Roth et al. [61]. In most references, bilinear tension softening is assumed. For the generation of a saw-tooth law, it is more convenient to make use of a more or less smoothened bilinear softening law, namely exponential tension softening, while maintaining the same amount of fracture energy such that influence on the total energy dissipation of the structure is limited. Since the scale of the structure is significantly larger than previously considered cases, issues related to constitutive snap-back might arise, as the ultimate strain is inversely proportional to the crack band and thus the element size. For this case study, only a single analysis is performed to limit computational efforts. As has been concluded in Section 7.6.1, quadratic triangular elements are most suitable for complex curved crack patterns and therefore, CT12M elements are applied. For the generated mesh that is shown by Figure 7.40, an element size of 750 mm is used. Invoking the detailed analysis properties of Table C.6, the continuum exponential softening is transferred to a saw-tooth law with 13 saw-teeth in Figure 7.41. Although the relatively large element sizes result in quite brittle constitutive behaviour, no constitutive snap-back is obtained. Nonlinear material behaviour is assigned to relevant parts of the structure and larger elements are used at the base of the dam to reduce computational efforts. Despite these measures, 4793 and 46061 elements are used for regular SLA and the sublayer model respectively, the latter one being multiple times bigger as a result of the parallel elastic-brittle sublayer definitions.
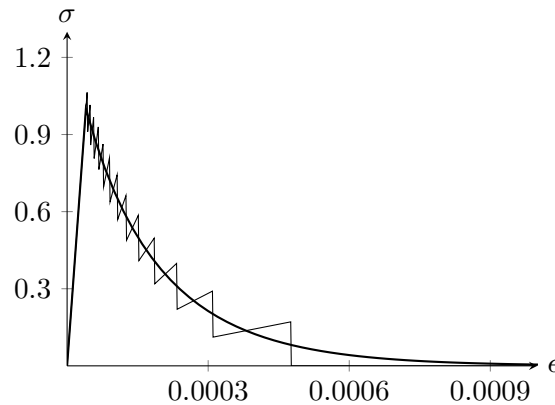
FIGURE 7.41: Continuum exponential tension softening law together
with the corresponding saw-tooth law for Case 5b

The self-weight load is applied as a global load within DIANA FEA. Furthermore, the initial reservoir pressure is applied as a hydrostatic load. Since no damage occurs during application of both of these loads, the loads can be applied simultaneously in the first load stage. Subsequently, the proportionally increasing overflow pressure is simulated with the aid of a uniformly distributed load in the second load stage. Deformations are vertically and horizontally restrained along the bottom edge of the dam. Crack bands are specified according to a zig-zag propagation pattern [62]. During the analyses, the crest (top) displacement is monitored and plotted against the overflow height *H*. The results are plotted in Figure 7.42 for the first 40 mm (to clarify the course of the curve), for the complete paths of regular SLA and the sublayer model separately and for all analyses (including NLFEA) combined. For both regular SLA and the sublayer model, the development of the crack paths is shown by Figures 7.43 and 7.44 respectively.

During the first loading stage, no damage is found and an initial crest displacement of approximately 14 mm is observed (which is in fact the linear elastic solution). Next, an increasing lateral overflow pressure is applied and damage gradually develops around the notch. Development of the crack path is explained with the aid of Figure 7.43, corresponding to regular SLA. Initially, the crack propagates diagonally downwards until step 2301 of the analysis. The upper part of the dam is pushed over, which, combined with increasing compressive stresses at the downstream side, drives the crack downwards. When comparing the crack path of step 2301 with NLFEA crack paths in Figure 7.39, substantial differences are observed: the crack does not propagate far enough in horizontal direction. These differences are most likely the result of the permanent damage increments that come with SLA-type of procedures: the load path and thereby the direction of crack propagation are initiated by a relatively small lateral overflow pressure compared to the self-weight, while changing stress states due to the non-proportional loading might require the transition to a different crack path. On top of that, the crack path seems to be slightly suffering to mesh-directional bias in the first part of the crack path. Ultimately, a secondary crack path is developed in steps 3701 and 4601, which is more in line with the NLFEA references and is caused by increasing lateral overflow pressure compared to the vertical self-weight load. The formation of a secondary crack inherently causes trouble for SLA-type of approaches, as the initial crack path is prone to crack closure and unloading issues. In step 7301, the initial crack path closes and the secondary load path further propagates. Since regular SLA is not really able to adapt itself to

(A) First 40 mm SLA and SM

(B) Complete path SLA

(C) Complete path SM

(D) Combined SLA, SM and NFLEA
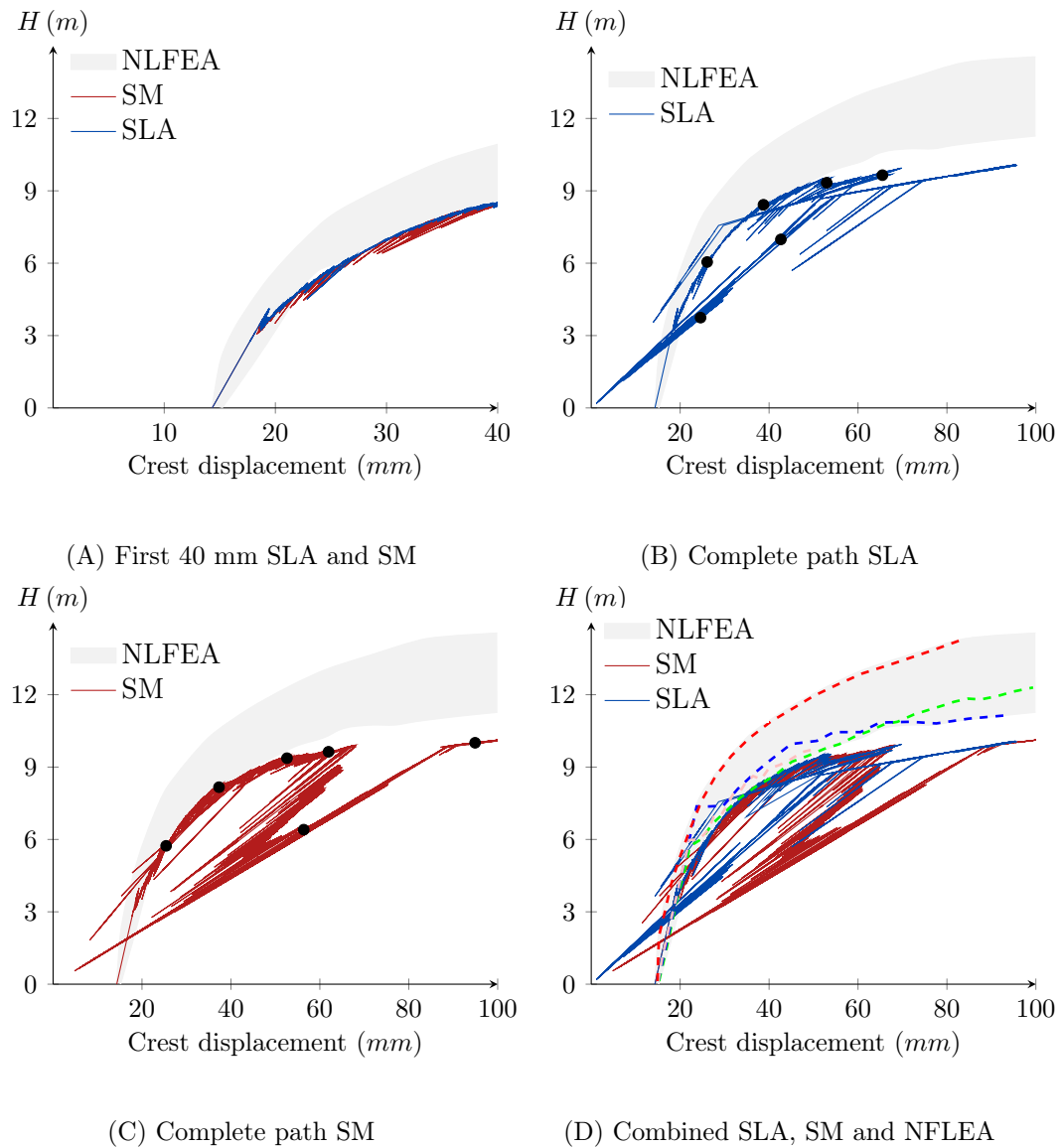
FIGURE 7.42: Crest (top) displacement versus overflow height H for A) the first 40 mm, B) regular SLA only, C) sublayer model only and D) all combined with NLFEA solutions included as well (colors corresponding to Figure 7.39). Black dots represent moments of snap-shots Figures 7.43 and 7.44

(A) Step 1001 - 26.1 *mm*   (B) Step 2301 - 38.7 *mm*   (C) Step 3701 - 53.0 *mm*

(D) Step 4601 - 65.5 *mm*   (E) Step 7301 - 24.6 *mm*   (F) Step 11001 - 42.7 *mm*

FIGURE 7.43: Development of crack strain for regular SLA for 6 steps
of the analysis together with corresponding crest displacement

(A) Step 1001 - 25.4 *mm*   (B) Step 2301 - 37.3 *mm*   (C) Step 3701 - 52.6 *mm*

(D) Step 4601 - 62.0 *mm*   (E) Step 7301 - 56.4 *mm*   (F) Step 11001 - 94.9 *mm*

FIGURE 7.44: Development of crack strain for sublayer model for 6
steps of analysis together with corresponding crest displacement

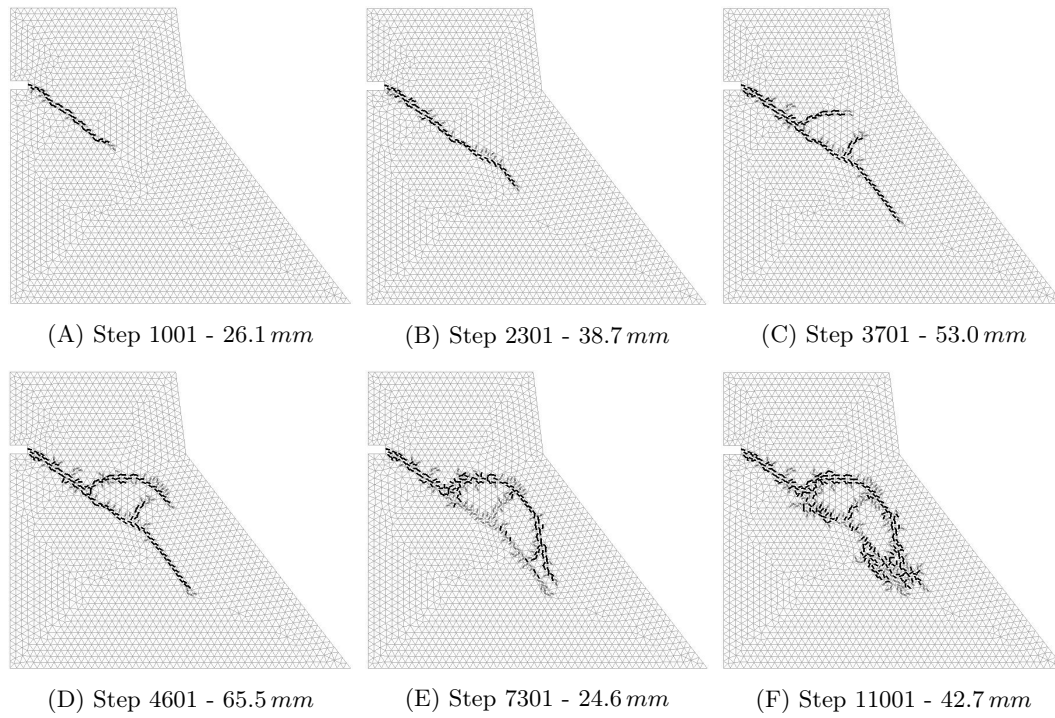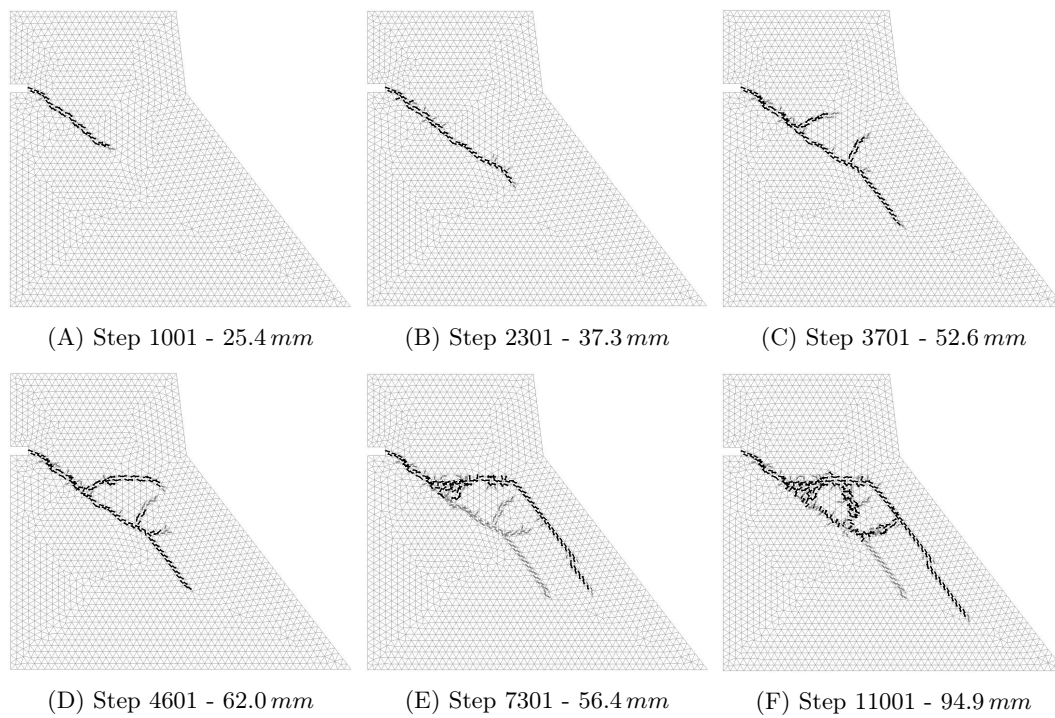these changing stress and crack states, a very diffuse and troubling crack pattern is found at the end of the analysis in step 11001. The secondary crack path is influenced by the initial crack path and ultimately, they blend to one big cracked zone that is not able to propagate further. On top of that, the NLFEA crack path is lost as well, since the crack bends down (almost vertically) too soon. The described issues are also observed in the overflow-displacement curve of Figure 7.42B. Up until the fourth black dot, representing the moment of crack path snap-shots, a smooth load-path is found. However, severe issues emerge once the initial crack closes: big secant snap-backs combined with almost horizontal snap-backs as a result of crack-closure are found. In order to make sure that these issues are not entirely depending on the applied mesh, several meshes with varying elements sizes and triangular/quadrilateral elements have been tested for regular SLA, all showing the same type of issues (even more diffuse crack patterns were obtained for quadrilaterals).

Next, the crack path corresponding to the sublayer model, as shown in Figure 7.44, is considered. Up until step 3701, the crack strain plots are more or less the same as for regular SLA. A straight crack path is found and hardly any crack rotations are generated. However, differences become clear after step 4601. The secondary crack path develops for the same reasons as for regular SLA, but the sublayer model proves to be better able to adapt itself to changing stress and crack states. A very localized secondary crack path is found, which is not influenced by the closed initial crack path and is in line with NLFEA crack paths. Where regular SLA resulted in a diffuse blended crack zone due to the two crack paths coalescing, the sublayer model seems to result in two individual crack paths, of which the secondary crack path is dominant. When taking a closer look on the crack paths in Figure 7.45, large rotations are found at the start of the secondary crack path for the sublayer model.
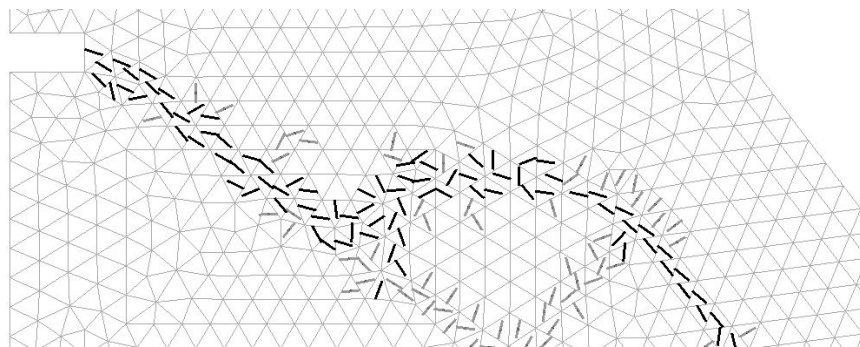
(A) Regular SLA - step 7301
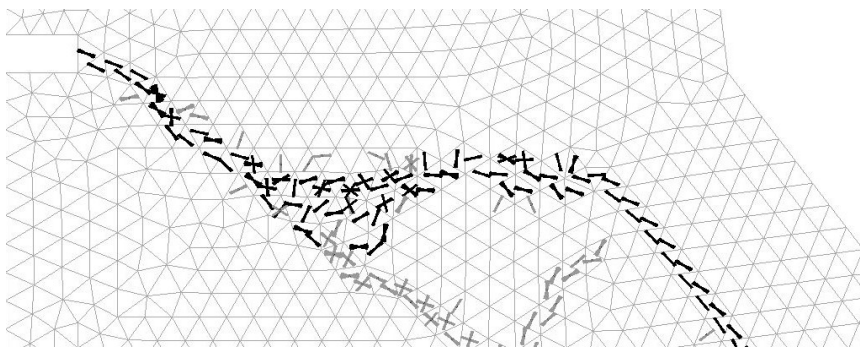
(B) Sublayer model - step 7301

FIGURE 7.45: Zoomed-in crack paths for both regular SLA and the
sublayer model for step 7301

Apparently, the model tries to correct the cracks to be in line with the correct secondary path, allowing for a more accurate description of the secondary crack propagation. For regular SLA, all crack directions are fixed and obscure cracks are required to partially correct the crack path. When comparing the crack path of the sublayer model with the mentioned references, best agreement is found with the results of Roth et al. [61], which does not show a horizontal crack path at the notch as well (where others have a pronounced initial horizontal path).

From the overflow-displacement graphs in Figure 7.42 and the constant load multipliers, as plotted for both methods in Figure 7.46, required for non-proportional loading, the following observations are made:

- For the first 40 mm of the crest displacement path, good agreement is found between regular SLA, the sublayer model and the referenced NLFEA. No notable differences between regular SLA and the sublayer model are observed, since hardly any crack rotations take place in this stage.

- Beyond reaching a crest displacement of roughly 60 mm, severe snap-backs and crack-closure effects are observed for regular SLA. A very peaky and messy path is followed, indicating a poor description of the behaviour. At the start of crack closure (around step 5000), the constant load multiplier λ_{const} reduces to values as low as 0.42, indicating that the model encounters trouble in redistributing the non-proportional load during crack-closure. After development of the diffuse zone of cracks at step 11000, the load is able to recover.

- Compared to the peaky curve of regular SLA, a much smoother curve is obtained by the sublayer model. During the first 60 mm, some pronounced snap-backs are observed, which are also recognized in the constant load multiplier plot. These bigger snap-backs for the sublayer model are in line with previous cases: the more exact description of stress states requires bigger load reductions to allow for the redistribution of stresses that are released after a damage increment. In line with regular SLA, constant load reduction is required during redistribution of the stresses caused by crack-closure. The constant load multiplier reduces to 0.60, which means that significantly less constant load reduction is required for the sublayer model, indicating that the model is better able to redistribute the stresses that arise from the changing crack state. After roughly 10000 steps, the full load is recovered and the secondary crack path further propagates, completely in line with NLFEA. To this end, the drop in the overflow - displacement curve can be interpreted as a redistribution that is required to switch from the initial crack path to the secondary crack path.

- During the first 60 mm, the overflow - displacement curves for both regular SLA and the sublayer model match well with NLFEA results. Especially the results by Roth et al., Bhattacharjee and Léger, and Ghrib and Tinawi are approximated properly. After stress redistribution caused by crack closure, both methods are able to continue a load-path that is reasonably in line with NLFEA. However, the crack path that is found by the sublayer model shows much better agreement with NLFEA solutions.

As discussed by Bhattacharjee and Léger [7], less severe problems with mesh directional bias are found compared to the scaled concrete dam. According to them, the external forces due to self-weight and full reservoir pressure are strong enough to overcome the spurious influences of mesh-following tendencies. In this study, some
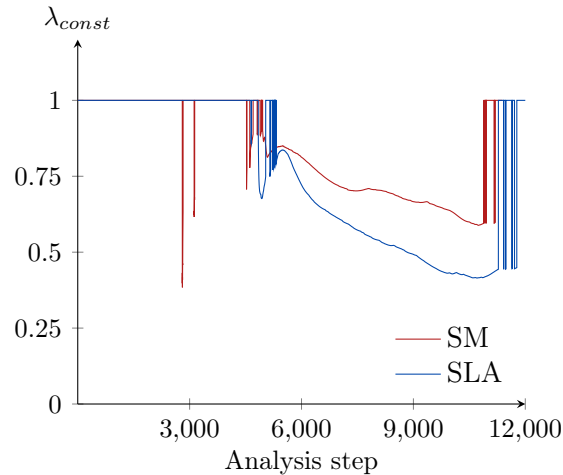
FIGURE 7.46: Comparison of constant load factor λ_{const} for both regular SLA and sublayer model for Case 5b

mesh-directional bias effects are encountered around the notch. However, compared to Case 5a in Section 7.6.1, much less pronounced effects of mesh-directional bias are observed, supporting the explanation of Bhattacharjee and Léger. For the sublayer model, the secondary crack ultimately propagates along the mesh lines, although it is not known if this happens due to mesh-directional bias or because the mesh is in line with the actual correct direction of crack propagation (see crack paths NLFEA).

To conclude, it is noted that this case might be too complex for SLA-type of procedures, due to the troubling emergence of crack-closure, stress rotations and non-proportional loading for this case. However, by pushing the methods to their limits, fundamental differences between regular SLA and the sublayer model can be best studied. The sublayer model being able to gradually overcome the effects of crack-closure, stress rotations and non-proportional loading is a very promising step forwards in the development of sequentially linear analysis and its application to practical cases.

7.7   Discussion

In this chapter, the sublayer model has been tested for a wide range of structural cases. Beside comparison between regular SLA and the sublayer model, the suitability of several element types has been tested as well, with the focus on quadrilateral elements. Table 7.8 gives an overview of the suitability for three types of quadrilateral elements, namely linear Q8MEM with reduced and regular integration and quadratic CQ16M with regular integration, for SLA-type of approaches (so both regular SLA and the sublayer model) for the considered cases. Case 5b is not included, since this case used triangular elements instead. For simple straight crack paths like the notched beam, linear elements are most suitable, especially when making use of reduced integration. For straight cracks, quadratic elements are too sophisticated and additional spurious stresses are observed. However, quadratic elements are recommended for all curved and diffuse crack paths, since the elements interpolation scheme allows for a more accurate and realistic description of curved crack paths, which becomes especially clear for the shear-notched beam. As an alternative, linear elements with reduced integration can be used for simple curved crack cases, although the obtained crack path is more or less the collection of piece-wise straight

Case	Loading	Crack pattern	Q8MEM 1 IP	Q8MEM 2x2 IP	CQ16M
1	prop.	straight	++	+	+/-
2	prop.	curved	+	- -	++
3	non-prop.	curved	+/-	- -	+
4	non-prop.	diffuse	- -	+/-	+
5a	prop.	curved	- -	-	+

TABLE 7.8: Suitability of different quadrilateral elements for the considered cases for an SLA-type of approach (both SLA and sublayer model). Minimum - - and maximum ++

cracks. For the facade and the concrete dam cases, linear elements with reduced integration are too simplistic, and no satisfying results can be obtained. Linear elements with regular integration suffer to very pronounced mesh-directional bias and are therefore not suitable for SLA-type of approaches (see for example the shear notched beam and double-edge-notched beam).

For the double-edge-notched beam and the concrete dam test cases, some tests are performed with both linear and quadratic triangular elements. Especially for quadratic triangular elements, mesh-directional bias was observed to reduce, although the mesh-directional issues are not completely solved. Potentially, the influence of mesh-directional bias can be reduced by using random triangular meshes. Further research is required to substantiate the latter statement. It can however be concluded that quadratic elements, triangular and quadrilateral, are preferred above linear elements for application in engineering practice due to their reliable and robust performance. With the aid of the sublayer model, the general performance of different elements relatively to each other does not change: for same cases, the sublayer model is able to work-around element-related issues, for example for analysis (B) of the full scale facade, but in general, element-related issues are maintained.

Differences between regular SLA and the sublayer model are widely observed and can be divided over the following three levels:

1. *Differences on element level.* The sublayer model allows for crack rotation on element level, such that stresses are monitored in a plane that is more in line with the principal stress direction and less over-stiff behaviour is observed (less stress locking), in line with the findings of Chapter 6. For structural cases, rotating cracks are mainly observed due to changing stress states and due to 'smoothening' of the crack path (which becomes for example clear for analysis (G) of Case 5a).

2. *Differences on local level: surrounding elements.* If stress locking takes place on element level, stresses larger than the elements capacity might be observed, potentially causing spurious stresses and cracks to develop in surrounding elements as well. With the aid of the sublayer model, less stress locking on element level is obtained, implicitly resulting in less spurious stresses in surrounding elements. Furthermore, once spurious stresses do develop in surrounding elements, the sublayer model allows for correction, such that further development of spurious stresses is counteracted. Also, once the crack propagates into elements that are already partly cracked due to spurious stresses, the uncracked sublayers can still follow the main crack path, while for regular SLA the incorrect spurious crack direction would be followed.

3. *Differences on global/structural level.* Especially for the performed full scale analyses, different paths of crack propagation and ultimately different collapse mechanisms are found. On structural level, the sublayer model is better able to cope with the effects of crack-closure, unloading and non-proportional loading. In fact, the uncracked sublayers are able to adapt to the current state, where on the contrary, the crack direction of the complete element for regular SLA is fixed based on the state at the moment of damage initiation.

For Cases 1, 2, 3 and 5a, differences are mostly found on levels 1 and 2: on element level crack rotations are found and as a result, less spurious stresses are generated, which becomes especially clear for Cases 1 and 2, both showing a smaller localization band for the sublayer model. As a result, more flexible behaviour is found, which can also be seen in the load-displacement curves of the cases. In order to quantify crack rotations, Figure 7.47 entails the crack rotations for fully developed cracks, together with a zoomed in view of the relevant parts of the crack paths. For Case 1, crack rotations up to 37 degrees are found, which are required to correct for the development of U-turns, as described in Section 7.2. For Case 2, crack rotations up to 42 degrees are found around the notch. During crack propagation, the crack rotation gradually reduces to roughly 10 degrees at the vertical part of the crack path. For the double-edge-notched beam in Case 3, a maximum crack rotation of 21 degrees is observed at the notch, where the rest of the crack path exhibits minor crack rotations of roughly 10 degrees. Since for Case 3 (average crack rotation in the order of 10 degrees) smaller crack rotations take place compared to Cases 1 and 2 (average crack rotation in the order of 30 degrees), smaller differences are found in the curves and crack plots of Case 3, in line with the single element tests in Chapter 6 and the theoretical framework that is introduced in Section 6.6.

For Cases 4 and 5b, differences are mostly found on level 3. For the facade, both linear and quadratic elements gave more realistic collapse mechanisms for the sublayer model. Regular SLA did not allow for the formation of a compressive strut in the right pillar, since tensile cracks were directed almost vertically here. As a result, some severe crack closure effects were encountered for regular SLA. Similar results were reported for Case 5b at the formation of a secondary load path: where regular SLA was not able to overcome the effects of crack closure and a blended zone of spurious cracks was obtained, the sublayer model resulted in a localized crack pattern that propagates in line with NLFEA solutions from literature. Apparently, the sublayer model is better able to adapt to changing stress states during the analysis. Since changing stress states are often obtained for full scale complex cases (with non-proportional loading, formation of alternative crack paths and crack closure effects), severe differences on structural level are found between both methods.

For applications in engineering practice, the third level of differences is most of interest: the ultimate collapse mechanism is in general more important than the post-peak behaviour being somewhat stiffer due to spurious stresses. To this end, the structural differences that are found for full scale cases are very promising. The main feature of the sublayer model in the context of practical application is not necessarily the reduction of spurious stresses due to crack rotations, but is rather found in the ability of the model to adapt itself to suit the current stress state as accurate as possible. SLA-type of approaches have been criticized for their often limited range of application in practice, since issues with crack closure, non-proportional loading and cyclic loads were often encountered. In the authors opinion, the sublayer model is a valuable contribution towards a more robust and in practice generally applicable sequentially linear analysis.
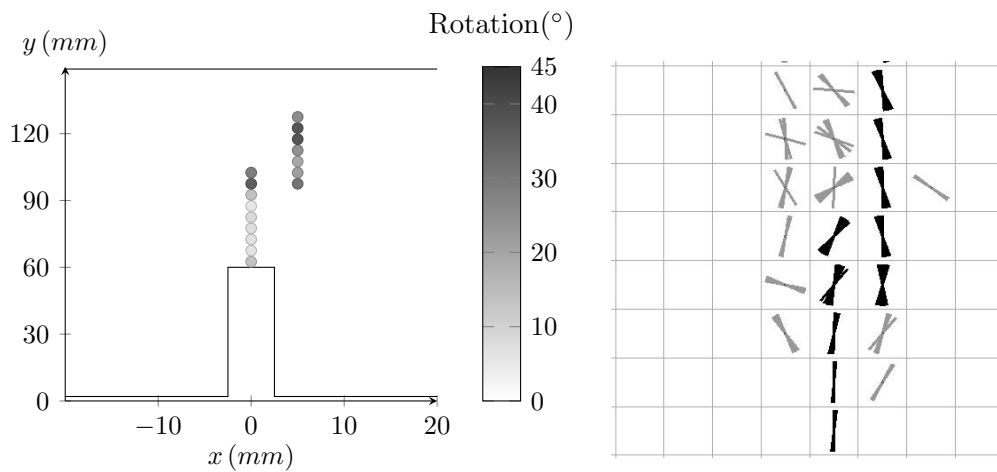
(A) Case 1 - analysis (F) - at mid-span deflection of 1.0 mm
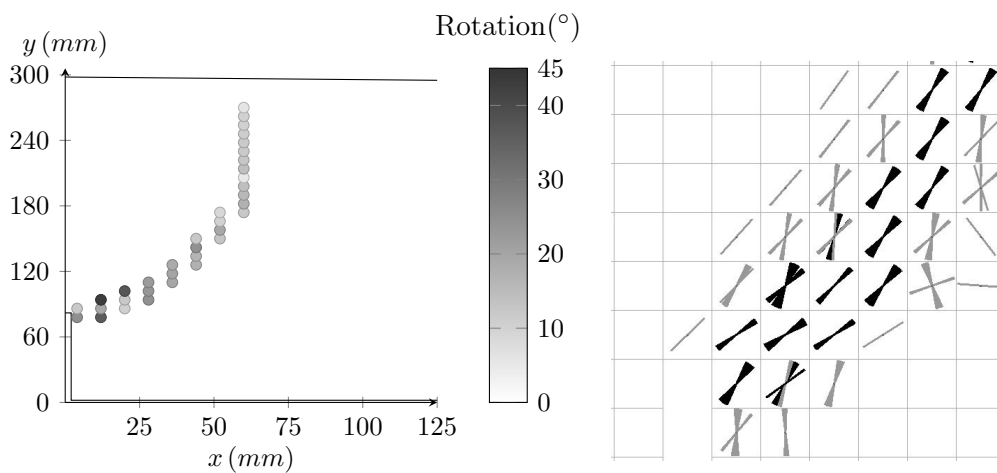
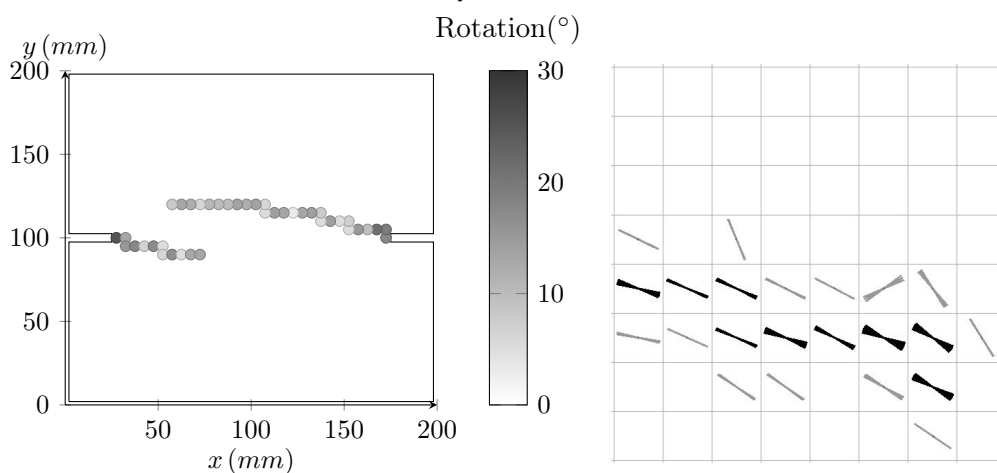(B) Case 2 - analysis (C) - at CMSD of 0.20 mm

(C) Case 3 - analysis (C) - at $\delta_{average} = 0.1\,mm$

FIGURE 7.47: On the left, scatter plot of crack rotations in fully developed cracks and on the right, zoomed crack paths at considered moments (black = fully developed and gray = under development)

Chapter 8

3D analysis: theory and verification

In this chapter, the theoretical framework of the sublayer model is extended towards 3-dimensional problems, which are briefly discussed in Section 3.5. This study focuses on 3D solid elements, although it is noted that a similar approach can be followed for shell elements as well. First, the theoretical framework is discussed and derived in Section 8.1. Then, in line with Chapter 6, a single element test is performed in Section 8.2, followed by a structural test, in line with Chapter 7, on an inclined notched beam in Section 8.3. To conclude, Section 8.4 gives an overview and discusses some possible drawbacks of the proposed framework.

8.1 Theoretical framework

In order to make the transition from 2D analysis to 3D analysis, two additional measures are required. First, the plane stress-strain relations should be expanded to fit 3D-continuum stress states. Secondly, the transition from saw-tooth law to sublayer material properties requires some extra attention in the case of 3D. Both are discussed in this section, starting with 3D stress-strain relations for the isotropic undamaged and orthotropic damaged states.

Orthotropic fixed smeared crack model
A 3D-continuum element with an x-y-z coordinate system is considered. Figure 8.1 entails positive definitions of all entrees of the stress tensor. The first index refers to the plane on which the stress is working and the second index follows the direction in which the stress is pointed. Moment equilibrium requires stresses $\sigma_{ij} = \sigma_{ji}$ for all $i \neq j$ and hence, the stress tensor is symmetric, such that in total six individual stresses are defined. The strain ϵ and stress σ are related by the compliance matrix C according to

$$\epsilon = C\,\sigma \tag{8.1}$$

and inversely, the stress and strain are related by the stiffness matrix D according to

$$\sigma = C^{-1}\,\epsilon = D\,\epsilon \tag{8.2}$$

The compliance matrix is compiled out of the individual uniaxial contributions of all stress components. For example the strain ϵ_{xx} is given by

$$\epsilon_{xx} = \frac{\sigma_{xx}}{E_x} - \frac{\nu_{xy}\,\sigma_{yy}}{E_y} - \frac{\nu_{xz}\,\sigma_{zz}}{E_z} \tag{8.3}$$

which is derived by the combined contributions of Hooke's law and Poisson effects and where E_x, E_y and E_z are the orthotropic stiffnesses (isotropic material behaviour
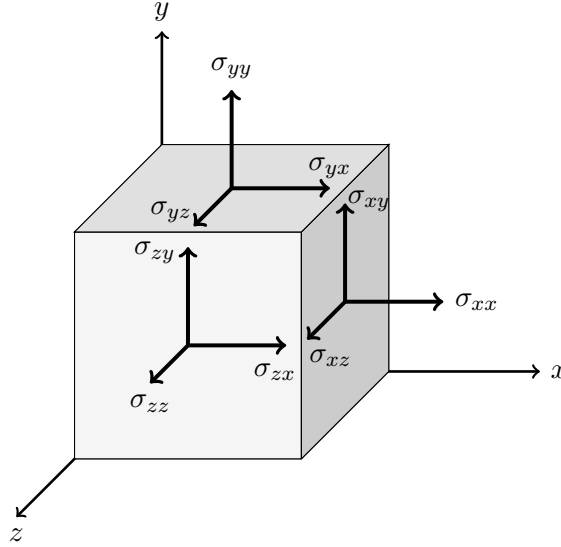
FIGURE 8.1: Positive definitions of stresses in a 3D-continuum with
x-y-z coordinate system

can be described as well by setting all stiffnesses to E_0). The Poisson's ratio ν_{ij} is defined as the contraction in i-direction due to extension in j-direction. Following the same procedure, the total compliance matrix is found by

$$
\begin{bmatrix} \epsilon_{xx} \\ \epsilon_{yy} \\ \epsilon_{zz} \\ \gamma_{xy} \\ \gamma_{yz} \\ \gamma_{zx} \end{bmatrix} = \begin{bmatrix} \dfrac{1}{E_x} & -\dfrac{\nu_{xy}}{E_y} & -\dfrac{\nu_{xz}}{E_z} & 0 & 0 & 0 \\[2mm] -\dfrac{\nu_{yx}}{E_x} & \dfrac{1}{E_y} & -\dfrac{\nu_{yz}}{E_z} & 0 & 0 & 0 \\[2mm] -\dfrac{\nu_{zx}}{E_x} & -\dfrac{\nu_{zy}}{E_y} & \dfrac{1}{E_z} & 0 & 0 & 0 \\[2mm] 0 & 0 & 0 & \dfrac{1}{G_{xy}} & 0 & 0 \\[2mm] 0 & 0 & 0 & 0 & \dfrac{1}{G_{yz}} & 0 \\[2mm] 0 & 0 & 0 & 0 & 0 & \dfrac{1}{G_{zx}} \end{bmatrix} \begin{bmatrix} \sigma_{xx} \\ \sigma_{yy} \\ \sigma_{zz} \\ \sigma_{xy} \\ \sigma_{yz} \\ \sigma_{zx} \end{bmatrix} \tag{8.4}
$$

Based on Equation 8.2, the stiffness matrix D can be found by inverting Equation 8.4, leading to

$$
D = \begin{bmatrix} D_{normal} & 0 \\ 0 & D_{shear} \end{bmatrix} \tag{8.5}
$$

with D_{normal} given by

$$
\frac{1}{A} \begin{bmatrix} \left(\nu_{yz}^2 \frac{E_y}{E_z}\right) E_x & -\left(\nu_{xy} + \nu_{yz}\nu_{zx}\frac{E_y}{E_x}\right) E_x & -\left(\nu_{xy}\nu_{yz} + \nu_{zx}\frac{E_z}{E_x}\right) E_x \\[2mm] -\left(\nu_{yz}\nu_{zx} + \nu_{xy}\frac{E_x}{E_y}\right) E_y & \left(\nu_{zx}^2 \frac{E_z}{E_x}\right) E_y & -\left(\nu_{yz} + \nu_{xy}\nu_{zx}\frac{E_z}{E_y}\right) E_y \\[2mm] -\left(\nu_{zx} + \nu_{xy}\nu_{yz}\frac{E_x}{E_z}\right) E_z & -\left(\nu_{xy}\nu_{zx} + \nu_{yz}\frac{E_y}{E_z}\right) E_z & \left(\nu_{xy}^2 \frac{E_x}{E_y}\right) E_z \end{bmatrix} \tag{8.6}
$$

and D_{shear} by

$$D_{shear} = \frac{1}{A} \begin{bmatrix} G_{xy} & 0 & 0 \\ 0 & G_{yz} & 0 \\ 0 & 0 & G_{zx} \end{bmatrix} \tag{8.7}$$

with

$$A = \frac{E_x E_y E_z}{-E_x E_y E_z + \nu_{xy}^2 E_x^2 E_z + \nu_{zx}^2 E_z^2 E_y + \nu_{yz}^2 E_y^2 E_x + 2\nu_{xy}\nu_{yz}\nu_{zx}E_x E_y E_z} \tag{8.8}$$

As long as the material is undamaged, isotropic material behaviour is assumed and stresses and strains can be considered in global $x - y - z$ configuration. For isotropic material behaviour, stiffnesses, Poisson's moduli and shear moduli in all directions equal E_0, ν_0 and G_0 (see Equation 2.13) respectively. Hence, in 3D, the isotropic stress and strain are related by

$$D = \frac{E_0}{(1+\nu_0)(1-2\nu_0)} \begin{bmatrix} 1-\nu_0 & \nu_0 & \nu_0 & 0 & 0 & 0 \\ \nu_0 & 1-\nu_0 & \nu_0 & 0 & 0 & 0 \\ \nu_0 & \nu_0 & 1-\nu_0 & 0 & 0 & 0 \\ 0 & 0 & 0 & \frac{1-2\nu_0}{2} & 0 & 0 \\ 0 & 0 & 0 & 0 & \frac{1-2\nu_0}{2} & 0 \\ 0 & 0 & 0 & 0 & 0 & \frac{1-2\nu_0}{2} \end{bmatrix} \tag{8.9}$$

Once the biggest principal stress σ_1 exceeds the tensile (or eventually compressive) strength of the material, a crack is initiated along the plane that is aligned perpendicular to σ_1. From this point on, the material behaves orthotropic with stiffness matrix according to Equation 8.5. The crack direction is fixed and a local $n - s - t$ coordinate system is introduced that describes the three axes of orthotropy, with the n-axis aligned with σ_1, perpendicular to the crack, and the s, t-axes aligned with σ_2 and σ_3 respectively. In the current 3-dimensional framework, both secondary and tertiary directions are fixed upon crack initiation. As mentioned by Pari et al. [57], fixation of the secondary and tertiary crack directions could be postponed until damage is obtained in a secondary direction, allowing a more realistic description of the cracking process. In local $n - s - t$ configuration, all orthotropic relations are defined exactly the same as in the global $x - y - z$ coordinate system: only the indices change accordingly, such that

$$\begin{bmatrix} \sigma_{nn} \\ \sigma_{ss} \\ \sigma_{tt} \\ \sigma_{ns} \\ \sigma_{st} \\ \sigma_{tn} \end{bmatrix} = D_{n,s,t} \begin{bmatrix} \epsilon_{nn} \\ \epsilon_{ss} \\ \epsilon_{tt} \\ \gamma_{ns} \\ \gamma_{st} \\ \gamma_{tn} \end{bmatrix} \tag{8.10}$$

In line with Equation 2.9, a damage based reduction of the Poisson's moduli is applied that occurs on a similar rate as the reduction of the corresponding stiffness according to

$$\nu_{sn} = \nu_{tn} = \nu_0 \frac{E_n}{E_0} \qquad \nu_{ns} = \nu_{ts} = \nu_0 \frac{E_s}{E_0} \qquad \nu_{nt} = \nu_{st} = \nu_0 \frac{E_t}{E_0} \tag{8.11}$$

Furthermore, in line with the 2D shear retention behaviour for plane stress states, as described by Equation 2.13, the 3D shear retention behaviour is described as follows

$$G_{ns} = \frac{\min\left(E_n, E_s\right)}{2\left(1 + \nu_0 \frac{\min\left(E_n, E_s\right)}{E_0}\right)} \qquad G_{st} = \frac{\min\left(E_s, E_t\right)}{2\left(1 + \nu_0 \frac{\min\left(E_s, E_t\right)}{E_0}\right)}$$

$$G_{tn} = \frac{\min\left(E_t, E_n\right)}{2\left(1 + \nu_0 \frac{\min\left(E_t, E_n\right)}{E_0}\right)} \tag{8.12}$$

SLA applied to 3D solid elements under proportional loading has been developed by Voormeeren [80]. A further elaboration to non-proportional loading in 3D is recently published by Pari et al. [57], as already discussed in Section 3.5. Furthermore, DeJong et al. [20] incorporated shell elements in the framework of SLA. In fact, the application of SLA to shell or solid elements is governed by the same fundamental principles: upon damage initiation, the axes of orthotropy are fixed, along which the stresses are monitored during the remainder of the analysis, and once the saw-tooth strength is reached, damage increments are performed along that specific axis according to the specified saw-tooth law. In 2D, damage increments are allowed in n, t-directions according to Chapter 3 and in 3D, damage can take place in n, s, t-directions. The definition of the uniaxial saw-tooth laws does not change. Furthermore, global stresses in x, y, z-directions are obtained from local stresses in n, s, t-directions with the aid of a 6x6 rotation matrix, which can be determined based on the eigenvectors of the stress.

Sublayer model theory
In Chapters 4 and 5, the 2D-theory of the sublayer model has been derived and explained. In 3D, the main principles of the model also hold. In line with the 2D sublayer model, the total volume of the element (or volume corresponding to an integration point) is split in a certain amount of elastic perfectly brittle overlay elements, each having their own stiffness, strength and fixed crack direction. In this way, the 3D model utilizes a fixed cracking model per sublayer and mimics a rotating crack on element level. For 2D, it was arbitrarily assumed that all sublayers have the same thickness t_0/N. The choice of thickness did not influence the finite element geometry as such that no additional nodes were required. However, in 3D, a similar measure would require multiple nodes over the thickness of the solid element to connect all sublayers. Therefore, all sublayer elements are required to have a volume that is equal to the total elements volume. In fact, the sublayer elements more or less work as *overlay* elements in 3D, all sharing the same nodes. In Figure 8.2, solid sublayer elements (A), (B) and (C) all have the same volume as total element (D). Each of the sublayer elements has its own fixed axes of orthotropy. The superposition of (A)-(C) results in a multidirectional crack in total element (D). Where in 2D, the crack
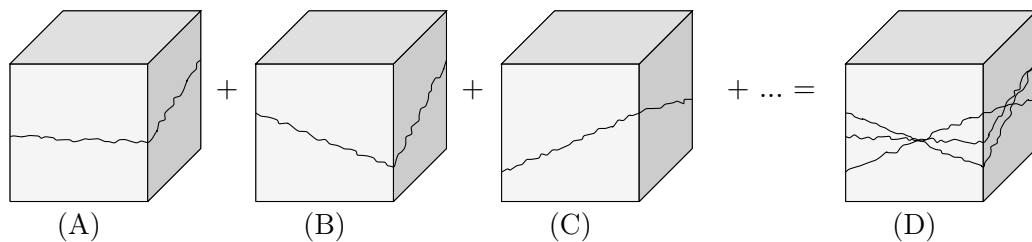

(A)   (B)   (C)   (D)

FIGURE 8.2: Superposition of sublayer elements (A), (B) and (C) with fixed cracking plane, leading to total element (D) with a multidirectional crack

plane could be defined using a single angle, in 3D, each direction has its own crack angle. Since all sublayer elements share the same nodes, the total number of nodes in the finite element model is maintained, while the total number of integration points increases. In 3D, the name *sublayer model* becomes a bit vague, since in fact overlay volumes are used. However, the name 'sublayer model' is more appropriate than 'subvolume model', since one could incorrectly interpret the model as the superposition of sub-volumes, each having a volume V_0/N, where V_0 is the volume of the total element. For the sake of coherence with the rest of this thesis, the same name is allocated to the 2D and 3D models, although it is recognized that a more suitable name is possible.

Upon crack initiation in a specific sublayer, a transition is made from the undamaged isotropic stiffness matrix formulation of Equation 8.9 to the damaged orthotropic stiffness matrix of Equation 8.5, and a brittle damage increment is performed in the local n-direction of that sublayer. Hence, $E_n = 0$ and according to Equation 8.11, $v_{sn} = v_{tn} = 0$ and following Equation 8.12, $G_{ns} = G_{tn} = 0$, such that the stress-strain relation reduces to

$$
\begin{bmatrix} \sigma_{nn} \\ \sigma_{ss} \\ \sigma_{tt} \\ \sigma_{ns} \\ \sigma_{st} \\ \sigma_{tn} \end{bmatrix} = \frac{1}{1 - v_{ts}v_{st}} \begin{bmatrix} 0 & 0 & 0 & 0 & 0 & 0 \\ 0 & E_s & v_{st}E_s & 0 & 0 & 0 \\ 0 & v_{ts}E_t & E_t & 0 & 0 & 0 \\ 0 & 0 & 0 & 0 & 0 & 0 \\ 0 & 0 & 0 & 0 & (1 - v_{ts}v_{st})\,G_{st} & 0 \\ 0 & 0 & 0 & 0 & 0 & 0 \end{bmatrix} \begin{bmatrix} \epsilon_{nn} \\ \epsilon_{ss} \\ \epsilon_{tt} \\ \gamma_{ns} \\ \gamma_{st} \\ \gamma_{tn} \end{bmatrix} \tag{8.13}
$$

which is exactly equal to the plane stress orthotropic formulation of Equation 2.8, describing the plane stress state in the plane perpendicular to the primary axis n. In the s, t-plane, secondary and tertiary cracks can develop in the s and t-directions respectively. Once the sublayers tensile strength is reached in either the s or t-direction, a brittle damage increment is performed in the critical direction. For example, when the tensile strength is reached in the s-direction, $E_s = 0$ and therefore $v_{ns} = v_{ts} = G_{st} = 0$, such that

$$
\begin{bmatrix} \sigma_{nn} \\ \sigma_{ss} \\ \sigma_{tt} \\ \sigma_{ns} \\ \sigma_{st} \\ \sigma_{tn} \end{bmatrix} = \begin{bmatrix} 0 & 0 & 0 & 0 & 0 & 0 \\ 0 & 0 & 0 & 0 & 0 & 0 \\ 0 & 0 & E_t & 0 & 0 & 0 \\ 0 & 0 & 0 & 0 & 0 & 0 \\ 0 & 0 & 0 & 0 & 0 & 0 \\ 0 & 0 & 0 & 0 & 0 & 0 \end{bmatrix} \begin{bmatrix} \epsilon_{nn} \\ \epsilon_{ss} \\ \epsilon_{tt} \\ \gamma_{ns} \\ \gamma_{st} \\ \gamma_{tn} \end{bmatrix} \tag{8.14}
$$

which is completely in line with the 2D sublayer model after a brittle damage increment in the primary crack direction (see Equation 4.7). Once the tensile strength is reached in the tertiary crack direction as well, the complete load carrying capacity of the sublayer element is gone.

In Chapter 5, the transitions from 1) continuum law to saw-tooth law and 2) saw-tooth law to sublayer material properties were elaborated. For the theoretical framework of 3D, the first transition does not change: the uniaxial continuum law (e.g. linear tension softening) is transferred to a saw-tooth law based on the ripple-band algorithm. However, the second transition does require some minor changes. In the 2D model, it is assumed that all sublayers have the same thickness t_0/N. For the 3D model, all sublayer elements have the same volume and thus the same dimensions as the total element. To that end, the derivation of Equations 5.10 and
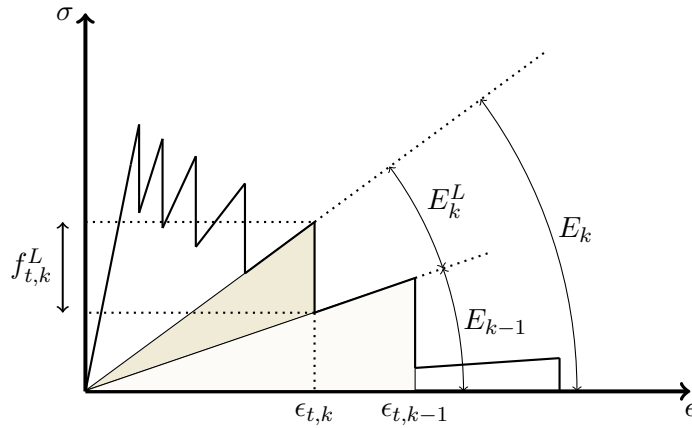
FIGURE 8.3: Schematization of transition from saw-tooth law to sub-
layer material properties, compare with Figure 5.3

5.11 slightly changes: the contribution of a single sublayer does not have to be scaled
to the total element volume, since the sublayer already has the same dimensions as
the total element. Therefore, the stiffness contribution of a single sublayer to the total
element behaviour changes from E_k^L/N to E_k^L and the stress contribution changes
accordingly. Hence, with the aid of Figure 8.3, the sublayer element properties in 3D
are determined by

$$E_k^L = E_k - E_{k-1} \qquad (8.15)$$

and

$$f_{t,k}^L = E_k^L \, \epsilon_{t,k} \qquad (8.16)$$

Invoking Equations 8.15 and 8.16, all properties of the sublayer elements have
been determined: volume V_0, stiffness E_k^L and tensile strength $f_{t,k}^L$ (compressive
strengths can be determined in the same manner). Apart from the discussed parts,
the sublayer model algorithm as schematized in Figure 4.6 remains exactly the same.
In this way, sequentially linear analysis with a 3D sublayer model can be performed
in the remainder of this chapter, building on the knowledge that is obtained for 2D.
Furthermore, the procedure as explained in Appendix B is applied, with only slight
changes in the transition from saw-tooth law to sublayer properties.

8.2   Verification on element level

Before the 3D application of the sublayer model is tested on structural level, a sin-
gle element test is performed. In line with Section 6.5, a non-proportional load that
is similar to the tension-shear problem by Willam et al. [83] is defined for 3D. The
same material properties and crack band as for 2D are used for the 3D test case. The
continuum linear tension softening law is discretized using a ripple band parameter
$p = 0.05$, generating 17 saw-teeth and hence, 17 elastic-perfectly brittle sublayer ele-
ments. Loading on the single element consists of two stages, which are both shown
by Figure 8.4. During loading stage (A), the element is loaded by tensile straining
along the x-direction, while Poisson effects are counteracted for in the other direc-
tions. Once damage is initiated and a crack in the y, z-plane is formed, perpendicular
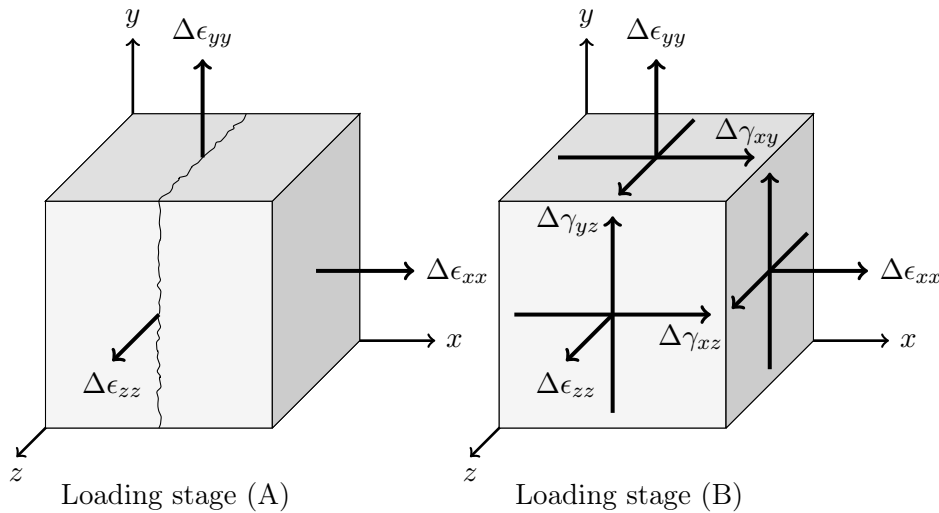to the tensile loading, the loading is changed to stage (B). During this stage, arbitrary

FIGURE 8.4: Loading stages of the 3D tension-shear problem: (A) tensile load up until first damage and (B) tension-shear load

	$\Delta\epsilon_{xx}$	$\Delta\epsilon_{yy}$	$\Delta\epsilon_{zz}$	$\Delta\gamma_{xy}$	$\Delta\gamma_{xz}$	$\Delta\gamma_{yz}$
Stage (A)	1	$-\nu_0$	$-\nu_0$	0	0	0
Stage (B)	0.5	0.75	2	1	0.5	0.5

TABLE 8.1: Relative composition of the two loading stages of the 3D tension-shear problem

strain increments in all six strain-entries are defined relative to each other: three normal strains ϵ_{xx}, ϵ_{yy} and ϵ_{zz} and three shear strains γ_{xy}, γ_{xz} and γ_{yz}. Table 8.1 gives a detailed overview on the relative load increment compositions of both stages (A) and (B). Although the load is arbitrarily chosen, a dominating strain in z-direction is applied on purpose to enforce the development of some severe crack rotations from the y,z-plane to the x,y-plane. All shear terms are positively prescribed, such that in each plane shear deformations are found that are in line with the shear deformations in Section 6.5. Hence, in each plane, a tensile tie is expected to form.

The element is modelled with a linear 8-noded brick HX24L element with a single integration point. The uniform strain state allows for reduced integration. On top of that, visualization of the cracks becomes more clear using a single integration point. Loading is applied under displacement control and some degrees of freedoms are restrained, such that the applied strain field is simulated properly. Three types of analyses are performed: 1) NLFEA based on a rotating crack model with damage based reduction of the Poisson's modulus, 2) regular SLA with $p = 0.05$ and variable shear retention and 3) the sublayer model with $p = 0.05$ as well and elastic-perfectly brittle sublayer elements that share the same nodes, following the theoretical framework of Section 8.1. Each of the sublayers is allowed to crack three times (in n, s, t-directions), although some directions might be susceptible to compression and remain uncracked, since only tensile damage is included.

Figure 8.6 contains the stress-strain plots for all six components for all performed analyses, considered in the global coordinate system. First, the results obtained with regular SLA are discussed. At the end of loading stage (A), damage is initiated in the y, z-plane, perpendicular to the uniaxial loading. Upon crack initiation, the n, s, t-axes of orthotropy are fixed in line with the global x, y, z-axes. Since the global and

local coordinate systems match, the normal stress-strain relation in x-direction directly follows the inputted tension softening law. The normal y and z components are slightly influenced by Poisson effects. Secondary and tertiary cracking takes place, such that ultimately, the crack in the x, y-plane becomes dominant. However, the fixed crack model of regular SLA implies that no shear related (diagonal) cracks can form, such that a rather abrupt transition from the initially cracked y, z-plane to the x, y-plane is obtained. On top of that, the loading is dominated but not completely governed by the normal z-component, such that the ultimate crack direction is expected to be inclined (and not perfectly in line with the x, y-plane). For these reasons, large differences are found between regular SLA and rotating crack NLFEA in the stress-strain plots, especially for the shear-related terms.

Figure 8.5 entails the crack development for five steps (A)-(E) of the sublayer model. The point of view of this figure is in line with Figure 8.4 and crack strains are visualized as projections on the element faces (such that in total three different projections are possible). After crack initiation in step (A), the crack starts to rotate in steps (B) and (C). For example in the x, y-plane, a crack rotation in line with Figure 6.12 is observed. As a result of the shear deformations, tension ties are developed in each plane, causing severe crack rotations. Both the x, z and y, z-planes show similar rotations. In order to comply with the dominant normal load direction (z), secondary cracking takes place in steps (D) and (E), such that ultimately, a crack is found that reveals combined damage in shear and uniaxial tension in z-direction. Where regular SLA results in a crack that is dominated by uniaxial tension, the sublayer model is able to describe a more gradual crack rotation that is better in line with the actual prescribed principal strain directions. To this end, damage increments are

(A) $\gamma_{xy} = 0$ (B) $\gamma_{xy} = 3.52 \cdot 10^{-5}$ (C) $\gamma_{xy} = 7.78 \cdot 10^{-5}$

(D) $\gamma_{xy} = 9.77 \cdot 10^{-5}$ (E) $\gamma_{xy} = 1.65 \cdot 10^{-4}$
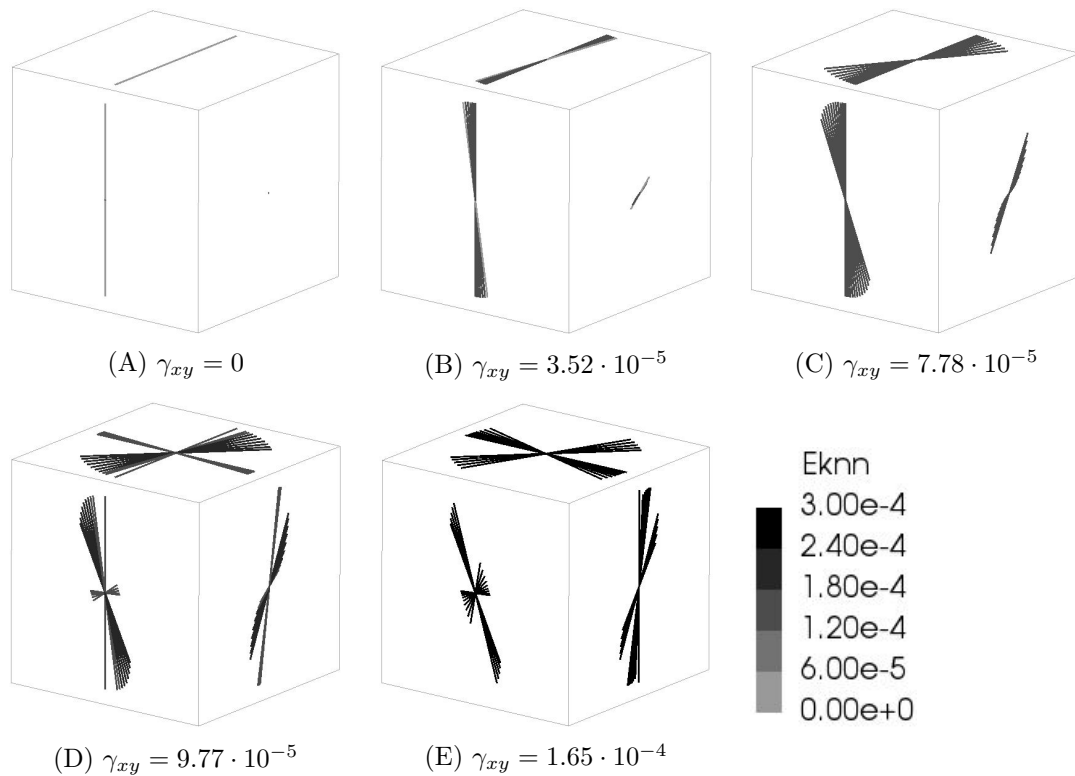
FIGURE 8.5: Crack development for specific u, mimicking a rotating crack with *Eknn* the normal strain in a crack ($\epsilon_u = 3.00 \cdot 10^{-4}$), point of view in line with Figure 8.4

(A) Relation $\sigma_{xx} - \epsilon_{xx}$

(B) Relation $\sigma_{yy} - \epsilon_{yy}$

(C) Relation $\sigma_{zz} - \epsilon_{zz}$

(D) Relation $\sigma_{xy} - \gamma_{xy}$

(E) Relation $\sigma_{xz} - \gamma_{xz}$

(F) Relation $\sigma_{yz} - \gamma_{yz}$

FIGURE 8.6: Stress-strain relations for NLFEA, regular SLA and the sublayer model for the 3D tension-shear problem

performed in directions that better approximate the principal directions, such that the effects of stress locking are reduced. When taking a closer look to Figure 8.6, it is observed that the sublayer model better aproximates the NLFEA results, especially for the shear related terms. In line with the findings of Section 6.5, some deviations are found for the normal stress components, alt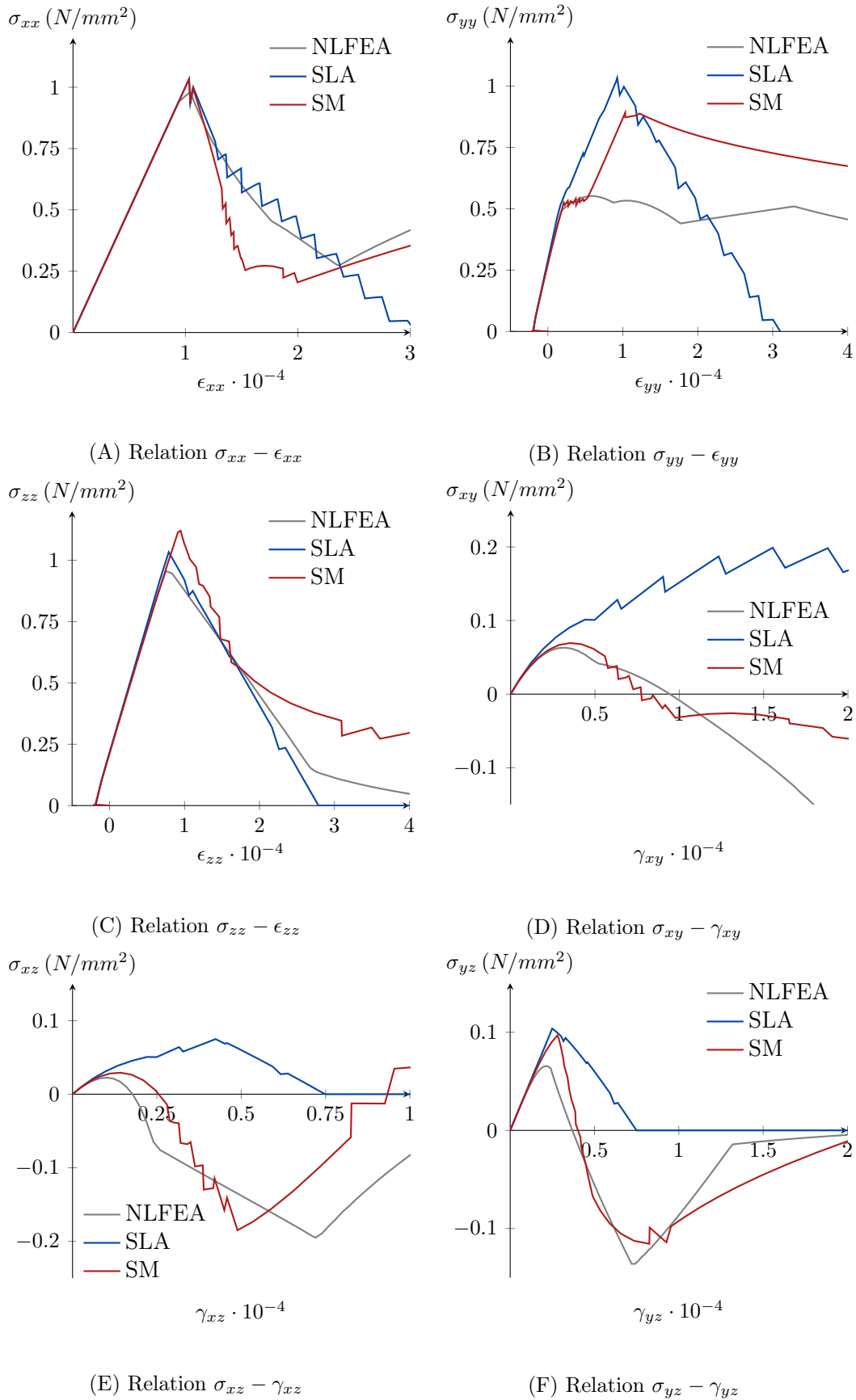hough for large strains (strains bigger than the ultimate strain), the plots of the sublayer model qualitatively better match NLFEA. Based on this single element test, it can be concluded that the 3-dimensional sublayer model entails the same behaviour and follows the same principles as the 2-dimensional model. Therefore, all discussed matter of Chapter 6 can be straight-forwardly applied to 3D problems as well. Instead of two damage increments, 3D analysis allows for three damage increments. For this case, not all directions were entirely damaged, since the loading apparently gave rise to the development of compressive struts as well.

8.3   Verification on structural level

Next, the application of the 3D sublayer model is verified on structural level. In Chapter 7, it has been observed that differences between regular SLA and the sub-layer model are found for curved crack propagation (e.g. for the shear notched beam and double-edge-notched beam). Therefore, 3D non-planar crack propagation is considered with the aid of the skewed notched beam in a three-point bending test. The skewed notched beam has been used by others as a benchmark test to verify 3D (often XFEM related) numerical algorithms [16, 41, 57]. The geometry, as shown by Figure 8.7, is in line with the 2D notched beam of Section 7.2, although the notch has a height of only 30 mm and is applied under an angle of 45 degrees, such that the front and rear notches are 60 *mm* apart. The geometry is taken from the study of Pari et al. on non-proportional loading [57]. For the purpose of this thesis, the loading is restricted to a proportional vertical mid-span line load $f = F/t$, where $t = 120\,mm$. This restriction seems justified, since non-planar crack propagation is also expected for proportional loading and solving cubic equations for non-proportional loading for each sublayer becomes very computationally expensive. Applied material properties of the specimen are listed in Table 8.2 and are exactly equal to Section 7.2. Linear tension softening is assumed.

Initially, the finite element model by Pari et al. [57] was applied (see Figure 18b in their paper). However, with a total of 111142 elements, of which 94785 elements
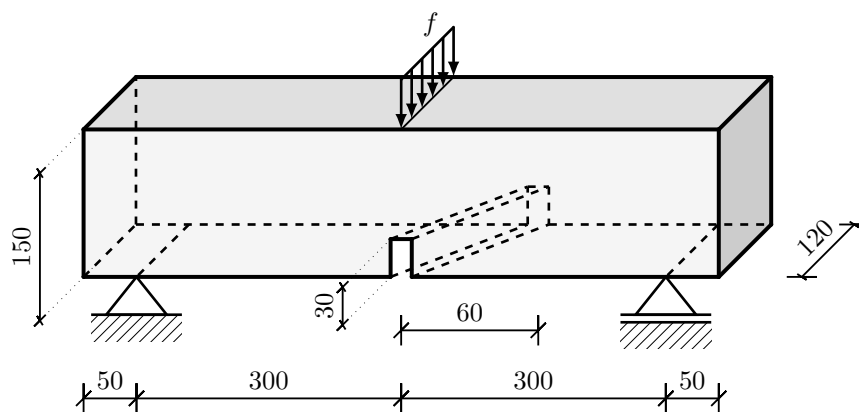

FIGURE 8.7: Geometry of the skewed notched beam in a three-point bending test and all dimensions in mm

Quantity		Value	Unit
Tensile strength	f_t	3.78	N/mm^2
Initial stiffness	E_0	16000	N/mm^2
Poisson's modulus	ν_0	0.15	-
Fracture energy	G_f	0.30	N/mm

TABLE 8.2: Material properties of the skewed notched beam, taken from Pari et al. [57] (similar to Table 7.2)
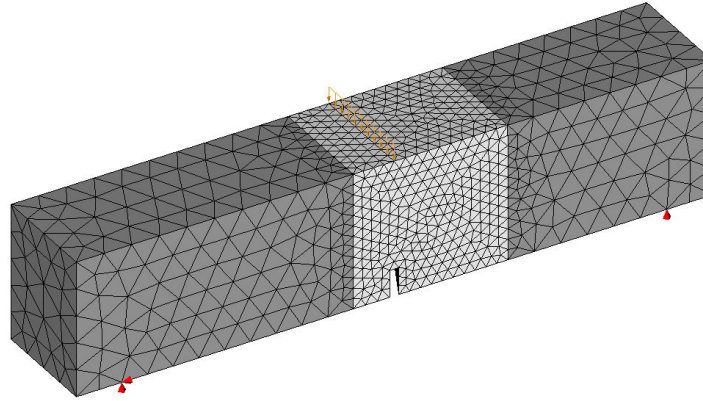

FIGURE 8.8: Finite element model for the skewed notched beam with nonlinear material behaviour assigned to bright area

were assigned nonlinear material behaviour, the computational efforts required for the sublayer model (in which the nonlinear elements are copied several times) are out of proportion. The analysis with regular SLA takes roughly a week on a relatively fast computer and the sublayer model is therefore expected to take at least a month. Obviously, this is not practical. Therefore, the mesh by Pari et al. is slightly adapted in this thesis. As can be seen in Figure 8.8, the zone of nonlinear material behaviour (bright zone) is reduced based on the zones where damage was observed by Pari et al. Furthermore, the notch width is increased from 5 *mm* to 10 *mm* and the element size in the nonlinear area is increased from 7.5 *mm* to 12 *mm*. Also, the element size in the linear regime is changed from 20 *mm* to 30 *mm*. In this way, the total number of elements reduces to 17836, of which 12642 elements are assigned nonlinear material behaviour, resulting in a reduction to 16.4% and 13.3% respectively compared to the original mesh by Pari et al. As a result of the coarser mesh, effects of mesh-directional bias possibly increase, although the mesh of Figure 8.8 can still be classified as a relatively fine mesh in the nonlinear zone. Loading is applied as a mid-span line load f, such that the total load $F = f\,t$, and line supports are created at both sides of the beam.

For 3-dimensional elements, DIANA assumes by default a crack band $h = \sqrt[3]{V}$, independent of the element type. As discussed by Voormeeren [80], the real crack band can significantly deviate from this assumed band, since cracks can potentially deviate from the mesh lines in multiple directions. As a measure, projection based crack bands could be used. However, for the purpose of this thesis, the default crack band suffices. The current implementation of the sublayer model, as discussed in Appendix B, requires a single crack band that is valid for all nonlinear elements. The volumes of the elements vary along the applied mesh and hence, each nonlinear element has its own crack band and subsequently its own saw-tooth law. A nonlinear
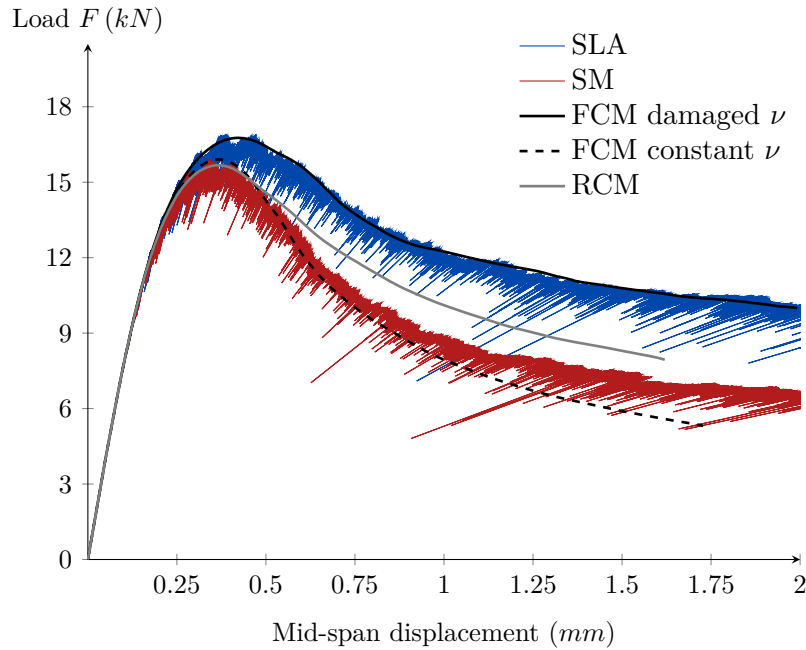
FIGURE 8.9: Load *F* versus mid-span displacement for the skewed
notched beam for regular SLA, the sublayer model and NLFEA

finite element analysis with a single load step has been performed and as an output,
the element-wise crack bands were generated. It is observed that the crack bands in
the nonlinear area vary between $5 - 7\,mm$ and therefore, all nonlinear elements are
assigned $h = 6\,mm$, such that the sublayer model implementation can be applied. To
ensure a fair comparison, all performed analyses in this section invoke the same con-
stant crack band. In line with Pari et al., four-noded linear pyramid TE12L elements
with single integration point are applied, such that constant strain distributions are
found over the entire elements. Further detailed information on the SLA-type of
analyses can be found in Table C.7.

In Figure 8.9, the total load *F* is plotted versus the mid-span displacement for all
performed analysis. For the performed NLFEA, the solutions are plotted up until
the moment that convergence was lost. The mid-span displacement is defined as
the average vertical displacement of the two upper-side corners above the mid-span
notch. For the inclined notched beam, clear differences are observed between regular
SLA and the sublayer model. In line with the findings in 2D, the sublayer model
exhibits more flexible behaviour in 3D as well: a lower peak load is found ($15.8\,kN$
versus $16.7\,kN$) and significantly less energy is dissipated, such that at a mid-span
displacement of 2 mm, the load carrying capacity is reduced by 33% ($6.7\,kN$ versus
$10\,kN$). Most differences are generated directly after the peak and are maintained
during the remainder of the analyses. Furthermore, several nonlinear finite element
analyses have been performed. All NLFEA simulations invoke a Newton-Raphson
iteration scheme with displacement steps of 0.012 mm and an energy norm of 0.0001
as convergence criteria. The following types of simulations are performed:

- NLFEA based on a fixed crack model (FCM) with damage based reduction of
  the Poisson's modulus ν and variable shear retention, being the counterpart
  of regular SLA. To this end, the obtained load-displacement curve shows very
  good agreement with regular SLA.

- NLFEA based on a fixed crack model (FCM) with no damage based reduction of ν, such that a constant ν is applied and variable shear retention, in line with the NLFEA by Pari et al. [57]. The constant ν is not in line with the theoretical framework of regular SLA and therefore clear differences are found between both analyses. Since ν is not reduced during damage increments, larger spurious stresses develop within the crack plane, ensuring quicker application of damage increments and therefore, the post-peak load reduces relatively fast as well. The found solution is in line with the results of Pari et al., although it is repeated that the constant ν results in a fundamentally different approach and therefore, one-to-one comparison with regular SLA does not make sense.

- NLFEA based on a rotating crack model (RCM) with damage based reduction of ν and shear retention based on the principle of coaxiality. With this model, a more flexible response is found compared to regular SLA. The load-displacement curve is qualitatively similar to the curve of the sublayer model: the same peak load is predicted and both analyses seem to converge to approximately the same load. However, as has already been discussed in Chapter 6, the sublayer model is not able to exactly match with RCM due to previously cracked sublayers (with outdated crack angles) contributing to the total behaviour. To that end, it is a remarkable finding that the sublayer model for this case results in an even more flexible response than RCM, indicating the presence of even less spurious stresses, where one would expect a somewhat stiffer response of the sublayer model compared to RCM. This observation is substantiated later on in this section. It can however be concluded that better agreement with the rotating crack model is encountered by invoking the 3D implementation of the sublayer model.

With the aid of so-called cutting planes, on which all crossed elements project their cracks, six cracks strain plots are generated from the front side to the rear side of the inclined notched beam in Figure 8.10 and from the bottom to the top in Figure 8.11. A clearly curved 3-dimensional crack pattern is observed for both methods. Starting from the front side, the straight vertically directed crack gradually transfers to an inclined curved crack at the rear side of the beam. Furthermore, starting from the bottom side of the beam, the crack gradually straightens towards the top, rotating from the notch direction towards the direction of the line load. In this way, a non-planar 3-dimensional crack path is obtained above the inclined notch. Effects of mesh directional bias appears to be rather limited and hence, application of the coarser mesh (compared to Pari et al.) is justified.

Before comparison with the NLFEA crack paths, the paths of regular SLA and the sublayer model are compared. In line with the U-turns that were found for the notched beam of Section 7.2, the crack paths corresponding to regular SLA in Figure 8.10 seem to be lost near the top: for all cutting planes, the crack directions at the crack tip start to deviate from the direction of crack propagation, such that ultimately, almost horizontally aligned cracks are found at the crack tip. Crack directions in regular SLA are fixed and hence, further crack propagation is arrested near the top. In this way, spurious stresses enforce the crack path to be lost. To correct for these horizontally aligned crack, the sublayer model exhibits pronounced crack rotations at this location, such that further crack propagation is possible. To this end, further propagated fully developed cracks are observed for the sublayer model. Furthermore, bigger bands of spurious stresses near the top are found for regular SLA as a result of the lost crack path. The latter statement is suported by Figure 8.11, in which differences are found in the width of the localization band, especially for

(A) SLA - 1 mm (B) SLA - 24 mm (C) SLA - 48 mm

(D) SM - 1 mm (E) SM - 24 mm (F) SM - 48 mm

(G) SLA - 72 mm (H) SLA - 96 mm (I) SLA - 119 mm

(J) SM - 72 mm (K) SM - 96 mm (L) SM - 119 mm
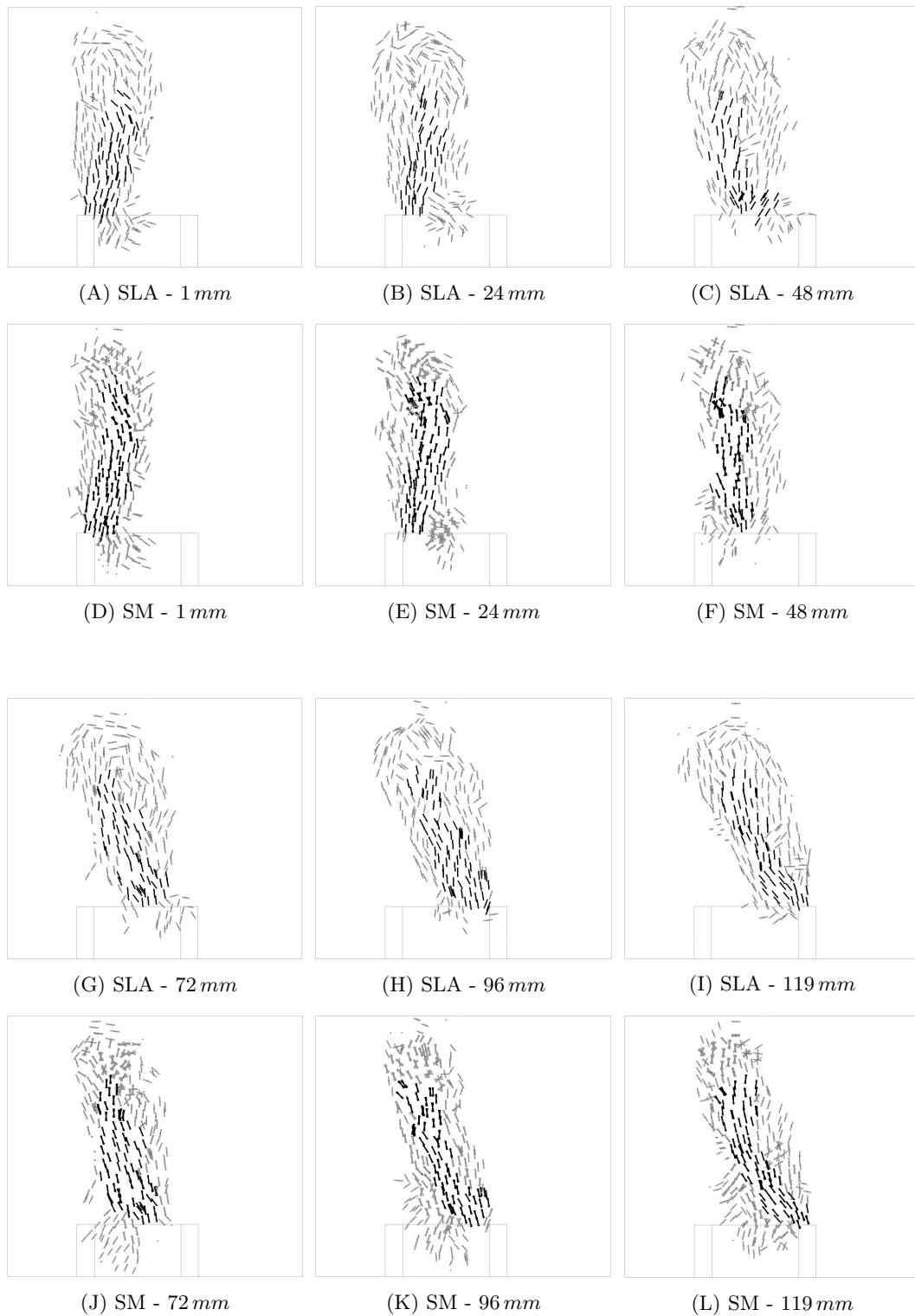
FIGURE 8.10: Crack strain plots in a vertical plane from front (0 mm) to rear (120 mm), where the front is the front side as shown in Figure 8.8, for regular SLA and the sublayer model for a mid-span displacement of 1.2 mm

(A) SLA - 31 mm (B) SLA - 45 mm (C) SLA - 60 mm

(D) SM - 31 mm (E) SM - 45 mm (F) SM - 60 mm

(G) SLA - 75 mm (H) SLA - 90 mm (I) SLA - 120 mm

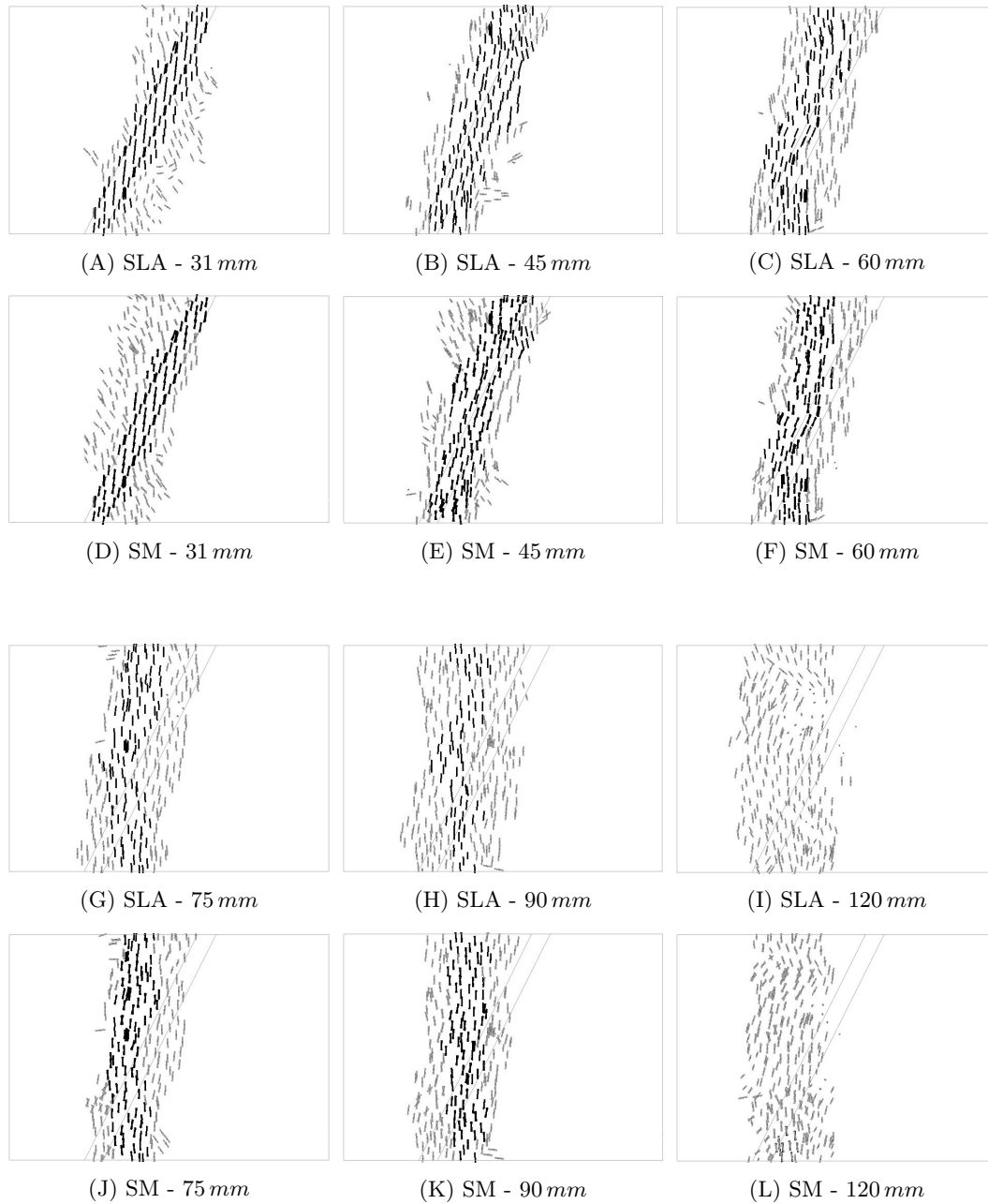(J) SM - 75 mm (K) SM - 90 mm (L) SM - 120 mm

FIGURE 8.11: Crack strain plots in a horizontal plane from bottom (0 mm) to top (150 mm), where the bottom is the bottom side as shown in Figure 8.8, for regular SLA and the sublayer model for a mid-span displacement of 1.2 mm

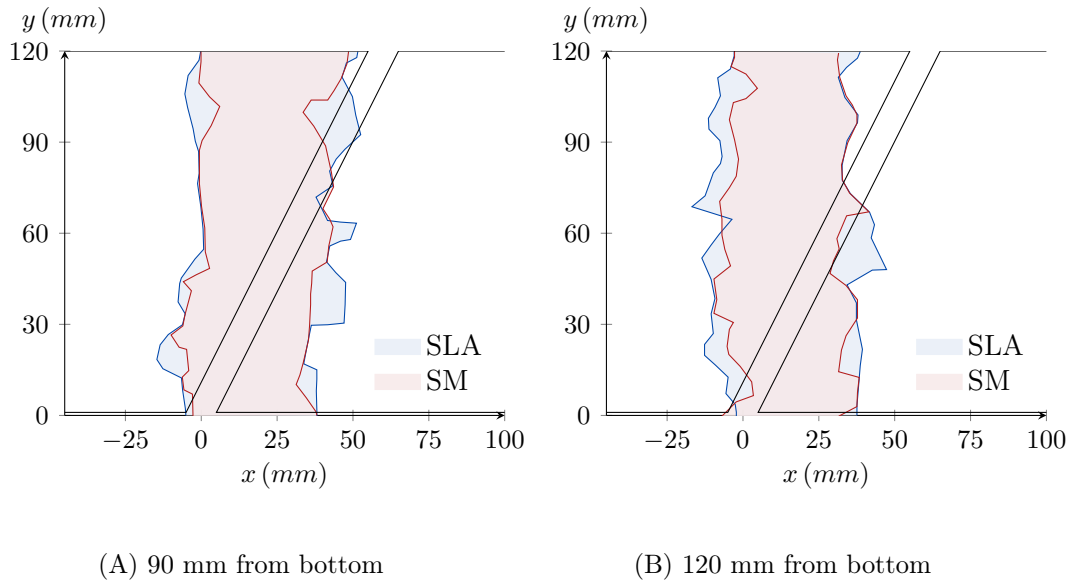(A) 90 mm from bottom   (B) 120 mm from bottom

FIGURE 8.12: Comparison of crack paths regular SLA and sublayer
model in the horizontal planes 90 mm and 120 mm from the bottom

heights 90 mm and 120mm from the bottom. Figure 8.12 gives an overlay of the crack paths for these two specific heights. Based on this overlay, it is concluded that the amount of spurious stresses is significantly reduced by the sublayer model. Combined with the more correct crack path at the top, this results in a less stiff response with less spurious energy dissipation compared to regular SLA, as can be observed in the load-displacement curve.

   Next, the crack paths of the NLFEA simulations based on fixed and rotating crack model, with damage based reduction of ν, are compared with their counterparts, regular SLA and the sublayer model respectively, in Figure 8.13. As already concluded by Pari et al. [57], the crack strain plots of NLFEA fixed crack model (FCM) and regular SLA are very similar. Although FCM results in a slightly wider localization band, both exhibit the same main crack path and a U-turn type of behaviour at the top, troubling further crack propagation. The similarity also explains the excellent agreement between the load-displacement curves of FCM and regular SLA. The crack strain plots of NLFEA rotating crack model (RCM) and the sublayer model also show similarities. The fully developed crack paths show an almost one-to-one agreement. Also, the additional crack zone next to the notch is similarly captured by both analyses. However, as becomes very clear from subfigures (B) and (F), RCM results in a wider band of spurious stresses compared to the sublayer model. Apparently, the SLA-type of procedure restricts the development of spurious crack paths, explaining the even more flexible behaviour that is obtained by the sublayer model in the load-displacement curve. A possible cause of this remarkable observation might be that for SLA-type of procedures, only a single damage increment is performed at a time, potentially allowing for a certain degree of self-correction in the next steps, while for NLFEA, damage increments are performed in any step anywhere throughout the structure, such that a complete zone of integration points can enter the spurious regime simultaneously. To this end, it is less likely for SLA-type of procedures that large zones of spurious stresses develop. Although a more thorough study on the generation of spurious stresses in RCM and FCM would be interesting, especially compared to SLA-type of analyses, such a study is beyond the scope of this thesis.

(A) FCM - 1 *mm*   (B) RCM - 1 *mm*   (C) FCM - 119 *mm*   (D) RCM - 119 *mm*

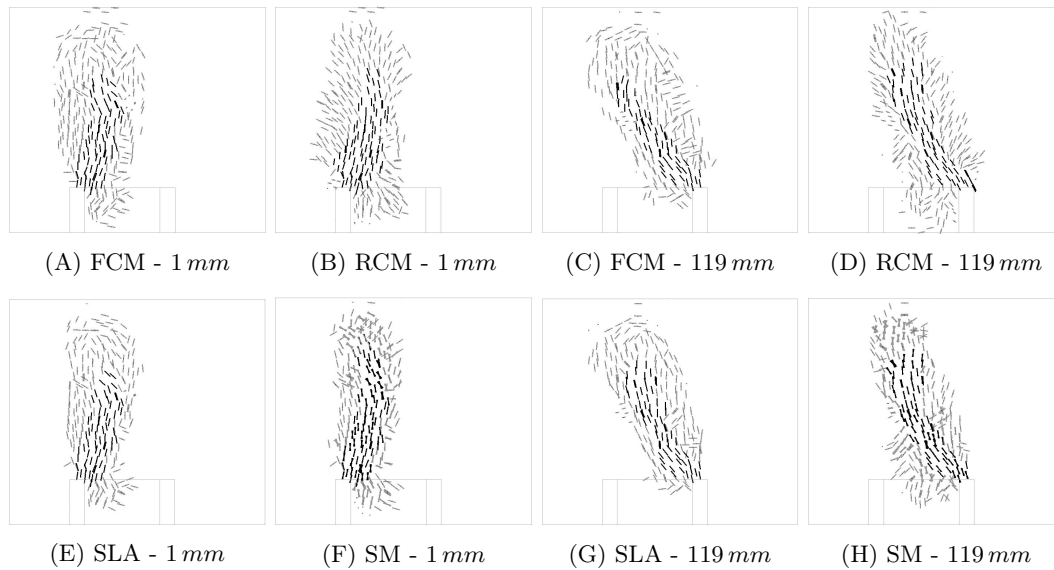(E) SLA - 1 *mm*   (F) SM - 1 *mm*   (G) SLA - 119 *mm*   (H) SM - 119 *mm*

FIGURE 8.13: Comparison of crack paths FCM and RCM NLFEA with regular SLA and the sublayer model in vertical planes at 1 and 119 mm from front side for a mid-span displacement of 1.2 mm

8.4 Discussion

In this chapter, it has been shown that the same principles as discussed in previous chapters can be applied to 3D problems as well. The proposed 3D implementation is tested on element level and on structural level and proved to be in line with a NLFEA rotating crack model. For the structural case, even more desirable solutions with less spurious stresses were obtained using the sublayer model compared to NLFEA. Although the results are very promising, the computation efforts that come along with SLA-type of procedures for 3D problems are a severe drawback. On top of that, additional computational efforts are required for the sublayer model, in which multiple overlay volume elements are applied. For example for the inclined notched beam, regular SLA takes roughly a day to reach a mid-span displacement of 2 mm (in 25000 steps) and the sublayer model takes approximately 6 days to reach the same displacement (in 24700 steps). On the contrary, the NLFEA simulations were only a matter of a few hours (up until the moment that convergence is lost). In order to apply regular SLA and especially the sublayer model to 3D problems in practice, additional research is required to significantly reduce computational efforts.

Lastly, it is noted that 3-dimensional structures with a relatively small thickness can be modelled with the aid of shell elements as well. Although the current theoretical framework of the sublayer model is restricted to 2D membrane and 3D solid elements, application to shell elements is possible following the same principles as discussed in this chapter. DeJong et al. [20] already extended the framework of regular SLA towards shell elements. In fact, shell elements are described by a 3-dimensional stress-strain relation, where normal stresses are only considered within the plane of the shell (n, s-plane), while including all three shear components. To that end, only E_n and E_s are applied and hence, two brittle damage increments are performed per sublayer shell element. With the aid of shell elements, computational efforts can be significantly reduced and therefore, it might be interesting to extend the theoretical framework of the sublayer model towards shell elements as well.

Chapter 9

Improvements and extensions

In this chapter, some improvements and extensions to the sublayer model are discussed on a conceptual level. If possible, simplistic tests are performed to substantiate the proposals. It is however noted that the main goal of this chapter is to address some concepts that can be used as an inspiration to further develop the framework of the sublayer model. First, the tapered ripple band formulation is discussed in Section 9.1, followed by the interaction between tension and compression in Section 9.2. Next, crack-closure effects are briefly discussed in Section 9.3. Lastly, computational efforts are further studied and an improved algorithm is proposed in Section 9.4.

9.1 Tapered ripple band formulation

In this section, the so-called *tapered ripple band* formulation is introduced. First, the motivation is substantiated, followed by a theoretical derivation. Lastly, the proposed tapered ripple band formulation is applied to the shear notched beam.

Motivation

For the single element tests in Chapter 6, it has been concluded that at the onset of cracking, the stress and strain states of the critical sublayer are exactly equal to NLFEA that is based on a rotating crack model. To that end, when considering an element in which all damage increments are performed and the entire saw-tooth curve is passed, it can be said that the sublayers belonging to the last few saw-teeth are 'most correct'. On a structural level, for example for analysis (A) of the shear notched beam of Section 7.3, a similar phenomena is observed. In Figure 9.1, crack strain plots are shown for four different sublayers, varying from the first sublayer to crack ($k = N$) to the last to crack ($k = 1$). Most spurious stresses seem to take place in

(A) Layer $k = N = 19$ (B) Layer $k = 17$ (C) Layer $k = 14$ (D) Layer $k = 1$
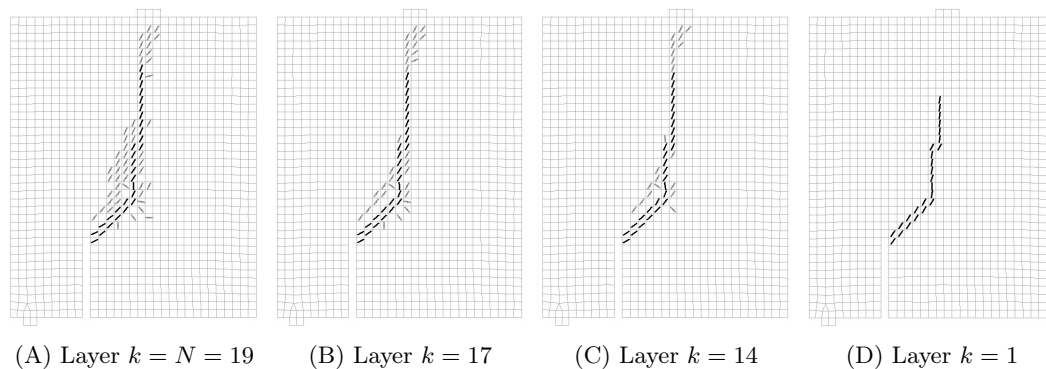
FIGURE 9.1: Crack strain plots for four sublayers k of analysis (A) as performed in Section 7.3 with the sublayer model

the first few sublayers that crack, corresponding to relatively small strains. Sublayer $k = 1$ does not show any spurious stresses at all. On top of that, the crack rotation of sublayer $k = 1$ is, compared to other sublayers, best adapted to the actual stress state (since its crack direction is most up-to-date). Although the first sublayers to crack are required to redistribute stresses upon damage initiation and to initiate the correct crack path, the last sublayers to crack reveal most accurate behaviour and therefore, it is desirable to increase the amount of 'last sublayers', while maintaining the same amount of first sublayers to ensure a proper level of accuracy at crack initiation.

However, for the current ripple band formulation, as a result of the decreasing secant stiffness for increasing strain, most saw-teeth are found around ϵ_t and least saw-teeth are found around ϵ_u, as can be seen in Figures 5.5 and 5.7. Upon reduction of the ripple band parameter p, the number of saw-teeth increases. As will be shown later in this section, this results mainly in an increase of saw-teeth around ϵ_t, while it might be more optimal to mainly increase the number of 'last sublayers' instead for the aforementioned reasons. To this end, the tapered ripple band formulation is proposed. An additional ripple band parameter r is introduced such that the ripple band linearly decreases from pf_t at ϵ_t to $(p - r)f_t$ at ultimate strain ϵ_u, as visualized by Figure 9.2. The tapered ripple band is a measure to effectively increase the accuracy of the analysis by having more saw-teeth at the end of the saw-tooth curve, while reducing the required additional computational efforts compared to the standard ripple band formulation. In this way, more efficient use is made of the sublayers and computational efforts are limited. Furthermore, as has been observed for the shear notched beam in Figure 9.1, spurious stresses are mostly found in the first few sublayers. Since the first few sublayers do not change and the total number of sublayers increases for the tapered ripple band formulation, the relative influence of the first few sublayers on the total elements behaviour reduces and hence, the effects of spurious stresses are expected to reduce accordingly.

Derivation

For simplicity, the derivation is limited to linear tension softening, although the same concepts can be used for other nonlinear tension softening laws as well. In the case of nonlinear softening, the ultimate strain ϵ_u is the strain for which 98% of the fracture energy has dissipated. The derivation of the tapered ripple band algorithm is in line with the derivation of the regular ripple band in Section 5.2. The first branch
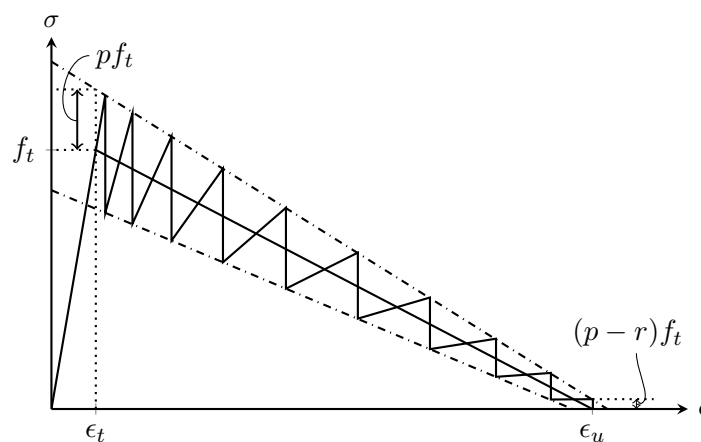

FIGURE 9.2: Visualization of the tapered ripple band concept, compare to the regular ripple band concept of Figure 5.2

is a linear elastic branch with stiffness E_0. Once the tensile strength f_t is reached, the second branch with negative slope D is entered. The upper and bottom tapered ripple bands have negative slopes D^+ and D^- respectively, given by

$$D^+ = \frac{(1+r)f_t}{\epsilon_u - \epsilon_t} \quad \text{and} \quad D^- = \frac{(1-r)f_t}{\epsilon_u - \epsilon_t} \tag{9.1}$$

such that the upper tapered ripple band is described by

$$\sigma^+ = D^+(\epsilon_t - \epsilon) + (1+p)f_t \tag{9.2}$$

Considering a specific saw-tooth i, the point of intersection $\epsilon_{t,i}$ between the secant elastic branch with stiffness E_i and the upper tapered ripple band is found by solving the following equality:

$$E_i \epsilon_{t,i} = D^+(\epsilon_t - \epsilon_{t,i}) + (1+p)f_t \tag{9.3}$$

from which $\epsilon_{t,i}$ is found by

$$\epsilon_{t,i} = \frac{D^+\epsilon_t + (1+p)f_t}{D + E_i} \tag{9.4}$$

Note the similarities between Equations 5.4 and 9.4. Next, the saw-tooth tensile strength on the upper band is determined by $f_{t,i}^+ = \epsilon_{t,i} E_i$. In the regular ripple band formulation, a constant vertical stress drop $\Delta = 2pf_t$ is applied to obtain $f_{t,i}^-$. For the tapered ripple band formulation, the size of the drop Δ linearly reduces for increasing strain. For $\epsilon = \epsilon_t$, the vertical drop equals $2pf_t$ and for $\epsilon = \epsilon_u$, the drop equals $2(p-r)f_t$, such that in between, the drop Δ is described by

$$\Delta = 2\left(p - \frac{\epsilon_{t,i} - \epsilon_t}{\epsilon_u - \epsilon_t}r\right)f_t \tag{9.5}$$

and subsequently

$$f_{t,i}^- = f_{t,i}^+ - \Delta \tag{9.6}$$

Lastly, the stiffness of the following saw-tooth is determined by substitution of Equations 9.4 and 9.6 in

$$E_{i+1} = \frac{f_{t,i}^-}{\epsilon_{t,i}} \tag{9.7}$$

The described process is repeated until $f_{t,i}^+ < 2(p-r)f_t$, meaning that the last saw-tooth is reached. Parameter r is restricted to $0 \le r \le p$. For $r = 0$, the regular ripple band formulation is obtained. Reducing p mainly results in more saw-teeth around ϵ_t and reducing r mainly results in more saw-teeth around ϵ_u.

Application
To exemplify the proposed tapered ripple band formulation, the algorithm is applied to the shear notched beam. For the sake of simplicity, linear tension softening is applied instead of Hordijk softening. The same material properties as listed in Table 7.3 are used, although the fracture energy G_f is reduced to $0.1 \, N/mm$ to take account of the neglected 'tail' of the nonlinear softening curve (similar to the approach of DeJong et al. [21]). Analysis (A) of Section 7.3 is revisited, making use of linear elements with reduced integration. In this section, four saw-tooth laws are applied:

- *Saw-tooth curve (A)*: Regular ripple band with $p = 0.15$ and $N = 14$

- *Saw-tooth curve (B)*: Regular ripple band with $p = 0.112$ and $N = 19$

- *Saw-tooth curve (C)*: Regular ripple band with $p = 0.086$ and $N = 24$

- *Saw-tooth curve (D)*: Tapered ripple band with $p = 0.15$, $r = 0.12$ and $N = 19$

Figure 9.3 gives an overview of the four saw-tooth laws. Saw-tooth curve (A) is taken as a starting point. In order to increase the accuracy of the analysis, one could increase the number of saw-teeth. This can be achieved in two ways: either by reduction of p in curve (B) following the regular ripple band or by increasing r while maintaining the same p in curve (D) following the tapered ripple band. When comparing curves (A), (B) and (D), it is observed that curve (B) entails more saw-teeth in the first stage of softening, while curve (D) shows more saw-teeth in the final stage of softening. The number of 'last sublayers' increases significantly for curve (D) and more accurate results are expected since these last layers reduce the influence of spurious stresses and correct the crack direction, as discussed before. Even when p is further reduced in curve (C) based on a regular ripple band, the number of saw-teeth in the final stage of softening is lower compared to curve (D) and most additional saw-teeth are found in the first stage of softening.

The load - CMSD graphs for all four saw-tooth curves are shown by Figure 9.4. The graphs belonging to curves (A)-(C) are based on the regular ripple band formulation and indicate that an increasing number of saw-teeth results in a more flexible response and less energy dissipation. Both curves (B) and (D) have 19 sublayers. However, with the tapered ripple band formulation of curve (D), significant differences are found compared to the regular ripple band formulation of curve (B). Apparently, less stress locking is observed when making use of the tapered ripple band. Curves (C) and (D) give similar results, although curve (C) invokes 24 sublayers and curve (D) only 19 sublayers, marking a clear fundamental difference between both methods. With this graph, a promising feature of the tapered ripple band formulation is demonstrated: to obtain the same level of accuracy, the tapered ripple band requires less saw-teeth compared to the regular ripple band and hence, more efficient use is made of the sublayer model and a measure to reduce computational efforts is offered. For the sublayer model, which is computationally quite demanding, a potential reduction of sublayers becomes very attractive for two reasons. Firstly, the total number of sublayers and therefore the number of elements in the finite element model reduces. Secondly, the total number of events that is required to reach a specific state reduces, as there are less sublayers defined. Since curve (C) uses 26% more saw-teeth as curve (D), it is expected that curve (C) requires roughly the same percentage of additional events compared to curve (D). In this way, computational efforts can be signicantly reduced.

Lastly, Figure 9.5 gives an overview of the crack strain plots for all four saw-tooth curves. The crack strain plots confirm the described findings. The crack paths that are obtained by curves (C) and (D) are similar and even a smaller localization band with less spurious stresses seems to be found by curve (D). Compared to curves (A) and (B), clear differences are observed regarding the width of the localization band and the accuracy of the crack path, indicating that the tapered ripple band formulation offers an improvement to the sublayer model.

Further research is required in order to offer some guidelines on how to optimize the saw-tooth curves and to understand which values should be assigned to the tapered ripple band parameters p and r. Furthermore, more case studies should be performed to rule out the possibility that the results of this study are case-specific.

(A) Ripple: $p = 0.15$, $N = 14$

(B) Ripple: $p = 0.112$, $N = 19$

(C) Ripple: $p = 0.086$, $N = 24$

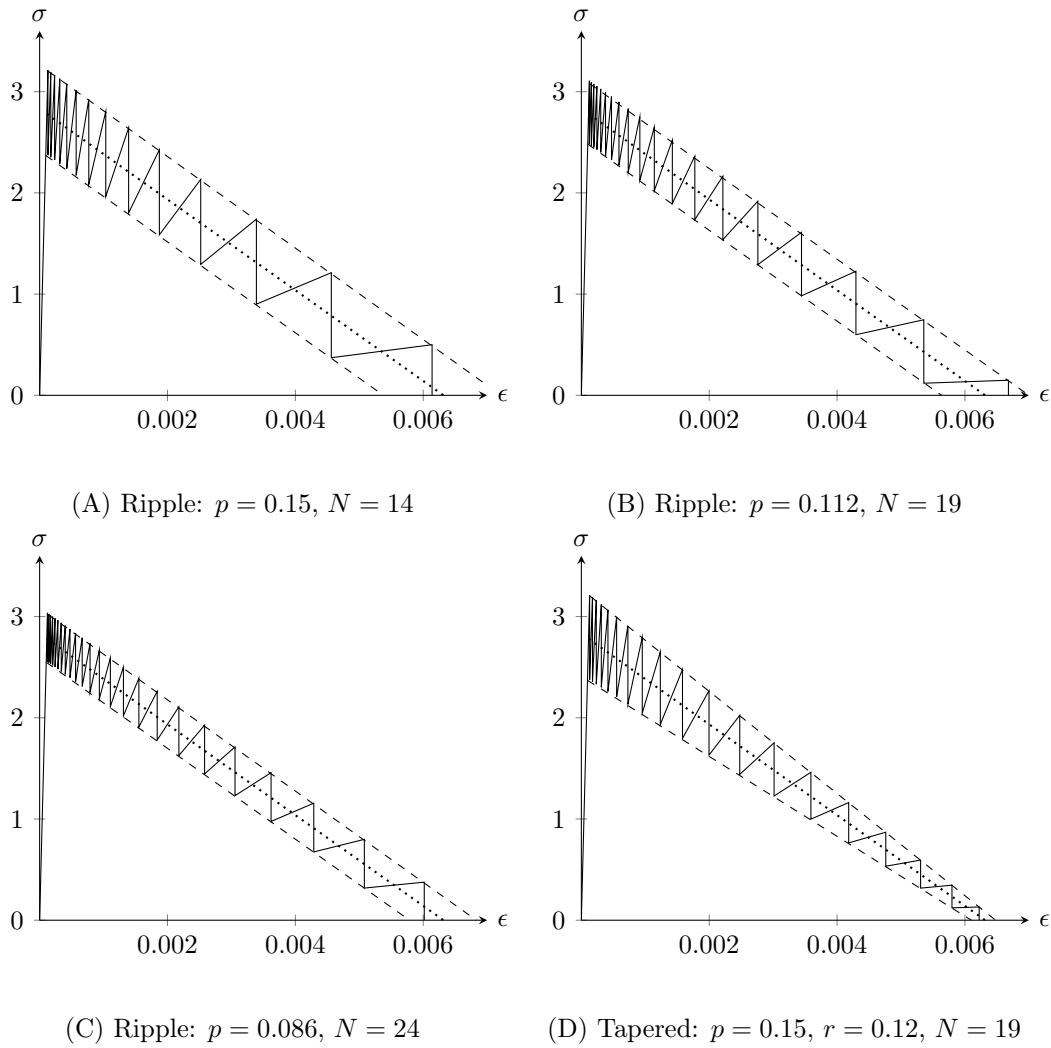(D) Tapered: $p = 0.15$, $r = 0.12$, $N = 19$

FIGURE 9.3: Overview of the four applied saw-tooth laws for both the regular and tapered ripple band for linear tension softening
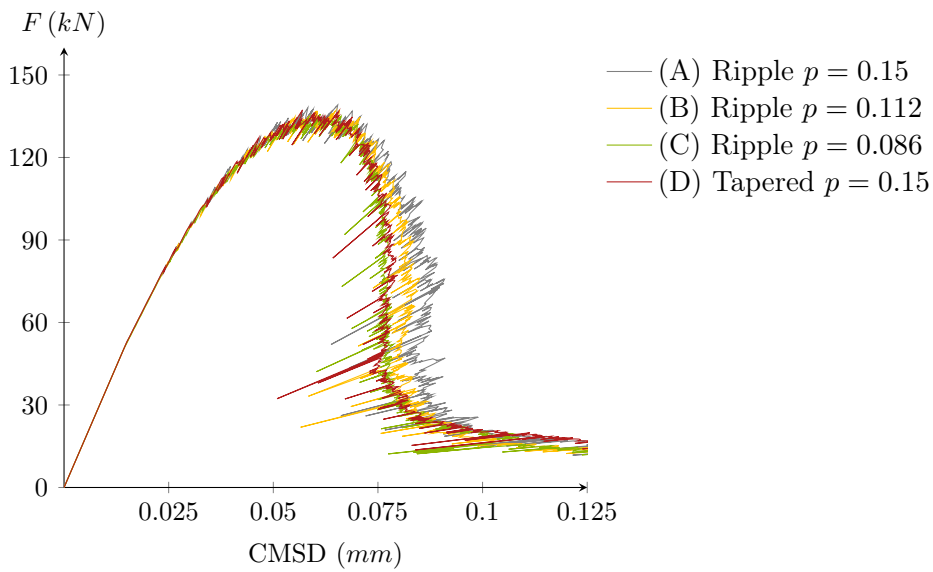

FIGURE 9.4: Load on the shear notched beam versus CMSD for different ripple and tapered saw-tooth laws
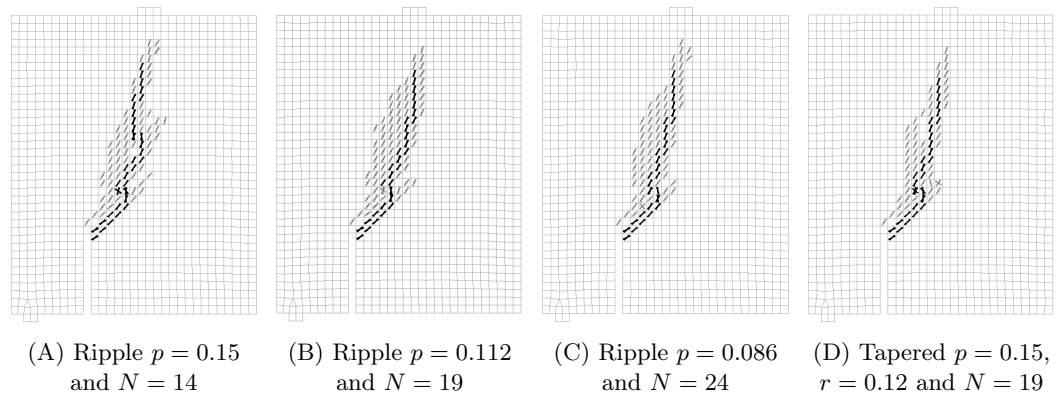
| (A) Ripple $p = 0.15$ and $N = 14$ | (B) Ripple $p = 0.112$ and $N = 19$ | (C) Ripple $p = 0.086$ and $N = 24$ | (D) Tapered $p = 0.15$, $r = 0.12$ and $N = 19$ |

FIGURE 9.5: Crack strain plots for a CMSD of $0.10\,mm$ for all four saw-tooth laws

9.2   Interaction tension and compression

In this section, some conceptual extensions to sequentially linear analysis are proposed regarding the interaction of tension and compression for both the primary and secondary crack initiation in 2D. The framework of SLA does not include any tension-compression interaction yet and therefore, some attention is paid to the implementation in regular SLA as well, although the main focus of this section is put on the sublayer model. It is noted that the extensions in this section are merely conceptual: no tests are performed. The purpose of this section is to contribute to the development of SLA-type of approaches in general. First, the stress-interaction during primary crack initiation is discussed. Especially under combined tension and compression in the principal directions, significant effects of stress-interaction can be observed. Secondly, the formation of a laterally cracked compressive strut according to Vecchio and Collins is described. As discussed in Section 2.3.5, the compressive strength of the concrete strut is related to the lateral tensile strain.

Interaction primary crack initiation
For uni-axial stress states, damage is initiated upon reaching the tensile or compressive strength. In the current 2D and 3D frameworks, the axes of orthotropy are fixed and damage is initiated once the strength is reached in one of the principal stress directions. To this end, the current crack initiation criterium is in line with a Rankine type of yield surface, which is shown by Figure 9.6. However, as briefly discussed in Section 2.1, Kupfer et al. [43] observed interaction between the principal stresses. Especially for combined tension and compression, a significant strength reduction was found (see Figure 2.3). To that end, many crack criteria have been developed during the years. In this section, a linear interpolation for combined tension and compression is assumed, as shown by Figure 9.6, in line with a Mohr-Coulomb type of yield surface. However, the Mohr-Coulomb yield surface relates the tensile and compressive strengths by internal friction and cohesion parameters. In this study, these material parameters are not used and the compressive and tensile strengths are assumed to be predefined values. In this way, a very simple linear yield surface is created, enveloped by criteria (1) to (4), in line with the experimental results by Kupfer et al. In these criteria, strengths f_t and f_c are positive and negative values respectively.

For proportional loading, principal stresses σ_1 and σ_2 are fully dependent on the load multiplier λ. In the current framework, a primary crack is initiated once the
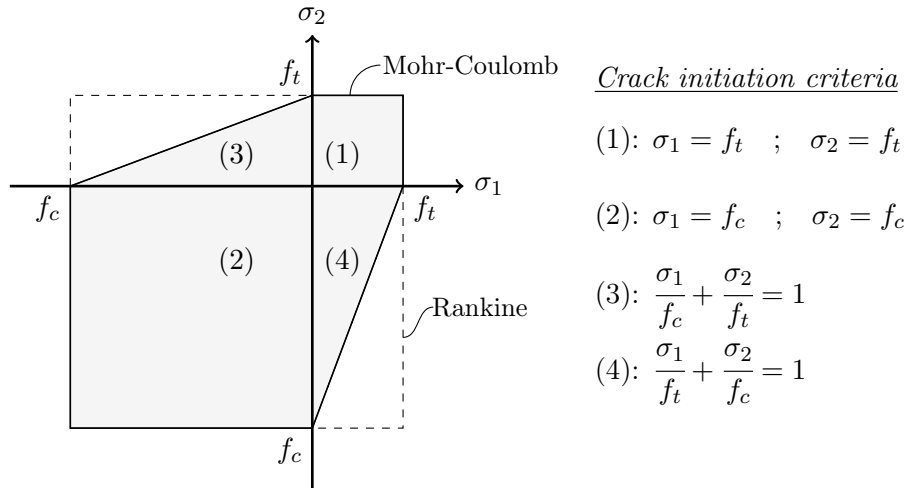
FIGURE 9.6: Crack initiation for biaxial stress states with Rankine and
Mohr-Coulomb types of criteria

maximum principal stress reaches the strength (either compressive or tensile). By
definition, σ_1 is the largest stress. For criteria (1) and (2), the current implementation
suffices, which is given by

$$
\begin{aligned}
(1): & \quad \sigma_1(\lambda) = \lambda \sigma_{1,B} = f_t \quad \rightarrow \quad \lambda = \frac{f_t}{\sigma_{1,B}} \\
(2): & \quad \sigma_2(\lambda) = \lambda \sigma_{2,B} = f_c \quad \rightarrow \quad \lambda = \frac{f_c}{\sigma_{2,B}}
\end{aligned}
\tag{9.8}
$$

where B represents the proportional reference load, in line with the derivation in
Section 3.5, and both the tensile and compressive capacities are monitored. From
Equations 9.8, two values for λ are straightforwardly solved for each integration
point. For criteria (3) and (4), λ is determined from

$$
\begin{aligned}
(3): & \quad \frac{\lambda \sigma_{1,B}}{f_c} + \frac{\lambda \sigma_{2,B}}{f_t} = 1 \quad \rightarrow \quad \lambda = \left(\frac{\sigma_{1,B}}{f_c} + \frac{\sigma_{2,B}}{f_t} \right)^{-1} \\
(4): & \quad \frac{\lambda \sigma_{1,B}}{f_t} + \frac{\lambda \sigma_{2,B}}{f_c} = 1 \quad \rightarrow \quad \lambda = \left(\frac{\sigma_{1,B}}{f_t} + \frac{\sigma_{2,B}}{f_c} \right)^{-1}
\end{aligned}
\tag{9.9}
$$

respectively, from which again two values for λ can be found. In fact, the solutions
λ of Equations 9.8 and 9.9 describe the crossing points of a linear line in σ_1, σ_2-space
with the yield surface. This linear line is fully dependent on λ, crosses the origin
and therefore only has two crossing points with the yield surface. Hence, two of
the criteria will not result in a value and should not be added to the total set of load
multipliers from which λ_{crit} is determined. Since all relations are linear, proportional
loading does not require complex solving algorithms and therefore, the set of load
multipliers is determined straightforwardly.

For non-proportional loading, implementation of the interaction between ten-
sion and compression for primary crack initiation becomes a bit more complex. For
criteria (1) and (2), the derivation by DeJong et al. [21] is followed. Principal stresses
σ_1 and σ_2 are found from

$$
\sigma_{1,2}(\lambda) = \frac{1}{2}(\sigma_{xx} + \sigma_{yy}) \pm \sqrt{\frac{1}{4}(\sigma_{xx} - \sigma_{yy})^2 + \sigma_{xy}^2}
\tag{9.10}
$$

where

$$
\begin{aligned}
\sigma_{xx} &= \sigma_{xx,A} + \lambda\sigma_{xx,B} \\
\sigma_{yy} &= \sigma_{yy,A} + \lambda\sigma_{yy,B} \\
\sigma_{xy} &= \sigma_{xy,A} + \lambda\sigma_{xy,B}
\end{aligned}
\tag{9.11}
$$

in which A represents the initial constant non-proportional loading and B the increasing proportional loading. The principal stresses are non-linearly related to λ. For criteria (1) and (2), the principal stress is set equal to the strength, from which λ is solved subsequently. For criteria (3) and (4), interaction between σ_1 and σ_2 is observed according to Figure 9.6, leading to

$$
\begin{aligned}
(3):\quad & \frac{\sigma_1(\lambda)}{f_c} + \frac{\sigma_2(\lambda)}{f_t} = 1 \\
(4):\quad & \frac{\sigma_1(\lambda)}{f_t} + \frac{\sigma_2(\lambda)}{f_c} = 1
\end{aligned}
\tag{9.12}
$$

in which the principal stresses $\sigma_{1,2}(\lambda)$ follow from Equation 9.10. After substitution of the principal stresses, a quadratic equation is found which can be solved analytically for λ, in line with the current framework. Although the solution becomes more elaborate, no fundamental differences arise between the current framework and the proposed extended framework. In fact, intersections between the nonlinear curve in σ_1, σ_2-space and the yield contour are searched for, such that a set of load multipliers is determined for which constitutively allowable stress states are found. Following the constrained maximalization analogy of Van de Graaf [29], load multiplier sets are obtained on integration point level by the four crack initiation criteria and subsequently, a common load multiplier set on model level is searched for, from which the critical load multiplier is obtained. If there is no common set of load multipliers possible, the double load multiplier strategy is applied, in which the last successful combination of the initial load and the proportional load is multiplied to fulfill all constitutive laws.

Although it is mentioned that Equations 9.12 can be solved analytically, no solution is given in this thesis: the multi-line analytic solution is not relevant for the purpose of this thesis and becomes unreadable. Lastly, it is noted that the implementation of interaction for primary crack initiation is exactly the same for both regular SLA and the sublayer model.

Interaction secondary crack initiation
In Section 2.3.5, the compressive behaviour of laterally cracked concrete is discussed. Especially for reinforced concrete, compressive struts are able to form in the secondary crack direction. Vecchio and Collins [77] performed a wide variety of tests to be able to capture the influence of lateral tensile strains on the struts compressive strength. For fully developed tensile cracks, the compressive strength reduces to approximately 40%. To that end, Hendriks and Rots [31] applied a softening parameter $\beta = 0.4$ after the initiation of damage. However, for intermediate strains, this value of β might be inaccurate. In this section, a framework is proposed to account for the effects of lateral cracking on the secondary compressive crack initiation (and damage increments for regular SLA), in line with the findings of Vecchio and Collins.

In their study, Vecchio and Collins [77] proposed two models to encounter the effects of lateral cracks on the compressive strength. In model A, both the peak stress and corresponding compressive strain are reduced by the same factor β, which is given by Equation 2.27. In this model, the strength reduction depends on the
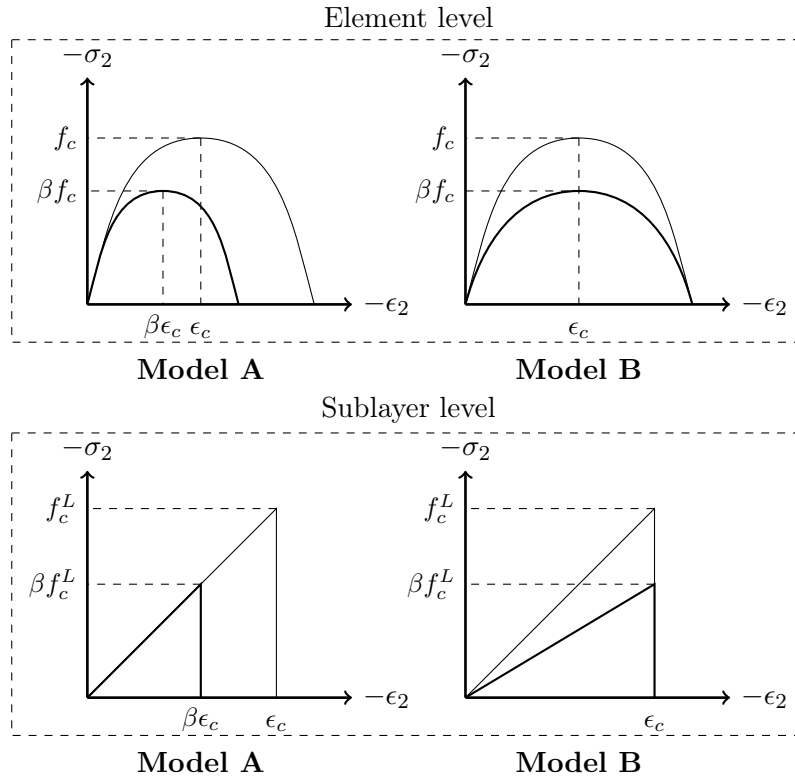
FIGURE 9.7: Visualization of models A and B of Vecchio and Collins [77] on element level and on sublayer level

strain in both the tensile and compressive directions. For model B, only the peak stress is reduced by β, which is described by Equation 2.30. For this model, the strength reduction is merely a function of the lateral tensile strain. The adapted constitutive laws on element level and sublayer level are shown by Figure 9.7. On sublayer level, a elastic-perfectly brittle constitutive law is observed. For model A, the sublayer strength is reduced while maintaining the stiffness, where for model B both the sublayer strength and stiffness are reduced. In this way, the stiffness becomes strain dependent for model B, which is not very suitable for an SLA-type of analysis, since the linear elastic analysis requires a specified stiffness. On top of that, Vecchio and Collins mention that the highest correlation with experimental data was obtained for model A. Therefore, it is proposed to combine the sublayer model with model A. In this way, a better correlation with the data is obtained, while maintaining the sublayer stiffnesses and reducing the tensile strengths in line with the previously described interaction for primary crack initiation. For completeness, the applied reduction factor β is given here.

$$\beta = \frac{1}{1 + K_c K_f} \tag{9.13}$$

with

$$K_c = 0.35 \left(\frac{-\epsilon_1}{\epsilon_2} - 0.28 \right)^{0.80} \geq 1.0 \tag{9.14}$$

and

$$K_f = 0.1825\sqrt{f_c} \geq 1.0 \qquad (9.15)$$

Reduction factor β is determined per sublayer, since all sublayers potentially have different axes of orthotropy and thus different definitions of ϵ_1 and ϵ_2 directions. Although on element level, all sublayers have the same strain, the fixed crack model on sublayer level results in local ϵ_1 and ϵ_2 which are not in line with the principal strain directions. Parameter K_f takes the influence of the material strength on the reduction factor β into account. The sublayer strengths do not have a real physical meaning and therefore, it is proposed to assign the same K_f, which is determined based on the real material strength, to all sublayers.

For proportional loading, both ϵ_1 and ϵ_2 are linearly related to load multiplier λ. Hence, the ratio ϵ_1/ϵ_2 in Equation 9.14 becomes a constant value that is independent of λ. Therefore, the compressive strength for secondary compressive cracking reduces to βf_c, such that

$$\sigma_2(\lambda) = \lambda\sigma_{2,B} = \beta f_c \qquad (9.16)$$

from which λ can be easily solved. In line with the interaction for primary crack initiation, only the strength criteria are influenced. Equation 9.16 describes the intersection between a linearly increasing σ_2 and the reduced strength.

For non-proportional loading, both ϵ_1 and ϵ_2 become non-linearly related to λ, such that ratio ϵ_1/ϵ_2 becomes a nonlinear function of λ. Equation 9.14 reduces to

$$K_c = 0.35 \left(\frac{-(\epsilon_{1,A} + \lambda\epsilon_{1,B})}{\epsilon_{2,A} + \lambda\epsilon_{2,B}} - 0.28 \right)^{0.80} \geq 1.0 \qquad (9.17)$$

and the reduction factor β becomes a function of λ as well, leading to

$$\sigma_2(\lambda) = \beta(\lambda)f_c \qquad (9.18)$$

In this way, the implementation becomes very similar to the one for primary crack initiation: after substitution of Equations 9.10 and 9.13, nonlinear equation 9.18 is solved to λ. Since the expression for K_c is quite complex, it is proposed to solve λ with the aid of a numerical nonlinear solver. In this thesis, no further attention is paid on how to solve for λ. After finding λ, the regular procedure by Van de Graaf [29] is followed. For regular SLA, the constitutive law and thus the saw-tooth law become strain-dependent, such that the saw-tooth law should be continuously adjusted. Within the sublayer model, each sublayer only has a single saw-tooth, thereby significantly reducing the complexity of the problem. In fact, the transition from saw-tooth law to a set of single saw-tooth sublayers allows for a procedure in which only the strengths of the sublayers are influenced. However, the same approach as proposed for the sublayer model can be applied to regular SLA as well.

Lastly, it is noted that also another type of interaction exists, namely for laterally confined concrete in compression. Laterally confined concrete exhibits higher compressive strengths, as the concrete is in fact laterally pre-compressed, restricting the occurrence of concrete crushing. Although some theoretical frameworks exist to take account of this interaction, it was found that these were too complex to be straightforwardly combined with the framework of SLA (although it might be possible). Therefore, for the time being, these effects are not further considered in this thesis, although further research into this topic is recommended to allow for a more general application.

9.3 Crack-closure effects

One of the main assumptions of SLA-type of analyses is secant loading and unloading, as has been briefly discussed in Section 3.5. To this end, cracks completely close during unloading. However, in experiments with cyclic loading on concrete structures, often a type of hysteresis is observed as a result of non-secant unloading, which can not be captured within the current framework of SLA. Furthermore, damage increments are permanent such that the damaged stiffness is maintained during load reversal, while in reality, the closing crack should regain its original stiffness (as visualized in Figure 3.5 and discussed by Pari et al. [58]). Crack-closure occurs when the stress in a cracked element reduces or even reverses, which is quite common for cyclic loading. On top of that, local stress redistributions might enforce severely changing or even reversing stress states as well. Crack-closure does not by definition require a complete reversal of the stress state, but can also take place when the stress state significantly rotates (e.g. by 70 degrees), such that the active crack is arrested or even unloaded. In this section, the current framework of regular SLA and the sublayer model are considered and no new improvements or extensions are proposed: this section merely gives an overview on the performance of both models under crack closure and stress reversal.

The effects of crack-closure can be considered on two levels: locally, considering the response of a single element to changing/reversing load conditions, and globally, focusing on the structural response regarding stress redistributions, adaptability and development of the collapse mechanism. Locally, regular SLA can only adapt to changing load conditions by damage increments in the fixed crack directions (either in the primary or secondary direction), restricting the adaptability of the model. On a global level, regular SLA offers some more flexibility: surrounding undamaged elements may crack to adjust the global behaviour such that the local incorrect behaviour is corrected/compensated for. However, for increasing crack-closure effects, regular SLA might result in a locked-in situation, as has been observed for the full scale facade in Section 7.5 and the concrete dam in Section 7.6.2, due to the surrounding cracked elements not being able to correct the behaviour anymore.

For regular SLA, not only the performed damage increments are permanent: also the direction of damage is fixed, leading to additional issues for changing and/or reversing stress states. Although for the sublayer model, damage increments are permanent as well, the direction of damage on element level can change, allowing for the development of different types of fractures within a single element, which are restricted for regular SLA. Therefore, the sublayer model offers locally more adaptability to changes/reversal of stress states. In order to exemplify this statement, crack development of an imaginary element with six sublayers subjected to an arbitrary undefined load path is visualized by Figure 9.8. During the first three steps, tensile damage is initiated. Subsequently, the load is changed such that in the following five steps, compressive damage increments are applied and the tensile crack is arrested (or possibly even closes). Since the first three sublayers (A)-(C) already cracked in tension, their crack directions are fixed. However, sublayers (D) and (E) are uncracked and can fully adapt to the changing load conditions. In this way, the sublayer model is able to partly cope with the effects of crack-closure, although limited to the uncracked part of the total element. In the last four steps, loading is again switched such that tensile damage increments are performed. Ultimately, four out of six sublayers have their axes of orthotropy fixed by a tensile load and two out of six by compressive load. Although the effects of permanent damage increments remain, it is shown that the sublayer model offers more adaptability on local level.
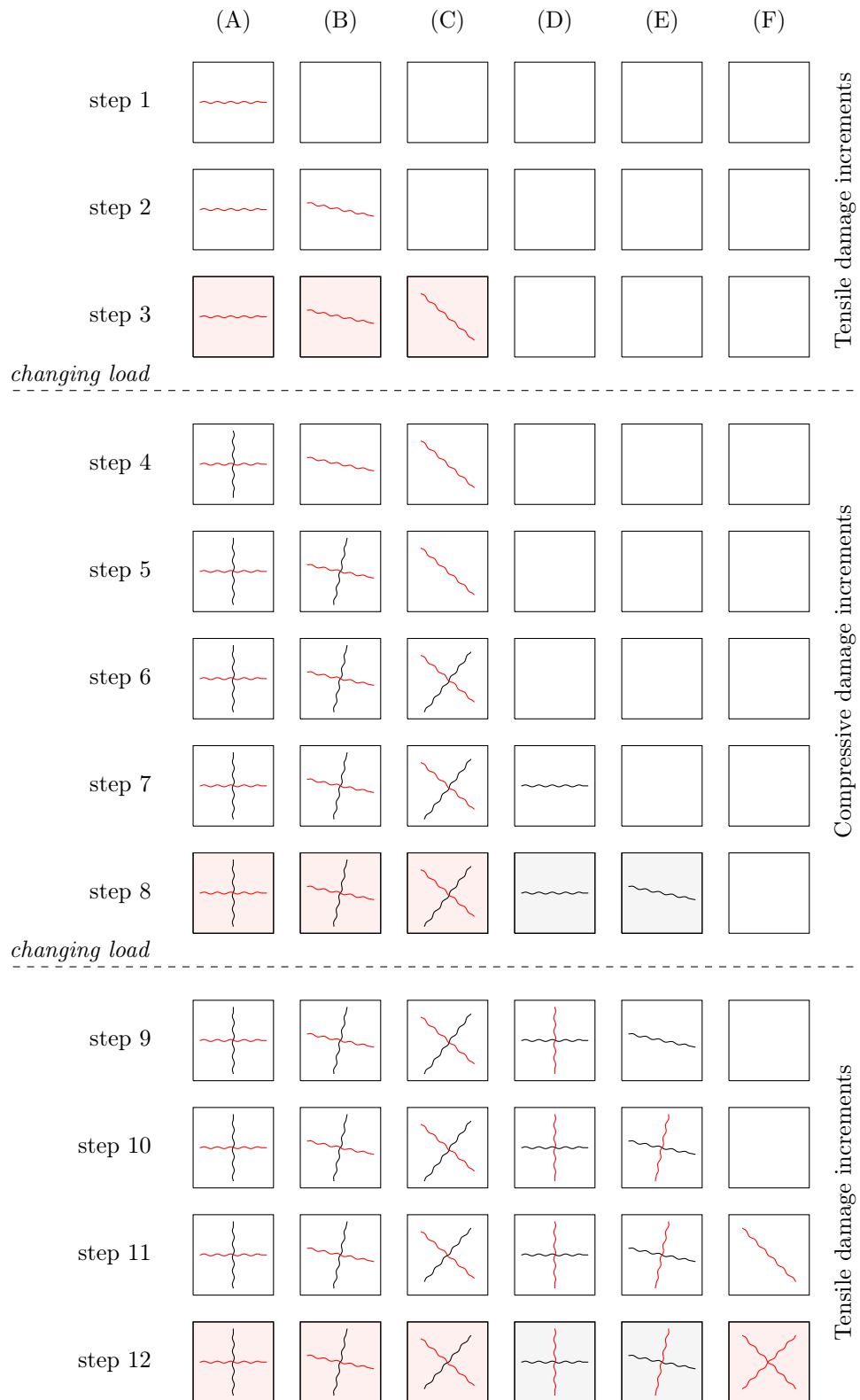
FIGURE 9.8: Development of cracks for an element with sublayers (A)-(F) under arbitrary loading, red represents a tensile crack and black represents a compressive crush band. Colored sublayers indicate if the crack is initiated under tensile or compressive loading

As already shown by the full scale facade and the concrete dam in Chapter 7, the sublayer model is also better able to cope with the effects of crack-closure on a global level. The increased flexibility on local level combined with the surrounding elements, that are also better able to handle stress redistributions, results in a more accurate description of further crack propagation. In this way, locked-in situations that are observed for regular SLA can be partly overcome with the aid of a sublayer model, although issues related to permanent damage increments are maintained.

In order to reduce the influence of tensile damage increments on the compressive behaviour (and vice versa), Pari et al. [58] proposed a new crack closure algorithm for regular SLA, which incorporates status parameters to check for the previous stress states of the critical element. For example, if the element is in tension in the current cycle, while it was in compression in the previous cycle, the stiffness is reset to the original value. For the sublayer model, a similar approach should be possible as well, although some modifications are required. Upon damage initiation, the total stiffness perpendicular to the crack is lost. To that end, no further damage increments will be performed for that sublayer in that specific direction and hence, that direction will never be the critical direction again. During load reversal, only the status parameter of the critical multiplier is monitored and therefore, the lost stiffness of a cracked sublayer can never be reset to the initial stiffness. Hence, an adapted algoritm is required, which possibly monitors status parameters on element level instead of on sublayer level. Lastly, it is noted that the tapered ripple band formulation of Section 9.1 might reduce the issues of crack-closure as well. As crack-closure often takes place in a progressed damaged state, the increased number of sublayers near the end of the softening potentially allows for more adaptability compared to the ripple band formulation. However, further research is required to validate these measures.

9.4 Computational efforts

During this study, a wide range of test cases has been considered. It was consistently observed that the sublayer model is much more computationally demanding than regular SLA (where regular SLA in itself is already quite demanding compared to incremental iterative alternatives). In this section, some more attention is paid to the current algorithm and the origin of the observed differences. Furthermore, an improved algorithm is proposed to reduce the computational efforts of the sublayer model significantly.

Current algorithm DIANA FEA
In order to understand where differences are coming from, the current sequentially linear algorithm as implemented in the software of DIANA FEA is briefly discussed. The algorithm is subdivided in several *building blocks* to make the code transparent. First, the model is initialized: geometry, material properties, saw-tooth laws and loads are read and processed. Then, the characteristic cycle of SLA-analyses (see Figure 4.6) is started. For SLA-type of analysis, three of the building blocks are of most importance:

- *SOLVE*: a linear elastic analysis is performed for the reference load(s) and the nodal displacements are solved.

- *STREAC*: for each integration point, stresses and strains are determined based on the nodal displacements, making use of element stiffness matrix D to relate

stresses and strains and matrix B to transfer nodal displacements to strains in the integration points.

- *SLSCAL*: for each integration point with non-linear material behaviour, the load multiplier in each direction is calculated based on the stress state and the current strength of the integration point. From these load multipliers, the critical load multiplier and corresponding integration points are found. If there is no common set of load multipliers, the double load multiplier strategy by Van de Graaf [29] is applied. Next, the analysis results are scaled, a damage increment is performed and the stiffness matrix is updated.

This scheme is repeated up until a certain user-defined state is reached. At the end of the analysis, the *POST* building block is started. In this block, the analysis results are processed such that they can be straightforwardly read and visualized by the user.

Understanding the problem

The computational efforts that come along with both regular SLA and the sublayer model are exemplified with the aid of a case study: analysis (F) of the notched beam in Section 7.2 is reconsidered. Both analyses are run up until a mid-span displacement of 2 mm. Regular SLA takes 2300 steps to reach this state, while the sublayer model only requires 1870 steps to reach the same state. As discussed in Section 7.2, a smaller localization band is observed for the sublayer model and hence, less damage increments are required. The analyses are run without the generation of any output, such that computational efforts can be compared one-to-one. Figure 9.9 compares the CPU (central processing unit) times for the important building blocks of both models for (A) the entire analysis up until 2 mm, (B) per 1000 steps and (C) the contributions of the three building blocks relative to the total CPU time. Per 1000 steps, the analysis with the sublayer model takes roughly 5 times longer than for regular SLA. Since the sublayer model requires in total less steps, the factor reduces to approximately 4, which is still a severe increase in computational efforts. As can be clearly observed in the bar charts, most additional CPU time can be attributed to building blocks STREAC and SLSCAL, taking per 1000 steps respectively 8.4 and 4.8 times longer for the sublayer model. Where for regular SLA, the CPU times are equally divided over the three blocks (and some leftover percentages are required for pre- and post-processing), the sublayer model severely changes this distribution, as 54.55% of the total CPU-time is allocated to the STREAC block and only 12.07% to the SOLVE block.

As previously discussed, the STREAC block calculates the stresses and strains, which are required to determine the load multipliers in all directions, for each integration point. For the sublayer model, the total number of nodes is maintained. However, the parallel set of N sublayers multiplies the total number of integration points with non-linear material behaviour with a factor N. To this end, stresses and strains are calculated for N times more integration points compared to regular SLA, resulting in very pronounced additional computational efforts in the STREAC block for the sublayer model. Subsequently, the total number of load multipliers increases accordingly, also increasing the efforts required to obtain the critical load multiplier in the SLSCAL block. Since the SOLVE block is mainly governed by the total number of nodes contributing to the stiffness matrix K, the differences between the two methods are less pronounced compared to the STREAC and SLSCAL blocks.
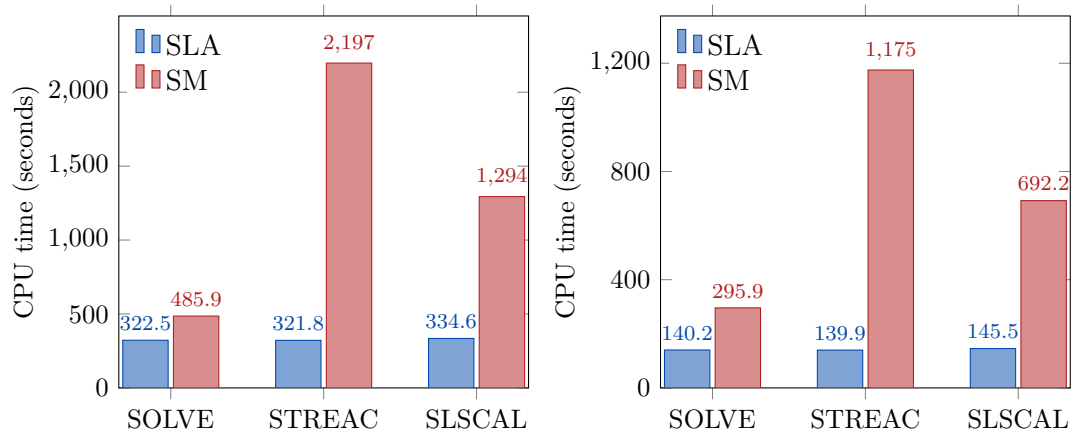
(A) CPU time total analysis (to 2 mm)

(B) CPU time per 1000 steps
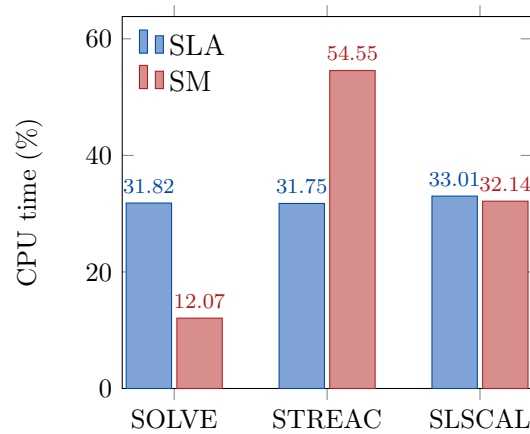
(C) Relative to total CPU time

FIGURE 9.9: Computational efforts for analysis (F) of the notched beam (Section 7.2) of the different subroutines for both regular SLA and the sublayer model

Both of the analyses are run without the generation of output to allow for a fair comparison, since the selection of output is very user-dependent. Generally speaking, more output results in larger CPU-times, especially for tensor-quantities like the (crack) strain and stress etc. In the current manual implementation, output is generated for each sublayer, making the POST block very heavy compared to regular SLA. Therefore, it is recommended to limit the intermediate output as much as possible: stress and strain plots for all elements for each step do not make any sense and it is much more effective to only ask for these quantities each 100 steps (for example).

Proposed algorithm
Most of the additional computation time for the sublayer model is found in the STREAC and SLSCAL blocks and therefore, this section merely focuses on improvements to these two blocks. It will be shown that the computational efforts of both blocks can be reduced by the same measure. In the current algorithm, stresses and strain are determined for all integration points. For regular SLA, these quantities are required for all non-linear integration points, since the location and direction of the

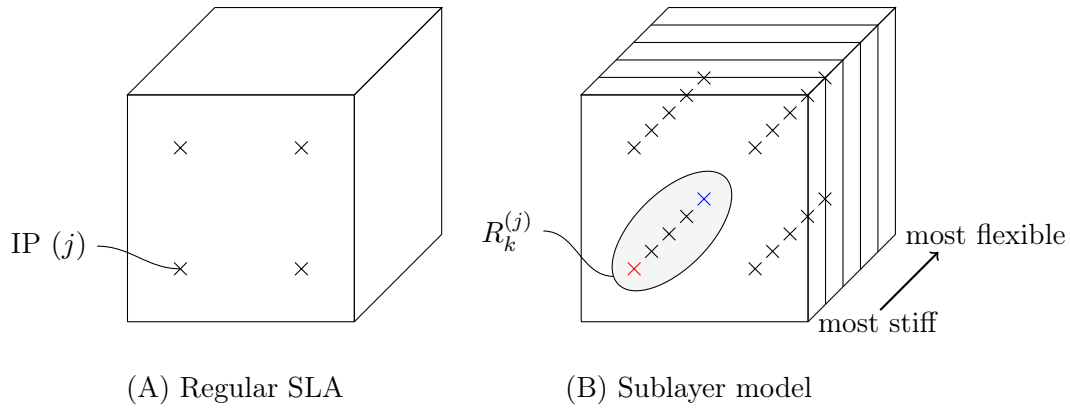(A) Regular SLA   (B) Sublayer model

FIGURE 9.10: Visualization of definition IP set $R_k^{(j)}$ for the sublayer model. The blue and red IPs represent $R_1^{(j)}$ and $R_N^{(j)}$ respectively

integration point corresponding to the critical load multiplier are not known in advance. For the sublayer model, each sublayer element has its own integration points, such that the total number of integration points in the non-linear zone increases by a factor N compared to the original mesh. Within the current algorithm, stress states of all integration points are monitored, such that the amount of calculated stress, strain and load multipliers increases by a factor N as well, making the sublayer model very computationally demanding.

For the parallel spring example of Section 4.1, the order of failure is known in advance: first, the stiffest spring, which takes most of the load, fails, followed by the second stiffest spring, such that ultimately, the most flexible spring is the last to fail (as can also be observed in the load-displacement curves of Figure 4.2). Following the same line of thinking, the order of cracking of the sublayers within a single element is known in advance: the second stiffest sublayer can only crack once the stiffest sublayer is already cracked, since the crack strain corresponding to the second saw-tooth is by definition larger than the crack strain of the first saw-tooth (ignoring constitutive snap-back). Hence, it does not make any sense to monitor the load multipliers of sublayers that are not the stiffest contribution to the considered element, as it is known for sure that these sublayers will not become critical in the current cycle.

Formally speaking, all overlaying integration points are bundled in a set $R_k^{(j)}$, in which j represents the integration point index in the original mesh and k is the sublayer index, as introduced in Chapter 5, such that for each original integration point j, a set of overlaying integration points is defined. For 2D, the set $R_k^{(j)}$ is visualized by Figure 9.10. For $k = 1$, the most flexible sublayer (being the last to crack) is selected and for $k = N$, the stiffest sublayer is obtained, such that by definition

$$E_k^L > E_{k-1}^L \tag{9.19}$$

and hence, integration point $R_k^{(j)}$ always cracks prior to integration point $R_{k-1}^{(j)}$. If the entire set of integration points in undamaged, only integration point $R_N^{(j)}$ has to be monitored. Therefore, for the considered set of integration points, stresses, strains and load multipliers only have to be calculated for integration point $R_N^{(j)}$, where the current STREAC and SLSCAL blocks calculate these quantities for the entire set $R_k^{(j)}$. On structural level, a set Q is defined, which contains all integration points in which
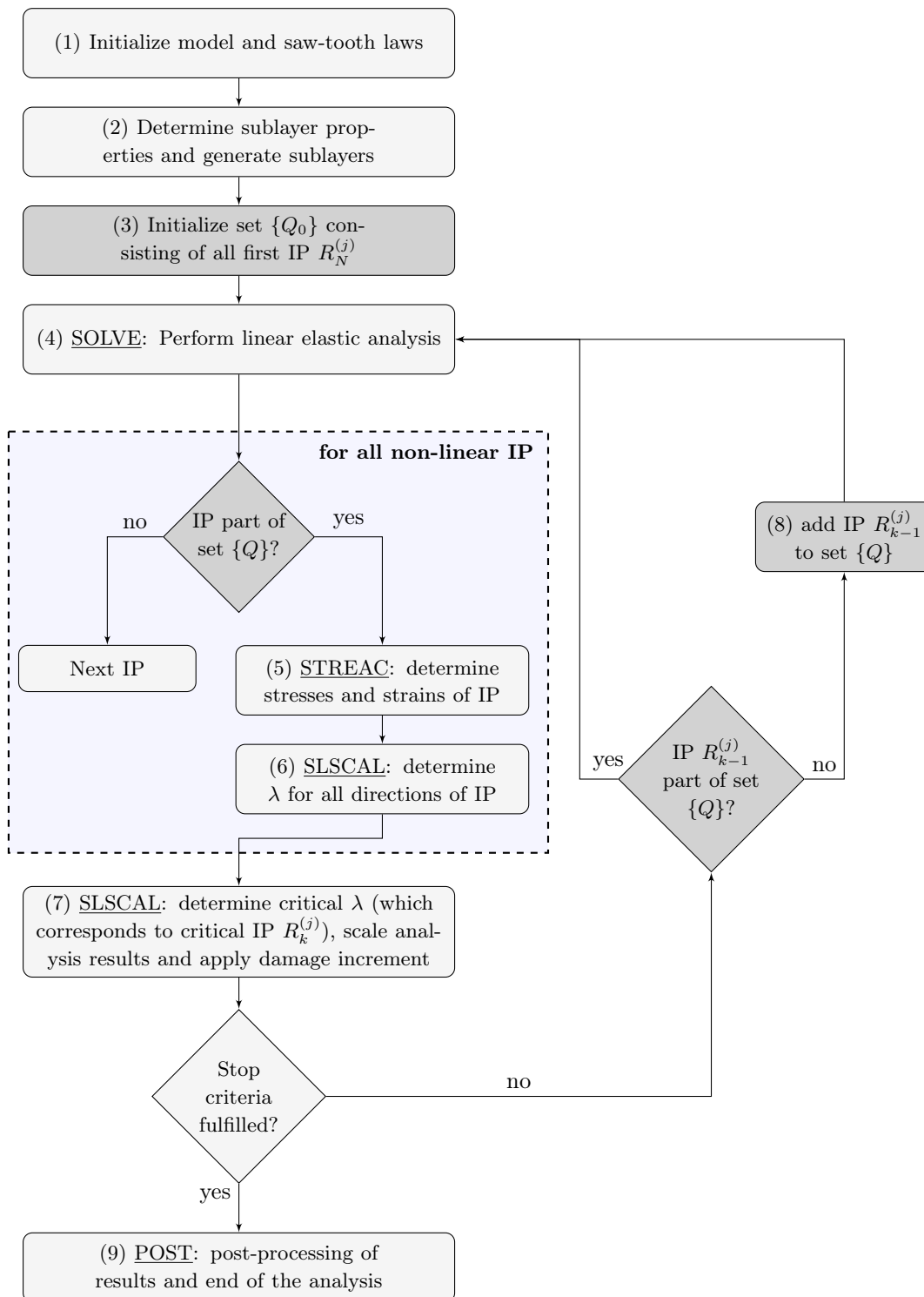
FIGURE 9.11: Flowchart for proposed algorithm to reduce compu-
tational efforts in subroutines STREAC and SLSCAL, with the addi-
tional steps highlighted

damage can potentially take place. For the first cycle of the sequentially linear analysis, set Q only contains all integration points $R_N^{(j)}$, reducing the total monitored non-linear integration points by a factor N. In this way, for the first step of the sublayer model, the same number of integration points are considered as for regular SLA, severely reducing computational efforts. Once damage is initiated in an integration point $R_k^{(j)}$, which is by definition part of set Q, the next integration point to crack $R_{k-1}^{(j)}$ is added to set Q. The total number of monitored integration points gradually increases upon damage propagation. However, as the damaged band of elements compared to the total zone that is assigned nonlinear material behaviour is relatively small and only a single integration point is monitored for the uncracked integration point sets, the total number of integration points in set Q compared to the total number of integration points is expected to be rather small throughout the entire analysis. For example for analysis (C) of the shear notched beam, only 83 of the 585 non-linear elements are cracked in Figure 7.12C. For all 502 uncracked elements, only the stiffest integration point is monitored in the proposed algorithm, while the current algorithm considers the integration points of all N sublayers of these 502 uncracked elements, marking a clear difference between the current and proposed algorithms. On top of that, for partially cracked sets of integration points (say 5 out of 12 sublayers cracked), only a part of the set of integration points is monitored (6 out of 12 for this case) by the proposed algorithm.

The proposed improved algorithm is captured within the flowchart of Figure 9.11. Instead of performing the STREAC and SLSCAL blocks for all integration points of all sublayers, the blocks are only performed for the integration points that are part of set Q. Once damage is initiated in an integration point, the consecutive integration point to crack is added to Q. In this way, computational efforts of the STREAC and SLSCAL blocks are expected to significantly reduce, such that eventually, the sublayer model can compete with regular SLA. It has already been shown that in the first step of the analysis, the amount of calculations in the STREAC and SLSCAL blocks is exactly the same for regular SLA and the sublayer model. It is noted that the proposed algorithm only improves the current algorithm for steps of the analysis where the user does not want stresses and strains as an output, since these quantities are simply only calculated for entrees of set Q. However, in general, it is not needed to have stress and strain quantities for all steps (5000 for example). In practice, it might be sufficient to output stresses and strains per 200 steps (for example). In these steps, the set of Q should be overruled and stresses and strains should be calculated for all integration points of the structure.

Additionally, it is noted that all sublayers that share the same nodes have the same *B*-matrix. In order to limit the required storage, it is recommended to store for each element a single *B*-matrix, which captures all sublayers.

Compared to regular SLA, the sublayer model generally requires less damage increments to reach a specific displacement. This, combined with the improved proposed algorithm which to a large extent tackles the additional computational efforts that are found in the STREAC and SLSCAL blocks, makes the sublayer model a very promising approach, which, to the authors belief, can ultimately compete with the computational efforts that come with regular SLA.

Chapter 10

Conclusions and recommendations

In this study, the framework of regular sequentially linear analysis has been extended towards the sublayer model, which subdivides each element in a parallel set of elastic-perfectly brittle sublayers, each having their own fixed crack direction. The superposition of sublayers results on element level in a rotating crack and therefore, the sublayer model is observed to mimic a rotating crack, thereby contributing to a more realistic description of damage propagation in quasi-brittle concrete structures. This thesis proceeded on the promising conceptual work of Hendriks and Rots [31] and aimed to further develop the sublayer model towards a more general application in practice. For the sake of completeness, the goal of this Master's thesis is repeated:

> *The goal of this Master's thesis is to further **elaborate**, **generalize** and **verify** the sublayer model for quasi-brittle materials and capture the influence of rotating cracks on the structural response **within** the framework of existing regular sequentially linear analysis.*

In this chapter, the core findings, conclusions and recommendations for further research are substantiated. First, Section 10.1 entails an overview of this work's contributions to the development of the sublayer model. Verification studies have been performed for these new developments. Section 10.2 encompasses the main conclusions of this study. Lastly, recommendations for further research are listed and briefly discussed in Section 10.3.

10.1 New developments

In this thesis, the following contributions to the sublayer model, as initially proposed by Hendriks and Rots, are developed:

1. *Generalize*: **a general transition from any particular saw-tooth law to elastic-perfectly brittle sublayer material properties has been proposed** in Chapter 5, bridging the gap between the sublayer model and the framework of regular SLA. The proposed algorithm decouples all saw-teeth, such that for uniaxial loading, each saw-tooth represents the contribution of a single sublayer. The general transition proved to hold for constitutive snap-back as well and is extended to combined tensile and compressive constitutive laws. Furthermore, the theoretical case of an infinite number of sublayers with infinitesimal thickness has been studied, in which the sublayer stiffness and strength were described by continuous functions. The set of continuous formulations by Hendriks and Rots has been extended to linear tension softening and ideal constant compressive crushing in Chapter 4.

2. *Elaborate*: **a manual externalized implementation of the sublayer model has been developed**. Maple scripts are written to make the transition from continuum law to saw-tooth law to sublayer properties and subsequently, a Matlab-script automatically generates an input file for DIANA Finite Element Analysis, in which sublayer properties are allocated to specific overlay elements. Ultimately, this externalized implementation should be internalized within the software of DIANA. However, for the purpose of this thesis, the externalized implementation suffices.

3. *Elaborate and generalize*: **the 2-dimensional framework of the sublayer model has been extended to 3-dimensional problems** in Chapter 8. Use has been made of elastic-perfectly brittle overlay solid elements that share the same nodes. To that end, all overlay sublayer elements have the same volume as the total element. With some minor adjustments, the general transition from saw-tooth law to sublayer properties holds for 3D problems as well. For each integration point, three brittle damage increments are allowed: one for each fixed axis of orthotropy.

4. *Elaborate*: **conceptual improvements to the sublayer model have been proposed** in Chapter 9. Firstly, the tapered ripple band has been developed, which is a measure to effectively increase the accuracy of the analysis by adding more saw-teeth near the end of the softening curve, while limiting the total required number of saw-teeth such that additional computational efforts are limited. Furthermore, concepts have been proposed to cope with the interaction between tension and compression on both the primary and secondary crack initiation. For both interactions, the calculation of stresses does not change: merely the elements stress capacity is influenced and hence, both interactions can be captured by the same procedure. Lastly, an improved algorithm has been developed that significantly reduces the computational efforts that come with the sublayer model, by monitoring only those integration points that can actually become critical, instead of monitoring all integration points, which has proved to be very computationally demanding.

10.2   Conclusions

The proposed sublayer model has been subjected to several case studies on single element level and on structural level for both 2D and 3D. Furthermore, the type of loading is varied and different types of finite element types are considered. This section entails the main findings and conclusions of this study and thereby focuses on the *verify* part of the main goal.

1. **On single element level, the sublayer model is better able to approximate a rotating crack model compared to regular SLA, such that the effects of stress locking are reduced**. From the single element tests in Chapter 6 it was found that the brittle damage increments inherently result in damage based reduction of the Poisson's modulus. Furthermore, it was concluded that shear retention occurs implicitly as a consequence of the rotating crack plane over the different sublayers. The tension-shear (Willam) problem marked clear differences between regular SLA and the sublayer model: a rotating crack is mimicked by the superposition of sublayers with each their own crack direction, thereby better approximating the rotating crack model, which by definition co-rotates

with the principal stresses. At the onset of cracking in a specific sublayer, the crack plane was found to be exactly in line with the current principal directions. However, previously cracked sublayers with out-dated crack directions contribute to the total elements behaviour as well, hence causing deviations compared to a NLFEA rotating crack model. Compared to the sublayer model, regular SLA entailed considerably larger effects of stress-locking due to the fixed crack not co-rotating with the principal stress directions, allowing for stresses exceeding the tensile strength.

2. **On structural level, the sublayer model consistently exhibits less wide bands of spurious stresses around the main crack path, thus leading to less energy dissipation and therefore, more flexible post-peak response is observed**. In Chapter 7, a wide range of structural case studies has been performed. Apparently, as a result of the crack directions on single element level being more in line with the principal stress directions along the main crack path, less spurious stresses are developed in the surrounding elements as well, which was clearly observed for the notched beam and shear notched beam.

3. **The sublayer model is able to overcome bifurcations by following asymmetric failure modes, but is meanwhile able to correct itself when a locally asymmetric failure mode is undesired**. On the contrary, the advantage of regular SLA to follow asymmetric failure modes and overcome bifurcations, comes with the disadvantage of potentially enforcing locally asymmetric failure modes for symmetric problems. For both the notched beam and double-edge-notched beam, regular SLA inherently resulted in a gradually increasing locally asymmetric crack path since damage increments could only be performed at one location at a time. With the aid of the sublayer model, the development of this local asymmetry was restricted.

4. **The sublayer model is better able to adapt to changing stress states, which for example take place for non proportional loading, stress redistributions and crack closure, especially for full scale structures**. For application in practice, this might be the most relevant conclusion. Especially for the tested full scale problems (the full scale facade and concrete dam), more physically justified collapse mechanisms have been observed for the sublayer model, where the solution path of regular SLA seemed to be lost as a result of the fixed crack model being unable to adapt itself to changing stress states after the initiation of damage. By invoking the sublayer model, it has been shown that crack-closure can be overcome by redistribution of stresses, although the stiffness is not able to recover.

5. **The frameworks of regular SLA and the sublayer model are equivalent to their incremental-iterative counterparts, being the fixed crack (FCM) and rotating crack (RCM) models respectively**. In literature, the rotating crack model has been reported to increase issues pertaining to mesh-directional bias. As the sublayer model aims to mimic a rotating crack, issues related to mesh-directional bias increase for the sublayer model as well, as was clearly shown for the scaled concrete dam. The advantage of a rotating crack model comes with the disadvantage of possibly correcting the crack direction to maintain a mesh-following tendency. For the performed structural case studies in Chapter 7, proper agreement with incremental-iterative analyses from literature has been observed.

6. **Quadratic elements, both quadrilateral and triangular, consistently reduce the issues related to mesh-directional bias for both regular SLA and the sublayer model and therefore, these elements are concluded to be most robust**. To this end, quadratic elements are recommended for robust and reliable application in engineering practice. On the contrary, linear quadrilateral elements with a regular integration scheme were proved to show very poor behaviour regarding mesh-directional bias. Although linear quadrilateral elements with reduced integration were shown to give reasonable results for simple cases, it is not recommended to apply this type of element to practical cases. If, for any reason, one wants to apply linear elements, it is recommended to make use of triangular linear elements. Lastly, it is noted that SLA-type of approaches in general suffer to issues related to mesh-directional bias to a certain extent, which for example became clear for the double-edge-notched beam with triangular elements.

7. **The 3-dimensional framework of the sublayer model is consistent with the 2-dimensional framework, such that all previous conclusions hold for application to 3D as well**. In Chapter 8, the framework has been extended towards 3-dimensional structures. For the inclined notched beam, a more flexible response and a more narrow localization band have been observed, consistent with the findings for the 2D notched beam. Furthermore, it has been shown that SLA-type of procedures inherently generate less spurious stresses compared to their incremental iterative counterparts for 3D. In fact, the single damage increment at a time allows for a certain degree of self-correction, while for incremental iterative procedures, damage increments are performed in any step anywhere throughout the structure.

8. **The tapered ripple band formulation requires less sublayers to obtain the same level of accuracy compared to the currently applied ripple band formulation and is therefore less computationally demanding**. It has been shown that the last sublayers to crack reveal the most accurate behaviour and therefore, it is desirable to increase the amount of 'last sublayers', while maintaining the same amount of first sublayers to ensure a proper level of accuracy after crack initiation. A case study was performed for the shear notched beam, showing that the tapered ripple band formulation reduced the number of required saw-teeth by 26% compared to the regular ripple band for reaching the same level of accuracy. To this end, the tapered ripple band results in less sublayers in the finite element model and reduces the required number of damage increments to reach a specific state, such that more efficient use is made of the sublayers.

9. **The current manual externalized implementation of the sublayer model requires approximately 4 to 5 times more computational efforts compared to regular SLA**, where regular SLA in itself is already quite demanding compared to incremental iterative approaches (although the required man-hours are much lower for SLA due to its robustness). Especially for 3D problems, this might result in unrealistic and non-practical computation times. In order to make the sublayer model computationally more interesting, an improved algorithm has been proposed, in which, contrary to the current algorithm that monitors all integration points, only those integration points are considered that actually can become critical in that specific step. In this way, it was found that for the first analysis step, the improved algorithm of the sublayer model

monitored the same number of integration points as regular SLA and that during the rest of the analysis, the monitored set of integration points gradually increases, thereby allowing for a considerable gain in computational efforts, potentially making the sublayer model compete with the computational efforts that come with regular SLA, especially when considering a combination with the tapered ripple band formulation.

In this thesis, the sublayer model is proved to mimic a rotating crack within the framework of existing regular sequentially linear analysis. Compared to regular SLA, effects of stress locking are reduced, less wide localization bands are found and a more realistic collapse pattern is observed, thereby making the sublayer model more interesting for application in engineering practice. Furthermore, the framework is expanded towards 3-dimensional structures and concepts are proposed to further improve the sublayer model regarding computational efforts. In the authors opinion, the contributions of this thesis are a step towards a robust generally applicable computational method to simulate the complex structural behaviour of quasi-brittle materials.

10.3   Recommendations

The first recommendations for further research are directly related to the proposed extensions and improvements of Chapter 9. Especially the tapered ripple band and improved algorithm are very promising to effectively reduce computational efforts and therefore, further research is required in order to further elaborate and validate these concepts. On top of that, it is recommended to perform a variation study to further understand and optimize the selection of ripple band parameters p and r. It might be useful to develop guidelines that describe the relation between the ripple band parameters and the obtained level of accuracy, to mitigate application in practice. Another option to further optimize computational efforts would be to allocate different ripple band parameters to different parts of the structure: many saw-teeth on places where a high level of detail is required and few saw-teeth on places where accuracy is not the main priority.

In the second place, further research is recommended on how to reduce issues related to mesh-directional bias for the sublayer model. Throughout this thesis, it has been consistently observed that the crack path tried to follow the mesh, which became especially prevailing for linear quadrilateral elements with regular integration. Potentially, random triangular meshes might reduce these effects. On top of that, the sublayer model can be combined with crack tracking algorithms, in line with the works of Slobbe [71] and Cook et al. [17], who both successfully implemented crack tracking algorithms within the framework of regular SLA. In further research, it might be interesting to combine similar measures with the framework of the sublayer model to allow for a less mesh-dependent and more localized crack path propagation.

In this thesis, it has been concluded that the problems related to crack-closure are partly solved by the sublayer model: the stresses are able to redistribute, such that the structure can properly overcome the changing stress state, contrary to regular SLA. However, the permanent damage increments do not allow for recovering of the stiffness during unloading and/or crack-closure, locally (and potentially globally) leading to incorrect results. Upon stress reversal, the cracked sublayers should retain their initial stiffness. To this end, in line with previous studies on sequentially linear

analysis in general, further research is recommended to capture the effects of crack-closure on constitutive level as well. As discussed by Pari et al. [58], a possible measure would be to include status parameters, which compare the current stress state with the previous stress state. Furthermore, for the sublayer model specifically, it might be able to completely decouple the tensile and compressive parts of the constitutive laws, in line with the saw-teeth being decoupled by the brittle sublayers. However, further research is required to substantiate these measures. Crack-closure is a general problem for SLA-type of procedures and therefore, it is expected that the issues of regular SLA and the sublayer model can be solved by the same type of measure.

Lastly, it is noted that for application in engineering practice, the framework should be extended towards reinforced concrete, rather than focusing on merely plane concrete. Reinforcement can be included within the finite element model in two ways: either by beam elements representing the reinforcement between finite elements models or by embedded reinforcement, which is included in the stiffness matrix of the element. The former approach is already possible with the current framework, as the beam elements in between finite elements are not influenced by the sublayers. However, the latter approach requires some additional efforts: as the reinforcement becomes part of the element, the generation (in fact copying) of the sublayer elements might become troubling. Merely the plane concrete element should be copied several times, while maintaining the same stiffness terms for the embedded reinforcement. On top of that, the formation of compressive concrete struts according to Vecchio and Collins [77] becomes relevant for reinforced concrete structures. To this end, it is recommended to extend future research towards the simulation of reinforced concrete structures as well.

Appendix A

General transition from a different point of view

In this appendix, the general transition from saw-tooth law to sublayer model as derived in Section 5.2 is elaborated from a different point of view. As a starting point, it was assumed in Section 5.2 that all sublayers have the same thickness $\Delta t_k^L = t/N$. This assumption results in a straightforward scaling of sublayer stresses to the total element thickness t. However, it is not the only option. In this appendix, a different starting point is taken: all sublayers are assumed to have the same stiffness E_0 and different thickness Δt_k^L. Furthermore, it is discussed whether both starting points give the same output.

The stiffness contribution E_k^L of a specific sublayer k with stiffness E_0 relative to the total thickness t is found by

$$E_k^L = \frac{\Delta t_k^L}{t} E_0 \tag{A.1}$$

The difference between the known stiffnesses E_k and E_{k-1} is the contribution of sublayer k, and hence

$$E_k = \frac{\Delta t_k^L}{t} E_0 + E_{k-1} \tag{A.2}$$

which is also visualized by Figure A.1. From Equation A.2, the thickness Δt_k^L can be solved, leading to
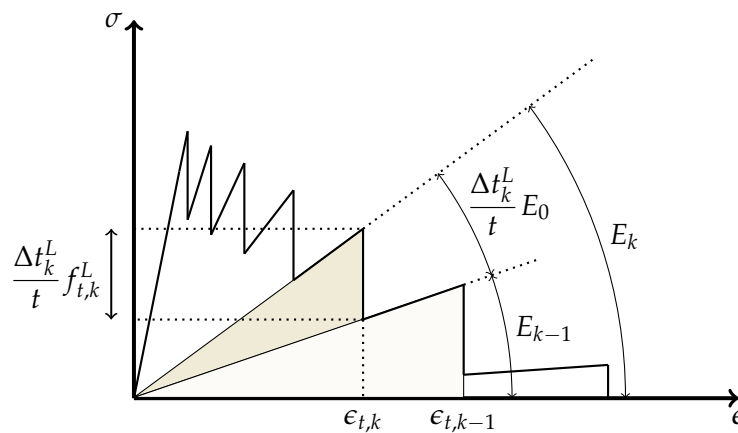

FIGURE A.1: Schematization of step (3): transition saw-tooth law to sublayer model properties from a different point of view

$$\Delta t_k^L = \frac{(E_k - E_{k-1})}{E_0} t \tag{A.3}$$

and the strength of a sublayer is now found by

$$f_{t,k}^L \frac{\Delta t_k^L}{t} = \epsilon_{t,k} \frac{\Delta t_k^l}{t} E_0 \quad \text{so} \quad f_{t,k}^L = E_0 \, \epsilon_{t,k} \tag{A.4}$$

With the aid of Equations A.3 and A.4, the general transition is also possible assuming the same stiffness for all sublayers. Next, it is investigated if both approaches result in the same behaviour by comparing the elements stiffness and strength for uniaxial loading for a specific saw-tooth k. The stiffness of an element is described by Equation 4.9:

$$\boldsymbol{K}_e = \int_\Omega \boldsymbol{B}^T \boldsymbol{D} \, \boldsymbol{B} \, d\Omega \tag{A.5}$$

For a single sublayer, the stiffness matrix $\boldsymbol{K}_{e,k}$ is subsequently found by integration over the thickness of the considered sublayer

$$\boldsymbol{K}_{e,k} = \boldsymbol{B}^T \boldsymbol{D}_k \, \boldsymbol{B} \, \Delta t_k^L \tag{A.6}$$

The constitutive material law $\boldsymbol{D}_k$ is proportional to the stiffness, as can be seen in Equations 4.4 and 4.7. If both approaches give the same behaviour on sublayer level and thus the same stiffness $\boldsymbol{K}_{e,k}$, the following equality should hold:

$$E_0 \, \Delta t_k^L \stackrel{?}{=} E_k^l \frac{t}{N} \tag{A.7}$$

with on the left hand side the proportional stiffness term for the approach of this appendix and on the right hand side the proportional stiffness term assuming that all sublayers have the same thickness.

Furthermore, the same strength properties should be found, meaning that the vertical stress drop at a damage increment for both methods should be the same, leading to

$$f_{t,k}^L \frac{\Delta t_k^L}{t} \stackrel{?}{=} \frac{f_{t,k}^L}{N} \quad \text{so} \quad E_0 \, \epsilon_{t,k} \frac{\Delta t_k^L}{t} \stackrel{?}{=} \frac{E_k^L \, \epsilon_{t,k}}{N} \tag{A.8}$$

which after rewriting becomes equivalent to Equation A.7. Both the strength and stiffness requirement result in the same equality that should hold. The correctness of the equality is shown by substitution of Equations A.3 and 5.10 in Equation A.7

$$E_0 \left[\frac{(E_k - E_{k-1})}{E_0} t \right] \stackrel{?}{=} N(E_k - E_{k-1}) \frac{t}{N} \tag{A.9}$$

which can be further elaborated to

$$(E_k - E_{k-1})t = (E_k - E_{k-1})t \tag{A.10}$$

from which can be concluded that the stiffness and strength of the considered sublayer are the same for both approaches. As the element stiffness matrix is a superposition of the sublayers, the stiffness and strength on element level will also be the same and hence, it is verified that both of the approaches are equivalent.

Appendix B

Working with the sublayer model

In this appendix, some relevant application issues of the sublayer model are addressed. Furthermore, the practical implementation for the purpose of this thesis is discussed. All finite element analyses are performed with *DIANA Finite Element Analysis* version *10.3beta*. Ultimately, the algorithm should be completely internalized within DIANA such that the user only has to define continuum material properties and ripple band properties. Subsequently, sublayers should be generated during the analysis and results on sublayer level are transformed to element results, which are presented to the user. For the purpose of this thesis, an externalized algorithm suffices and programming within the DIANA environment is not required. The applied algorithm for this thesis is shown by Figure B.1. A certain continuum law is taken as input. In the current algorithm, all elements have the same crack band h
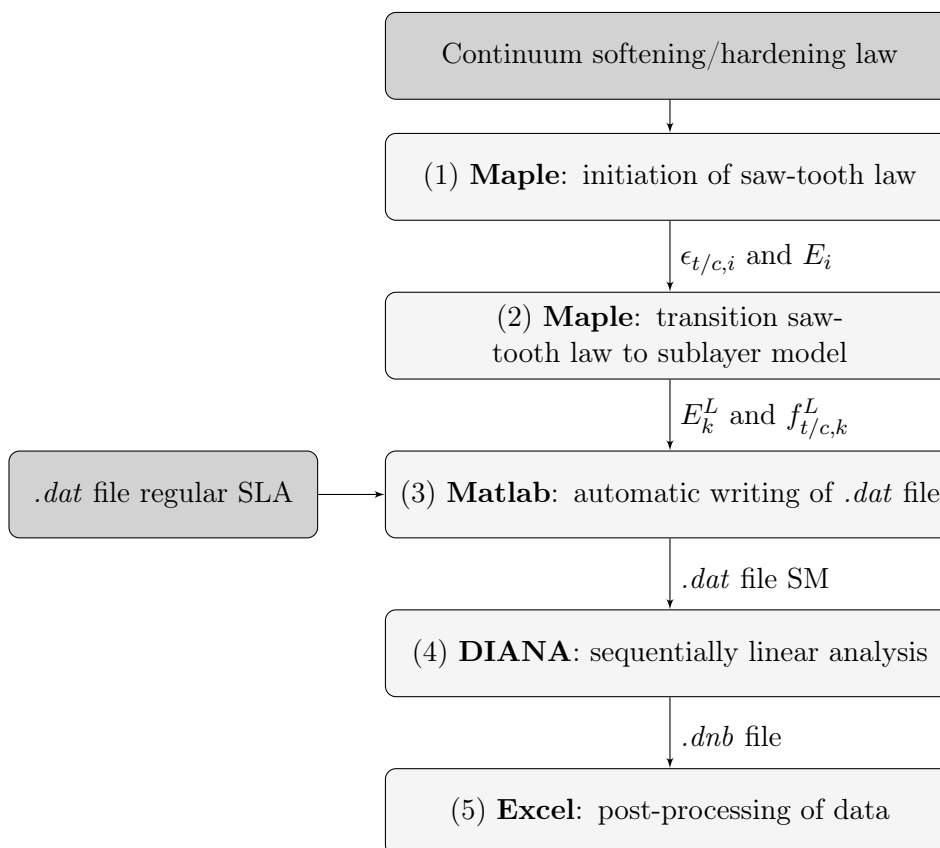

FIGURE B.1: Flowchart of the algorithm that is used for application of the sublayer model in this thesis, together with input and output flow and applied software

and therefore the same continuum law, such that all elements have the same sub-
layers. Ultimately, the algorithm should be able to handle elements with different
crack bands. For the purpose of this thesis, the starting point of one single crack
band h suffices. In step (1), the saw-tooth law is initiated and the strains $\epsilon_{t/c,i}$ and
stiffnesses E_i corresponding to the saw-teeth are inputted in step (2), in which the
transition from saw-tooth law to sublayer properties is made using the theory of
Chapter 5. Both steps (1) and (2) are performed within the symbolic environment of
Maple. Next, the *.dat* file, which describes the geometry of the structure, is automati-
cally generated within Matlab in step (3) based on the sublayer properties of step (2).
The *.dat* file of regular SLA is taken as input and after some small manual changes of
the file such that it describes a single brittle sublayer, the Matlab code transforms the
.dat file to a file with N brittle sublayers. The Matlab code takes the sheet that has the
keyword *NONLINEAR* in the name and copies it N times, each time with different
material properties and increasing element numbers. Furthermore, the thickness of
the elements is reduced. All sublayers of a specific element share the same nodes,
such that they can be seen as *overlay* elements. The number of nodes is the same as
regular SLA and the number of integration points increases. Steps (1) to (3) can be
seen as a sort of pre-processing prior to the finite element analysis.

In step (4), a sequentially linear analysis in DIANA is performed based on the
generated *.dat* file. Within the SLA analysis with brittle sublayers, the stiffness per-
pendicular to the crack is (almost completely) reduced to zero. For numerical pur-
poses, a very small part of the stiffness is automatically maintained by DIANA dur-
ing the analysis. The shear retention factor and Poisson's ratio reduce accordingly,
since they are both proportional to the stiffness. The analysis in DIANA generates a
.dnb file, which can be read in the Interactive Environment of DIANA. Properties that
are the same for all sublayers, e.g. strains and displacements, can be directly used.
On the contrary, the extraction of stresses on element level requires an additional
step. Each sublayer has its own crack direction, stiffness and strength and there-
fore, each sublayer has its own specific stress state. Since the sublayers are stacked
and all have the same thickness, the total element stresses are calculated as the av-
eraged stress over the sublayers. For the time being, it is not possible to directly use
the stress plots in the Interactive Environment of DIANA. In step (5), the described
averaging process is performed in Excel, such that stress-strain plots can be made.
In this way, a complete algorithm is described that entails pre-processing, the finite
element analysis itself and post-processing.

Underneath, an example single element *.dat* file for regular SLA is shown. The
purpose of this example code is to exemplify the structure of the file and the values
of physical quantities are not of importance.

```
     : Diana Datafile written by Diana 10.3
'UNITS'
LENGTH MM
FORCE N
'DIRECTIONS'
   1    1.00000E+00    0.00000E+00    0.00000E+00
   2    0.00000E+00    1.00000E+00    0.00000E+00
   3    0.00000E+00    0.00000E+00    1.00000E+00
'MODEL'
DIMENS "2D"
GRAVDI 2
GRAVAC  -9.81000E+03
'COORDINATES'
   1    2.00000E+01    2.00000E+01    0.00000E+00
   2    2.00000E+01    0.00000E+00    0.00000E+00
```

```
   3   0.00000E+00    0.00000E+00    0.00000E+00
   4   0.00000E+00    2.00000E+01    0.00000E+00
'MATERI'
   1 NAME   NONLINEAR_1
     YOUNG    1.00000E+04
     POISON   2.00000E-01
     TENCRV LINEPS
     TENSTR   2.00000E+00
     TENPAR   0.3536067892E-02 0.01 0.1
     NDAMLE   50
     SLASHR VARIAB
'GEOMET'
   1 GCNAME SHEET
     GEOMDL MEMBRA
     THICK    1.00000E+00
'DATA'
   1 INTEGR REDUCE
'ELEMENTS'
SET  "Sheet 1"
CONNECT
   1 Q8MEM  2 1 4 3
MATERIAL 1
GEOMETRY 1
DATA 1
'LOADS'
CASE 1
NAME "Geometry load case 1"
DEFORM
/ 1 2 / TR 1   1.00000E-01
'SUPPOR'
NAME "Support 1"
/ 1-4 / TR 1
/ 1-4 / TR 2
'END'
```

Next, an example single element *.dat* file for the sublayer model is shown. The example file consists of two sublayers with the same thickness $t_0/2$, with a 'BRITTL' material definition, meaning that the stiffness perpendicular to the crack is reduced to zero upon crack initiation. Two overlay elements are defined, both with different material properties, but sharing the same nodes. The purpose of this example file is to illustrate the structure of a *.dat* file for the sublayer model. For structural applications, many more elements and sublayers are used.

```
: Diana Datafile written by Diana 10.3
'UNITS'
LENGTH MM
FORCE N
'DIRECTIONS'
   1   1.00000E+00    0.00000E+00    0.00000E+00
   2   0.00000E+00    1.00000E+00    0.00000E+00
   3   0.00000E+00    0.00000E+00    1.00000E+00
'MODEL'
DIMENS "2D"
GRAVDI 2
GRAVAC  -9.81000E+03
'COORDINATES'
   1   2.00000E+01    2.00000E+01    0.00000E+00
   2   2.00000E+01    0.00000E+00    0.00000E+00
   3   0.00000E+00    0.00000E+00    0.00000E+00
   4   0.00000E+00    2.00000E+01    0.00000E+00
```

```
'MATERI'
   1 NAME   LINEAR
     YOUNG    1.00000E+04
     POISON   2.00000E-01
   2 NAME   NONLINEAR_1
     YOUNG    4.00357E+02
     POISON   0.2
     TENCRV BRITTL
     TENSTR  3.00600E+00
     TENPAR  0.001
     NDAMLE  2
     SLASHR VARIAB
   3 NAME   NONLINEAR_2
     YOUNG    1.11746E+03
     POISON   0.2
     TENCRV BRITTL
     TENSTR  6.00557E+00
     TENPAR  0.001
     NDAMLE  2
     SLASHR VARIAB
 'GEOMET'
   1 NAME   THICK
     GCNAME SHEET
     GEOMDL MEMBRA
     THICK    1.00000E+00
   2 NAME   NONLINEAR_1
     GCNAME SHEET
     GEOMDL MEMBRA
     THICK    0.50000E+00
'DATA'
   1 INTEGR REDUCE
'ELEMENTS'
SET   "NONLINEAR_1"
CONNECT
   1 Q8MEM  2 1 4 3
MATERIAL 2
GEOMETRY 2
DATA 1
SET   "NONLINEAR_2"
CONNECT
 2 Q8MEM 2 1 4 3
MATERIAL 3
GEOMETRY 2
DATA 1
'LOADS'
CASE 1
NAME "Geometry load case 1"
DEFORM
/ 1 2 / TR 1   1.00000E-01
'SUPPOR'
NAME "Support 1"
/ 1-4 / TR 1
/ 1-4 / TR 2
'END'
```

Appendix C

Analysis properties of structural case studies

In this appendix, the properties (ripple band parameter p, crack band h, element size, number of saw-teeth N etc.) of the analyses that are performed in Chapters 7 and 8 are listed.

Case	Element type	Scheme	Size (mm)	h (mm)	Softening law	p	N
A	Q8MEM	1 IP	10	10	linear	0.10	22
B	Q8MEM	2x2 IP	10	10	linear	0.10	22
C	CQ16M	2x2 IP	10	5	linear	0.10	25
	CQ16M	2x2 IP	10	5	exponential	0.125	19
D	Q8MEM	1 IP	5	5	linear	0.10	25
E	Q8MEM	2x2 IP	5	5	linear	0.10	25
	Q8MEM	2x2 IP	5	5	exponential	0.125	19
F	CQ16M	2x2 IP	5	2.5	linear	0.13	22

TABLE C.1: Overview of performed analyses for structural verification case 1: notched beam (Section 7.2)

Case	Element type	Scheme	Size (mm)	h (mm)	Softening law	p	N
A	Q8MEM	1 IP	8	11.31	Hordijk	0.11	19
B	Q8MEM	2x2 IP	8	11.31	Hordijk	0.11	19
C	CQ16M	2x2 IP	8	8	Hordijk	0.115	19

TABLE C.2: Overview of performed analyses for structural verification case 2: shear notched beam (Section 7.3)

Case	Element type	Scheme	Size (mm)	h (mm)	Softening law	p	N
A	Q8MEM	1 IP	5	7.07	Hordijk	0.11	19
B	Q8MEM	2x2 IP	5	7.07	Hordijk	0.11	19
C	CQ16M	2x2 IP	5	5	Hordijk	0.12	19
D	T6MEM	1 IP	5	5	Hordijk	0.12	19
E	CT12M	3 IP	5	3.54	Hordijk	0.127	19

TABLE C.3: Overview of performed analyses for structural verification case 3: double-edge-notched beam (Section 7.4)

Case	Element type	Scheme	Size (mm)	h (mm)	Softening law	p	N
A	Q8MEM	1 IP	230	325.3	linear	0.105	19
B	Q8MEM	2x2 IP	230	325.3	linear	0.105	19
C	CQ16M	2x2 IP	230	230	linear	0.11	19

TABLE C.4: Overview of performed analyses for structural verification case 4: full scale facade (Section 7.5)

Case	Element type	Scheme	Size (mm)	h (mm)	Softening law	p	N
A	Q8MEM	2x2 IP	60	84.85	Hordijk	0.09	14
B	CQ16M	2x2 IP	60	60	Hordijk	0.10	14
C	Q8MEM	2x2 IP	30	42.43	Hordijk	0.12	13
D	CQ16M	2x2 IP	30	30	Hordijk	0.12	14
E	T6MEM	1 IP	60	60	Hordijk	0.10	14
F	CT12M	3 IP	60	42.43	Hordijk	0.12	13
G	T6MEM	1 IP	30	30	Hordijk	0.12	14
H	CT12M	3 IP	30	21.21	Hordijk	0.13	14

TABLE C.5: Overview of performed analyses for structural verification case 5a: scaled concrete dam with proportional loading (Section 7.6.1)

Case	Element type	Scheme	Size (mm)	h (mm)	Softening law	p	N
A	CT12M	3 IP	750	530.3	exponential	0.09	13

TABLE C.6: Overview of performed analysis for structural verification case 5b: full scale Konya Dam with non-proportional loading (Section 7.6.2)

Case	Element type	Scheme	Size (mm)	h (mm)	Softening law	p	N
A	TE12L	1 IP	12	6	linear	0.2	12

TABLE C.7: Overview of performed analysis for structural verification in 3D: skewed notched beam (Section 8.3)

Bibliography

[1]   J. Alfaiate and L. J. Sluys. "On the use of non-iterative methods in cohesive fracture". In: *International Journal of Fracture* 210.1 (2018), pp. 167–186. DOI: 10.1007/s10704-018-0270-2.

[2]   M. Arrea and A. Ingraffea. *Mixed Mode Crack Propagation in Mortar and Concrete*. Report 81-13, Department of Structural Engineering, Cornell University, 1982.

[3]   G. I. Barenblatt. "The Mathematical Theory of Equilibrium Cracks in Brittle Fracture". In: ed. by H. L. Dryden, Th. von Kármán, G. Kuerti, F. H. van den Dungen, and L. Howarth. Vol. 7. Advances in Applied Mechanics. Elsevier, 1962, pp. 55 –129. DOI: 10.1016/S0065-2156(08)70121-2.

[4]   Z. P. Bazant. "Fracture mechanics of concrete structures". In: Proceedings of the First International Conference on Fracture Mechanics of Concrete Structures (FraMCoS1). Ed. by Z. P. Bazant. Breckenridge, Colorado: Elsevier Applied Sciences, London, 1992, pp. 1–140.

[5]   Z. P. Bažant and B. Oh. "Crack Band Theory for Fracture of Concrete". In: *Matériaux et Constructions* 16 (1983), pp. 155–177. DOI: 10.1007/BF02486267.

[6]   W. J. Beranek and G. J. Hobbelman. "2D and 3D-Modelling of concrete as an assemblage of spheres: revaluation of the failure criterion". In: Proceedings of the Second International Conference on Fracture Mechanics of Concrete Structures (FRaMCoS-2). Ed. by F. H. Wittmann. Freiburg, 1995, pp. 965–978.

[7]   S. S. Bhattacharjee and P. Léger. "Application of NLFM Models to Predict Cracking in Concrete Gravity Dams". In: *Journal of Structural Engineering* 120.4 (1994), pp. 1255–1271. DOI: 10.1061/(ASCE)0733-9445(1994)120:4(1255).

[8]   J. Blaauwendraad and H. J. Grootenboer. *Essentials for discrete crack analysis*. IABSE Colloquium on advanced mechanics of reinforced concrete, Delft, 1981, pp. 263–272.

[9]   R. de Borst, M. A. Crisfield, J. Remmers, and C. Verhoosel. *Non-Linear Finite Element Analysis of Solids and Structures: Second Edition*. Wiley, Chichester, 2012. DOI: 10.1002/9781118375938.

[10] R. de Borst and P. Nauta. "Non-orthogonal cracks in a smeared finite element model". In: *Engineering Computations* 2.1 (1985), pp. 35–46. DOI: 10.1108/eb023599.

[11] R. de Borst and J. Pamin. "Gradient plasticity in numerical simulation of concrete cracking". In: *European Journal of Mechanics. A, Solids* 15.2 (1996), pp. 295–320.

[12] S. Brasile, R. Casciaro, and G. Formica. "Multilevel approach for brick masonry walls – Part I: A numerical strategy for the nonlinear analysis". In: *Computer Methods in Applied Mechanics and Engineering* 196.49 (2007), pp. 4934 –4951. DOI: 10.1016/j.cma.2007.06.021.

[13]   A. Carpinteri, S. Valente, G. Ferrara, and L. Imperato. "Experimental and numerical fracture modelling of a gravity dam". In: Proceedings of the First International Conference on Fracture Mechanics of Concrete Structures (FraMCoS1). Ed. by Z. P. Bazant. Breckenridge, Colorado: Elsevier Applied Sciences, London, 1992, pp. 351–360.

[14]   D. A. Cendón, J. C. Gálvez, M. Elices, and J. Planas. "Modelling the fracture of concrete under mixed loading". In: *International Journal of Fracture* 103.3 (2000), pp. 293–310. DOI: 10.1023/A:1007687025575.

[15]   M. Cervera and M. Chiumenti. "Smeared crack approach: back to the original track". In: *International Journal for Numerical and Analytical Methods in Geomechanics* 30.12 (2006), pp. 1173–1199. DOI: 10.1002/nag.518.

[16]   D. Colombo. "An implicit geometrical approach to level sets update for 3D non planar X-FEM crack propagation". In: *Computer Methods in Applied Mechanics and Engineering* 237-240 (2012), pp. 39 –50. DOI: 10.1016/j.cma.2012.04.020.

[17]   A. C. Cook, S. S. Vel, and S. E. Johnson. "Pervasive cracking of heterogeneous brittle materials using a multi-directional smeared crack band model". In: *International Journal of Mechanical Sciences* 149 (2018), pp. 459 –474. DOI: 10.1016/j.ijmecsci.2017.09.016.

[18]   R. J. Cope, P. V. Rao, L. A. Clark, and P. Norris. "Modelling of reinforced concrete behaviour for finite element analysis of bridge slabs". In: *Numerical methods for non-linear problems* 1 (1980), pp. 457–470.

[19]   H. A. W. Cornelissen, D. A. Hordijk, and H. W. Reinhardt. "Experimental determination of crack softening characteristics of normalweight and lightweight concrete". In: *HERON* 31.2 (1986).

[20]   M. J. DeJong, B. Belletti, M. A. N. Hendriks, and J. G. Rots. "Shell elements for sequentially linear analysis: Lateral failure of masonry structures". In: *Engineering Structures* 31.7 (2009), pp. 1382 –1392. DOI: 10.1016/j.engstruct.2009.02.007.

[21]   M. J. DeJong, M. A. N. Hendriks, and J. G. Rots. "Sequentially linear analysis of fracture under non-proportional loading". In: *Engineering Fracture Mechanics* 75.18 (2008), pp. 5042 –5056. DOI: 10.1016/j.engfracmech.2008.07.003.

[22]   D. S. Dugdale. "Yielding of steel sheets containing slits". In: *Journal of Mechanics Physics of Solids* 8 (1960), pp. 100–104. DOI: 10.1016/0022-5096(60)90013-2.

[23]   J. Eliáš, P. Frantík, and M. Vořechovský. "Improved sequentially linear solution procedure". In: *Engineering Fracture Mechanics* 77.12 (2010), pp. 2263 –2276. DOI: 10.1016/j.engfracmech.2010.05.018.

[24]   P. H. Feenstra. *Computational Aspects of Biaxial Stress in Plain and Reinforced Concrete*. PhD dissertation, Delft University of Technology, 1993.

[25]   P. H. Feenstra, J. G. Rots, A Arnesen, J. G. Teigen, and K. V. Hoiseth. "A 3D constitutive model for concrete based on a co-rotational concept". In: Computational modelling of concrete structures: proceedings of EURO-C 1998. Ed. by R. de Borst, N. Bicanic, H. Mang, and G. Meschke. Balkema, Rotterdam, 1998, pp. 13–22.

[26] L. Gambarotta and S. Lagomarsino. "Damage models for the seismic response of brick masonry shear walls. Part II: the continuum model and its applications". In: *Earthquake Engineering & Structural Dynamics* 26.4 (1997), pp. 441–462. DOI: `10.1002/(SICI)1096-9845(199704)26:4<441::AID-EQE651>3.0.CO;2-0`.

[27] F. Ghrib and R. Tinawi. "Nonlinear Behavior of Concrete Dams Using Damage Mechanics". In: *Journal of Engineering Mechanics* 121.4 (1995), pp. 513–527. DOI: `10.1061/(ASCE)0733-9399(1995)121:4(513)`.

[28] G. Gioia, Z. Bažant, and B. P. Pohl. "Is no-tension dam design always safe?–a numerical study". In: *Dam Engineering* 3.1 (1992), pp. 23–34.

[29] A. V. van de Graaf. *Sequentially linear analysis for simulating brittle failure*. PhD dissertation, Delft University of Technology, 2017. DOI: `10.4233/uuid:dd9ea945-136c-4b74-bae2-f1a8cf9a6ed9`.

[30] X. Gu, X. Jin, and Y. Zhou. *Basic Principles of Concrete Structures*. Springer-Verlag Berlin Heidelberg, 2016. DOI: `10.1007/978-3-662-48565-1`.

[31] M. A. N. Hendriks and J. G. Rots. "Elastic-brittle fraction model for concrete and masonry structures". In: Computational modelling of concrete structures: proceedings of EURO-C 2014. Ed. by N. Bicanic, H. Mang, G. Meschke, and R. de Borst. CRC Press/Balkema, Leiden, 2014, pp. 495–503.

[32] M. A. N. Hendriks and J. G. Rots. "Sequentially linear versus nonlinear analysis of RC structures". In: *Engineering Computations* 30.6 (2013), pp. 792–801. DOI: `10.1108/EC-May-2012-0105`.

[33] H. J. Herrmann, A. Hansen, and S. Roux. "Fracture of disordered, elastic lattices in two dimensions". In: *Phys. Rev. B* 39 (1 1989), pp. 637–648. DOI: `10.1103/PhysRevB.39.637`.

[34] A. Hillerborg. "Numerical methods to simulate softening and fracture of concrete". In: Fracture mechanics of concrete: Structural application and numerical calculation. Ed. by G. C. Sih and A. Di Tomasso. Springer Netherlands, 1984, pp. 141–170.

[35] A. Hillerborg, M. Modéer, and P. E. Petersson. "Analysis of crack formation and crack growth in concrete by means of fracture mechanics and finite elements". In: *Cement and Concrete Research* 6.6 (1976), pp. 773 –781. DOI: `10.1016/0008-8846(76)90007-7`.

[36] E. Hognestad. "A study of combined bending and axial load in reinforced concrete". In: *Univ. of Illinois Engineering Experiment Station* (1951).

[37] S. Invernizzi, D. Trovato, M. A. N. Hendriks, and A. V. van de Graaf. "Sequentially linear modelling of local snap-back in extremely brittle structures". In: *Engineering Structures* 33.5 (2011), pp. 1617 –1625. DOI: `10.1016/j.engstruct.2011.01.031`.

[38] M. Jirásek and P. Grassl. "Evaluation of directional mesh bias in concrete fracture simulations using continuum damage models". In: *Engineering Fracture Mechanics* 75.8 (2008), pp. 1921 –1943. DOI: `10.1016/j.engfracmech.2007.11.010`.

[39] M. Jirásek and T. Zimmermann. "Analysis of Rotating Crack Model". In: *Journal of Engineering Mechanics* 124.8 (1998), pp. 842–851. DOI: `10.1061/(ASCE)0733-9399(1998)124:8(842)`.

[40] M. Jirásek and T. Zimmermann. "Rotating Crack Model with Transition to Scalar Damage". In: *Journal of Engineering Mechanics* 124.3 (1998), pp. 277–284. DOI: 10.1061/(ASCE)0733-9399(1998)124:3(277).

[41] P. Jäger, P. Steinmann, and E. Kuhl. "Modeling three-dimensional crack propagation—A comparison of crack path tracking strategies". In: *International Journal for Numerical Methods in Engineering* 76.9 (2008), pp. 1328–1352. DOI: 10.1002/nme.2353.

[42] M. D. Kotsovos. "Effect of testing techniques on the post-ultimate behaviour of concrete in compression". In: *Matériaux et Construction* 16.1 (1983), pp. 3–12. DOI: 10.1007/BF02474861.

[43] H. Kupfer, H. K. Hilsdorf, and H. Rusch. "Behaviour of Concrete under biaxial stresses". In: *Journal of the American Concrete Institute* 66.8 (1969), pp. 656–666.

[44] S. H. Kwon, Z. Zhao, and S. P. Shah. "Effect of specimen size on fracture energy and softening curve of concrete: Part II. Inverse analysis and softening curve". In: *Cement and Concrete Research* 38.8 (2008), pp. 1061 –1069. DOI: 10.1016/j.cemconres.2008.03.014.

[45] L. D. Leibengood, D. Darwin, and R. H. Dodds. "Parameters affecting FE analysis of concrete structures". In: *Journal of Structural Engineering* 112.2 (1986), pp. 326–341.

[46] J. Li, X. Gao, X. Fu, C. Wu, and G. Lin. "A Nonlinear Crack Model for Concrete Structure Based on an Extended Scaled Boundary Finite Element Method". In: *Applied Sciences* 8.7 (2018). DOI: 10.3390/app8071067.

[47] Y. J. Li and T. Zimmerman. "Numerical evaluation of the rotating crack model". In: *Computers Structures* 69.4 (1998), pp. 487 –497. DOI: 10.1016/S0045-7949(98)00118-7.

[48] R. W. Litton. *A contribution to the analysis of Concrete Structures under cyclic loading*. PhD dissertation, University of California, Berkeley (USA), 1974.

[49] J. Liu. "Simulating quasi-brittle failures including damage-induced softening based on the mechanism of stress redistribution". In: *Applied Mathematical Modelling* 55 (2018), pp. 685 –697. DOI: 10.1016/j.apm.2017.11.014.

[50] G. Magenes, G. Kingsley, and G. Calvi. *Seismic Testing of a Full-Scale, Two-Story Masonry Building: Test Procedure and Measured Experimental Response prototype. Experimental and numerical investigation on a brick masonry building*. GNDT Rep. 3.0. Pavia (Italy), 1995. DOI: 10.13140/RG.2.1.4590.2962.

[51] V. Mariani, A. T. Slobbe, M. A. N. Hendriks, and J. G. Rots. "Application of Sequentially Linear Analysis to the seismic assessment of slender masonry towers". In: Proceedings of the International Conference on Structural Engineering, Mechanics and Computation (SEMC 2013). Cape Town, South Africa: Taylor Francis, London, 2013. DOI: 10.1201/b15963-337.

[52] G. Meschke and P. Dumstorff. "Energy-based modeling of cohesive and cohesionless cracks via X-FEM". In: *Computer Methods in Applied Mechanics and Engineering* 196.21 (2007), pp. 2338 –2357. DOI: 10.1016/j.cma.2006.11.016.

[53] A. Munjiza, K. R. F. Andrews, and J. K. White. "Combined single and smeared crack model in combined finite-discrete element analysis". In: *International Journal for Numerical Methods in Engineering* 44.1 (1999), pp. 41–57. DOI: 10.1002/(SICI)1097-0207(19990110)44:1<41::AID-NME487>3.0.CO;2-A.

[54] D. Ngo and A. C. Scordelis. "Finite element analysis of reinforced concrete beams". In: *Journal of the American Concrete Institute* 64.3 (1967), pp. 152–163.

[55] M. B. Nooru-Mohamed. *Mixed-mode fracture of concrete: An experimental approach*. PhD dissertation, Delft University of Technology, 1992.

[56] J. Ožbolt and H. W. Reinhardt. "Numerical study of mixed-mode fracture in concrete". In: *International Journal of Fracture* 118.2 (2002), pp. 145–162. DOI: 10.1023/A:1022886127806.

[57] M. Pari, M. A. N. Hendriks, and J. G. Rots. "Non-proportional loading in Sequentially Linear Analysis for 3-D stress states". In: *International Journal for Numerical Methods in Engineering* (2019). DOI: 10.1002/nme.6060.

[58] M. Pari, M. A. N. Hendriks, and J. G. Rots. "Sequentially linear analysis on masonry walls - a new crack closure algorithm". In: Proceedings of the 13th Canadian Masonry Symposium. Ed. by Y. Liu and D. Stubbs. Halifax, Canada: Canada Masonry Design Centre, 2017.

[59] Y. R. Rashid. "Ultimate strength analysis of prestressed concrete pressure vessels". In: *Nuclear Engineering and Design* 7.4 (1968), pp. 334 –344. DOI: 10.1016/0029-5493(68)90066-6.

[60] H. W. Reinhardt. "Fracture mechanics of an elastic softening material like concrete". In: *HERON* 29.2 (1985).

[61] S. N. Roth, P. Léger, and A. Soulaïmani. "A combined XFEM–damage mechanics approach for concrete crack propagation". In: *Computer Methods in Applied Mechanics and Engineering* 283 (2015), pp. 923 –955. DOI: 10.1016/j.cma.2014.10.043.

[62] J. G. Rots. *Computational modeling of concrete fracture*. PhD dissertation, Delft University of Technology, 1988.

[63] J. G. Rots. "Sequentially linear continuum model for concrete fracture". In: Fourth International Conference on Fracture Mechanics of Concrete and Concrete Structures. Ed. by R. de Borst, J. Mazars, G. Pijaudier-Cabot, and J. G. M. van Mier. Vol. 2. Swets Zeitlinger, Lisse, 2001, pp. 831–839.

[64] J. G. Rots, B. Belletti, and S. Invernizzi. "Robust modeling of RC structures with an "event-by-event" strategy". In: *Engineering Fracture Mechanics* 75.3 (2008). International Conference of Crack Paths, pp. 590 –614. DOI: 10.1016/j.engfracmech.2007.03.027.

[65] J. G. Rots and R. de Borst. "Analysis of Mixed-Mode Fracture in Concrete". In: *Journal of Engineering Mechanics* 113.11 (1987), pp. 1739–1758. DOI: 10.1061/(ASCE)0733-9399(1987)113:11(1739).

[66] J. G. Rots and S. Invernizzi. "Regularized sequentially linear saw-tooth softening model". In: *International Journal for Numerical and Analytical Methods in Geomechanics* 28.7-8 (2004), pp. 821–856. DOI: 10.1002/nag.371.

[67] J. G. Rots, S. Invernizzi, B. Belletti, and M. A. N. Hendriks. "Circumventing bifurcations in structural softening". In: Computational Modeling on Concrete, Masonry and Fiber-reinforced Composites. Ed. by M. A. N. Hendriks and S. Billington. Delft, The Netherlands, 2009, pp. 49–52.

[68] J. G. Rots, P. Nauta, G. M. A. Kusters, and J. Blaauwendraad. "Smeared crack approach and fracture localization in concrete". In: *HERON* 30.1 (1985).

[69] R. Sarkhosh, J. C. Walraven, J. A. Den Uijl, and C. R. Braam. *Shear Capacity of Concrete Beams under Sustained Loading - Experimental results*. Delft University of Technology, 2013.

[70] H. E. J. G. Schlangen. *Experimental and numerical analysis of fracture processes in concrete*. PhD dissertation, Delft University of Technology, 1980.

[71] A. T. Slobbe. *Propagation and band width of smeared cracks*. PhD dissertation, Delft University of Technology, 2015. DOI: 10.4233/uuid:6c5cbe8e-89a8-460d-857f-c3403789fec4.

[72] A. T. Slobbe. *Sequentially linear analysis of shear critical reinforced concrete beams*. Master's thesis, Delft University of Technology, 2010.

[73] A. T. Slobbe, M. A. N. Hendriks, and J. G. Rots. "Sequentially linear analysis of shear critical reinforced concrete beams without shear reinforcement". In: *Finite Elements in Analysis and Design* 50 (2012), pp. 108 –124. DOI: 10.1016/j.finel.2011.09.002.

[74] A. T. Slobbe, M. A. N. Hendriks, and J. G. Rots. "Smoothing the propagation of smeared cracks". In: *Engineering Fracture Mechanics* 132 (2014), pp. 147 –168. DOI: 10.1016/j.engfracmech.2014.10.020.

[75] E. Thorenfeldt, A. Tomaszewicz, and J. J. Jensen. "Mechanical properties of high-strength concrete and applications in design". In: In Proceedings of the Symposium Utilization of High-Strength Concrete. Stavanger, Normay, 1987, pp. 149–159.

[76] J. G. M. Van Mier, S. P. Shah, M. Arnaud, J. P. Balayssac, and A. Bascoul et al. "Strain-softening of concrete in uniaxial compression". In: *Materials and Structures/Materiaux et Constructions* 30.198 (1997), pp. 195–209.

[77] F. J. Vecchio and M. P. Collins. "Compression Response of Cracked Reinforced Concrete". In: *Journal of Structural Engineering* 119.12 (1993), pp. 3590–3610. DOI: 10.1061/(ASCE)0733-9445(1993)119:12(3590).

[78] F. J. Vecchio and M. P. Collins. "The Modified Compression-Field Theory for Reinforced Concrete Elements Subjected to Shear". In: *Journal of the American Concrete Institute* 83 (1986), pp. 219–231.

[79] C. V. Verhoosel, J. J. C. Remmers, and M. A. Gutiérrez. "A dissipation-based arc-length method for robust simulation of brittle and ductile failure". In: *International Journal for Numerical Methods in Engineering* 77.9 (2009), pp. 1290–1321. DOI: 10.1002/nme.2447.

[80] L. O. Voormeeren. *Extension and verifcation of Sequentially Linear Analysis to solid elements*. Master's thesis, Delft University of Technology, 2011.

[81] J. Vorel and W. P. Boshoff. "Computational modelling of real structures made of Strain-hardening Cement-based Composites". In: *Applied Mathematics and Computation* 267 (2015), pp. 562–570. DOI: 10.1016/j.amc.2015.01.056.

[82] J. C. Walraven. *Aggregate interlock: A theoretical and experimental analysis*. PhD dissertation, Delft University of Technology, 1980.

[83] K. Willam, E. Pramono, and S. Sture. "Fundamental issues of smeared crack models". In: Proceedings of the SEM-RILEM International Conference on Fracture of Concrete and Rock. Ed. by S. P. Shah and S. E. Swartz. Bethel: SEM, 1987.

[84] C. Yu, P. C. J. Hoogenboom, and J. G. Rots. "Incremental sequentially linear analysis to control failure for quasi-brittle materials and structures including non-proportional loading". In: *Engineering Fracture Mechanics* 202 (2018), pp. 332 –349. DOI: 10.1016/j.engfracmech.2018.07.036.

[85] Z. Zhao, S. H. Kwon, and S. P. Shah. "Effect of specimen size on fracture energy and softening curve of concrete: Part I. Experiments and fracture energy". In: *Cement and Concrete Research* 38.8 (2008), pp. 1049 –1060. DOI: 10.1016/j.cemconres.2008.03.017.